SOLUTION OF NONLINEAR DYNAMIC STRUCTURAL SYSTEMS BY A HYBRID FREQUENCY-TIME DOMAIN APPROACH

by

JAMES DANIEL KAWAMOTO

Bachelor of Science in Civil Engineering
University of California, Berkeley
(1979)

Master of Science in Civil Engineering
Massachusetts Institute of Technology
(1982)

SUBMITTED TO THE DEPARTMENT OF CIVIL ENGINEERING
IN PARTIAL FULFILLMENT OF THE
REQUIREMENTS FOR THE DEGREE OF

DOCTOR OF PHILOSOPHY

at the

MASSACHUSETTS INSTITUTE OF TECHNOLOGY

June 1983

Signature of Author _____
Department of Civil Engineering
March 25, 1983

Certified by _____
Jerome J. Connor
Thesis Supervisor

Accepted by _____
Francois M. M. Morel
Chairman, Departmental Committee on Graduate Students

To My Family

for their

Understanding and Encouragement

SOLUTION OF NONLINEAR DYNAMIC STRUCTURAL SYSTEMS BY A HYBRID FREQUENCY-TIME DOMAIN APPROACH

by

JAMES D. KAWAMOTO

Submitted to the Department of Civil Engineering on March 25, 1983, in partial fulfillment of the requirements for the degree of Doctor of Philosophy.

ABSTRACT

This thesis presented the development and application of an iterative frequency domain solution technique for nonlinear dynamic structural systems. The scheme, referred to as the hybrid frequency-time domain approach, combines the pseudo-force formulation with a mode superposition analysis. Nonlinearities are evaluated in the time domain, and the solution is derived in the frequency domain, implying the use of a theoretically exact numerical integrator.

In conjunction with the development of the new solution technique, stability and accuracy analyses of numerical integrators were surveyed, leading to the presentation of an alternate analysis scheme in the frequency domain. The time and frequency domain accuracy and stability analyses were shown equivalent for the free vibration problem. Extensions to arbitrary loadings are easily handled in the frequency domain.

Various case studies of seismically excited systems demonstrated the developmental considerations for the hybrid frequency-time domain scheme. The results indicated that the new solution scheme can accurately reproduce the response. The scheme was particularly attractive when numerical integration considerations severely restricted the time step size for a direct time integration analysis.

Thesis Supervisor: Jerome J. Connor
Title: Professor of Civil Engineering

ACKNOWLEDGEMENTS

I extend my appreciation to the members of my doctoral committee, Professor Connor, Professor Witmer, Professor Buyukozturk, Professor Kausel, and Professor Sunder. In particular, I thank Professor Connor for acting as my doctoral committee chairman and my research supervisor during my stay at MIT.

I would also like to thank INTEVEP for partially supporting my research and studies during the last three years.

Finally, I express my gratitude to Kong Ann Soon, as a research colleague and friend, for sharing the frustrations, joys, and memories.

TABLE OF CONTENTS

LIST OF FIGURES

LIST OF TABLES

LIST OF SYMBOLS

Symbol	Description
a_n	approximate acceleration response at time t_n, chapter 4
a_n	cosine Fourier series coefficient, chapter 5
$\underline{A}$	amplification matrix
AD	amplitude decay
$\tilde{A}_o$	surface where traction vector is applied
b_n	sine Fourier series coefficient
$\underline{B}$	body force vector
$\underline{\underline{B}}$	left Cauchy-Green deformation tensor
c_n	complex Fourier series coefficient
$\underline{C}$	damping matrix
$\underline{\underline{C}}$	right Cauchy-Green deformation tensor
C_M	inertia coefficient
$\underline{C}_v$	artificial viscous damping matrix
$\underline{d}^i$	difference between residual forces of successive iterations
d_n	approximate displacement response at time t_n
dA	differential surface area
dm	differential mass
dV	differential volume
$\underline{\underline{D}}$	rate of deformation tensor
$\underline{\underline{e}}$	Almansi strain tensor
E^{ijkl}	fourth order elastic modulus tensor
E_{sec}	secant Young's modulus

f^h	artificial hysteretic damping force
f_N	Nyquist frequency
f_o	cutoff frequency
f^v	artificial viscous damping force
f_y	Ramberg-Osgood material model parameter
$\underline{f}_u$	residual force vector
$\underline{F}$	external force vector
$\underline{F}^h$	artificial hysteretic damping force vector
$\underline{F}^{NL}$	pseudo-force vector
$\underline{F}^{OD}$	off-diagonal force vector
$\underline{F}^v$	artificial viscous damping force vector
F_y	yield stress
$\underline{\underline{F}}$	deformation gradient tensor
$\underline{\underline{F}}^{-1}$	spatial deformation gradient tensor
$F(\omega)$	forcing function in the frequency domain
$\Delta\underline{F}_{eff}$	effective load vector
g	gravitational acceleration constant
$\underline{g}_i$	base vectors in the reference configuration of a convected body-fixed coordinate system
$\underline{G}$	quasi-Newton updated stiffness matrix
$\underline{G}_I$	base vectors in the current configuration of a convected body-fixed coordinate system
h	impulse response function
$\underline{H}$	transfer function
$\underline{\tilde{H}}$	approximate numerical integration transfer function
$\underline{H}_e$	exact transfer function

$\underline{i}_I$, $\underline{i}^I$ $\underline{i}_i$, $\underline{i}^i$	base vectors for a rectangular Cartesian coordinate system
$\underline{I}$	internal force vector
$\underline{J}$	transformation matrix from a local to a global coordinate system
$\underline{K}$	stiffness matrix
$\underline{K}_{eff}$	effective stiffness matrix
$\underline{K}_l$	linear stiffness matrix
$\underline{K}_{nl}$	nonlinear stiffness matrix
$\underline{K}_{sec}$	secant stiffness matrix
$\underline{K}_t$	tangent stiffness matrix
$\underline{L}$	load operator
$\underline{M}$	mass matrix
N	number of points in load history
$\underline{N}$	outward normal vector
NB	number of points in frequency spectrum
q_m	element nodal generalized displacement of node m
q^*	global nodal generalized displacement
$\Delta\underline{\tilde{q}}^i$	ith displacement correction
Q	response in the frequency domain
$\underline{r}$	position vector in deformed configuration
$\underline{R}$	position vector in undeformed configuration
$\underline{\underline{R}}$	rotation tensor
S	number of cycles
$\underline{\underline{S}}$	2nd Piola-Kirchhoff stress tensor
t	time

$\underline{t}$	traction vector with respect to undeformed configuration
t_n	nth discrete time step
Δt	time increment
T	structural period
$\underline{T}$	traction vector
$\overline{T}$	approximate period
T_i	ith structural period
$\underline{u}$	displacement vector
$\dot{\underline{u}}$	velocity vector
$\ddot{\underline{u}}$	acceleration vector
u_y	Ramberg-Osgood material model parameter
$\underline{\underline{U}}$	right stretch tensor
v_n	approximate velocity response at time t_n
$\underline{V}$	velocity vector
$\underline{\underline{V}}$	left stretch tensor
V_o	reference volume
$\underline{W}$	convergence residual
$\underline{\underline{W}}$	spin tensor
W_e	external virtual work
W_i	internal virtual work
x_i	reference coordinates for a rectangular Cartesian coordinate system
X_I	current coordinates for a rectangular Cartesian coordinate system
$\underline{y}$	generalized displacement
$\tilde{\underline{y}}$	unconverged generalized response

$\underline{y}^i$	difference between residual forces of successive iterations
Y	generalized response in frequency domain
z	state vector, chapter 4
z	z-transform, chapter 5
$\underline{\underline{\gamma}}$	Green-Lagrange strain tensor
$\underline{\underline{\gamma}}^e$	elastic strain tensor
$\underline{\underline{\gamma}}^p$	plastic strain tensor
$\underline{\Gamma}$	generalized damping matrix normalized with respect to the mass matrix
δ	Dirac delta function
$\overline{\delta}$	logarithmic decay
$\delta\underline{u}$	infinitesimal virtual displacement vector
δW_e	infinitesimal external virtual work
δW_i	infinitesimal internal virtual work
$\underline{\Lambda}$	diagonal matrix containing eigenvalues
ξ	viscous damping ratio
ξ_h	artificial hysteretic damping ratio
ξ_i	curvilinear coordinates for a convected body-fixed coordinate system
ξ_v	artificial viscous damping ratio
$\underline{\Xi}$	generalized force vector
ρ	mass density in present configuration
ρ_o	mass density in deformed configuration
ρ_s	spectral radius
$\underline{\underline{\sigma}}$	Cauchy stress tensor
$\overset{\circ}{\underline{\underline{\sigma}}}$	Jaumann rate of the Cauchy stress tensor

$\underline{\underline{\tau}}$	Kirchhoff stress tensor
$\underline{\underline{\tau}}^{\circ}$	Jaumann rate of Kirchhoff stress tensor
$\underline{\Phi}$	eigenvector (mode shape)
$\underline{\Phi}_l$	linear eigenvector
$\underline{\Phi}_{nl}$	nonlinear eigenvector
$\underline{\Phi}_i(\xi^j)$	displacement interpolation function
ω	circular frequency
ω_c	four times highest load frequency
$\bar{\omega}$	structural frequency
$\tilde{\omega}$	approximate structural frequency
$\tilde{\omega}_D$	approximate damped structural frequency
ω_{max}	highest load frequency
$\bar{\omega}_{max}$	highest structural frequency
Ω	circular frequency multiplied by time increment
$\underline{\underline{1}}$	fundamental or metric tensor
$\{_{m\ n}^{\ s}\}$	Christoffel symbol of the second kind

CHAPTER 1

INTRODUCTION

Considerable advances in the analytical capability of engineers, achieved during the last two decades with the introduction of the digital computer, have reduced the time allocated to tedious calculations and provided the tools necessary to analyze highly complex problems, previously relegated to the status of academic interest. This increased capability has encouraged the extension of structures into more severe environments and simultaneously resulted in less conservative designs approaching the ultimate member capacities.

The analysis of these structures by traditional linear elastic techniques is adequate when the design loads are easily predicted and the possibility of failure poses no threats to life. Many situations, however, involve uncertain load conditions and extreme consequences to the ecosystem in the event of failure. Nuclear reactor containment systems, aircraft, buildings, and offshore

drilling platforms are but a few examples. The load may be an earthquake, tornado, hurricane, or even a flock of birds. The probabilistic nature of the system prompts questions related to the design level (should the structure be designed for the 100 year or 1000 year earthquake?), the behavior of individual structural members (how accurate is the material model?), the construction quality (do we actually construct the structure we specify?), and the response of the entire system (do our analytical tools accurately reproduce the structural response?).

Design philosophies have transformed as the analytical capabilities have expanded. Simple enlargements in member sizes as the load level increases, although allowing the continued use of a linear elastic analysis, cannot always be justified due to significant cost increases and possible technological limitations, as exemplified by the increased weight of aircraft structures requiring larger engines. These considerations have engendered the development of design codes consisting of two design levels. The first level, often referred to as the strength level design, requires the structure to remain linear elastic for a load level expected once during the structure's life. The second level, referred to as the ductility level design, accounts for the probabilistic nature of the structure and loading and provides a measure of the inherent structural safety. A load level corresponding to a situation with an extremely small probability of occurrence is specified, and the

structure must be designed to withstand this load without any loss of lives and minimal impact on the environment. The ductility level design stipulates a load level much higher than that of the strength level, and hence the designer often prefers to exploit the energy absorbing properties of the structure to withstand this load by allowing the structural members to yield and buckle, in other words, become inelastic, rather than redesigning the structure to remain linear elastic and incurring the increased structural cost.

As a result, the computational capability for nonlinear continuum mechanics problems has been developed, expanded, and refined to estimate the nonlinear transient response of structural systems subjected to impact and longer term loads including both kinematic and material nonlinearities. Numerous computer codes are available for general purpose and extremely specialized applications. Additional contributions to the time domain solution technique in terms of numerical integrators and equilibrium iterators and alternate schemes such as the incremental and pseudo-force formulations and the development of more realistic material models continuously induce revisions in this numerical solution library.

The ability to reproduce the actual response of particular structural systems is indeed amazing. The computational cost for conducting a nonlinear analysis,

however, is often prohibitive and limits the analyst to a few extensive large scale analyses if not highly simplified renditions of the original structure. Parameter studies, the underlying foundation by which engineers develop a "feel" for the structural behavior, are usually out of the question. Even super computers on the market today cannot handle all nonlinear problems. The apparent inefficiency of the direct time integration approach for particular problems may stem from numerical stability and accuracy constraints that have no relation to the actual physical behavior of the system, but unnecessarily increase the solution cost. Even when the time integration approach is fairly efficient, various limitations such as the inability to handle frequency dependent stiffness and damping terms prevent the actual system from being modelled properly.

The purpose of this research study, consequently, has been to develop and examine the feasibility of an alternate iterative frequency domain solution technique for nonlinear dynamic structural problems that can produce results with any desired level of accuracy. Applications are oriented toward the nonlinear transient response of seismically excited systems.

This proposed solution scheme, called the hybrid frequency-time domain analysis approach, consists of an iterative solution in the frequency domain with nonlinearities being evaluated in the time domain combined

with a mode superposition approach and updating of the nonlinear modes. A frequency domain solution in essence implies the use of a theoretically exact numerical integrator, and the mode superposition approach allows a significant reduction in the problem size. Both kinematic and material nonlinearities are considered.

The thesis first presents the theoretical formulation followed by a review of current solution techniques and a description of the new solution scheme, and concludes with case studies.

Chapter 2 establishes the foundation of nonlinear continuum mechanics. A brief review of tensor analysis is presented and then the various stress and strain measures are derived from fundamental kinematic definitions. The chapter proceeds on to the energy equations and develops the displacement-based finite element form of the governing equations. A condensed discussion on the constitutive relations concludes the chapter.

In Chapter 3 the different forms of the equations of motion are defined. Assumptions in deriving and limitations in using each form are emphasized. The chapter then discusses various "exact" solution methods, including some recent proposals such as nonlinear mode superposition. Components of the standard direct time integration solution technique are examined in detail.

Numerical integration schemes forming the basis of time integration approaches are studied in Chapter 4 to identify problems associated with numerical integrators, and hence to provide an incentive to use the theoretically exact numerical integrator of a frequency domain analysis. Accuracy and stability analyses are presented in their standard time domain form, and then an alternate formulation in the frequency domain is discussed. The chapter concludes with case studies of nonlinear analyses.

Chapter 5 presents the hybrid frequency-time domain analysis scheme. The chapter begins with a review of the frequency domain analysis and a mathematical presentation of Fourier series and transforms and their numerical implementation. The second part of the chapter describes the hybrid frequency-time domain scheme and examines in detail numerical considerations associated with its development. A discussion of its distinguishing features and suitability concludes the chapter.

The actual application of the hybrid frequency-time domain analysis to seismically excited structural systems is presented in Chapter 6. Each study lists pertinent numerical parameters, allowing a reasonable comparison between the direct time integration and proposed approach. Results are presented in response history form.

Chapter 7 summarizes the research project and provides conclusions related to the new solution scheme.

CHAPTER 2

NONLINEAR CONTINUUM MECHANICS

This chapter establishes the foundation for analyzing nonlinear dynamic structural problems. The various stress and strain measures and the formulation of the governing equations are presented in their most general form, allowing all kinematic nonlinearities in terms of finite strains and rotations and material nonlinearities consisting of path and time dependent behavior. A rigorous mathematical development is followed to ensure that the governing equations are consistent with the theoretical basis. Tensor analysis is applied throughout the presentation to elegantly transform complex abstract definitions into practical equations while maintaining the generality of their application.

The governing equations are derived in a rigorous form to admit all nonlinearities. As a consequence of maintaining mathematical rigor, the presentation may at times appear wordy and pedantic, but a full appreciation of

the generality of nonlinear analyses can be attained only by understanding the subtle qualities of their underlying principles. Nonlinear analyses are not simple extensions of linear analyses obtained by "adding" a couple more structural matrices to the governing equations of motion. Accepting finite strains and rotations engenders a host of definitions for stress and strain quantities, in turn entailing constitutive relations consistent with the selected definitions. The ultimate purpose of conducting nonlinear analyses is to reproduce the actual observed behavior, and consequently any mathematical inconsistency defeats this premise. This chapter follows the outline of classical texts on continuum mechanics such as those by Sedov, Flugge, Malvern, and Prager (25,44,67,73,74) and the more recent report by Rodal and Witmer (72) and text by Bathe (6).

2.1 REVIEW OF TENSOR ANALYSIS

The physical laws governing the deformation of continuous media must be independent of the frame of reference since the properties of the media itself are reference frame independent. The kinematics of deformable media, however, are frame dependent being defined either in the reference configuration or the current deformed configuration. These properties of possessing reference independent governing laws and reference dependent geometrical descriptions are satisfied by tensors and tensor

equations which are invariant quantities, but whose components are frame dependent. Zero order tensors are scalars and first order tensors, vectors. Stress and strain measures introduced later are second order tensors while the elastic modulus is a fourth order tensor. The following presentation is limited to three-dimensional Euclidean space. In reference frames accelerating relative to each other the invariance of the physical laws is satisfied only by the use of tensors in four-dimensional space-time.

Two frames of reference are necessary in continuum mechanics, the current (deformed) configuration and the reference configuration, also defined as the initial (undeformed) configuration. The basis vectors spanning the tensor space can be defined in a rectangular Cartesian coordinate system or more generally in a curvilinear coordinate system.

The notation used here is similar to that of Rodal and Witmer (72). Scalars are denoted by simple letters; vectors, by underlined letters; and second order tensors, by doubly underlined letters. Vector components are identified by their corresponding letter with a single index while tensors are also identified by their same simple letter with double indices. The indices are lower case when the tensor is defined in the reference configuration and upper case when defined in the current configuration. The selection of upper or lower case letters for a rectangular

Cartesian system is arbitrary since the basis remains independent of the configuration. Tensor components in a Cartesian coordinate system are identified by a circumflex sign ("^") on top of the kernel letter.

2.1.1 Scalars and Vectors

A scalar can be defined as a quantity consisting of a single component that is invariant under a coordinate transformation.

Vectors consist of more than one component and can be represented as

$$\underline{v} = v^1\underline{b}_1 + \ldots + v^n\underline{b}_n = \sum_{k=1}^{n} v^i\underline{b}_i = v^i\underline{b}_i \qquad (2.1)$$

where the $\underline{b}_i$ form a basis for $\underline{r}$ and the v^i are the contravariant components. The RHS (right hand side) of the third equality in Eq. 2.1 is written in indicial notation where a summation is implied over any repeated index. Notice that in an n-dimensional space $\mathbb{R}^n$ there exists an infinite number of bases $\underline{b}$ such that each $\underline{b}$ consists of a set of n linearly independent vectors $\underline{b}_i$. The $\underline{b}_i$ need not be orthonormal or even orthogonal.

The vector $\underline{v}$ can also be written in terms of its covariant components v_i with respect to the basis $\underline{b}^i$ as

$$\underline{v} = v_i\underline{b}^i \qquad (2.2)$$

Some general definitions and equalities of vectors are presented next. Given two vectors $\underline{u}$ and $\underline{v}$ where

$$\underline{u} = u^i \underline{b}_i \qquad \underline{v} = v^j \underline{b}_j \tag{2.3}$$

we have

$$\underline{u} \cdot \underline{v} = u^i v^j \underline{b}_i \cdot \underline{b}_j = u^i v^j b_{ij} \tag{2.4}$$

where the operation in Eq. 2.4 is defined as the dot or scalar product of $\underline{u}$ and $\underline{v}$ and

$$b_{ij} \equiv \underline{b}_i \cdot \underline{b}_j \equiv b_{ji} \tag{2.5}$$

Dual (or reciprocal) base vectors $\underline{b}^\ell$ are defined such that

$$\underline{b}_k \cdot \underline{b}^l = \delta^l_k \tag{2.6}$$

where δ^ℓ_k is the Kronecker delta defined by

$$\delta^l_k = \begin{cases} 1, & r=s \\ 0, & r \neq s \end{cases} \tag{2.7}$$

For the special case of an orthonormal set of basis vectors, the dual basis is identical to the given basis.

Taking the dot product of Eq. 2.1 with $\underline{b}^i$ and Eq. 2.2 with $\underline{b}_i$ and using the equality in Eq. 2.6, we obtain the vector components

$$v_k = \underline{v} \cdot \underline{b}_k$$

$$v^l = \underline{v} \cdot \underline{b}^l \tag{2.8}$$

The fundamental tensor components g_{ij}, g^{ij}, $g^{i.}_{.j}$, $g^{.j}_{i.}$ are defined as

$$g_{ij} \equiv \underline{b}_i \cdot \underline{b}_j \qquad g^{ij} \equiv \underline{b}^i \cdot \underline{b}^j \qquad g^{i.}_{.j} \equiv \underline{b}^i \cdot \underline{b}_j \qquad g^{.j}_{i.} \equiv \underline{b}_i \cdot \underline{b}^j \tag{2.9}$$

Using Eqs. 2.1, 2.2, 2.8, and 2.9 the following relations between the contravariant and covariant components of $\underline{v}$ can be established:

$$\begin{aligned} v_i &= \underline{v} \cdot \underline{b}_i = v^j \underline{b}_j \cdot \underline{b}_i = v^j g_{ij} \\ &= v_j \underline{b}^j \cdot \underline{b}_i = v_j g^{j.}_{.i} = v_j \delta^j_i \end{aligned} \tag{2.10}$$

$$\begin{aligned} v^i &= \underline{v} \cdot \underline{b}^i = v_j \underline{b}^j \cdot \underline{b}^i = v_j g^{ij} \\ &= v^j \underline{b}_j \cdot \underline{b}^i = v^j g^{.i}_{j.} = v_j \delta^i_j \end{aligned}$$

The first and third lines of Eq. 2.10 represent the process of lowering and raising indices. This process can also be applied to the basis vectors as follows:

$$\underline{b}^j = g^{ji} \underline{b}_i \qquad \underline{b}_j = g_{ji} \underline{b}^i \tag{2.11}$$

Notice that Eq. 2.11 holds for any arbitrary vectors $\underline{b}^i$ and $\underline{b}_j$. In particular, if $\underline{b}^j = \underline{g}^j$ and $\underline{b}_j = \underline{g}_j$, we have

$$\underline{g}^j = g^{ji} \underline{g}_i \qquad \underline{g}_j = g_{ji} \underline{g}^i \tag{2.12}$$

Therefore,

$$\begin{aligned} \delta^j_i &= \underline{g}_i \cdot \underline{g}^j = g_{ik} \underline{g}^k \cdot g^{jl} \underline{g}_l \\ &= g_{ik} g^{jl} \underline{g}^k \cdot \underline{g}_l \\ &= g_{ik} g^{jl} \delta^k_l \\ &= g_{ik} g^{kj} \end{aligned} \tag{2.13}$$

In other words

$$\left[g^{ij}\right] = \left[g_{ij}\right]^{-1} \tag{2.14}$$

where [ ] represents a matrix. From Eqs. 2.1, 2.2, 2.9, and 2.13 we then have

$$\begin{aligned} \underline{v} &= v_j \underline{b}^j = v_j g_{ij} g^{ij} \underline{b}^j \\ &= v_j \, \underline{b}^j \cdot g_{ij} \underline{b}^i \underline{b}^j \\ &= \underline{v} \cdot g_{ij} \underline{b}^i \underline{b}^j = \underline{v} \cdot \underline{\underline{1}} = \underline{\underline{1}} \cdot \underline{v} \end{aligned} \tag{2.15}$$

Similarly we can show that

$$\underline{\underline{1}} = g_{ij} \underline{b}^i \underline{b}^j = g^{ij} \underline{b}_i \underline{b}_j \tag{2.16}$$

where the unit tensor $\underline{\underline{1}}$ is defined as the fundamental tensor or metric tensor.

The partial derivatives of a vector with respect to spatial coordinates are derived next. When a vector is differentiated in Euclidean space with respect to a scalar variable, another vector expressed in terms of the original basis vectors is obtained. The derivatives of the covariant and contravariant bases are therefore

$$\begin{aligned} \frac{\partial \underline{g}_m}{\partial \xi^n} &= \left\{ \begin{matrix} s \\ m \; n \end{matrix} \right\} \underline{g}_s \\ \frac{\partial \underline{g}_m}{\partial \xi n} &= -\left\{ \begin{matrix} m \\ n \; s \end{matrix} \right\} \underline{g}_s \end{aligned} \tag{2.17}$$

where the $\{_{m\ n}^{\ s}\}$ are defined as the Christoffel symbols of the second kind given as

$$\left\{ \begin{matrix} s \\ m\ n \end{matrix} \right\} \equiv \underline{g}_s \cdot \frac{\partial \underline{g}_m}{\partial \xi^n} = 0.5 g^{sp} \left(\frac{\partial g_{mp}}{\partial \xi^n} + \frac{\partial g_{np}}{\partial \xi^m} - \frac{\partial g_{mn}}{\partial \xi^p} \right) \tag{2.18}$$

Notice that in a Cartesian coordinate system the basis vectors are constant, and hence $\{_{m\ n}^{\ s}\} = 0$. The covariant derivative of a covariant vector component v_i can be derived as follows:

$$\begin{aligned} \frac{\partial \underline{v}}{\partial \xi^s} &= \frac{\partial}{\partial \xi^j} (v_i \underline{g}^i) = \frac{\partial v_i}{\partial \xi^j} \underline{g}^i + v_i \frac{\partial \underline{g}^i}{\partial \xi^j} \\ &= \frac{\partial v_i}{\partial \xi^j} \underline{g}^i - v_i \left\{ \begin{matrix} i \\ j\ k \end{matrix} \right\} \underline{g}^k \\ &= \frac{\partial v_i}{\partial \xi^j} - v_k \left\{ \begin{matrix} k \\ i\ j \end{matrix} \right\} \underline{g}^i \\ &\equiv v_{i,j} \underline{g}^i \end{aligned} \tag{2.19}$$

Therefore,

$$v_{i,j} = \frac{\partial v_i}{\partial \xi^j} - v_k \left\{ \begin{matrix} k \\ i\ j \end{matrix} \right\} \tag{2.20}$$

Similarly, the covariant derivatives of a contravariant vector component v_i can be derived, with the final expression given as

$$v^i{}_{,j} = \frac{\partial v_i}{\partial \xi^j} + v^k \left\{ \begin{matrix} i \\ k\ j \end{matrix} \right\} \tag{2.21}$$

Also by differentiating Eq. 2.6 with respect to ξ^j and letting $\underline{b}^i = \underline{g}^i$, we obtain

$$\frac{\partial \underline{g}^i}{\partial \xi^j} = -\left\{ \begin{matrix} i \\ s\ j \end{matrix} \right\} \underline{g}^s = -\left\{ \begin{matrix} i \\ j\ s \end{matrix} \right\} \underline{g}^s \tag{2.22}$$

We can also show that

$$\frac{\partial \underline{g}^m}{\partial \xi^n} = \frac{\partial \underline{g}^m}{\partial \xi^i} \frac{\partial \xi^i}{\partial \xi_n} = \frac{\partial \underline{g}^m}{\partial \xi^i} g^{ni} = -g^{ni} \left\{ \begin{matrix} m \\ s\ i \end{matrix} \right\} \underline{g}^s \tag{2.23}$$

2.1.2 Second-Order Tensors

A second-order tensor is defined as a linear vector function, which given one vector, assigns another vector (a linear vector function F has the property that $F(a\underline{u}+b\underline{v}) = aF(\underline{u})+bF(\underline{v})$ for arbitrary vectors $\underline{u}$ and $\underline{v}$ and scalars a and b). In other words

$$\underline{u} = \underline{\underline{T}} \cdot \underline{v} \tag{2.24}$$

Since the vectors $\underline{u}$ and $\underline{v}$ can be expanded in terms of either their covariant, u_i and v_j, or their contravariant components, u^i and v^j, the components of $\underline{\underline{T}}$ can be expressed in four forms

$$\begin{aligned} u_i &= T_{ij} v^j \\ u^i &= T^{ij} v_j \\ u_i &= T^{\cdot j}_{i\cdot} v_j \\ u^i &= T^{i\cdot}_{\cdot j} v^j \end{aligned} \tag{2.25}$$

Notice that $T_{i.}^{\cdot j}$ is not necessarily equal to $T_{.j}^{i.}$.

Any second-order tensor $\underline{\underline{T}}$ can be represented by a dyadic. A dyadic is a linear combination of dyads where a dyad is the open product of two vectors $\underline{u}$ and $\underline{v}$. A similar expansion is possible for higher order tensors by using polyadics and polyads. In mathematical notation

$$\underline{\underline{T}} = T^{rs}\underline{b}_r\underline{b}_s = T_{rs}\underline{b}^r\underline{b}^s = T^{r\cdot}_{\cdot s}\underline{b}_r\underline{b}^s = T_{r\cdot}^{\cdot s}\underline{b}^r\underline{b}_s \tag{2.26}$$

The process of raising and lowering indices is identical to that shown for vectors. From Eq. 2.26 we have

$$T^{rs}\underline{b}_r\underline{b}_s - T_{ij}\underline{b}^i\underline{b}^j = \underline{\underline{0}} \tag{2.27}$$

which implies

$$T^{rs}\underline{b}_r\underline{b}_s - T_{ij}b^{ir}b^{js}\underline{b}_r\underline{b}_s = \underline{\underline{0}} \tag{2.28}$$

Therefore,

$$(T^{rs} - T_{ij}b^{ir}b^{js})\underline{b}_r\underline{b}_s = \underline{\underline{0}} \tag{2.29}$$

Taking the dot product of both sides of Eq. 2.29 first with $\underline{b}^t$ and then with $\underline{b}^s$, we obtain

$$T^{rs} = b^{ir}b^{js}T_{ij} \tag{2.30a}$$

and similarly

$$T_{rs} = b_{ir} b_{js} T^{ij}$$

$$T^{r.}_{.s} = b^{ir} b_{js} T^{.j}_{i.} \qquad (2.30b)$$

$$T^{.s}_{r.} = b_{ir} b^{js} T^{i.}_{.j}$$

The components T_{ij} of the tensor $\underline{\underline{T}}$ are derived by using Eqs. 2.1, 2.7, 2.24, and 2.25. By applying the dot product of $\underline{b}_i$ to both sides of Eq. 2.24, we obtain

$$\underline{b}_i \cdot \underline{u} = u_i = \underline{b}_i \cdot (\underline{\underline{T}} \cdot \underline{b}_k v^k)$$
$$= (\underline{b}_i \cdot \underline{\underline{T}} \cdot \underline{b}_k) v^k \qquad (2.31)$$

Comparing Eq. 2.31 with 2.25 we conclude that

$$T_{ik} = \underline{b}_i \cdot \underline{\underline{T}} \cdot \underline{b}_k \qquad (2.32a)$$

and similarly

$$T^{ik} = \underline{b}^i \cdot \underline{\underline{T}} \cdot \underline{b}^k$$

$$T^{.k}_{i.} = \underline{b}_i \cdot \underline{\underline{T}} \cdot \underline{b}^k \qquad (2.32b)$$

$$T^{i.}_{.k} = \underline{b}^i \cdot \underline{\underline{T}} \cdot \underline{b}_k$$

The transpose $\underline{\underline{S}}$ of a tensor $\underline{\underline{T}}$ is defined such that for any vector $\underline{v}$

$$\underline{\underline{T}}\cdot\underline{v} = \underline{v}\cdot\underline{\underline{S}} \tag{2.33}$$

In other words,

$$\begin{aligned} \underline{\underline{T}} &= \underline{\underline{S}}^{T} \\ \underline{\underline{S}} &= \underline{\underline{T}}^{T} \end{aligned} \tag{2.34}$$

In the particular case that

$$\underline{\underline{T}}\cdot\underline{v} = \underline{v}\cdot\underline{\underline{T}} \tag{2.35}$$

$\underline{\underline{T}}$ is a symmetric tensor, and $\underline{\underline{T}}$ is skew symmetric when

$$\underline{\underline{T}}\cdot\underline{v} = -\underline{v}\cdot\underline{\underline{T}} \tag{2.36}$$

The tensor (or operational) product of two second order tensors is defined by

$$\begin{aligned} \underline{\underline{T}}\cdot\underline{\underline{S}} &= T^{ij}\underline{g}_i\underline{g}_j\cdot S^{mn}\underline{g}_m\underline{g}_n \\ &= T^{ij}S^{mn}g_{jm}\underline{g}_i\underline{g}_n \\ &= T^{ij}S_{j}^{\cdot n}\underline{g}_i\underline{g}_n \\ &= T^{ij}S_{jn}\underline{g}_i\underline{g}^n \\ &= T_{ij}S^{jn}\underline{g}^i\underline{g}^n \\ &= \ \ldots \end{aligned} \tag{2.37}$$

Notice that the tensor product of any second or higher order tensor with $\underline{\underline{1}}$ produces the original tensor, and consequently $\underline{\underline{1}}$ is often referred to as the "unit" tensor.

Two scalar products of second order tensors are defined by

$$\begin{aligned}\underline{\underline{T}}:\underline{\underline{S}} &= (T^{ij}\underline{g}_i\,\underline{g}_j):(S_{kl}\underline{g}^k\underline{g}^l)\\ &= T^{ij}S_{kl}(\underline{g}_i\cdot\underline{g}^k)(\underline{g}_j\cdot\underline{g}^l)\\ &= T^{ij}S_{kl}\,\delta^k_i\,\delta^l_j\\ &= T^{ij}S_{ij} = T_{ij}S^{ij} = T^{i\cdot}_{\cdot j}S^{\cdot j}_{i\cdot} = T^{\cdot j}_{i\cdot}S^{i\cdot}_{\cdot j}\end{aligned} \tag{2.38a}$$

and similarly

$$\underline{\underline{T}}\cdot\cdot\underline{\underline{S}} = T^{ij}S_{ji} = T_{ij}S^{ji} = T^{i\cdot}_{\cdot j}S^{\cdot i}_{j\cdot} = T^{\cdot j}_{i\cdot}S^{j\cdot}_{\cdot i} \tag{2.38b}$$

Finally, derivatives of second order tensors can be obtained. Since $\underline{\underline{T}} = T^{rs}\underline{g}_r\underline{g}_s$, we have

$$\begin{aligned}\frac{\partial\,\underline{\underline{T}}}{\partial\xi^p} &= \frac{\partial T^{rs}}{\partial\xi^p}\underline{g}_r\underline{g}_s + T^{ks}\frac{\partial\underline{g}_k}{\partial\xi^p}\underline{g}_s + T^{rk}\underline{g}_r\frac{\partial\underline{g}_k}{\partial\xi^p}\\ &= \frac{\partial T^{rs}}{\partial\xi^p}\,\underline{g}_r\underline{g}_s + T^{ks}\left\{\begin{matrix}r\\k\;\;p\end{matrix}\right\}\underline{g}_r\underline{g}_s + T^{rk}\left\{\begin{matrix}s\\k\;\;p\end{matrix}\right\}\underline{g}_r\underline{g}_s\\ &= T^{rs}{}_{,p}\underline{g}_r\underline{g}_s = \left(\frac{\partial T^{rs}}{\partial\xi^p} + T^{ks}\left\{\begin{matrix}r\\k\;\;p\end{matrix}\right\} + T^{rk}\left\{\begin{matrix}s\\k\;\;p\end{matrix}\right\}\right)\underline{g}_r\underline{g}_s\end{aligned} \tag{2.39}$$

Therefore,

$$
\begin{aligned}
T^{rs}{}_{,p} &= \frac{\partial T^{rs}}{\partial \xi^p} + T^{ks}\left\{ {r \atop k\ p} \right\} + T^{rk}\left\{ {s \atop k\ p} \right\} \\
T^{rs}{}_{,p} &= \frac{\partial T_{rs}}{\partial \xi^p} - T_{ks}\left\{ {k \atop r\ p} \right\} - T_{rk}\left\{ {k \atop s\ p} \right\} \\
T^{r.}_{\ .s,p} &= \frac{\partial T^{r.}_{\ .s}}{\partial \xi^p} + T^{k.}_{\ .s}\left\{ {r \atop k\ p} \right\} - T^{r.}_{\ .k}\left\{ {k \atop s\ p} \right\}
\end{aligned}
\tag{2.40}
$$

such that

$$
\frac{\partial \underline{\underline{T}}}{\partial \xi^p} = T^{rs}{}_{,p}\underline{g}_r\underline{g}_s = T_{rs,p}\underline{g}^r\underline{g}^s = T^{r.}_{\ .s,p}\,\underline{g}_r\underline{g}^s \tag{2.41}
$$

2.2 KINEMATICS

Describing a continuum's motion and its location with respect to a reference frame is referred to as kinematics. Measures of motion include the velocity of particles in the medium and the deformation of the continuum, expressed in terms of strain.

For problems related to solid continua it is often convenient to follow particles in the continuum and describe their motion with respect to a reference configuration. This approach is called the Lagrangian (or material) formulation in contrast to the Eulerian formulation where we consider the motion of particles through a stationary control volume. The Eulerian approach is more appropriate for fluid flow problems. If the reference configuration

corresponds to that at time t=0 (initial, undeformed configuration), a total Lagrangian formulation is being used, while if the reference configuration is that of the most recently considered configuration, then an updated Lagrangian formulation is being used.

The advantages of describing the kinematics of a deformable medium with tensors now become evident, since tensor components are coordinate system dependent and yet, easily transferred from one frame of reference to another.

In the reference configuration all terms will be denoted by lower case letters and in the current configuration, upper case letters. For a rectangular Cartesian coordinate system, or inertial system, the reference coordinates will be defined by x_i while the current coordinates, by X_I. The base vectors are $\underline{i}_I = \underline{i}^I = \underline{i}_i = \underline{i}^i$. A convected body-fixed (intrinsic) coordinate system deforming in common with the continuum will also be used. The curvilinear coordinates for such a system are given by ξ_i with base vectors $\underline{g}_i$ in the reference configuration and $\underline{G}_I$ in the current configuration.

2.2.1 Displacement, Deformation Gradients and Tensors

A particle's location in the deformed and undeformed configurations is given by the position vectors $\underline{r}$ and $\underline{R}$, defined from the origin of the Cartesian system X_I, as shown in Fig. 2.1. Therefore

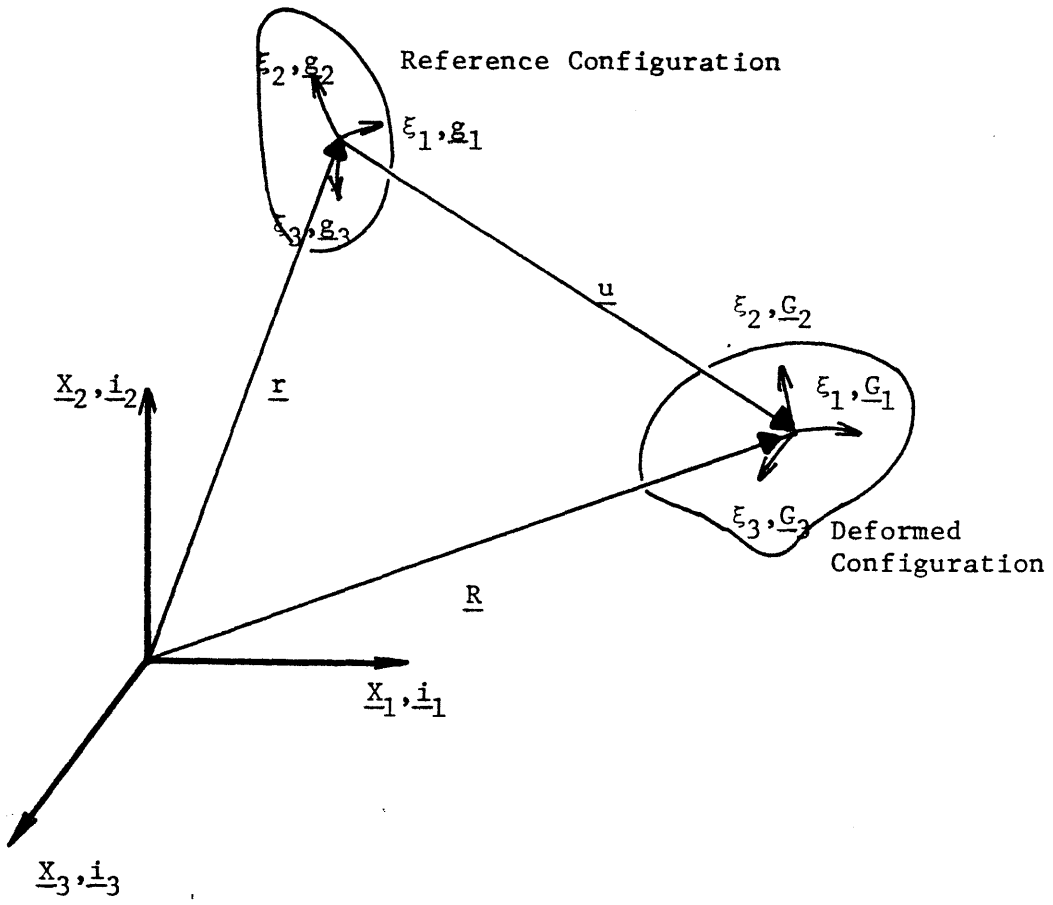

Fig. 2.1 Notation for Reference and Deformed Curvilinear Coordinate Systems Moving in a Cartesian Coordinate System

$$\underline{r} = x_i \underline{i}_i \qquad \underline{R} = X_I \underline{i}_i \tag{2.42}$$

Also

$$\begin{aligned} d\underline{r} &= dx_i \underline{i}_i = d\xi^i \underline{g}_i = d\xi_i \underline{g}^i \\ d\underline{R} &= dX_I \underline{i}_i = d\xi^i \underline{G}_I = d\xi_i \underline{G}^I \end{aligned} \tag{2.43}$$

As a result, the basis vectors can be expressed as

$$\underline{g}_i = \frac{\partial \underline{r}}{\partial \xi^i} = \frac{\partial x_j}{\partial \xi^i} \underline{i}_j \qquad \underline{G}_I = \frac{\partial \underline{R}}{\partial \xi^i} = \frac{\partial X_j}{\partial \xi^i} \underline{i}_j \tag{2.44}$$

Since $\underline{g}_i$ and $\underline{G}_I$ are vectors, all equations from section 2.1 are applicable.

The displacement vector $\underline{u}$ is defined next as

$$\underline{u} = \underline{R} - \underline{r} \tag{2.45}$$

In terms of basis vectors we have

$$\underline{u} = u_i \underline{g}^i = u^i \underline{g}_i = U_I \underline{G}^I = U^I \underline{G}_I = \hat{u}_i \underline{i}_i \tag{2.46}$$

The velocity vector $\underline{v}$ is the time derivative of $\underline{u}$ such that

$$\underline{v} \equiv \dot{\underline{u}} \equiv \left[\frac{\partial \underline{u}}{\partial t}\right]_{\xi i} = (\dot{\underline{R}} - \dot{\underline{r}}) = \dot{\underline{R}} \tag{2.47}$$

and

$$\underline{v} = v_i \underline{g}^i = v^i \underline{g}_i = V_I \underline{G}^I = V^I \underline{G}_I \tag{2.48}$$

Using Eqs. 2.19, 2.47, and 2.48 the time derivative of the deformed basis vector is derived as follows:

$$\dot{\underline{G}}_I = \left[\frac{\partial \dot{\underline{R}}}{\partial \xi^i}\right] = \frac{\partial}{\partial \xi^i}\dot{\underline{R}} = \frac{\partial \underline{V}}{\partial \xi^i} = V^J{}_{,I}\underline{G}_J \qquad (2.49)$$
$$= V_{J,I}\underline{G}^J$$

Furthermore, by differentiating the equality $\underline{G}^I \cdot \underline{G}_J = \delta^I_J$ with respect to time, the time derivative of the contravariant basis vectors is given as

$$\dot{\underline{G}}^I = -V^I{}_{,J}\underline{G}^J = -V^I{}_{,J}\underline{G}_J \qquad (2.50)$$

The deformation gradient $\underline{\underline{F}}$ is a tensor associating with each vector $d\underline{r}$ at $\underline{r}$ a vector $d\underline{R}$ at $\underline{R}$. In mathematical symbols

$$d\underline{R} = \underline{\underline{F}} \cdot d\underline{r} = d\underline{r} \cdot \underline{\underline{F}}^T \qquad (2.51)$$

By definition the rectangular Cartesian components of $\underline{\underline{F}}$ are given by $\frac{\partial X_I}{\partial x_j}$. The same result can be derived by expanding Eq. 2.51 as follows:

$$d\underline{R} = \underline{\underline{F}} \cdot d\underline{r} = (\hat{F}_{Ij}\underline{i}_I\underline{i}_j) \cdot (dx_k\underline{i}_k) \qquad (2.52)$$
$$= \hat{F}_{Ij}dx_j\underline{i}_I$$

Using Eq. 2.42 we then have

$$d\underline{X}_I \underline{i}_i = \underline{F}_{Ij} dx_j \underline{i}_i \tag{2.53}$$

implying

$$\hat{F}_{Ij} = \frac{\partial X_I}{\partial x_j} \tag{2.54}$$

Furthermore, by using the equivalent of Eq. 2.45 in a Cartesian coordinate system, we can show that

$$\hat{F}_{Ij} = \delta^i_j + \frac{\partial \hat{u}_i}{\partial x_j} \tag{2.55}$$

Also

$$\underline{G}_I = \underline{\underline{F}} \cdot \underline{g}_i = \underline{g}_i \cdot \underline{\underline{F}}^T \tag{2.56}$$

implying

$$\underline{\underline{F}} = \underline{G}_I \underline{g}^i \tag{2.57}$$

The components of $\underline{\underline{F}}$ in a convected system are derived by expanding Eq. 2.56

$$\underline{G}_J = \underline{\underline{F}} \cdot \underline{g}_j = (F^j_{.k} \underline{g}_i \underline{g}^k) \cdot \underline{g}_j = F^{i.}_{.j} \underline{g}_i \tag{2.58}$$

From Eqs. 2.44 and 2.45 we have

$$\underline{G}_I - \underline{g}_j = \frac{\partial}{\partial \xi^j}(\underline{R} - \underline{r}) = \frac{\partial \underline{u}}{\partial \xi^j} \tag{2.59}$$

Using Eq. 2.34, Eq. 2.59 is transformed as follows:

$$\underline{G}_I - \underline{g}_j = u_{i,j}\underline{g}^i = u^i{}_{,j}\underline{g}_i \tag{2.60}$$

Therefore,

$$\begin{aligned}\underline{G}_I &= \underline{g}_j + u_{i,j}\underline{g}^i = (g_{ij} + u_{i,j})\underline{g}^i \\ &= \underline{g}_j + u^i{}_{,j}\underline{g}_i = (\delta^i_j + u^i{}_{,j})\underline{g}_i\end{aligned} \tag{2.61}$$

Comparing Eqs. 2.58 and 2.61 we conclude

$$\begin{aligned}F_{ij} &= g_{ij} + u_{i,j} \\ F^{i.}_{.j} &= \delta^i_j + u^i{}_{,j}\end{aligned} \tag{2.62}$$

and similarly

$$\begin{aligned}F^{ij} &= g^{ij} + u^i{}_{,}{}^j \\ F^{.j}_{i.} &= \delta^j_i + u_i{}_{,}{}^j\end{aligned} \tag{2.63}$$

We next examine the spatial deformation gradient tensor $\underline{\underline{F}}^{-1}$ with the properties

$$\begin{aligned}d\underline{r} &= \underline{\underline{F}}^{-1}\cdot d\underline{R} = d\underline{R}\cdot(\underline{\underline{F}}^{-1})^T \\ \underline{g}_i &= \underline{\underline{F}}^{-1}\cdot\underline{G}_I = \underline{G}_I\cdot(\underline{\underline{F}}^{-1})^T\end{aligned} \tag{2.64}$$

By a similar procedure as before it can be shown that

$$(\hat{F}^{-1})_{iJ} = \frac{\partial x_i}{\partial X_j} = \delta_{ij} - \frac{\partial \hat{u}_i}{\partial X_j} \tag{2.65}$$

In terms of convected coordinates

$$\begin{aligned} (F^{-1})^{iJ} &= G^{IJ} \\ (F^{-1})_{iJ} &= g_{ij} \\ (F^{-1})^{i.}_{.J} &= \delta^i_j \\ (F^{-1})^{.J}_{i.} &= g_{ik}G^{KJ} \end{aligned} \tag{2.66}$$

and

$$\begin{aligned} (F^{-1})_{IJ} &= G_{IJ} - U_{I,J} \\ (F^{-1})^{IJ} &= G^{IJ} - U^{I\ J}_{\ ,} \\ (F^{-1})^{I.}_{.J} &= \delta^i_j - U^I_{\ ,J} \\ (F^{-1})^{.J}_{I.} &= \delta^j_i - U_{I,}^{\ \ J} \end{aligned} \tag{2.67}$$

The right Cauchy-Green deformation tensor $\underline{\underline{C}}$ is defined as

$$\underline{\underline{C}} = \underline{\underline{U}}^2 = \underline{\underline{U}}\cdot\underline{\underline{U}} = \underline{\underline{F}}^T\cdot\underline{\underline{F}} \tag{2.68}$$

and the left Cauchy-Green deformation tensor $\underline{\underline{B}}$ as

$$\underline{\underline{B}} = \underline{\underline{V}}^2 = \underline{\underline{V}}.\underline{\underline{V}} = \underline{\underline{F}}.\underline{\underline{F}}^T \tag{2.69}$$

where $\underline{\underline{U}}$ and $\underline{\underline{V}}$ are defined by applying the polar decomposition theorem to $\underline{\underline{F}}$ such that

$$\underline{\underline{F}} = \underline{\underline{R}}\cdot\underline{\underline{U}} = \underline{\underline{V}}\cdot\underline{\underline{R}} \tag{2.70}$$

$\underline{\underline{R}}$ is an orthogonal tensor defined as the rotation tensor and $\underline{\underline{U}}$ and $\underline{\underline{V}}$ are symmetric, positive definite tensors defined, respectively, as the right and left stretch tensors. Therefore, the application of $\underline{\underline{F}}$ to $d\underline{r}$ can be viewed as a stretching of $d\underline{r}$ by $\underline{\underline{U}}$ and then $\underline{\underline{R}}$ applying a rigid rotation to obtain $d\underline{R}$ (similarly defined for $\underline{\underline{V}}$). From Eqs. 2.68, 2.69, and 2.70 it is evident that

$$\underline{\underline{B}} = \underline{\underline{R}}\cdot\underline{\underline{C}}\cdot\underline{\underline{R}}^T \tag{2.71}$$

Using the previously derived results for the components of $\underline{\underline{F}}$, we have

$$\begin{aligned}
\hat{C}_{ij} &= (\hat{F}_{iK})^T\hat{F}_{Kj} = \hat{F}_{Ki}\hat{F}_{Kj} = \frac{\partial X_K}{\partial x_i}\frac{\partial X_K}{\partial x_j} \\
&= (\delta_i^k + \frac{\partial \hat{u}_k}{\partial x_i})(\delta^k_j + \frac{\partial \hat{u}_k}{\partial x_j}) \\
&= \delta_{ij} + \frac{\partial \hat{u}_i}{\partial x_j} + \frac{\partial \hat{u}_j}{\partial x_i} + \frac{\partial \hat{u}_k}{\partial x_i}\frac{\partial \hat{u}_k}{\partial x_j}
\end{aligned} \tag{2.72}$$

In convected coordinates we can also show

$$
\begin{aligned}
C_{ij} &= (F_{ik})^{T} F^{k.}_{.j} = F_{ki} F^{k.}_{.j} = G_{IJ} \\
&= (g_{ij} + u_{k,i})(\delta^{k}_{j} + u^{k}_{\ ,j}) \\
&= g_{ij} + u_{i,j} + u_{j,i} + u^{k}_{\ ,j} u_{k,i}
\end{aligned}
\tag{2.73}
$$

and

$$
\begin{aligned}
C^{ij} &= g^{ij} + u^{i}_{\ ,}{}^{j} + u^{j}_{\ ,}{}^{i} + u^{k}_{\ ,}{}^{j} u_{k,}{}^{i} \\
C^{i}_{j} &= g^{ij} + u^{i}_{\ ,j} + u_{j,}{}^{i} + u_{k,}{}^{i} u^{k}_{\ ,j}
\end{aligned}
\tag{2.74}
$$

2.2.2 Strain Tensors

Using the definitions of deformation gradients and tensors given in section 2.2.1, various measures of strain will now be established. For large deformation and rotation problems a unique measure of strain no longer exists, and therefore strain measures should be selected such that they are numerically easy to implement and compatible with the various constitutive relations. These strain measures should also display no variation under rigid body motions. In the special case of small strain problems, all definitions should reduce to the same form. Many of the common strain measures are defined in terms of squared

length, which is intrinsically appealing since Euclidian distance is generally measured in terms of squared values.

We first define the Green-Lagrange strain tensor $\underline{\underline{\gamma}}$ as

$$\underline{\underline{\gamma}} = 0.5(\underline{\underline{C}} - \underline{\underline{1}}) \tag{2.75}$$

From our previous definitions we then have

$$\underline{\underline{\gamma}} = 0.5(\underline{\underline{U}}^2 - \underline{\underline{1}}) = 0.5(\underline{\underline{F}}^T \cdot \underline{\underline{F}} - \underline{\underline{1}}) \tag{2.76}$$

Also by noting that

$$\begin{aligned} (dS)^2 - (ds)^2 &= d\underline{R} \cdot d\underline{R} - d\underline{r} \cdot d\underline{r} \\ &= d\underline{r} \cdot \underline{\underline{C}} \cdot d\underline{r} - d\underline{r} \cdot \underline{\underline{1}} \cdot d\underline{r} \\ &= d\underline{r} \cdot (\underline{\underline{C}} - \underline{\underline{1}}) \cdot d\underline{r} \end{aligned} \tag{2.77}$$

and comparing this result with Eq. 2.75, we deduce that

$$d\underline{r} \cdot \underline{\underline{\gamma}} \cdot d\underline{r} = \frac{(dS)^2 - (ds)^2}{2} \tag{2.78}$$

The components of the Green-Lagrange strain tensor are given as follows:

$$\begin{aligned} \gamma_{ij} &= 0.5(\hat{C}_{ij} - \delta_{ij}) = 0.5\left(\frac{\partial X_k}{\partial x_i}\frac{\partial X_k}{\partial x_j} - \delta_{ij}\right) \\ &= 0.5\left(\frac{\partial \hat{u}_i}{\partial x_j} + \frac{\partial \hat{u}_j}{\partial x_i} + \frac{\partial \hat{u}_k}{\partial x_i}\frac{\partial \hat{u}_k}{\partial x_j}\right) \end{aligned} \tag{2.79}$$

$$\gamma_{ij} = 0.5(C_{ij}-g_{ij})=0.5(G_{IJ}-g_{ij}) =0.5(u_{i,j}+u_{j,i}+u^{k}{}_{,j}u_{k,i})$$

$$\gamma^{i}_{j} = 0.5(C_{ij}-\delta^{i}_{j})=0.5(g^{ik}G_{KJ}-\delta^{i}_{j})=0.5(u^{i}{}_{,j}+u_{j}{}_{,}{}^{i}+u^{k}{}_{,j}u_{k,}{}^{i}) \quad (2.79)$$

$$\gamma^{ij} = 0.5(C^{ij}-g^{ij})=0.5(g^{il}g^{jk}G_{LK}-g^{ij})=0.5(u^{i}{}_{,}{}^{j}+u^{j}{}_{,}{}^{i}+u^{k}{}_{,}{}^{j}u_{k,}{}^{i})$$

In contrast to the Green-Lagrange strain tensor given in terms of derivatives of displacements with respect to reference coordinates, the Almansi tensor is defined by derivatives of displacements with respect to current coordinates. Therefore, the Almansi tensor $\underline{\underline{e}}$ is given as

$$\begin{aligned}\underline{\underline{e}} &= 0.5(\underline{\underline{1}} - \underline{\underline{B}}^{-1}) \\ &= 0.5(\underline{\underline{1}} - (\underline{\underline{V}}^{2})^{-1}) \\ &= 0.5(\underline{\underline{1}} - (\underline{\underline{F}}^{-1})^{T}.(\underline{\underline{F}}^{-1}))\end{aligned} \quad (2.80)$$

Using a similar process as before, it can be shown that

$$\underline{dR}.\underline{\underline{e}}.\underline{dR} = \frac{(dS)^{2} - (ds)^{2}}{2} \quad (2.81)$$

and

$$\begin{aligned}\hat{e}_{IJ} &= 0.5(\delta_{ij} - \frac{\partial x_k}{\partial X_I}\frac{\partial x_k}{\partial X_J}) = 0.5(\frac{\partial \hat{U}_i}{\partial X_J} + \frac{\partial \hat{U}_j}{\partial X_I} - \frac{\partial \hat{U}_k}{\partial X_I}\frac{\partial \hat{U}_k}{\partial X_J} \\ e_{IJ} &= 0.5(G_{IJ} - g_{ij}) = 0.5(U_{I,J} + U_{J,I} - U^{K}{}_{,J}U_{K,I}) \\ e^{I}_{J} &= 0.5(\delta^{i}_{j} - G^{IK}g_{kj}) = 0.5(U^{I}{}_{,J} + U_{J,}{}^{I} - U^{K}{}_{,J}U_{K,}{}^{I}) \\ e^{IJ} &= 0.5(G^{IJ} - G^{IL}G^{JK}g_{lk}) = 0.5(U^{I}{}_{,}{}^{J} + U^{J}{}_{,}{}^{I} - U^{K}{}_{,}{}^{J}U_{K,}{}^{I})\end{aligned} \quad (2.82)$$

Other strain measures in terms of linear length or logarithmic length also exist, but we shall limit ourselves to the most commonly used Green-Lagrange and Almansi strain tensors.

The time derivatives of strain are required for rate-type constitutive equations. The rate of deformation tensor $\underline{\underline{D}}$ is defined as

$$\underline{\underline{D}} = \dot{\underline{\underline{U}}}_t(t) = \dot{\underline{\underline{V}}}_t(t) \tag{2.83}$$

where the $\underline{\underline{U}}$ and $\underline{\underline{V}}$ are the stretch tensors defined previously and the subscript t refers to the configuration at time t. An alternate definition of the deformation tensors in covariant component form is given as follows:

$$2D_{IJ}d\xi^i d\xi^j = (dS^2 - ds^2)\dot{} = (d\dot{S}^2) \tag{2.84}$$

where $D_{IJ} = \dot{\gamma}_{ij} = \dot{e}_{IJ}$. Therefore from Eq. 2.79 and Eq. 2.49

$$\begin{aligned} D_{IJ} \equiv \dot{\gamma}_{ij} &= 0.5(G_{IJ} - g_{ij})\dot{} = 0.5\dot{G}_{IJ} \\ &= 0.5(\underline{G}_I \cdot \underline{G}_J)\dot{} \\ &= 0.5(\underline{G}_I \cdot \dot{\underline{G}}_J + \dot{\underline{G}}_I \cdot \underline{G}_J) \\ &= (\underline{G}_I \cdot V_{K,J}\underline{G}^K + V_{L,I}\underline{G}^L \cdot \underline{G}_J) \\ &= 0.5(V_{I,J} + V_{J,I}) \end{aligned} \tag{2.85a}$$

Similarly we can show that

$$
\begin{aligned}
D^{IJ} &= 0.5(V^{I}{}_{,}{}^{J} + V^{J}{}_{,}{}^{I}) \\
D^{I}_{J} &= 0.5(V^{I}{}_{,J} + V_{J,}{}^{I}) \\
\hat{D}_{IJ} &= 0.5\left(\frac{\partial \hat{V}_I}{\partial X_J} + \frac{\partial \hat{V}_J}{\partial X_I}\right)
\end{aligned}
\tag{2.85b}
$$

We now look at the material rate of the Almansi strain tensor in terms of its covariant components

$$
\begin{aligned}
\dot{\underline{\underline{e}}} &= (e_{IJ}\dot{\underline{G}}^{I}\underline{G}^{J}) \\
&= \dot{e}_{IJ}\underline{G}^{I}\underline{G}^{J} + e_{IJ}\dot{\underline{G}}^{I}\underline{G}^{J} + e_{IJ}\underline{G}^{I}\dot{\underline{G}}^{J}
\end{aligned}
\tag{2.86}
$$

Therefore $\dot{\underline{\underline{e}}}$ does not vanish for rigid body motions since $\dot{\underline{G}}^{K}$ contains rigid body components.

However, for the Green-Lagrange strain, $\dot{\underline{\gamma}}$ can be expanded such that

$$
\dot{\underline{\gamma}} = (\gamma_{ij}\dot{\underline{g}}^{i}\underline{g}^{j}) = \dot{\gamma}_{ij}\underline{g}^{i}\underline{g}^{j} \tag{2.87}
$$

and therefore $\dot{\underline{\gamma}}$ is a more appropriate measure for rate-type problems since it vanishes for rigid motions. We now derive the relation between $\underline{\underline{D}}$ and $\dot{\underline{\gamma}}$

$$
\begin{aligned}
\dot{\gamma}^{i}_{j} &= \dot{\gamma}_{kj}g^{ik} = D_{KJ}g^{ik} = G_{KL}D^{L}_{J}g^{ik} \\
&= (g_{kl} + 2\gamma_{kl})D^{L}_{J}g^{ik} \\
&= (\delta^{i}_{l} + 2\gamma^{i}_{l})D^{L}_{J}
\end{aligned}
\tag{2.88}
$$

Similar expressions can be found for the other component types.

2.3 STRESS TENSORS

The traction vector $\underline{T}$ is defined as the surface force per unit area

$$\underline{T} = \frac{d\underline{P}}{dA} \tag{2.89}$$

where $d\underline{P}$ is the force exerted across the differential surface with area dA and outward normal $\underline{N}$.

Beginning with this definition of the traction vector, various stress tensors can be defined. The Cauchy stress tensor $\underline{\underline{\sigma}}$ is defined by

$$\underline{T} = \underline{N} \cdot \underline{\underline{\sigma}} \tag{2.90}$$

Consequently, $\underline{\underline{\sigma}}$ is defined in the deformed space, and

$$\begin{aligned} \underline{\underline{\sigma}} &= \hat{\sigma}_{IJ}\underline{\hat{i}}_i\underline{\hat{i}}_j = \sigma^{IJ}\underline{G}_I\underline{G}_J = \sigma_{IJ}\underline{G}^I\underline{G}^J \\ &= \sigma^I_{\cdot J}\underline{G}_I\underline{G}^J = \sigma^{\cdot J}_{I\cdot}\underline{G}^I\underline{G}_J \end{aligned} \tag{2.91}$$

Using Eqs. 2.89-2.91, we then have

$$\begin{aligned} d\underline{P} &= \underline{N}\cdot\underline{\underline{\sigma}}dA = N_I\underline{G}^I\cdot\sigma^{JK}\underline{G}_J\underline{G}_K dA \\ &= N_I\sigma^{IK}\underline{G}_K dA \end{aligned} \tag{2.92}$$

Similarly $d\underline{P}$ can be expressed in terms of the undeformed configuration by using Nanson's relation

$$\rho_o n_i dA_o = \rho N_I dA \tag{2.93}$$

where $\rho = dm/dV$ is the mass density in the present configuration; $\rho_o = dm/dV_o$ is the mass density in the reference configuration; dm, the mass of the body with volume dV in the deformed configuration; and n_i, the covariant components of the unit normal to the differential surface area dA_o. Using Eq. 2.93 with 2.92, the following is derived

$$d\underline{P} = N_I \sigma^{IK} \underline{G}_K dA = \frac{\rho_o}{\rho} n_i \sigma^{IK} \underline{G}_K dA_o \tag{2.94}$$

The Kirchhoff stress tensor $\underline{\underline{\tau}}$ is next defined in terms of the Cauchy stress tensor as

$$\underline{\underline{\tau}} \equiv \frac{\rho_o}{\rho} \underline{\underline{\sigma}} \tag{2.95}$$

Therefore,

$$\underline{T} = \frac{\rho}{\rho_o} \underline{N} \cdot \underline{\underline{\tau}} \tag{2.96}$$

and

$$d\underline{P} = n_i \tau^{IK} \underline{G}_K dA_o \tag{2.97}$$

A traction vector $\underline{t}$ with respect to the undeformed configuration dA_o can be defined such that

$$\underline{t} = \frac{d\underline{P}}{dA_o} = n_i \tau^{IK} \underline{G}_K \tag{2.98}$$

Finally the 2nd Piola-Kirchhoff stress tensor $\underline{\underline{S}}$ is defined by

$$\underline{t} = \underline{n} \cdot (\underline{\underline{S}} \cdot \underline{\underline{F}}^T) \tag{2.99}$$

It can be shown that the contravariant components S^{ij} of the 2nd Piola-Kirchhoff stress are equal to the contravariant components of the Kirchhoff stress

$$S^{ij} = \tau^{IJ} \tag{2.100}$$

Therefore,

$$\tau^{I.}_{.K} G^{KJ} = S^{i.}_{.1} g^{1j} \tag{2.101}$$

or

$$\tau^{I.}_{.K} = S^{i.}_{.1} g^{1j} G_{JK} = S^{i.}_{.1} (\delta^i_1 + 2\,\gamma^i_1) \tag{2.102}$$

In general, the following relations between the various stress tensors can be derived:

$$\underline{\underline{\tau}} = \frac{\rho_o}{\rho} \underline{\underline{\sigma}} = \underline{\underline{F}} \cdot \underline{\underline{S}} \cdot \underline{\underline{F}}^T = \underline{\underline{R}} \cdot \underline{\underline{U}} \cdot \underline{\underline{S}} \cdot \underline{\underline{U}} \cdot \underline{\underline{R}}^T \tag{2.103}$$

$$\underline{\underline{S}} = \frac{\rho_o}{\rho} \underline{\underline{F}}^{-1} \cdot \underline{\underline{\sigma}} \cdot (\underline{\underline{F}}^{-1})^T = \frac{\rho_o}{\rho} \underline{\underline{U}}^{-1} \cdot \underline{\underline{R}}^T \cdot \underline{\underline{\sigma}} \cdot \underline{\underline{R}} \cdot \underline{\underline{U}}^{-1} \tag{2.104}$$

$$\underline{\underline{S}} = \underline{\underline{F}}^{-1} \cdot \underline{\underline{\tau}} \cdot (\underline{\underline{F}}^{-1})^T = \underline{\underline{U}}^{-1} \cdot \underline{\underline{R}}^T \cdot \underline{\underline{\tau}} \cdot \underline{\underline{R}} \cdot \underline{\underline{U}}^{-1} \tag{2.105}$$

$$\underline{\underline{\sigma}} = \frac{\rho}{\rho_o} \underline{\underline{F}} \cdot \underline{\underline{S}} \cdot \underline{\underline{F}}^T = \frac{\rho}{\rho_o} \underline{\underline{R}} \cdot \underline{\underline{U}} \cdot \underline{\underline{S}} \cdot \underline{\underline{U}} \cdot \underline{\underline{R}}^T \tag{2.106}$$

The use of different stress tensors allows an efficient numerical solution of the governing equations of motion. Some stress tensors are more compatible with the constitutive relations (2nd Piola-Kirchhoff stress tensor) while other stress tensors (Cauchy) give a "true" physical value of the stress.

In addition to the stress tensors, the rates of stress tensors must be defined such that incremental or rate dependent constitutive relations can be employed. The total rate of the traction vector less the rigid body rate gives the rate of the traction vector corresponding to pure deformation

$$\dot{\underline{T}} - (-\underline{T} \cdot \underline{W}) \tag{2.107}$$

where $\underline{\underline{W}}$ is the spin tensor

$$\underline{\underline{W}} \equiv \dot{\underline{\underline{R}}}_t(t) \tag{2.108}$$

Therefore,

$$\begin{aligned}\dot{\underline{T}} - (-\underline{T}\cdot\underline{W}) &= (\dot{\underline{N}}\cdot\underline{\sigma}) + (\underline{N}\cdot\dot{\underline{\sigma}})\cdot\underline{W} \\ &= \dot{\underline{N}}\cdot\underline{\sigma} + \underline{N}\cdot\dot{\underline{\sigma}} + \underline{N}\cdot(\underline{\sigma}\cdot\underline{W}) \\ &= \underline{N}\cdot(\dot{\underline{\sigma}} + \underline{\sigma}\cdot\underline{W} - \underline{W}\cdot\underline{\sigma}) \\ &= \underline{N}\cdot\overset{\circ}{\underline{\sigma}}\end{aligned} \tag{2.109}$$

where $\overset{\circ}{\underline{\sigma}}$ is the Jaumann (co-rotational) rate of the Cauchy stress

$$\overset{\circ}{\underline{\sigma}} = \dot{\underline{\sigma}} + \underline{\sigma}\cdot\underline{W} - \underline{W}\cdot\underline{\sigma} \tag{2.110}$$

Notice that for rigid body rotations $\dot{\underline{T}} = -\underline{T}\cdot\underline{W}$, and therefore $\dot{\underline{\sigma}} = \underline{0}$, implying that the Jaumann rate properly accounts for rigid body rotations. Furthermore, $\dot{\underline{\sigma}}$ can be expanded and the following obtained:

$$\dot{\underline{\sigma}} = \dot{\sigma}^{IJ}\underline{G}_I\underline{G}_J + \underline{D}\cdot\underline{\sigma} + \underline{\sigma}\cdot\underline{D} + \underline{W}\cdot\underline{\sigma} - \underline{\sigma}\cdot\underline{W} \tag{2.111}$$

and therefore

$$\overset{\circ}{\underline{\sigma}} = \dot{\sigma}^{IJ}\underline{G}_I\underline{G}_J + \underline{\sigma}\cdot\underline{D} + \underline{D}\cdot\underline{\sigma} \tag{2.112}$$

Notice that $\dot{\underline{\sigma}} = \underline{0}$ for rigid body rotations since $\underline{D} = \underline{0}$ for a rigid body motion. Similarly

$$\overset{\circ}{\underline{\sigma}} = \dot{\sigma}^{I}_{\cdot J}\underline{G}_I\underline{G}^J + \underline{D}\cdot\underline{\sigma} - \underline{\sigma}\cdot\underline{D} \tag{2.113}$$

We can also find the Jaumann rate of the Kirchhoff stress tensor

$$\overset{\circ}{\underline{\underline{\tau}}} = \left(\frac{\rho_o}{\rho} \underline{\underline{\sigma}} \right)^{\bullet} = \left(\frac{\rho_o}{\rho} \underline{\underline{1}} \cdot \underline{\underline{\sigma}} \right)^{\circ}$$
$$= \left(\frac{\rho_o}{\rho} \underline{\underline{1}} \right)^{\bullet} \cdot \underline{\underline{\sigma}} + \frac{\rho_o}{\rho} \underline{\underline{1}} \cdot \overset{\circ}{\underline{\underline{\sigma}}} \qquad (2.114)$$

which can be reduced to

$$\overset{\circ}{\underline{\underline{\tau}}} = \frac{\rho_o}{\rho} \left[\overset{\circ}{\underline{\underline{\sigma}}} + (\text{tr } \underline{\underline{D}}) \underline{\underline{\sigma}} \right] = \frac{\rho_o}{\rho} \overset{\circ}{\underline{\underline{\sigma}}} + (\text{tr } \underline{\underline{D}}) \underline{\underline{\tau}} \qquad (2.115)$$

2.4 ENERGY EQUATIONS

The governing equations of dynamic structural systems are developed in this section using a variational approach. Beginning with a body in equilibrium subjected to body forces and external surface tractions and satisfying the prescribed displacement boundary conditions, we employ the principle of virtual work which states that the external virtual work, δW_e, must equal the internal virtual work, δW_i. Therefore, a set of compatible, infinitesimal virtual displacements $\delta \underline{u}$, satisfying the essential boundary conditions, are imposed on the body and we obtain

$$\delta W_i = \delta W_e \qquad (2.116)$$

The internal virtual work W_i can be expressed in different forms depending on the specified definitions of stress and strain. In terms of the Cauchy stress we have

$$W_i = \int_v \int_t \underline{\underline{\sigma}} : \underline{\underline{D}} \, dt \, dV \tag{2.117}$$

and in component form

$$\begin{aligned} W_i &= \int_v \int_t \hat{\sigma}_{IJ} \hat{D}_{IJ} \, dt \, dV = \int_v \int_t \sigma^{IJ} D_{IJ} \, dt \, dV \\ &= \int_v \int_t \sigma_{IJ} D^{IJ} \, dt \, dV = \int_v \int_t \sigma \, {}^{I}_{J} D^{J}_{I} \, dt \, dV \end{aligned} \tag{2.118}$$

Equation 2.117 can also be expressed in the reference configuration

$$W_i = \int_t \int_{V_o} \underline{\underline{\sigma}} : \underline{\underline{D}} \, \frac{\rho_o}{\rho} \, dV_o \, dt \tag{2.119}$$

Using Eq. 2.95, the internal virtual work can be expressed in terms of the Kirchhoff stress tensor $\underline{\underline{\tau}}$ as

$$W_i = \int_t \int_{V_o} \underline{\underline{\tau}} : \underline{\underline{D}} \, dV_o dt \tag{2.120}$$

Similarly, we can represent the internal virtual work in terms of the 2nd Piola-Kirchhoff stress

$$W_i = \int_t \int_{V_o} \underline{\underline{S}} : \dot{\underline{\underline{\gamma}}} \, dV_o dt = \int_t \int_{V_o} 0.5 \underline{\underline{S}} : \dot{\underline{\underline{C}}} dV_o dt \tag{2.121}$$

Notice that all the scalar products ":" denote internal strain power per unit volume, and therefore from Eqs. 2.119, 2.120, and 2.121 it is evident that $\underline{\underline{\sigma}}$ and $\underline{\underline{D}}$ are energetically conjugate variables with respect to the current volume V while $\underline{\underline{\tau}}$ and $\underline{\underline{D}}$, $\underline{\underline{S}}$ and $\dot{\underline{\underline{\gamma}}}$, and $\underline{\underline{S}}$ and $\dot{\underline{\underline{C}}}$ are energetically conjugate variables with respect to the reference volume V_o.

The components of W_i in terms of the other energetically conjugate variables can now be given as

$$\begin{aligned} W_i &= \int_t \int_{V_o} \hat{\tau}_{IJ} \hat{D}_{IJ} dV_o dt = \int_t \int_{V_o} \tau^{IJ} D_{IJ} dV_o dt \\ &= \int_t \int_{V_o} \tau_{IJ} D^{IJ} dV_o dt = \int_t \int_{V_o} \tau^I_J D^J_I dV_o dt \end{aligned} \tag{2.122}$$

for the conjugate variables $\underline{\underline{\tau}}$ and $\underline{\underline{D}}$ and

$$\begin{aligned} W_i &= \int_t \int_{V_o} \hat{S}_{ij} \dot{\hat{\gamma}}_{ij} dV_o dt = \int_{V_o} \int_{\hat{\gamma}_{ij}} \hat{S}_{ij} d\hat{\gamma}_{ij} dV_o \\ &= \int_t \int_{V_o} S^{ij} \dot{\gamma}_{ij} dV_o dt = \int_{V_o} \int_{\gamma_{ij}} S^{ij} d\gamma_{ij} dV_o \\ &= \int_t \int_{V_o} S^i_j \dot{\gamma}^j_i dV_o dt = \int_{V_o} \int_{\gamma^j_i} S^i_j \, d\gamma^j_i \, dV_o \\ &= \int_t \int_{V_o} S_{ij} \dot{\gamma}^{ij} dV_o dt = \int_{V_o} \int_{\gamma_{ij}} S_{ij} d\gamma^{ij} dV_o \end{aligned} \tag{2.123}$$

for the conjugate variables $\underline{\underline{S}}$ and $\dot{\underline{\underline{\gamma}}} = 0.5\, \dot{\underline{\underline{C}}}$. Since $D_{IJ} = \dot{\gamma}_{ij} = \dot{e}_{IJ}$ and $\tau^{IJ} = S^{ij}$, we also have

$$\begin{aligned} W_i &= \int_t \int_V \sigma^{IJ} \dot{\gamma}_{ij} dV \, dt = \int_V \int_{\gamma_{ij}} \sigma^{IJ} d\gamma_{ij} dV \\ &= \int_t \int_V \sigma^{IJ} \dot{e}_{IJ} dV \, dt = \int_V \int_{e_{IJ}} \sigma^{IJ} de_{IJ} dV \\ &= \int_t \int_{V_o} \tau^{IJ} \dot{\gamma}_{ij} dV_o dt = \int_{V_o} \int_{\gamma_{ij}} \tau^{IJ} d\gamma_{ij} dV_o \end{aligned} \tag{2.124}$$

$$= \int_t \int_{V_o} \tau^{IJ} \dot{e}_{IJ} dV_o dt = \int_{V_o} \int_{e_{IJ}} \tau^{IJ} de_{IJ} dV_o$$

$$= \int_t \int_{V_o} S^{ij} D_{IJ} dV_o dt \qquad (2.124)$$

$$= \int_t \int_{V_o} S^{ij} \dot{e}_{IJ} dV_o dt = \int_{V_o} \int_{e_{IJ}} S^{ij} de_{IJ} dV_o$$

δW_i can now be derived using the equations presented above for the various expressions of W_i. For example, if the conjugate variables $\underline{\underline{S}}$ and $\dot{\underline{\underline{\gamma}}}$ are used, we have

$$\delta W_i = \int_{V_o} \underline{\underline{S}} : \delta \underline{\underline{\gamma}} \, dV_o$$
$$= \int_{V_o} S^{ij} \delta \gamma_{ij} \, dV_o \qquad (2.125)$$

Notice that in Eq. 2.125 all terms are defined with respect to the reference configuration (2nd Piola-Kirchhoff stress, Green-Lagrange strain, reference volume V_o), and therefore Eq. 2.125 applies to the total Lagrangian formulation.

The corresponding external virtual work is given as

$$\delta W_e = \int_{V_o} \rho_o \underline{B} \cdot \delta \underline{u} \, dV_o + \int_{\tilde{A}_o} \underline{t} \cdot \delta \underline{u} \, dA_o$$
$$= \int_{V_o} \rho_o B^i \delta u_i dV_o + \int_{\tilde{A}_o} t^i \delta u_i dA_o \qquad (2.126)$$

where $\underline{B}$ is the body force vector and $\underline{t}$ the external surface traction vector. $\tilde{A}_o$ corresponds to the surface where the traction vector is applied. Since $\underline{B}$ contains all body forces, using D´Alembert´s principle we have

$$\underline{B} = -\ddot{\underline{u}} + \underline{f} \qquad (2.127)$$

or

$$B^i = -\ddot{u}^i + f^i \qquad (2.128)$$

where $\ddot{\underline{u}}$ is the acceleration vector (inertia term) and $\underline{f}$ contains all other body forces such as the gravitational and magnetic forces. Therefore, in the undeformed configuration and using the conjugate variables $\underline{\underline{S}}$ and $\dot{\underline{\underline{\gamma}}}$, we have

$$\int_{V_o} \underline{\underline{S}} : \delta\underline{\underline{\gamma}} \, dV_o = \int_{V_o} \rho_o (\underline{f} - \ddot{\underline{u}}) \cdot \delta\underline{u} \, dV_o + \int_{\tilde{A}_o} \underline{t} \cdot \delta\underline{u} \, dA_o \qquad (2.129)$$

Taking the variation of Eqs. 2.76 and 2.79 we obtain

$$\delta\underline{\underline{\gamma}} = 0.5(\underline{\underline{F}}^T \cdot \delta\underline{\underline{F}} + \delta\underline{\underline{F}}^T \cdot \underline{\underline{F}}) \qquad (2.130)$$

and

$$\delta\gamma_{ij} = 0.5\left[(\delta^k_i + u^k{}_{,i})\delta u_{k,j} + (\delta^k_j + u^k{}_{,j})\delta u_{k,i}\right] \qquad (2.131)$$

Notice that since the variational principle was used to derive the energy equation, Eq. 2.129 contains the equilibrium equations and also the boundary conditions. In particular using Gauss's theorem it can be shown that

$$\left[S^{jk}(\delta^i_k + u^i{}_{,k})\right]_{,j} + \rho_o f^i = \rho_o \ddot{u}^i \qquad (2.132)$$

for the components of the equilibrium equation and

$$t^i = n_j S^{jk}(\delta^i_k + u^i{}_{,k}) \qquad (2.133)$$

for the components of the nonessential boundary conditions (prescribed surface tractions) referred to the reference configuration.

2.5 DISPLACEMENT-BASED FINITE ELEMENT FORMULATION OF THE GOVERNING EQUATIONS

The governing equations of motion are solved effectively using the finite element method (FEM) in conjunction with the digital computer. The basis of the finite element method consists of idealizing the continuum by an assemblage of finite elements. Each finite element has a finite number of nodes, with each node describing the element behavior by the use of interpolation functions. In other words, the coefficients of the interpolation functions are the generalized nodal responses, and hence the response at any point in the finite element is obtained by substituting the geometric coordinates of the point into the expression for the response given in terms of interpolation functions. In equation form we have

$$\begin{aligned} u_i(\xi^j,t) &= \lfloor \phi_i(\xi^j) \rfloor \{q_m(t)\} \\ &= \lfloor \phi^i(\xi^j) \rfloor \{q_m(t)\} \end{aligned} \tag{2.134}$$

where the $\phi_i(\xi^j)$ are displacement interpolation functions and the q_m's are the element nodal generalized displacements of element m. ($\lfloor\ \rfloor$ symbolizes a row vector and $\{\ \}$, a column vector). ξ^j represents the convected coordinates of any point in the element.

Using Eq. 2.134 we have

$$\delta u_i(\xi^j,t) = \lfloor \phi_i(\xi^j) \rfloor \{\delta q_m(t)\} \tag{2.135}$$

and

$$\ddot{u}_i(\xi^j,t) = \lfloor \phi_i(\xi^j) \rfloor \{\ddot{q}_m(t)\} \tag{2.136}$$

We can now express various kinematic quantities in terms of the interpolation functions. For example, the Green-Lagrange strain in Eq. 2.79 is given as

$$\gamma_{ij} = 0.5(u_{i,j} + u_{j,i} + u_{l,i}u^{l}{}_{,j}) \tag{2.137}$$

or

$$\begin{aligned}\gamma_{ij}(\xi^k,t) &= 0.5\lfloor \phi_{i,j}(\xi^k) + \phi_{j,i}(\xi^k) \rfloor \{q_m(t)\} \\ &\quad + 0.5\lfloor q_m(t) \rfloor \{\phi_{l,i}\} \lfloor \phi^{l}{}_{,j} \rfloor \{q_m(t)\} \\ &= \lfloor D_{ij} \rfloor \{q_m\} + 0.5\lfloor q_m \rfloor \{D_{li}\} \lfloor D^{l}{}_{j} \rfloor \{q_m\}\end{aligned} \tag{2.138}$$

where we used the differential gradient operators

$$\begin{aligned}\lfloor D_{ij} \rfloor &= 0.5\lfloor \phi_{i,j} + \phi_{j,i} \rfloor \\ \lfloor D_{li} \rfloor &= \lfloor \phi_{l,i} \rfloor \\ \lfloor D^{l}{}_{j} \rfloor &= \lfloor \phi^{l}{}_{,j} \rfloor\end{aligned} \tag{2.139}$$

We also have

$$\delta\gamma_{ij} = \lfloor D_{ij} \rfloor \{\delta q_m\} + \lfloor \delta q_m \rfloor \{D_{1i}\} \lfloor D^1{}_j \rfloor \{q_m\} \tag{2.140}$$

The entire continuum is described by the set of finite elements, and the principle of virtual work applies to the summation of the finite elements

$$\sum_{m=1}^{n} (\delta W_i)_m = \sum_{m=1}^{n} (\delta W_e)_m \tag{2.141}$$

where $(\delta W_i)_m$ is the internal virtual work of element m given by Eq. 2.125 and $(\delta W_e)_m$ is the external virtual work given by Eq. 2.129 (for the total Lagrangian formulation).

Substituting Eqs. 2.134 to 2.140 into Eq. 2.141 we obtain the finite element formulation of the energy equation (total Lagrangian form) given as follows:

$$\begin{aligned}\sum_{m=1}^{n} \lfloor \delta q_m \rfloor \Big(& \int_{(V_o)_m} \{D_{ij}\} S^{ij}\, dV_o + \int_{(V_o)_m} \{D_{1i}\} \lfloor D^1{}_j \rfloor S^{ij}\, dV_o \{q_m\} \\ & - \int_{(V_o)_m} \rho_o \{\phi_i\} f^i dV_o - \int_{(\tilde{A}_o)_m} \{\phi_i\}_s t^i\, dA_o \\ & + \int_{(V_o)_m} \rho_o \{\phi_i\} \lfloor \phi^i \rfloor\, dV_o \{\ddot{q}_m\} \Big) = 0\end{aligned} \tag{2.142}$$

where subscript s indicates that the interpolation function ϕ_i corresponds to the surface.

2.6 CONSTITUTIVE RELATIONS

This last section examines the relation between the stress and strain tensors, in other words the constitutive relations. The presentation will be as brief and general as possible since the development of constitutive relations is highly problem dependent and poses significant areas of research currently in progress.

The theory of plasticity considers the problem of evaluating the plastic portion of the strain tensor. We assume that a plastic strain tensor γ^p_{ij} exists such that

$$\gamma_{ij} = \gamma^e_{ij} + \gamma^p_{ij} \tag{2.143}$$

where γ^e_{ij} is the elastic strain tensor obtained from the stress tensor S^{ij} using conventional linear elastic stress-strain relations

$$S^{ij} = E^{ijkl}\,\gamma^e_{kl} \tag{2.144}$$

Notice that E^{ijkl} is the fourth order elastic modulus tensor relating the Green-Lagrange strain with the 2nd Piola-Kirchhoff stress tensor. Corresponding elastic modulus tensor are available for the other stress and strain measures.

Two different plasticity theories are available for deriving the plastic strain tensor. The deformation theory of plasticity assumes that there exists a one-to-one relation between the stress and strain tensors.

$$\gamma_{ij} = f(S^{ij}) \tag{2.145}$$

Because a one-to-one relation is assumed, this theory applies only to simple loading cases such as proportional loading. The incremental (flow) theory of plasticity, rather than using total strains, considers incremental strains $d\gamma_{ij}$, $d\gamma^{e}_{ij}$, and $d\gamma^{p}_{ij}$ and assumes a relation between the incremental stresses and strains, and in particular, considers the stress and strain rates

$$d\dot{\gamma}^{p}_{ij} = f(S_{ij}, d\dot{S}_{ij}, \ldots) \tag{2.146}$$

Plasticity theory consists of two basic ingredients: the flow rule and the strain hardening rule. The flow rule describes the plastic flow as a function of the stress and previous load history. Stated differently, the flow rule provides the direction of the strain rate produced by a given stress history. The strain hardening rule supplies the magnitude of the plastic flow. In general, we can define a surface inside the three-dimensional principal stress space where for stress combinations within the surface, the continuum remains elastic and for combinations outside, plastic flow occurs. This surface is called the

yield surface. Consequently, the hardening rule describes the evolution of the yield surface as plastic flow occurs.

We shall not examine the details of deriving the flow rule given various assumptions on the relation between stress and strain nor shall we examine the numerous strain hardening rules available, which are applicable to particular material types. It suffices to mention, that the field of constitutive relations is under considerable investigation. Finally, note that the constitutive relations may, in general, be of the form

$$\overset{\nabla}{\underline{\underline{\tau}}} = f(\underline{\underline{D}}, \underline{\underline{\tau}}) \tag{2.147}$$

In other words, the constitutive law may relate the Jaumann stress rate and the rate of deformation. Comparing Eq. 2.147 with Eq. 2.144, it is evident that Eq. 2.144 only applies to small strain problems since E^{ijkl} is constant. Furthermore, we may use a constitutive relation between the Cauchy stress tensor $\underline{\underline{\sigma}}$ and $\underline{\underline{D}}$, but in most cases Eq. 2.147 is more appropriate since thermodynamic principles are often employed to derive the constitutive relations, with the resulting expressions being less complicated in terms of the Kirchhoff stresses $\underline{\underline{\tau}}$.

CHAPTER 3

GOVERNING EQUATIONS OF MOTION AND THEIR NUMERICAL SOLUTION

Structural dynamic problems are represented mathematically by second order ordinary differential equations with initial conditions. The solution of these initial value problems for continuous systems is usually unavailable in closed form, and hence approximate solutions are derived numerically by spatial and temporal discretization of the continuous system. Finite elements are commonly used for the spatial discretization while finite difference methods are employed for the temporal discretization.

This chapter develops the governing equations of motion by expanding the energy equations of section 2.4. After deriving the exact governing equations, the equations are rearranged to be compatible with three different solution formulations: pure unconventional; pseudo-force; and tangent stiffness. A rigorous development is pursued and all assumptions are stated throughout the presentation to emphasize the limitations and applicability of each form of

the governing equations.

Following the derivation of the governing equations of motion, current popular numerical solution techniques such as direct time integration using explicit or implicit numerical integrators applied directly to the governing equations and alternate methods such as mode superposition techniques adapted to nonlinear problems are examined. The presentation emphasizes the accuracy properties of the various approaches and discusses techniques for obtaining reliable solutions.

3.1 EQUATIONS OF MOTION

Problems in structural dynamics can be categorized into steady state or transient response. This study considers the class of transient response problems where the response varies with time and is not periodic. Transient response problems can be further subdivided into wave propagation and structural type problems. In wave propagation problems the response is governed by the propagation of stress waves through the structure. Consequently, the response persists for a short duration and is characterized by an excitation of all modes in the structure. Examples include pile driving and blast type problems. Structural type problems exhibit a response on a more global scale such as the elongation and bending of structural members and usually

arise from long term, limited frequency content loadings represented by wind, wave, and seismic excitations, and consequently only the lowest structural modes contribute to the response.

The exact governing equation is viewed from three different perspectives in this section. Each form can be used equally well for structural response problems. Preference among the different approaches depends on the number of degrees of freedom and the allowable time increment compared to the number of numerical calculations per time step.

3.1.1 Exact Formulation

Beginning with the finite element form of the energy equation given by Eq. 2.142 and using the following substitutions

$$\underline{m} = \int_{(V_o)_m} \rho_o \{\Phi_i\} \lfloor \Phi^i \rfloor \, dV_o \tag{3.1}$$

$$\underline{p} = \int_{(V_o)_m} \{ D_{ij} \} S^{ij} dV_o \tag{3.2}$$

$$\underline{h} = \int_{(V_o)_m} \{ D_{1i} \} \lfloor D^1{}_j \rfloor \, S^{ij} dV_o \tag{3.3}$$

$$\underline{f} = \int_{(V_o)_m} \rho_o \{ \Phi_i \} f^i dV_o + \int_{(\tilde{A}_o)_m} \{ \Phi_i \}_s t^i dA_o \tag{3.4}$$

we obtain

$$\sum_{m=1}^{n} \lfloor \delta q_m \rfloor \, (\underline{m}\ddot{q}_m + \underline{p} + \underline{h}q - \underline{f}) = 0 \tag{3.5}$$

Equation 3.5 is then rewritten in terms of global nodal generalized displacements $\{\underline{q}^*\}$ by transferring the local displacements to the global displacements using the following relation:

$$\underline{q}^* = \underline{J}\underline{q} \tag{3.6}$$

where $\underline{J}$ is the transformation matrix from the local to the global coordinate reference frame. Therefore,

$$\sum_{m=1}^{n} \left[\delta \underline{q}_m^* \right] (\underline{m}^*\ddot{\underline{q}}^* + \underline{p}^* + \underline{h}^*\underline{q}^* - \underline{f}^*) = \underline{0} \tag{3.7}$$

where it can be shown that

$$\underline{m}^* = \underline{J}^T\underline{m}\underline{J} \tag{3.8}$$

$$\underline{p}^* = \underline{J}^T\underline{p} \tag{3.9}$$

$$\underline{h}^* = \underline{J}^T\underline{h}\underline{J} \tag{3.10}$$

$$\underline{f}^* = \underline{J}^T\underline{f} \tag{3.11}$$

Next we group together the linear and nonlinear contributions that are functions of the response and let

$$\underline{i} = \underline{p} + \underline{h}\underline{q} \tag{3.12}$$

and similarly

$$\underline{i}^* = \underline{J}^T\underline{i} = \underline{J}^T\underline{p} + \underline{J}^T\underline{h}\underline{q} \tag{3.13}$$

Therefore, we obtain

$$\sum_{m=1}^{n} \lfloor \delta \underline{q}_m \rfloor (m\ddot{\underline{q}}_m + \underline{i} - \underline{f}) = \underline{0} \tag{3.14}$$

and

$$\sum_{m=1}^{n} \lfloor \delta \underline{q}^*_m \rfloor (\underline{m}^*\ddot{\underline{q}}^* + \underline{i}^* - \underline{f}^*) = \underline{0} \tag{3.15}$$

We now define

$$\underline{M} \equiv \sum_{j=1}^{n} \underline{m}^* \tag{3.16}$$

$$\underline{I} \equiv \sum_{j=1}^{n} \underline{i}^* \tag{3.17}$$

$$\underline{F} \equiv \sum_{j=1}^{n} \underline{f}^* \tag{3.18}$$

Equation 3.15 can then be rewritten as

$$\lfloor \delta \underline{q}^* \rfloor (\underline{M}\ddot{\underline{q}}^* + \underline{I} - \underline{F}) = \underline{0} \tag{3.19}$$

Since $\lfloor \delta \underline{q}^* \rfloor$ contains independent and arbitrary components, Eq. 3.19 becomes

$$\underline{M}\ddot{\underline{q}}^* = -\underline{I} + \underline{F} \tag{3.20}$$

Equation 3.20 represents the exact form of the governing equations of motion. No assumptions have been made concerning the nature of loading or the response and in

particular, the constitutive relations. Rodal and Witmer (72) refer to Eq. 3.20 as the "unconventional" formulation; this form of the equation of motion applies to finite strain as well as to infinitesimal or "small" strain problems, and represents a compact and efficient numerical form. Other formulations which assume infinitesimal strains are called "conventional" formulations. The following three sections present alternate forms of the exact equations that are compatible with specific solution schemes.

3.1.2 Pure Unconventional Formulation

The pure unconventional form of the governing equation refers to solving Eq. 3.20 directly with either explicit or implicit numerical integration operators. Observe that the mass matrix $\underline{M}$ is the only structural matrix on the LHS (left hand side) of Eq. 3.20. The only unknown term on the RHS is the vector $\underline{I}$. When using explicit integrators, however, the numerical equations of motion are defined in terms of the previous time step, in other words, at a time when $\underline{M}$, $\underline{I}$, and $\underline{F}$ are known. As a result, all terms on the RHS of Eq. 3.20 are known and $\underline{q}^*$ is the only unknown in the entire equation.

A solution by an explicit integrator, therefore, is quite economical. The only matrix inversion involves the mass matrix (undamped problem). When given in a lumped mass form, the inverse of $\underline{M}$ is easily obtained by evaluating the reciprocals of its diagonal terms. Even if $\underline{M}$ is in a

consistent mass form, the inversion is executed only once at the beginning of the analysis (assuming that $\underline{M}$ is independent of time).

In general, the use of explicit operators with the pure unconventional formulation is economical and produces accurate and reliable results for small systems. Extensions to large systems also produce accurate results, but at a high computational cost due to the extremely small time increment required to ensure stability. The severe stability problems of explicit integrators thus limit the solution of Eq. 3.20 to problems where extremely small time increments are necessary not only to ensure stability but also accuracy, as exemplified by wave propagation problems, and to small structural response problems where the load duration is short. If the response must be evaluated over a "long" period of time, the computing burden may become excessive, therefore requiring other types of solution procedures and operators such as implicit schemes.

3.1.3 Pseudo-Force Formulation

The governing equation for the pseudo-force formulation is obtained by adding $\underline{K}\underline{q}^*$ to both sides of Eq. 3.20, where $\underline{K}$ is the initial linear elastic stiffness matrix

$$\underline{M}\ddot{\underline{q}}^* + \underline{K}\underline{q}^* = -\underline{I} + \underline{F} + \underline{K}\underline{q}^* \tag{3.21}$$

where

$$\underline{K} = \sum_{m=1}^{n} \underline{k}^* = \sum_{m=1}^{n} \underline{J}^T \int_{(V_o)_m} \{D_{ij}\} E^{ijkl} \lfloor D_{kl} \rfloor dV_o \, \underline{J} \tag{3.22}$$

and E^{ijkl} is given in Eq. 2.144. Equation 3.21 can be simplified further by grouping all response terms together

$$\underline{F}^{NL} = \underline{K}\underline{q}^* - \underline{I} \tag{3.23}$$

Therefore,

$$\underline{M}\ddot{\underline{q}}^* + \underline{K}\underline{q}^* = \underline{F} + \underline{F}^{NL} \tag{3.24}$$

Notice that in Eq. 3.24 no assumptions have been made concerning the constitutive relations. As a result, Eq. 3.24 applies to finite as well as infinitesimal strain problems and is referred to as the modified unconventional form. Another form, the conventional pseudo-force form, assumes that Eq. 2.144 is valid when evaluating $\underline{I}$, and therefore is restricted to infinitesimal strain problems. This conventional form, in addition to being more restricted than the unconventional form, requires many more computation steps and a larger storage. Furthermore, the calculations may often be numerically ill-conditioned, requiring extended precision.

By adding $\underline{K}\underline{q}^*$ to both sides of Eq. 3.20, stability and convergence problems are reduced considerably and a more convenient form is produced, appropriate for approximate

extrapolative schemes that predict $\underline{F}^{NL}$ or iterative schemes that solve for new $\underline{q}^*$ until $\underline{F}^{NL}$ converges. Explicit and implicit integrators are equally compatible with Eq. 3.24. Notice that the structural matrices on the LHS are factorized only once since they remain independent of time, and hence this solution approach is fairly economical. Its reliability, however, is questionable since the amount of error is unknown when using a force extrapolation approach with an implicit operator; the solution accuracy can be verified only by repeating the analysis with smaller time increments, thus reducing the technique's efficiency. However, Eq. 3.24 can also be solved iteratively to convergence within each time step by using various available iterative techniques with transient implicit operators (72,78).

3.1.4 Incremental Response Formulation

The incremental formulation for the equations of motion is derived by subtracting the exact form for the governing equations at time $t-\Delta t$ from those at time t to obtain

$$\underline{M}\,\Delta\ddot{\underline{q}}^* = -\Delta\underline{I} + \Delta\underline{F} \tag{3.25}$$

where

$$\Delta\ddot{\underline{q}}^* = \ddot{\underline{q}}^*_t - \ddot{\underline{q}}^*_{t-\Delta t} \tag{3.26}$$

$$\Delta\underline{I} = \underline{I}_t - \underline{I}_{t-\Delta t} \tag{3.27}$$

$$\Delta\underline{F} = \underline{F}_t - \underline{F}_{t-\Delta t} \tag{3.28}$$

$\Delta\underline{I}$ is then approximated by a Taylor series expansion to the first order

$$\Delta\underline{I} = (\partial\underline{I}/\partial\underline{q}^*)\Delta\underline{q}^* \tag{3.29}$$

to yield the tangent stiffness form of the incremental equations of motion given as

$$\underline{M}\Delta\ddot{\underline{q}}^* + \underline{K}_t\Delta\underline{q}^* = \Delta\underline{F} + \underline{f}_u \tag{3.30}$$

where the tangent stiffness $\underline{K}_t$ is defined by

$$\underline{K}_t = \partial \underline{I} / \partial \underline{q}^* \tag{3.31}$$

and $\underline{f}_u$ represents the residual force due to approximating the derivative of $\Delta \underline{I}$ by a finite difference expansion.

We shall next evaluate $\underline{K}_t$. From Eqs. 3.2, 3.3, and 3.12 we have at the local level

$$\underline{i} = \int_{(V_o)_m} \{ D_{ij} \} S^{ij} dV + \int_{(V_o)_m} \{ D_{1i} \} \lfloor D^1{}_j \rfloor \{q\} S^{ij} dV_o \tag{3.32}$$

Then from Eq. 3.31 we have

$$\begin{aligned} \underline{k}_t &= \partial \underline{i} / \partial \underline{q} \\ &= \int_{(V_o)_m} \{ D_{ij} \} \left[\partial S_{ij} / \partial \gamma_{kl} \right] \lfloor \partial \gamma_{kl} / \partial \underline{q} \rfloor \, dV_o \\ &\quad + \int_{(V_o)_m} \{ D_{1i} \} \lfloor D^1{}_j \rfloor \, S^{ij} dV_o \\ &\quad + \int_{(V_o)_m} \{ D_{1i} \} \lfloor D^1{}_j \rfloor \{q\} \left[\partial S^{ij} / \partial \gamma_{kl} \right] \lfloor \partial \gamma_{kl} / \partial \underline{q} \rfloor \, dV_o \end{aligned} \tag{3.33}$$

Also from Eq. 2.140 we have

$$\begin{aligned} \partial \gamma_{kl} / \partial \underline{q} &= \lfloor D_{kl} \rfloor + (1/2) \lfloor q \rfloor \{ D_{ck} \} \lfloor D^c{}_l \rfloor \\ &\quad + (1/2) \lfloor q \rfloor \{ D^c{}_l \} \lfloor D_{ck} \rfloor \end{aligned} \tag{3.34}$$

Finally at the local level we have

$$\begin{aligned} \underline{k}_t &= \int_{(V_o)_m} \{ D_{ij} \} \left[\partial S^{ij} / \partial \gamma_{kl} \right] \lfloor D_{kl} \rfloor \, dV_o \\ &\quad + (1/2) \int_{(V_o)_m} \{ D_{ij} \} \left[\partial S^{ij} / \partial \gamma_{kl} \right] \lfloor q \rfloor \{ D_{ck} \} \lfloor D^c{}_l \rfloor dV_o \\ &\quad + (1/2) \int_{(V_o)_m} \{ D_{ij} \} \left[\partial S^{ij} / \partial \gamma_{kl} \right] \lfloor q \rfloor \{ D^c{}_l \} \lfloor D_{ck} \rfloor \, dV_o \\ &\quad + \int_{(V_o)_m} \{ D_{li} \} \lfloor D^l{}_j \rfloor \, S^{ij} dV_o \end{aligned} \tag{3.35}$$

$$+\int_{(V_o)_m} \{D_{1i}\}\lfloor D^1{}_j\rfloor \{q\}\left[\partial S^{ij}/\partial\gamma_{kl}\right]\lfloor D_{kl}\rfloor\, dV_o \qquad (3.35)$$

$$+(1/2)\int_{(V_o)_m} \{D_{1i}\}\lfloor D^1{}_j\rfloor\{q\}\left[\partial S_{ij}/\partial\gamma_{kl}\right]\lfloor q\rfloor\{D_{ck}\}\lfloor D^c{}_l\rfloor\, dV_o$$

$$+(1/2)\int_{(V_o)_m} \{D_{1i}\}\lfloor D^1{}_j\rfloor\{q\}\left[\partial S_{ij}/\partial\gamma_{kl}\right]\lfloor q\rfloor\{D^c{}_l\}\lfloor D_{ck}\rfloor dV_o$$

On a global scale

$$\underline{k}_t^* = \underline{J}^T\underline{k}_t\underline{J} \qquad (3.36)$$

and

$$\underline{K}_t = \sum_{m=1}^{n}\underline{k}_t^* \qquad (3.37)$$

Recalling Eq. 3.30, notice that the equation of motion is not solved exactly due to the residual force term given as

$$\underline{f}_u = \underline{M}\Delta\ddot{\underline{q}}^* + \underline{K}_t\Delta\underline{q}^* - \Delta\underline{F} \qquad (3.38)$$

Various equilibrium iteration schemes must, therefore, be used in conjunction with the numerical integrators to minimize $\underline{f}_u$ in Eq. 3.30. In particular, Eq. 3.30 is first solved for $\Delta\ddot{\underline{q}}^o$, $\Delta\dot{\underline{q}}^o$, and $\Delta\underline{q}^o$ where the superscript o refers to the zeroth iteration. Next a correction $\Delta\tilde{\underline{q}}$ is evaluated such that Eq. 3.38 is satisfied. The new $\Delta\underline{q}^1 = \Delta\underline{q}^0 + \Delta\tilde{\underline{q}}^1$ is then used to evaluate a new $\Delta\underline{F}$ and the above process is repeated until $\underline{f}_u$ satisfies some convergence criterion. We note in general that, depending on the solution scheme, $\underline{K}_t$ may be reevaluated and refactorized a significant number of times throughout the analysis, therefore aggravating the computational cost considerably.

3.2 SOLUTION METHODS

This section discusses methods for obtaining numerical solutions to the governing equations of motion given by Eqs. 3.20, 3.24, and 3.30. The accuracy and stability characteristics of numerical integration operators are briefly discussed, and techniques for solving Eq. 3.38 (equilibrium iteration) are examined. Alternate techniques for deriving time history solutions are also considered. The presentation is limited to solution techniques capable theoretically of providing the "exact" response by varying the parameters governing the solution process (e.g., time increment size and convergence tolerance). These techniques, consequently, produce solutions deviating from the actual observed behavior only because of limitations in the structural modelling and constitutive relations.

3.2.1 Direct Time Integration Analyses

An accurate solution of the governing equations of motion is customarily arrived at by direct time integration techniques. The adjective direct refers to manipulating the entire geometric structural matrices, opposed to working with generalized matrices (mode superposition analysis), and the time integration pertains to temporal integration of the governing equations to derive the response.

Time integration techniques involve either explicit or implicit operators. Explicit methods operate on the equations of motion at time $t-\Delta t$ (i.e., at the time for which the solution is already known) while implicit methods consider the equation of motion at time t. In terms of the tangent stiffness form of the governing equations, for explicit methods we consider

$$\underline{M}\Delta\ddot{\underline{q}}^*(t-\Delta t) + \underline{K}_t\Delta\underline{q}^*(t-\Delta t) = \Delta\underline{F}(t-\Delta t) + \underline{f}_u(t-\Delta t) \tag{3.39}$$

and for implicit methods,

$$\underline{M}\Delta\ddot{\underline{q}}^*(t) + \underline{K}_t\Delta\underline{q}^*(t) = \Delta\underline{F}(t) + \underline{f}_u(t) \tag{3.40}$$

Explicit integration operators include the central difference predictor methods and the Runge-Kutta type operators. Implicit operators include the Newmark (50), Wilson-θ (10,87), Houbolt backward-difference (35), Park stiffly-stable (59), and the Hilber α-method (33,34).

All numerical operators in general assume some variation of the response during the time increment, and then given the response at the previous time step, the response at the current time step is calculated. As a result, dynamic equilibrium is satisfied only at discrete time steps t_n.

The two main considerations in selecting a numerical integrator are the stability and accuracy characteristics. Instability is defined as a divergence of the solution, and accuracy refers to numerical damping, frequency dispersion, truncation error, and the effect of spurious roots for multistep methods (60). A detailed examination of numerical integration is given in Chapter 4, and it suffices now to say that explicit methods are conditionally stable (unstable for a time step greater than a critical time step) while implicit methods are unconditionally stable for linear elastic problems. The extension to nonlinear problems may induce conditional stability in the implicit schemes depending on how the equations of motion are formulated and solved. In terms of accuracy, both implicit and explicit schemes have accuracy parameters that vary as a function of $\Delta t/T$ where Δt is the time increment and T, a natural structural period.

Accounting for the stability and accuracy limitations of the integration operators, we now consider how the governing differential equations are transformed into algebraic equations. All integration operators express the response at time t in terms of previous or future responses. For example, the central difference method assumes

$$\ddot{\underline{u}}(t) = (1/\Delta t^2)(\underline{u}(t+\Delta t) - 2\underline{u}(t) + \underline{u}(t-\Delta t)) \tag{3.41}$$

$$\dot{\underline{u}}(t) = (1/2\Delta t)(\underline{u}(t+\Delta t) - \underline{u}(t-\Delta t)) \tag{3.42}$$

This integration operator is most often used in conjunction with the pure unconventional form of the equations of motion, Eq. 3.20, at time $t-\Delta t$ to give

$$\underline{M}(1/\Delta t^2)(\underline{u}(t) - 2\underline{u}(t-\Delta t) + \underline{u}(t-2\Delta t)) = -\underline{I}(t-\Delta t) + \underline{F}(t-\Delta t) \quad (3.43)$$

and

$$(1/\Delta t^2)\underline{M}\underline{u}(t) = -\underline{I}(t-\Delta t) + \underline{F}(t-\Delta t) + (1/\Delta t^2)\underline{M}(2\underline{u}(t-\Delta t) - \underline{u}(t-2\Delta t)) \quad (3.44)$$

Notice that the only unknown is $\underline{u}(t)$ on the LHS.

We now consider the Newmark integration technique applied to the tangent stiffness form of the incremental equations of motion, Eq. 3.30. The Newmark method assumes

$$\dot{\underline{u}}(t) = \dot{\underline{u}}(t-\Delta t) + \left[(1-\delta)\ddot{\underline{u}}(t-\Delta t) + \delta\ddot{\underline{u}}(t)\right]\Delta t \quad (3.45)$$

$$\underline{u}(t) = \underline{u}(t-\Delta t) + \dot{\underline{u}}(t-\Delta t)\Delta t + \left[(0.5-\alpha)\ddot{\underline{u}}(t-\Delta t) + \alpha\ddot{\underline{u}}(t)\right]\Delta t^2 \quad (3.46)$$

where α and δ are integration parameters. Substituting Eqs. 3.45 and 3.46 into Eq. 3.30 at time t we obtain

$$\underline{M}\Delta\ddot{\underline{q}}(t) + \underline{K}_t\Big\{\Delta\underline{q}(t-\Delta t) + \Delta\dot{\underline{q}}(t-\Delta t)\Delta t + \left[(0.5-\alpha)\Delta\ddot{\underline{q}}(t-\Delta t) + \alpha\Delta\ddot{\underline{q}}(t)\right]\Delta t^2\Big\} = \Delta\underline{F}(t) + \underline{f}_u(t) \quad (3.47)$$

After many manipulations, Eq. 3.47 is rewritten in a form with all known quantities on the RHS and the only unknown, the incremental displacement at time t, on the LHS

$$((1/\alpha\Delta t^2)\underline{M} + \underline{K}_t)\Delta\underline{q}(t) = \Delta\underline{F}(t) + \left[\underline{M}((1/\alpha\Delta t^2)\Delta\underline{q}(t-\Delta t) + (1/\alpha\Delta t)\Delta\dot{\underline{q}}(t-\Delta t) + ((1/2\alpha)-1)\Delta\ddot{\underline{q}}(t-\Delta t))\right] + \underline{f}_u \tag{3.48}$$

or

$$\underline{K}_{eff}\,\Delta\underline{q}(t) \simeq \Delta\underline{F}_{eff} + \Delta\underline{F}(t) \tag{3.49}$$

where the effective stiffness matrix $\underline{K}_{eff}$ and effective load vector $\Delta\underline{F}_{eff}$ are given as

$$\underline{K}_{eff} = (1/\alpha\Delta t^2)\underline{M} + \underline{K}_t \tag{3.50}$$

$\Delta\underline{F}_{eff}$ = 2nd term in brackets on RHS of Eq. 3.48

The approximate equality in Eq. 3.49 is due to the omission of $\underline{f}_u$. Equation 3.49 can now be solved easily as in a static analysis by employing techniques such as a Gauss decomposition of $\underline{K}_{eff}$ and then back substitution to obtain $\Delta\underline{q}(t)$. Notice that in Eq. 3.44, we have $\underline{K}_{eff} = \frac{1}{\Delta t^2}\underline{M}$. As a result, Eq. 3.49 represents the algebraic form of the equations of motion for all numerical integration operators.

The pseudo-force and tangent stiffness forms of the equations of motion introduce additional considerations since in the pseudo-force form, Eq. 3.24, $\underline{F}^{NL}$ is a function of the response at time t, implying that an unknown variable is present on the RHS, while in the tangent stiffness form, Eq. 3.30, $\underline{f}_u$ is also an unknown variable since it is a function of the response at time t ($\underline{f}_u$ represents the residual force due to obtaining $\underline{K}_t$ by truncating the Taylor series expansion of $\underline{I}$). Equation 3.24 must be used, therefore, in conjunction with a technique that estimates $\underline{F}^{NL}(t)$ from $\underline{F}^{NL}$ at previous time steps by extrapolation methods, and Eq. 3.30 must be combined with a iterative technique to minimize $\underline{f}_u$.

The force vector $\underline{F}^{NL}$ is estimated by a Taylor series expansion

$$\underline{F}^{NL}(t) = \underline{F}^{NL}(t-\Delta t) + \Delta t\dot{\underline{F}}^{NL}(t-\Delta t) + O(h^2) \tag{3.51}$$

Then using, for example, a backward difference approximation, we obtain

$$\dot{\underline{F}}^{NL}(t-\Delta t) = (1/\Delta t)(\underline{F}^{NL}(t-\Delta t) - \underline{F}^{NL}(t-2\Delta t)) \tag{3.52}$$

Substituting Eq. 3.52 in Eq. 3.51, we have

$$\underline{F}^{NL}(t) = 2\underline{F}^{NL}(t-\Delta t) - \underline{F}^{NL}(t-2\Delta t) \tag{3.53}$$

and substituting Eq. 3.53 into Eq. 3.30 at time t, we arrive at

$$\underline{M}\ddot{\underline{q}}(t) + \underline{K}\underline{q}(t) = \underline{F}(t) + 2\underline{F}^{NL}(t-\Delta t) - \underline{F}^{NL}(t-2\Delta t) \tag{3.54}$$

Notice that Eq. 3.54 is approximate since $\dot{\underline{F}}^{NL}$ was replaced by a truncated Taylor series using a finite difference equation.

For the tangent stiffness formulation, the unknown variable is $\underline{f}_u$. To minimize the error in this case, we solve for a correction displacement $\Delta\tilde{\underline{q}}$ satisfying

$$\underline{K}_t^i \Delta\tilde{\underline{q}}^i(t) = \underline{f}_u(t)^{i-1} \qquad \text{(static analysis)} \tag{3.55}$$

Then the updated response $\Delta\underline{q}^i$ is given as

$$\Delta\underline{q}^i = \Delta\underline{q}^{i-1} + \Delta\tilde{\underline{q}}^i \tag{3.56}$$

The residual force vector is reevaluated next using Eq. 3.38 (notice that $\Delta\underline{F}$ is a function of $\Delta\underline{q}^i$). The procedure to minimize $\underline{f}_u$, referred to as equilibrium iteration, therefore consists of solving Eqs. 3.55, 3.56, and 3.38 until some convergence criterion is satisfied, whereupon the solution proceeds to the next time step. In Eq. 3.55, if $\underline{K}_t^i$ is reevaluated after each iteration, we are using a Newton iteration scheme. It is apparent that the reevaluation and refactorization of $\underline{K}_t$ is computationally expensive, and may render the tangent stiffness approach

highly inefficient compared to the pseudo-force and pure unconventional approaches. However, the $\underline{K}_t^i$ need not be constantly reevaluated. The following pages examine in more detail the different equilibrium iteration techniques available.

Numerous schemes have been developed for efficiently minimizing $\underline{f}_u^{i-1}$ in Eq. 3.38 and obtaining accurate estimates of $\Delta\tilde{\underline{q}}^i$ in Eq. 3.55. In general the main obstacles to the techniques' efficiency are due to reestablishing the Jacobian ($\underline{K}_t^i$) in Eq. 3.55 and numerically solving the equation to find a better approximation to $\Delta\underline{q}$. We shall investigate the Newton, modified Newton, and quasi-Newton methods.

In Newton's method, $\underline{K}_t^i$ in Eq. 3.55 is updated and refactorized after each iteration. This technique produces highly accurate results and converges quadratically once an approximation has been found in the neighborhood of the solution and if $\underline{I}'$ is continuous (21). However, each iteration consists of reforming the tangent stiffness matrix corresponding to the new configuration and then deriving the inverse or factorizing the stiffness matrix to solve Eq. 3.55. Evaluating the new stiffness matrix requires $O(n^2)$ operations while the numerical decomposition to find the approximation requires $O(n^3)$ operations. Such calculations for large systems can easily produce an economically intractable problem, thus necessitating the use of more effective techniques.

As a result, Newton's method has been modified such that the tangent stiffness matrix is not reevaluated after each iteration but rather at preselected intervals or when the solution begins to diverge. This technique, the modified Newton's method, significantly reduces the cost of reforming the stiffness matrix and implementing the numerical decomposition. Simply stated Eq. 3.55 is rewritten as

$$K_{\tau}^{i}\Delta\tilde{q}^{i}(t) = f_{u}(t)^{i-1} \qquad (3.57)$$

where $\tau<t$ is a previous time step or iterative cycle when equilibrium was satisfied.

Since the tangent stiffness matrix is not reevaluated after each iterative cycle or even during each time step, the convergence properties of the modified Newton method are less than quadratic. In the case where $\tau = t-\Delta t$ (update once during each time step), the modified Newton's method converges linearly. Greater convergence efficiency is obviously attained by reevaluating the stiffness matrix more often, but this process simultaneously reduces the technique's economic effectiveness. The analyst consequently must have a good "feel" for the degree of nonlinearity present in the problem to judiciously choose an efficient updating interval.

In the limit, $\tau=0$ and the evaluation and decomposition of the stiffness matrix is performed only once at time 0. This approach is referred to as the "initial stress" method. For highly nonlinear problems the solution may converge very slowly or even diverge, especially for stiffening systems, and consequently acceleration schemes such as the Aitken acceleration (2) are combined with the modified Newton technique, where the Aitken acceleration imposes the following correction:

$$\Delta \underline{q}^{i}(t) = \Delta \underline{q}^{i-1}(t) + \underline{\alpha}^{i-1} \Delta \tilde{\underline{q}}^{i}(t) \tag{3.58}$$

and $\underline{\alpha}^{i-1}$ is the acceleration coefficient matrix given as

$$\alpha_{jj}^{i-1} = \Delta \tilde{q}_{m}^{i-1}(t) / (\Delta \tilde{q}_{m}^{i-1}(t) - \Delta \tilde{q}_{m}^{i}(t)) \tag{3.59}$$

Due to the inefficiency of Newton's method and the poor convergence quality of the modified Newton method, a third scheme, the quasi-Newton method, has been investigated and recently applied to structural problems (7,21,22,29,45).

Historically speaking, the quasi-Newton method was first introduced by Davidon in 1959 and popularized by Fletcher and Powell in 1963 (21). In 1965 Broyden generalized the technique and applied it to the optimization of nonlinear systems of equations. Mathies and Strang in 1979 proposed its application to nonlinear continuum mechanics problems.

The conceptual framework underlying the quasi-Newton method is fairly simple. Rather than reevaluate the tangent stiffness matrix and derive its inverse or factorize it at each time step, the quasi-Newton method calculates a secant approximation to $\underline{K}_t^{-1}$. The computational cost after the first iteration is therefore due only to the evaluation of the secant approximation, yielding a number of operations of $O(n^2)$. The quasi-Newton equation is given as follows:

$$\underline{G}^i(\underline{q}(t))\underline{d}^{i-1} = \underline{f}_u^i - \underline{f}_u^{i-1} \tag{3.60}$$

where $\underline{G}^i$ is an approximation to $\underline{K}_t$ and $\underline{d}^{i-1}$ equals $\underline{q}^i(t)-\underline{q}^{i-1}(t)$. The Jacobian $\underline{G}^i$ is in essence obtained from $\underline{G}^{i-1}$ using a multi-dimensional generalization of the secant method given as

$$z^i = z^{i-1} - \left[\frac{z^{i-1} - z^{i-2}}{Z(z^{i-1}) - Z(z^{i-2})}\right] Z(z^{i-1}) \tag{3.61}$$

Various rank one updates were initially presented with the following form:

$$\underline{G}^i = \underline{G}^{i-1} + \frac{(\underline{y}^{i-1} - \underline{G}^{i-1}\underline{d}^{i-1})\underline{r}^T}{\underline{r}^T\underline{d}^{i-1}} \tag{3.62}$$

where $\underline{r}$ is an arbitrary vector such that $\underline{r}^T\underline{d}=0$ and $\underline{y}^{i-1} = \underline{f}_u^i-\underline{f}_u^{i-1}$(29).

In Broyden's rank one update, $\underline{r}=\underline{d}$ and

$$\underline{G}_B^i = \underline{G}^{i-1} + \frac{(\underline{y}^{i-1} - \underline{G}^{i-1}\underline{d}^{i-1})\underline{d}^{i-1^T}}{\underline{d}^{i-1^T}\underline{d}^{i-1}} \tag{3.63}$$

Similarly Davidon has suggested an update with $\underline{r}=\underline{y}^i-\underline{G}^{i-1}\underline{d}^{i-1}$ such that

$$\underline{G}_D^i = \underline{G}^{i-1} + \frac{(\underline{y}^{i-1} - \underline{G}^{i-1}\underline{d}^{i-1})(\underline{y}^{i-1} - \underline{G}^{i-1}\underline{d}^{i-1})^T}{(\underline{y}^{i-1} - \underline{G}^{i-1}\underline{d}^{i-1})^T\underline{d}^{i-1}} \tag{3.64}$$

Notice that $\underline{G}_B$ is unsymmetric and $\underline{G}_D$ is not necessarily positive definite.

Rank two updates have been proposed which in addition to being symmetric, are also positive definite. By insuring positive definiteness, the algorithm has a greater guarantee of numerical stability. The most popular rank two updates are the Davidon-Fletcher-Powell (DFP) given as

$$\underline{G}_{DFP}^i = (\underline{I} - \frac{\underline{y}^{i-1}\underline{d}^{i-1^T}}{\underline{y}^{i-1^T}\underline{d}^{i-1}})\,\underline{G}^{i-1}\,(\underline{I} - \frac{\underline{d}^{i-1}\underline{y}^{i-1^T}}{\underline{y}^{i-1^T}\underline{d}^{i-1}}) + \frac{\underline{y}^{i-1}\underline{y}^{i-1^T}}{\underline{y}^{i-1^T}\underline{d}} \tag{3.65}$$

and the Broyden-Fletcher-Goldfarb-Shanno (BFGS) given as

$$\underline{G}_{BFGS}^i = \underline{G}^{i-1} + \frac{\underline{y}^{i-1}\underline{y}^{i-1^T}}{\underline{y}^{i-1^T}\underline{d}^{i-1}} - \frac{\underline{G}^{i-1}\underline{y}^{i-1}\underline{y}^{i-1^T}\underline{G}^{i-1}}{\underline{d}^{i-1^T}\underline{G}^{i-1}\underline{d}^{i-1}} \tag{3.66}$$

In actual practice, the quasi-Newton scheme produces updates to the flexibility matrix rather than the stiffness matrix. Using the property

$$(\underline{A} + \alpha \underline{r}\underline{v}^T)^{-1} = \underline{A}^{-1} - \beta \underline{x}\underline{z}^T \tag{3.67}$$

where $\underline{x}=\underline{A}^{-1}\underline{r}$, $\underline{z}=\underline{A}^{-T}\underline{v}$, $\beta=(1+\alpha \underline{v}^T\underline{A}^{-1}\underline{r})^{-1}$, we can derive the inverse rank one update as

$$\underline{G}^{i\,-1} = \underline{G}^{i-1\,-1} + \frac{(\underline{d}^{i-1} - \underline{G}^{i-1\,-1}\underline{y}^{i-1})\underline{v}^{i-1\,T}}{\underline{v}^{i-1\,T}\underline{y}^{i-1}} \tag{3.68}$$

and similarly for rank two updates. In particular

$$\underline{G}_{BFGS}^{i\,-1} = (\underline{I} - \frac{\underline{d}^{i-1}\underline{y}^{i-1\,T}}{\underline{y}^{i-1\,T}\underline{d}^{i-1}})\underline{G}^{i-1\,-1}(\underline{I} - \frac{\underline{y}^{i-1}\underline{d}^{i-1\,T}}{\underline{y}^{i-1\,T}\underline{d}^{i-1}}) + \frac{\underline{d}^{i-1}\underline{d}^{i-1\,T}}{\underline{y}^{i-1\,T}\underline{d}^{i-1}} \tag{3.69}$$

The procedure for implementing the quasi-Newton method is as follows:

1. Evaluate $\underline{d}^i = -(\underline{G}^i)^{-1}\underline{f}_u^i$
2. Set $\underline{q}^{i+1}(t) = \underline{q}^i(t) + \underline{d}^i$
3. Compute $\underline{f}_u^{i+1}(t)$, and therefore $\underline{y}^i = \underline{f}_u^{i+1}(t) - \underline{f}_u^i(t)$
4. Derive new $\underline{G}^{i+1}$
5. Check convergence criteria
6. Repeat steps 1-5 until convergence is attained

To further accelerate the convergence rate, various line search schemes have been proposed. Rather than setting

$$\underline{q}^{i+1} = \underline{q}^{i} + \underline{d}^{i} \tag{3.70}$$

a line search is performed in the direction $\underline{d}_i$ to obtain an optimal scalar multiplier β such that

$$\underline{d}^{iT} \underline{f}_u \Big|_{\underline{q}^i + \beta \underline{d}^i} = 0 \tag{3.71}$$

Then

$$\underline{q}^{i+1} = \underline{q}^{i} + \beta \underline{d}^{i} \tag{3.72}$$

Although the line search should reduce the required number of iterations, the process of determining β is expensive. Bathe and Cimento (7) state that the convergence rate is satisfactory without the line search scheme when

$$\left| \underline{d}^{iT} \underline{f}_u \right|_{\underline{q}^i + \beta \underline{d}^i} \leq \eta \left| \underline{d}^{iT} \underline{f}_u \right|_{\underline{q}^i} \tag{3.73}$$

with $\eta = 0.5$.

Numerous papers discuss the convergence properties of the quasi-Newton method (22). In general, if various conditions are satisfied by the Jacobian in the neighborhood of the solution, it can be shown that local convergence occurs, either linearly or superlinearly. Superlinear convergence occurs when

$$\left\| \underline{q}^{i+1}(t) - \underline{q}^{*} \right\| \leq \alpha_i \left\| \underline{q}(t)^{i} - \underline{q}^{*} \right\| \tag{3.74}$$

where $\underline{q}^*$ is the exact solution and the sequence $\{\alpha_i\}$ converges to zero. The reader is referred to the references for further details.

Finally, it should be noted that in particular cases, the convergence using a quasi-Newton scheme may become extremely slow. After each iteration, the condition number of the new matrix is evaluated and if found larger than a set tolerance, the update is not implemented (otherwise the matrix becomes singular). In such cases of significant nonlinearities, the Newton method can be used for n iterations until the residual is less than a certain tolerance, and then the quasi-Newton scheme can be reimplemented.

With regard to all iteration schemes, Bathe (7) recommends the modified Newton combined with the Aitken acceleration for mildly nonlinear problems. However, if significant nonlinearities exist, then the less cost effective BFGS technique should be used. In general, dynamic analyses will not exhibit sudden changes in the response since the inertia terms tend to act as smootherners, inducing less iterations, and therefore the BFGS may still be economical.

Notice that the equilibrium iteration methods can also be combined with the force extrapolation scheme of the pseudo-force method. By doing so, approximations in the force extrapolation are offset by the iteration techniques.

A physical feel of how each equilibrium iteration method operates is grasped readily by considering a SDOF system. Both the Newton and modified Newton methods employ the tangent stiffness, the difference between the two being how often the tangent stiffness is reevaluated. The quasi-Newton method actually uses the secant flexibility, but can be interpreted as an updating scheme that produces the exact secant stiffness by adding terms to a previous secant stiffness. These three approaches for SDOF systems are shown in Fig. 3.1.

All iteration techniques require some definition of convergence. Briefly stated, the convergence criteria may be defined in terms of displacement, force, or energy residuals such that convergence occurs when

$$\frac{\left\| \underline{W}^{i}(t) - \underline{W}^{i-1}(t) \right\|_2}{\left\| \underline{W}^{i-1}(t) \right\|_2} < \epsilon \qquad (3.75)$$

or we can use

$$\frac{\left\| \underline{W}^{i}(t) \right\|_2 - \left\| \underline{W}^{i-1}(t) \right\|_2}{\left\| \underline{W}^{i-1}(t) \right\|_2} < \epsilon \qquad (3.76)$$

where $\underline{W}$ is the defined converging quantity, ϵ is the convergence tolerance, and the subscript 2 refers to the Euclidean norm. Since it can be easily shown that $\|x\| - \|y\| < \|x-y\|$, Eq. 3.75 is usually a more stringent criterion than Eq. 3.76. When $\underline{W}$ represents the displacement residual, the convergence requirements are fairly modest and may even give a false sense of

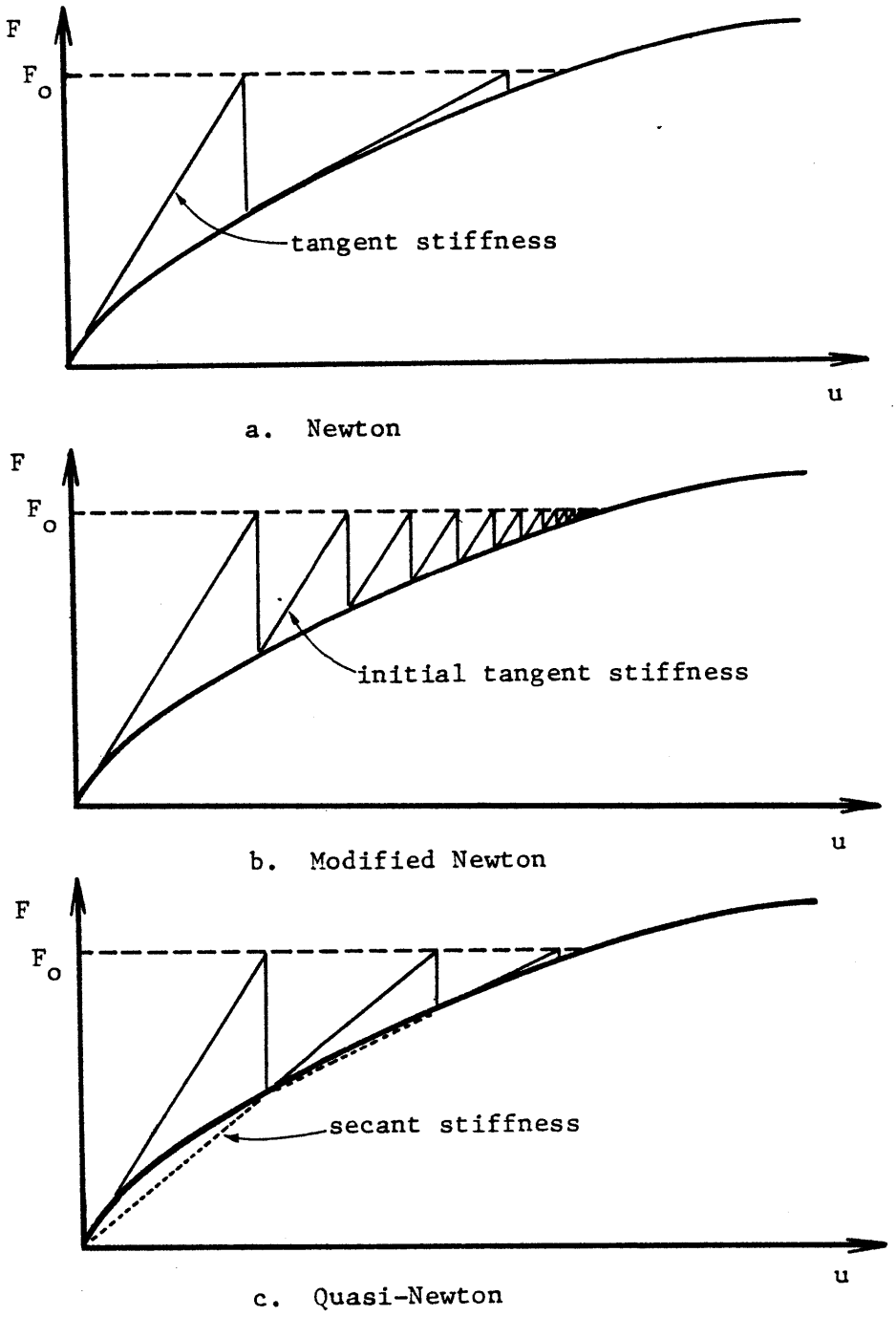

Fig. 3.1 Equilibrium Iteration Schemes Applied to SDOF Systems

convergence. Force criteria are more stringent since the stresses are derived from strains, which are the derivatives of displacements. Energy and force criteria are often used for stiffening structures while displacement and energy forms are used for softening structures (7).

As a general comment on the three types of solution formulations, the pure unconventional form combined with an explicit integrator exhibits the worst stability but good accuracy. In terms of implicit integrators, the tangent stiffness formulation demonstrates extremely good convergence and stability properties, while the pseudo-force method is also stable, but does not converge in all cases. However, because the pure unconventional and pseudo-force methods never involve any updating of the stiffness matrix, both approaches are fairly efficient, with the pure unconventional form being more efficient for small systems and pseudo-force form for large systems. The tangent stiffness formulation is extremely uneconomical when used in conjunction with the Newton method. Recent studies, however, indicate that the tangent stiffness method combined with a quasi-Newton iterator becomes highly attractive for problems with significant nonlinearities (78).

3.2.2 Nonlinear Modal Analysis in the Time Domain

The excessive cost for performing some nonlinear analyses, particularly when parameter studies are conducted, has prompted various researchers to adapt modal analysis techniques to the solution of nonlinear problems

(3,8,30,48,49,51,52,53,75,80). Some approaches have produced relatively good results economically while others have yielded marginal results at a cost comparable to time integration methods. This section identifies the major issues associated with adapting linear modal analysis techniques to nonlinear continuum mechanics problems.

The linear mode superposition technique gains its attractiveness mainly because complicated structures can be analyzed with a relatively small number of degrees of freedom. Given a large system whose geometry is fairly complex, but behavior is relatively simple, a typical direct time integration technique requires large structural matrices to model the structural geometry, even though the response can be derived by a linear combination of a small number of basis vectors -- more commonly referred to as mode shapes and derived from the following linear eigenvalue problem:

$$\underline{K}\underline{\Phi} = \underline{M}\underline{\Lambda}\underline{\Phi} \tag{3.77}$$

where $\underline{K}$ and $\underline{M}$ are the structural stiffness and mass matrices; $\underline{\Phi}$, the matrix of mode shapes or eigenvectors; and $\underline{\Lambda}$, the diagonal matrix containing the eigenvalues.

From a mathematical point of view the displacement vector $\underline{q}$ is defined as a linear combination of the eigenvectors $\underline{\Phi}$. In other words

$$\underline{q} = \underline{\Phi}\,\underline{y} \tag{3.78}$$

where $\underline{y}$ are the linear combination coefficients, referred to in engineering jargon as the generalized coordinates. If the matrices $\underline{K}$ and $\underline{M}$ are of size m, then there exist m eigenvectors and therefore m generalized coordinates. In most cases the response $\underline{q}$ can be represented by a reduced set of n eigenvectors, where $n<m$. By using only n eigenvectors to represent $\underline{q}$, $\underline{q}$ is transferred from the vector space $\mathbb{R}^m$ to a reduced vector space $\mathbb{R}^n$.

This concept of representing the response by a reduced vector space when applied to the equations of motion produces a smaller dynamic problem. More specifically, substitute $\underline{q}$ by its generalized coordinate representation $\underline{\Phi y}$ and then pre-multiply all matrices by $\underline{\Phi}^T$ to obtain a new set of equations given as

$$\underline{\ddot{y}} + \underline{\Gamma \dot{y}} + \underline{\Lambda y} = \underline{\Xi} \tag{3.79}$$

where $\underline{\Gamma} = \underline{\Phi^T C \Phi}$, $\underline{\Lambda} = \underline{\Phi^T K \Phi}$, $\underline{\Xi} = \underline{\Phi}^T \underline{F}$, and $\underline{\Phi}$ has been normalized with respect to $\underline{M}$ such that $\underline{\Phi}^T \underline{M \Phi} = \underline{I}$. Notice from Eq. 3.77 that $\underline{\Lambda}$ is diagonal. $\underline{\Gamma}$ is also diagonal when the Fawzy criterion is satisfied ($\underline{K M^{-1} C}$ is symmetric). Consequently, Eq. 3.79 represents a set of n uncoupled equations which can be solved independently using various numerical and analytical solution procedures for SDOF (single degree of freedom) systems. Even when advantage is not taken of the uncoupling or uncoupling does not occur, economy still results when $n<<m$ since the matrix sizes and computer

storage requirements are reduced. The final solution after solving for $\underline{y}$ is $\underline{q} = \underline{\Phi y}$.

To insure that the solution is economical, n should be much smaller than m. However, if n is too small, the response $\underline{q}$ cannot be represented adequately by the selected n eigenvectors $\underline{\Phi}$, and the analysis must be performed again with a larger n. Especially when the local structural response is desired, such as in fatigue analyses where the stresses must be determined accurately, or when the excitation varies considerably over the structure or contains very high frequency components, a large number of mode shapes must be employed, and the modal analysis approach may no longer be attractive (85).

In essence a Rayleigh-Ritz type analysis is performed when mode superposition is applied to nonlinear problems. Since the stiffness, damping, and mass matrices may in general change with time, the eigenvectors derived from the initial conditions no longer represent all deformed shapes, but may be considered the selected Ritz vectors. As a result it would be expected that the initial mode shapes may still adequately reproduce the actual nonlinear response if no significant changes occur in the structural matrices. Otherwise updates to the initial shapes or an alternate method for selecting shapes should be implemented. In any event, if the response is adequately represented, a significant economy results from the reduction in the matrix

sizes and the possibility of using larger time steps.

The major consideration in performing a nonlinear modal analysis and obtaining accurate results is selecting the appropriate basis vectors. In general the basis vectors should be linearly independent and span a substantial portion of the solution space, be easily and economically generated, and remain good representations of the response over long time periods (52). The first requirement ensures convergence of the Rayleigh-Ritz solution while the others enable economically derived and accurate answers.

Four methods currently described in the literature will be presented in the following paragraphs. The simplest method employs only the linear eigenvalues throughout the analysis (8,48,75). Although the linear basis vectors are adequate for mildly nonlinear problems, variations tend to become unacceptable for problems with significant geometric nonlinearities. Problems with highly localized nonlinear material behavior are also poorly reproduced. In general the number of eigenvalues adequately reproducing the linear response are also sufficient for the nonlinear analysis of stiffening structures, but may be inadequate for softening structures since in such cases the structural period increases, requiring more eigenvalues (8).

A similar modification of the first method employs linear basis vectors combined with basis vectors derived from the eigenvalue problem of the structure in some of its deformed nonlinear configurations (49,52). Using these vectors as the initial basis vectors, the analysis is performed with no updating. This method provides significant economies, but the selection of the nonlinear basis vectors without knowing the expected structural response requires considerable judgement on the part of the analyst.

The third method is a slight modification of the linear basis vector approach and uses linear updates to the initial vectors (3). Whenever the force residual $\underline{f}_u$ becomes greater than a certain tolerance, the basis vectors necessary to reduce the residual $\underline{f}_u$ are generated and then normalized with respect to the current set of basis vectors. Although this method yields more accurate results than the first method, it is expensive to perform since the entire stiffness matrix must be regenerated and the eigenvalue problem solved throughout the analysis.

The last method involves deriving the initial linear eigenvectors and then carrying out the analysis by updating whenever the residual $\underline{f}_u$ becomes excessive (51). Although similar to the third method, this method is more economical since the complete eigenvalue problem is never solved, but rather the super-variational approach generates

approximations to the current basis vectors from the previous vectors (84). As a result the response can theoretically always be represented adequately.

Briefly stated the super-variational approach first updates the eigenvalues using the following algorithm:

$$\omega_i^{2(k)} = \underline{\phi}_i^{(k-1)^T} \underline{K}(\underline{q}_n) \underline{\phi}_i^{(k-1)} \tag{3.80}$$

where k is the iteration number; i, the mode number; $\underline{K}(\underline{q}_n)$, the stiffness matrix at this step; and $\underline{\phi}_i$, the normalized basis vector. A correction factor α_{ij} is then defined as follows:

$$\alpha_{ij}^{(k)} = \frac{\underline{\phi}_j^{(k-1)^T} (\underline{K}(\underline{q}_n) - \omega_i^{2(k)} \underline{M}) \underline{\phi}_i^{(k-1)}}{\omega_j^{2(k)} - \omega_i^{2(k)}} \tag{3.81}$$

Finally the updated eigenvectors are derived using the following expression:

$$\underline{\phi}_i^{(k)} = c_i^{(k)} \left[\underline{\phi}_i^{(k-1)} - \sum_{j \neq i=1}^{n} \alpha_{ij}^{(k)} \underline{\phi}_j^{(k-1)} \right] \tag{3.82}$$

where n is the number of basis vectors and $c_i^{(k)}$ is a normalizing factor. Various studies using the super-variational approach indicate a quadratic convergence (51).

In general the mode superposition technique is economical in linear analyses when $n<<m$, but the solution may not be feasible for nonlinear problems when modal updates must be implemented. Even if no updates are

required, the response must be constantly transferred from the generalized coordinates to the natural coordinates to reevaluate the nonlinear terms in the pseudo-force approach and, when necessary, to reform the stiffness matrix, thus further reducing the solution efficiency.

3.2.3 Nonlinear Modal Analysis in the Frequency Domain

Although the use of a nonlinear modal analysis technique in the time domain may be more economical than the direct time integration solution, a numerical integrator is still used, and therefore accuracy and instability problems are present and may invalidate the results. This section addresses a nonlinear modal analysis method in the frequency domain, subsequently referred to as the hybrid frequency-time domain (HFT) technique.

Obtaining the solution in the frequency domain has the advantage of using a theoretically exact numerical integrator given in terms of the transfer function H (H approaches the exact form in the limit as the frequency spectrum range is extended to ∞ and the frequency increment tends to zero). Moreover, the analytical form of H can be modified such that it equals 0 for values above a specified frequency. In other words, an infinite artificial damping can be imposed at the higher frequencies.

In general the proposed hybrid frequency-time domain scheme employs the pseudo-force equations of motion in generalized form

$$\tilde{\underline{M}}\ddot{\underline{y}} + \tilde{\underline{C}}\dot{\underline{y}} + \tilde{\underline{K}}\underline{y} = \tilde{\underline{F}} + \tilde{\underline{F}}^{NL} \tag{3.83}$$

where the ~ denotes a generalized matrix. The transfer function $\underline{H}$ is therefore

$$\underline{H}(\omega) = (-\omega^2\tilde{\underline{M}} + i\omega\tilde{\underline{C}} + \tilde{\underline{K}})^{-1} \tag{3.84}$$

where ω is the circular frequency. The solution procedure consists of obtaining the response $\underline{Y}(\omega)$ in the frequency domain, transferring $\underline{Y}(\omega)$ to the time domain to evaluate $\tilde{\underline{F}}^{NL}$, transferring $\tilde{\underline{F}}^{NL}$ to the frequency domain, and iterating back and forth until the solution converges. Chapter 5 examines the computational efficiency and accuracy characteristics of the HFT method and describes in detail the mechanics of implementing an HFT analysis.

CHAPTER 4

ANALYSIS OF NUMERICAL INTEGRATION METHODS

The energy equations derived in Ch. 2 represent mathematically the dynamic nonlinear behavior of a continuum. These second order nonlinear ordinary differential equations pose an initial value problem whose analytical solution exists only for the most basic problems. Structural dynamic problems, consequently, are solved numerically by a spatial discretization using finite elements and a temporal discretization employing finite difference methods. More recent approaches include temporal discretization by finite elements (26,28,56,95) and spatial discretization by a spectral approach combining a series solution with transform methods (31). This chapter examines popular numerical integration techniques and their ability to produce precise solutions. Stability and accuracy are analyzed with standard time domain schemes, and an alternate approach in the frequency domain is presented. The practice of selecting an appropriate time increment is reviewed, and the chapter concludes with a summary of case studies and the

implications of extending accuracy and stability considerations to nonlinear analyses.

4.1 STABILITY AND ACCURACY ANALYSIS OF NUMERICAL INTEGRATION SCHEMES

Stability of a numerical integrator implies that the solution remains bounded as it progresses in time. Applying numerical integrators inherently involves approximating the differential equations by an algebraic system, whose errors and assumptions may lead to instability. The second feature is accuracy. Accurate solutions are attained by employing small time increments, but economic considerations dictate the use of large time increments. A compromise between these conflicting requirements is achieved by investigating the accuracy parameters as functions of the time increment to natural period ratio.

Although it is often convenient to examine stability and accuracy separately, it is stressed that the fundamental purpose of analyzing numerical integrators is to determine if the numerical solution converges. The necessary requisites for convergence are a stable and accurate solution, and consequently these two characteristics by themselves have no significance. Furthermore, stability can be considered a prerequisite for accuracy since accurate results are unattainable for an unstable solution, while the converse statement is untrue. The following discussion will emphasize the interrelation between stability and accuracy.

The solution of linear systems converges when the Lax equivalence theorem is satisfied (71). This theorem states simply that stability is a necessary and sufficient condition for convergence when the finite difference approximation of the governing equation is consistent. Convergence of the numerical integrator means that the numerical solution approaches the exact solution as the time increment tends to zero. Consistency implies that the finite difference approximation approaches the exact differential equation as the time increment becomes infinitesimal (the rate that the error decreases is defined as the order of accuracy). Stated differently, all terms must be approximated to the same time increment truncation error.

We now examine stability by considering the governing equation of motion for a linear problem

$$\underline{M}\ddot{\underline{q}} + \underline{C}\dot{\underline{q}} + \underline{K}\underline{q} = \underline{F} \tag{4.1}$$

with initial conditions $\underline{q}(0)$ and $\dot{\underline{q}}(0)$. If $\underline{C}$ satisfies the Fawzy criterion ($KM^{-1}C$ is symmetric), the eigenvalue problem produces classical normal modes, and Eq. 4.1 can be rewritten in generalized (normal-mode) form

$$\tilde{\underline{M}}\ddot{\underline{y}} + \tilde{\underline{C}}\dot{\underline{y}} + \tilde{\underline{K}}\underline{y} = \tilde{\underline{F}} \tag{4.2}$$

where each term is defined as in Eqs. 3.78 and 3.79 and all structural matrices are diagonal. As a result of Eq. 4.2, stability can be examined by considering separately the independent equations of each mode

$$\tilde{m}_i\ddot{y}_i + \tilde{c}_i\dot{y}_i + \tilde{k}_i y_i = \tilde{F}_i \tag{4.3}$$

The subscript i and tilda (~) are omitted in the subsequent development.

The free vibration solution to Eq. 4.3 is given analytically as

$$y(t) = e^{-\xi\bar{\omega}t}\left[\frac{\dot{y}(0) + y(0)\xi\bar{\omega}}{\bar{\omega}_D}\sin\bar{\omega}_D t + y(0)\cos\bar{\omega}_D t\right] \tag{4.4}$$

where

$$\bar{\omega} = \sqrt{k/m} \quad , \text{natural frequency}$$

$$\xi = c/2\bar{\omega}m \quad , \text{damping ratio} \tag{4.5}$$

$$\bar{\omega}_D = \bar{\omega}(1 - \xi^2)^{0.5} \quad , \text{damped frequency}$$

For an arbitrary forcing function F(t) the exact solution is given by Duhamel's integral

$$y(t) = (1/m\bar{\omega}_D)\int_o^t F(\tau)e^{-\xi\bar{\omega}(t-\tau)}\sin\bar{\omega}_D(t-\tau)d\tau \tag{4.6}$$
$$+ \text{damped free vibration (Eq. 4.4)}$$

or

$$y(t) = C_1(t)\sin\bar{\omega}_D t + C_2(t)\cos\bar{\omega}_D t + \text{damped free vibration} \tag{4.7}$$

where

$$C_1(t) = (1/m\bar{\omega}_D)\int_o^t F(\tau)\frac{e^{\xi\bar{\omega}\tau}}{e^{\xi\bar{\omega}t}}\cos\bar{\omega}_D\tau d\tau$$
$$C_2(t) = -(1/m\bar{\omega}_D)\int_o^t F(\tau)\frac{e^{\xi\bar{\omega}\tau}}{e^{\xi\bar{\omega}t}}\sin\bar{\omega}_D\tau d\tau \tag{4.8}$$

To facillate the evaluation of accuracy and stability characteristics, Eq. 4.7 is rewritten in terms of discrete time increments Δt using state vectors $\underline{z}$. The discrete form of the exact solution can then be compared with the discrete solution obtained with a numerical integrator. Considering the undamped case $\xi=0$ and assuming a linear load variation between successive time steps, Eq. 4.7 therefore becomes

$$\underline{z}(t+\Delta t) = \underline{A}\underline{z}(t) + \underline{L}\underline{f}(t) \tag{4.9}$$

with state vectors

$$\begin{aligned} \underline{z}(t) &= [\ y(t),\ \Delta t\dot{y}(t)\ ]^T \\ \underline{f}(t) &= [\ F(t),\ F(t+\Delta t)\ ]^T \end{aligned} \tag{4.10}$$

$\underline{A}$ is defined as the amplification matrix and $\underline{L}$, the load operator. In the general case of the underdamped problem, the amplification matrix is given as follows:

$$\begin{aligned} \underline{A} = e^{-\xi\bar{\Omega}} \begin{bmatrix} \cos\bar{\Omega}_D & \sin\bar{\Omega}_D/\bar{\Omega}_D \\ -\bar{\Omega}_D\sin\bar{\Omega}_D & \cos\bar{\Omega}_D \end{bmatrix} + \xi\, e^{-\xi\bar{\Omega}}\sin\bar{\Omega}_D \\ \cdot(1-\xi^2)^{-0.5} \begin{bmatrix} 1 & 0 \\ -\xi\bar{\Omega} & -1 \end{bmatrix} \end{aligned} \tag{4.11}$$

where

$$\bar{\Omega} = \bar{\omega}\Delta t$$

The corresponding expression for the load operator is quite involved. For the undamped problem, however, we have

$$\underline{L} = (1/k) \cdot \begin{bmatrix} \sin\bar{\Omega}\ /\ \bar{\Omega} & 1 \\ \cos\bar{\Omega} - 1 & 1 \end{bmatrix} - (1/k)\underline{A} \tag{4.12}$$

In the free vibration problem the state vector for the load is zero and we have

$$\underline{z}(t+\Delta t) = \underline{A}\underline{z}(t) \tag{4.13}$$

Equation 4.2 is solved numerically with the approximate response at time $n\Delta t$ being denoted by d_n, v_n, and a_n for the displacement, velocity, and acceleration, respectively. The recurrence relation given by Eq. 4.9 becomes

$$\underline{z}_{n+1} = \underline{A}\underline{z}_n + \underline{L}\underline{f}_n \tag{4.14}$$

with initial conditions

$$\begin{aligned} d_o &= q(0) \\ v_o &= \dot{q}(0) \\ a_o &= (F_o - cv_o - kd_o)/m \end{aligned} \tag{4.15}$$

Equation 4.14 can also be written in terms of the initial conditions to give

$$\underline{z}_{n+1} = \underline{A}^{n+1}\underline{z}_o + \sum_{i=1}^{n+1} \underline{A}^{n+1-i}\underline{L}\underline{f}_i \tag{4.16}$$

Notice that the actual form of $\underline{A}$ and $\underline{L}$ in Eq. 4.14 depends on the selected integration operator. In particular, the difference between the exact amplification matrix and load operator of Eqs. 4.11 and 4.12 and those of Eq. 4.14 provides a means of analyzing the stability and accuracy characteristics of the chosen operator. This difference can be construed as an error, and the propagation of the error

as n tends to infinity furnishes a measure of stability.

In a stability analysis it suffices to examine the solution behavior for the homogeneous form of Eq. 4.16

$$\underline{z}_n = \underline{A}^n \underline{z}_o \tag{4.17}$$

In other words, the finite difference approximate response of the non-forced system with nonzero initial conditions is examined to assess the stability and error features of the predicted response.

Assuming the eigenvectors of $\underline{A}$ are distinct, we apply a similarity transformation to $\underline{A}$ and obtain

$$\underline{A} = \underline{\phi \Lambda \phi}^{-1} \tag{4.18}$$

where $\underline{\Phi}$ contains the eigenvectors of $\underline{A}$ and $\underline{\Lambda}$ is a diagonal matrix consisting of the eigenvalues λ_i of $\underline{A}$. Therefore,

$$\underline{A}^n = \underline{\phi \Lambda}^n \underline{\phi}^{-1} \tag{4.19}$$

Notice in general that the state vectors corresponding to the numerical integrator are of order three such that

$$\underline{z}_n = (d_n, \Delta t v_n, \Delta t^2 a_n)^T \tag{4.20}$$

Therefore, $\underline{A}$ is a 3x3 matrix, and the eigenvalues of $\underline{A}$ are derived from its characteristic equation

$$\det (\underline{A} - \lambda \underline{I}) = -\lambda^3 + 2A_1 \lambda^2 - A_2 \lambda + A_3 = 0 \tag{4.21}$$

where

$\underline{I}$ = identity matrix

A_1 = half the trace of $\underline{A}$

A_2 = sum of the principal minors of $\underline{A}$

A_3 = determinant of $\underline{A}$

Using Eqs. 4.17 and 4.19 we have

$$d_n = c_1 \lambda_1^n + c_2 \lambda_2^n + c_3 \lambda_3^n \tag{4.22}$$

where the c_i are constants derived from the initial conditions.

In the following discussion, stability will be defined by $\underline{\Lambda}^n$ being bounded as n tends to infinity. Therefore, the spectral radius $\rho_s = \max\{\lambda_i\}$ must be less than or equal to one for $\underline{\Lambda}^n$ to be bounded. Notice that since ρ_s depends on Ω, $\underline{A}$ is given in terms of $\Omega = \omega \Delta t$. If a finite Ω_c exists such that the numerical integrator is stable for $0 < \Omega < \Omega_c$, the integration scheme is conditionally stable, and if the integrator is stable for all Ω, the scheme is unconditionally stable.

The above stability definition can be depicted visually by plotting the complex eigenvalues λ_i onto the complex λ plane. For a given time increment Δt, we can evaluate the corresponding λ_i and if they all fall within the unit circle $|\lambda| = 1$, the scheme is stable. An alternate procedure is to let $\lambda = (1+z)/(1-z)$ and substitute this expression into Eq. 4.21. Physical stability is then defined as the left half

of the complex Ω plane with the imaginary axis corresponding to undamped systems. Notice that implicit schemes are stable outside of their stability boundary, described by Eq. 4.21, while explicit schemes are stable inside their stability boundary.

We next examine accuracy characteristics of the numerical integrators. Assuming that the finite difference approximation satisfies consistency and stability occurs for an $\Omega_B>0$ with $0<\Omega<\Omega_B$, the Lax theorem ensures convergence. As a consequence, it can be shown mathematically that Eq. 4.21 has two complex conjugate roots λ_1 and λ_2 and a spurious root λ_3 such that $|\lambda_3|<|\lambda_{1,2}|<1$ and

$$\lambda_{1,2} = A + iB = e^{-\bar{\xi}\bar{\Omega} \pm i\bar{\Omega}_D} \tag{4.23}$$

where

$$\begin{aligned}
\bar{\Omega}_D &= \text{Atan } (B/A) \\
\bar{\xi} &= -\ln (A^2 + B^2)/2\bar{\Omega}_D \\
\bar{\Omega} &= \bar{\Omega}_D(1 - \xi^2)^{-0.5} \\
\tilde{\omega}_D &= \bar{\Omega}_D/\Delta t \\
\tilde{\omega} &= \bar{\Omega}/\Delta t \\
i &= \sqrt{-1}
\end{aligned} \tag{4.24}$$

Notice that the tilda (~) denotes approximate quantities.

Equation 4.22 can then be rewritten as (33)

$$d_n = e^{-\bar{\xi}\tilde{\omega}t_n}(c_1\cos\tilde{\omega}_D t_n + c_2\sin\tilde{\omega}_D t_n) + c_3\lambda_3^n \tag{4.25}$$

For two root (A_3=0) integration schemes (the Newmark method is included in this category), we can compare directly the numerical solution (Eq. 4.25) with the exact solution of Eq. 4.4. The numerical solution is exact only when $\bar{\xi}\tilde{\omega} = \xi\bar{\omega}$ and $\tilde{\omega}_D = \bar{\omega}_D$. Discrepancies between the two equations are characterized by the algorithmic damping ratio $\bar{\xi}$ and the relative period error (dispersion) $(\bar{T}-T)/T$ where $T=2\pi/\bar{\omega}$ and $\bar{T}=2\pi/\tilde{\omega}$. Other equivalent accuracy parameters for numerical dissipation include the amplitude decay $AD=1-d_{n+nD}/d_n$ and logarithmic decrement $\bar{\delta} = \ell n(d_n/d_{n+nD})$ where $nD=2\pi/\bar{\omega}_D\Delta t$.

An equivalent approach to analyze accuracy for two root schemes would be to rewrite Eq. 4.22 as (23,59,60,62)

$$d_n = c_1 e^{(a+ib)\bar{\omega}_D n\Delta t} + c_2 e^{(a-ib)\bar{\omega}_D n\Delta t} \tag{4.26a}$$

where $\bar{\omega}_D$ is the damped natural frequency of Eq. 4.3 and a and b are the numerical damping and phase shift parameters. In particular,

$$\begin{aligned} a &= -\xi\tilde{\Omega}/\bar{\Omega}_D \\ b &= \tilde{\Omega}_D/\bar{\Omega}_D \end{aligned} \tag{4.26b}$$

From Eq. 4.26b it is evident that the exact solution occurs when $a=-\xi(1-\xi^2)^{-0.5}$ and b=1 and also that instability occurs when a>0 or b is imaginary. Notice once again that a and b are functions of $\bar{\Omega}_D$.

4.2 SURVEY OF INTEGRATION SCHEMES

Integration schemes are classified into two basic categories: implicit and explicit. The explicit methods express the response in terms of the previous response, and hence are referred to as predictor methods, while implicit methods define the current response in terms of other current response quantities, and thus are called corrector methods (for example, the velocity and acceleration at time t may be defined as functions of the displacement at time t). As shown in previous sections, explicit methods involve minimal computational expense per time step, but require small time steps to eliminate instability, while the converse statement holds for implicit methods. The stability and accuracy characteristics of the explicit central difference (3 point) and implicit Newmark, Wilson-θ, Houbolt, Park, and Hilber schemes applied to linear problems are examined in this section.

Although the discussion limits itself to the more popular integration methods, it should be noted that new schemes are under constant development (11) with some having general applicability and others limited to specific problems. Recent developments include the implicit-explicit methods applied to systems with regions of high rigidity coupled with regions of high flexibility, such as in fluid-structure problems (13,14,15,36,37,41,61,63). Semi-implicit methods combining the stability and accuracy

characteristics of implicit methods and the non-matrix factorizing property of explicit methods are also under consideration (58,64,83). These new integration schemes, nevertheless, are subject to the same basic stability and accuracy questions.

Using the procedure outlined in section 4.1, the spectral radius ρ_s of the amplification matrix $\underline{A}$ can be derived as a function of $\overline{\Omega}$, and the results plotted onto the complex $\overline{\Omega}$-plane. Figure 4.1 depicts the spectral radius as a function of $\Delta t/T$, and Fig. 4.2 shows the stability regions for various schemes. Notice that Ω in Fig. 4.2 is equivalent to our $\overline{\omega}$, the exact undamped natural frequency. Accuracy is analyzed next, yielding results such as Fig. 4.3 for Eq. 4.25 ($\overline{\zeta}$ is the same as our $\overline{\xi}$, the algorithmic damping ratio, and τ, the period elongation defined by Eq. A.16) and Fig. 4.4 for Eq. 4.26. Similar accuracy plots can be derived for other physical damping ratios.

Figures 4.1-4.4 offer insight into the rationale behind selecting an appropriate integration scheme. The central difference method tends to be the favorite among explicit schemes. Park (60) demonstrates that the central difference method displays better stability and requires less computational cost than the predictor-corrector schemes, high-order Taylor series, and 4th-order Runge-Kutta scheme. Krieg (40) states that the central difference method has the

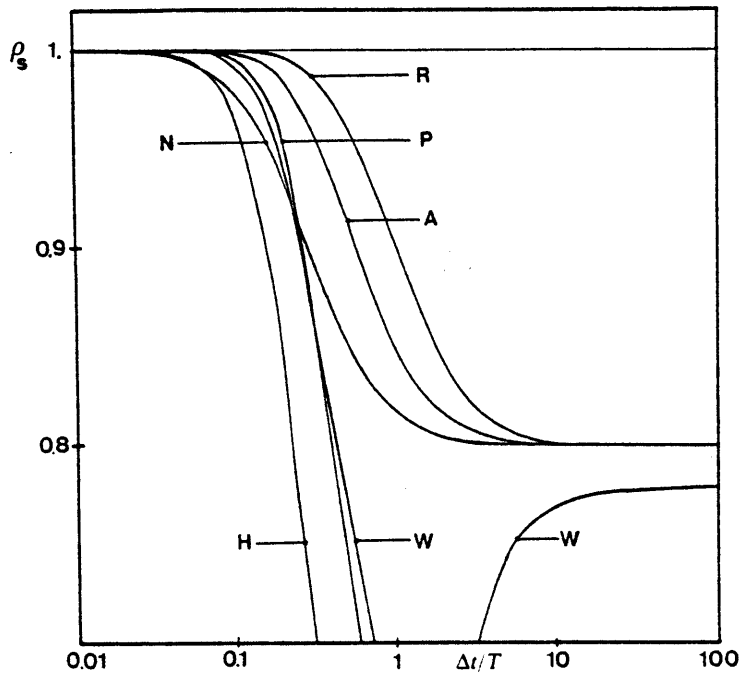

ABBREVIATIONS:

R : proposed ρ-method (ρ=0.8)

A : Hilber's α-method (α=-0.1111)

N : Newmark's algorithm (γ=0.6111, β=0.3086)

W: Wilson's algorithm (θ=1.4)

P : Park's algorithm

H : Houbolt's algorithm

Fig. 4.1 Spectral radii of the amplification matrix A as a function of $\Delta t/T$ (no physical damping)

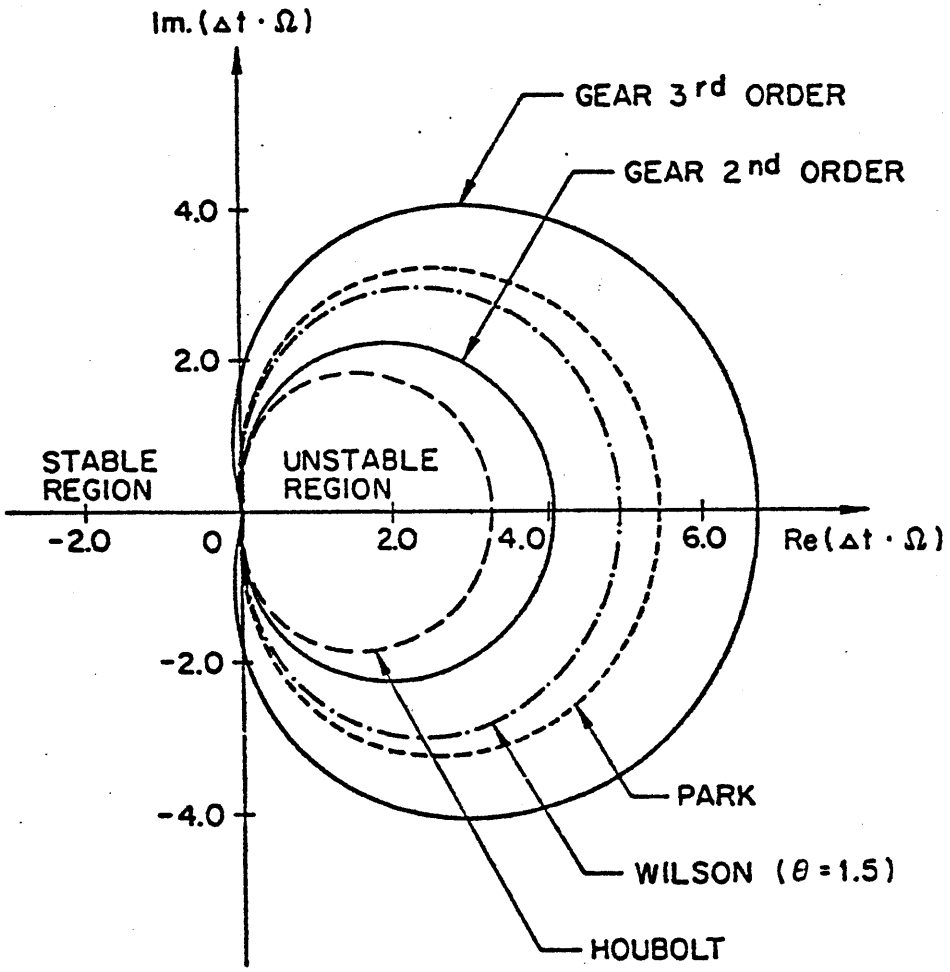

TRAPEZOIDAL RULE : ENTIRE LEFT-HAND PLANE INCLUDING IMAGINARY AXIS

CENTRAL DIFFERENCE : $-2j \leq \Omega \cdot \Delta t \leq 2j$

Fig. 4.2 **Stability Region of Multistep Methods** (60)

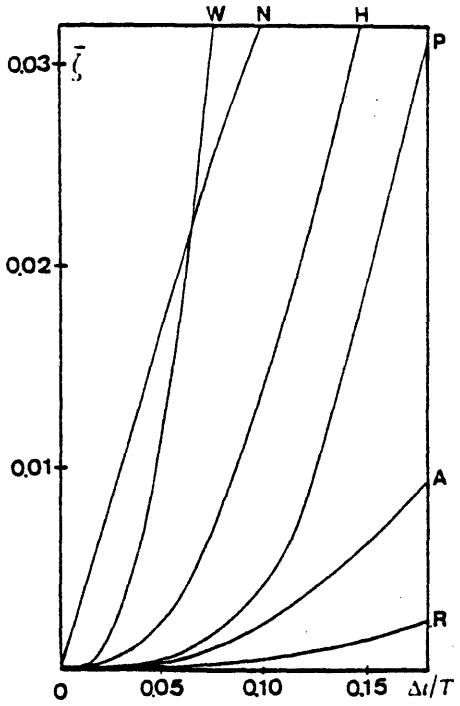

ABBREVIATIONS:

R : proposed ρ-method (ρ=0.8)

A : Hilber's α-method (α=-0.1111)

N : Newmark's algorithm (γ=0.6111, β=0.3086)

W: Wilson's algorithm (θ=1.4)

P : Park's algorithm

H : Houbolt's algorithm

Fig. 4.3a Algorithmic damping ratios $\bar{\zeta}$ as function of $\Delta t/T$ (no physical damping) (11)

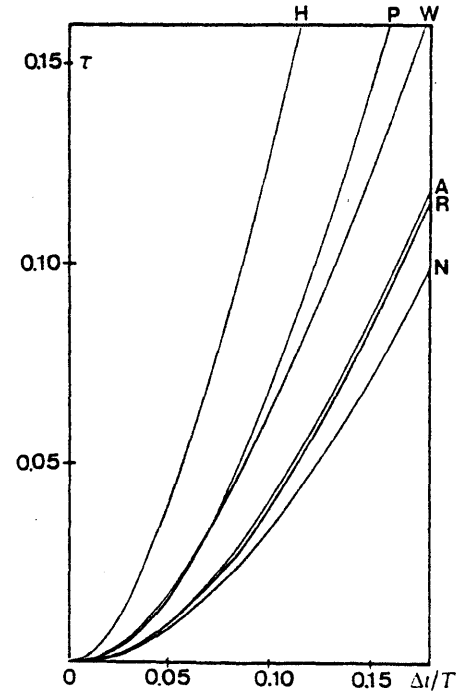

ABBREVIATIONS:

R : proposed ρ-method (ρ=0.8)

A : Hilber's α-method (α=-0.1111)

N : Newmark's algorithm (γ=0.6111, β=0.3086)

W: Wilson's algorithm (θ=1.4)

P : Park's algorithm

H : Houbolt's algorithm

Fig. 4.3b Relative period errors τ as a function of $\Delta t/T$ (no physical damping) (11)

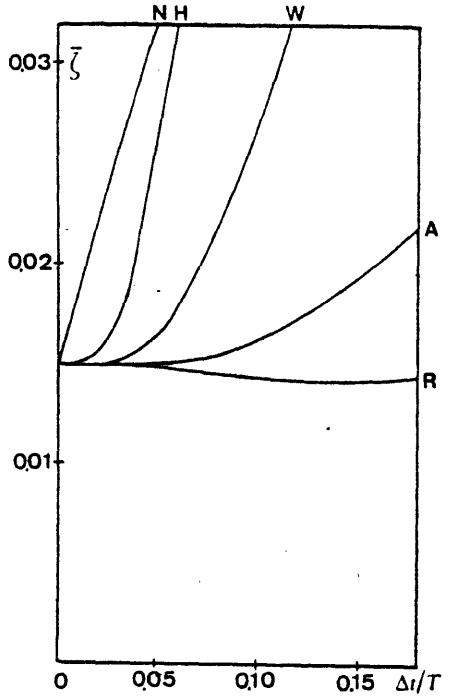

ABBREVIATIONS:

R : proposed ρ-method (ρ=0.8)

A : Hilber's α-method (α=-0.1111)

N : Newmark's algorithm (γ=0.6111, β=0.3086)

W: Wilson's algorithm (θ=1.4)

P : Park's algorithm

H : Houbolt's algorithm

Fig. 4.3c Algorithmic damping ratios $\bar{\zeta}$ as function of $\Delta t/T$ (1·5 per cent physical damping) (11)

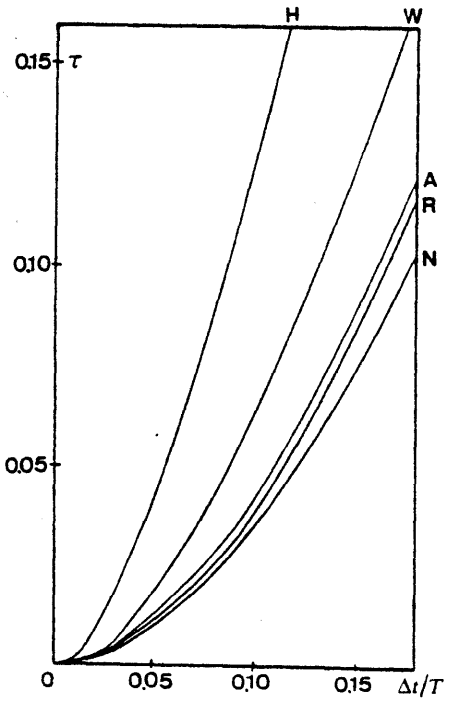

ABBREVIATIONS:

R : proposed ρ-method (ρ=0.8)

A : Hilber's α-method (α=-0.1111)

N : Newmark's algorithm (γ=0.6111, β=0.3086)

W: Wilson's algorithm (θ=1.4)

P : Park's algorithm

H : Houbolt's algorithm

Fig. 4.3d Relative period errors τ as a function of $\Delta t/T$ (1·5 per cent physical damping) (11)

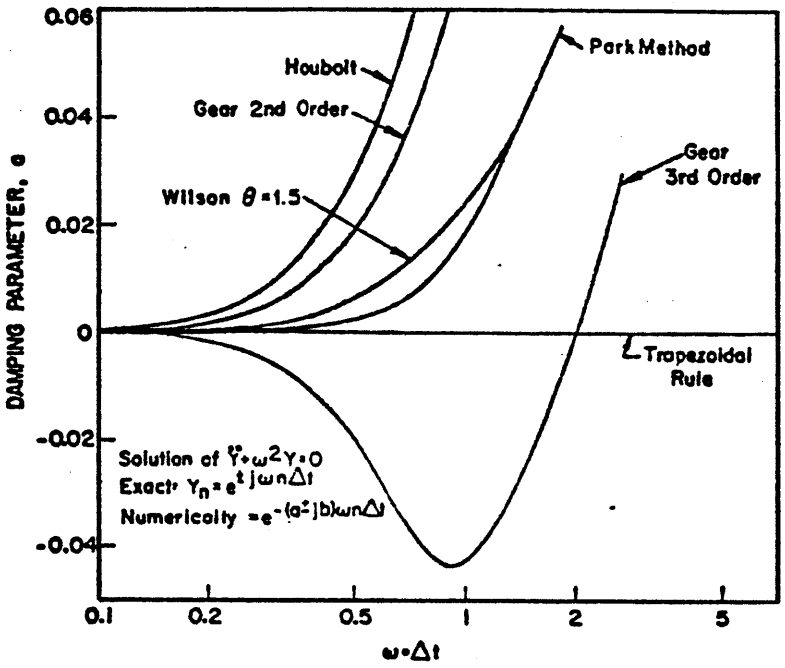

a. Damping Coefficients of Multistep Methods

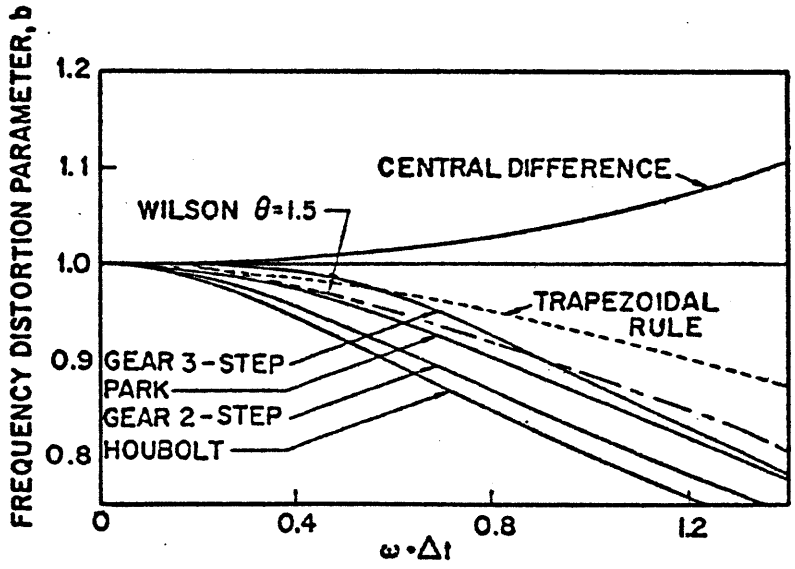

b. Frequency Distortion of Multistep Methods

Fig. 4.4 Damping and Frequency Distortion Parameters versus $\omega \Delta t$ (60)

largest critical time step of all explicit second order schemes, and furthermore that all explicit second order schemes are conditionally stable. In particular, Fig. 4.2 denotes the stability region of the central difference method to range from -2i to 2i. As a result, for the undamped free vibration problem (imaginary axis) we have $\bar{\omega}\Delta t<2$, implying for the critical time step

$$\Delta t_{cr} \leq 2/\bar{\omega} = T/\pi \qquad (4.27)$$

Notice from Fig. 4.4 that the central difference scheme exhibits a period compression.

The selection of a "best" implicit scheme is subject to interpretation. From Fig. 4.3 it appears that the recent scheme of Hilber (33) and that of Bazzi and Anderheggen (11) demonstrate good algorithmic damping and low relative period errors. Moreover, these two schemes have the capability to control the numerical dissipation by a nonphysical external parameter (α or ρ). The Newmark method (α=0.25, δ =0.5, trapezoidal rule), however, is also unconditionally stable and imposes no error in the specified physical damping, as shown in Fig. 4.4a.

As a consequence, it is emphasized that the choice of an appropriate numerical integrator also depends on the type of problem under consideration. If the spatial structural modelling is accurate up to the highest modes and it is expected that the loading will excite practically all modes,

then an "exact" numerical integrator is preferred. Most structural problems, however, consist of a numerical model that adequately represents the geometric structural shape and many of the lowest structural modes, but has no physical significance for the highest modes. Although the loading may excite only the lowest modes, the use of an approximate numerical integrator may induce numerical resonance leading to amplification of the physically insignificant high frequency response. This class of problems, consequently, is solved preferably by numerical integrators that damp out the high frequency response and remain stable at these frequencies, displaying no errors in the high frequency contribution.

4.3 LINEAR SYSTEMS THEORY APPROACH FOR ACCURACY AND STABILITY ANALYSES

The accuracy and stability analysis scheme presented in section 4.2 is usually applied to the homogeneous free vibration problem. Extensions to arbitrary load histories are often quite cumbersome, if not impossible. Accuracy, however, varies with the load history since the load vector is also expanded by the finite difference approximation, and hence the effect of the load vector should also be included in an accuracy analysis. Extending the accuracy analysis to a general load vector is possible by conducting numerical experiments, but this procedure is limited to a few simple load histories since the analytical solution for most problems cannot be derived in closed form. Furthermore,

the algorithmic damping ratio should be viewed as a quantity that varies as a function of the structural and excitation frequencies. This section presents an alternate approach by examining accuracy using linear systems theory. The basic procedure consists of comparing the exact frequency response function (often referred to as the transfer function) with the approximate frequency response function corresponding to the numerical integration scheme.

Advantages of the linear systems theory approach include the ability to examine the algorithmic damping as a function of the excitation frequency and how the finite difference expansion of the load vector affects the solution accuracy.

The procedure will now be described in detail. Consider the numerical approximation of the governing differential equation given by Eq. 4.3.

$$m\ddot{q}_n + c\dot{q}_n + kq_n = F_n \tag{4.28}$$

All numerical integrators expand the response in terms of other response quantities, and in general we have

$$\ddot{q}_n = \sum_{i=0}^{k} \alpha_i q_i$$
$$\dot{q}_n = \sum_{i=0}^{k} \beta_i q_i \tag{4.29}$$

where α_i and β_i are constants. Substituting Eq. 4.29 in Eq. 4.28 we obtain

$$m\sum_{i=0}^{k}\alpha_i q_i + c\sum_{i=0}^{k}\beta_i q_i + kq_n = \sum_{i=0}^{k}\gamma_i F_i \tag{4.30}$$

where the γ_i are constants. Equation 4.30 is transferred to the frequency domain using the discrete-time Fourier transform, and in particular at any frequency Ω the corresponding equation is obtained by the following substitutions:

$$\begin{aligned}
q_n &\longrightarrow e^{0}Q(\Omega)\\
q_{n-1} &\longrightarrow e^{-i\Omega}Q(\Omega)\\
q_{n-2} &\longrightarrow e^{-i2\Omega}Q(\Omega)\\
&\vdots\\
F_n &\longrightarrow e^{0}F(\Omega)\\
F_{n-1} &\longrightarrow e^{-i\Omega}F(\Omega)\\
F_{n-2} &\longrightarrow e^{-i2\Omega}F(\Omega)
\end{aligned} \tag{4.31}$$

yielding

$$\begin{aligned}
m\sum_{i=0}^{k}\alpha_i e^{-i\Omega(n-i)}Q(\Omega) + c\sum_{i=0}^{k}\beta_i e^{-i\Omega(n-i)}Q(\Omega)\\
+ke^{0}Q(\Omega) = \sum_{i=0}^{k}\gamma_i e^{-i\Omega(n-i)}F(\Omega)
\end{aligned} \tag{4.32}$$

Finally, the approximate transfer function corresponding to the numerical integrator is given by

$$\tilde{H}(\Omega) = Q(\Omega)/F(\Omega) \tag{4.33}$$

The analytical form for the exact transfer function $H_e(\omega)$ in Eq. 4.28 is given by

$$H_e(\Omega) = (-\omega^2 m + i\omega c + k)^{-1} \tag{4.34}$$

Measures of the period elongation and numerical dissipation can be derived by comparing Eqs. 4.33 and 4.34. In this particular development, the period elongation is derived by considering the shift of the resonant frequency of the approximate with respect to the exact transfer function. An algorithmic damping ratio is obtained by comparing the imaginary parts of Eqs. 4.33 and 4.34.

This frequency domain accuracy analysis was applied to the central difference (CD), Newmark (trapezoidal rule, N), Houbolt (H), and Park (P) integration schemes. The detailed calculations for the Park method are provided in Appendix A. The approximate transfer functions are as follows:

$$\tilde{H}_{CD}(\Omega) = (2a_1(\cos\Omega - 1) + i2a_2\sin\Omega + a_3)^{-1} \tag{4.35}$$

$$\tilde{H}_{N}(\Omega) = (1 + \cos\Omega)/((4a_1 + a_3)\cos\Omega + i4a_2\sin\Omega - 4a_1 + a_3) \tag{4.36}$$

$$\begin{aligned}\tilde{H}_{H}(\Omega) = {} & (2a_1 + 11a_2/3 + a_3 + (-5a_1-6a_2)e^{-i\Omega} \\ & + (4a_1+3a_3)e^{-i2\Omega} + (-a_1 - 2a_2/3)e^{-i3\Omega})^{-1}\end{aligned} \tag{4.37}$$

$$\begin{aligned}\tilde{H}_{P}(\Omega) = {} & (25a_1/9 + 10a_2/3 + a_3 + (-50a_1/6 - 5a_2)e^{-i\Omega} \\ & +(115a_1/12 + 2a_2)e^{-i2\Omega} + (-50a_1/9 - a_2/3)e^{-i3\Omega} \\ & + 11a_1/6e^{-i4\Omega} - a_1e^{-i5\Omega}/3 + a_1e^{-i6\Omega}/36)^{-1}\end{aligned} \tag{4.38}$$

where

$$\begin{aligned}\Omega &= \omega\Delta t \\ \bar{\omega}_n &= \text{natural frequency} \\ a_1 &= 1/4\pi^2 \\ a_2 &= \xi\Delta t\bar{\omega}_n a_1 \\ a_3 &= \Delta t^2\bar{\omega}_n^2 a_1 \\ \xi &= \text{viscous damping ratio}\end{aligned} \tag{4.39}$$

The exact transfer function is given as

$$H_e(\Omega) = (-\Omega^2 a_1 + i2a_2\Omega + a_3)^{-1} \tag{4.40}$$

Notice that Eqs. 4.35 to 4.40 have been nondimensionalized by multiplying the usual transfer function

$$H(\omega) = (-\omega^2 m + i\omega c + k)^{-1} \tag{4.41}$$

by $\frac{4\pi^2}{\Delta t^2}\cdot m$. Also the load frequency ω has been nondimensionalized to $\Omega = \omega\Delta t$.

Comparing Eq. 4.35 with 4.40, it is evident that the period compression in the central difference method is due to the difference between the terms corresponding to a_1 ($2(\cos\Omega - 1)$ cf. $-\Omega^2$). Also, the central difference scheme exhibits an algorithmic damping less than the specified damping because the approximate transfer function has imaginary term $2a_2\sin\Omega$ while the exact has $2a_2\Omega$. Similar statements apply to the Newmark method. Notice in particular that the specified viscous damping is not algebraically associated with any real term, and conversely that the a_1 and a_3 terms are not associated with any imaginary terms. Since $a_2 = 0$ for $\xi = 0$, the central difference and Newmark schemes impose no numerical dissipation when viscous damping is not specified.

The corresponding transfer functions for the Houbolt and Park schemes, Eqs. 4.37 and 4.38, indicate that the viscous damping is associated with real terms and therefore directly induces period elongation and the terms

corresponding to a_1 and a_3 directly induce numerical dissipation by affecting the imaginary components, contrary to the central difference and Newmark schemes.

Plots of the transfer functions are given in Figs. 4.5 to 4.12. The eight figures consist of four sets of two with the first set being the central difference; second, Newmark; third, Houbolt; and fourth, Park. The first figure of each set corresponds to a specified viscous damping ratio ξ=0.05 and the second, ξ=0.10. Figures a and b of each figure give the amplitude and phase plots for $\Delta t/T$ =0.05, and Figs. c and d give similar plots for $\Delta t/T$ =0.20. These plots are discrete representations of Eqs. 4.35-4.38 and Eq. 4.40. As a result, the maxima of each transfer function could not be captured exactly when plotted. Numerically obtained values for the maxima and the corresponding resonant frequency are provided in Table 4.1. In all plots the inverted hat "v" corresponds to the approximate transfer function and the solid line to the exact transfer function.

Notice that the central difference method provides the best estimate of the resonant frequency (least frequency distortion). Its use, however, is restricted because it is an explicit integrator. The Newmark method tends to demonstrate the least frequency distortion and artificial damping of the implicit methods, while the Houbolt is the worst of those considered. In general, the Newmark, Houbolt, and Park methods deamplify the response

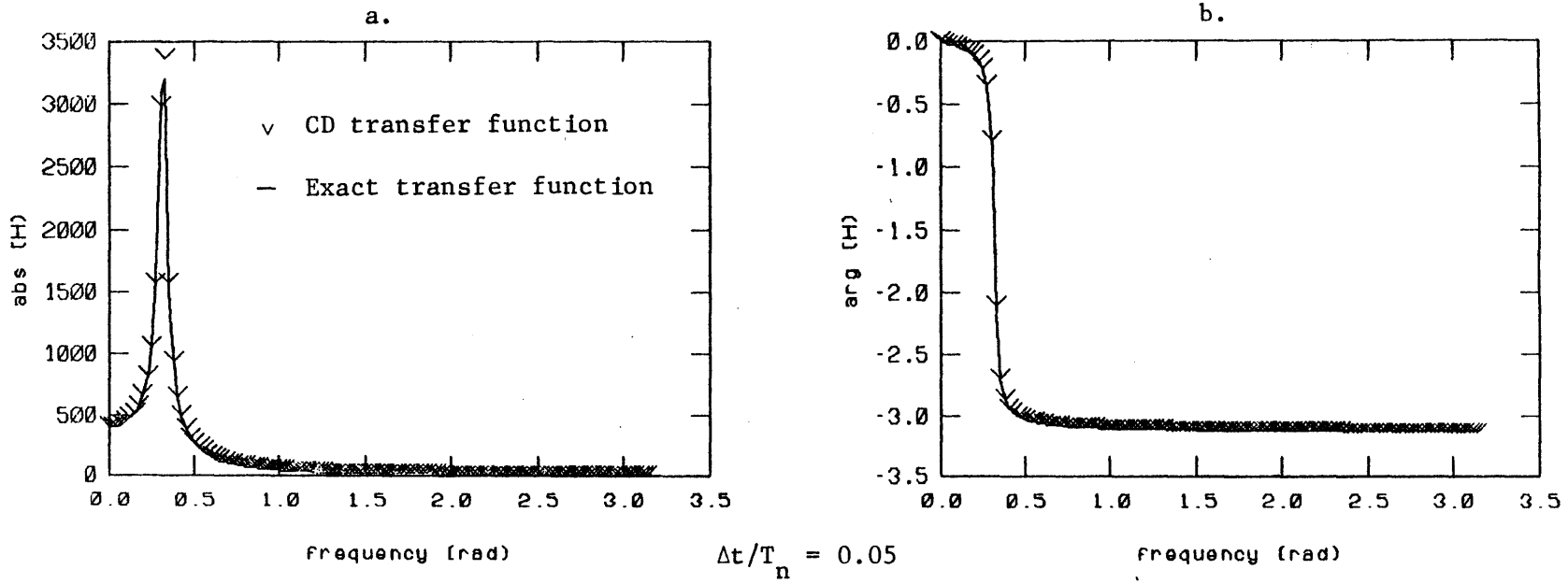

$\Delta t/T_n = 0.05$

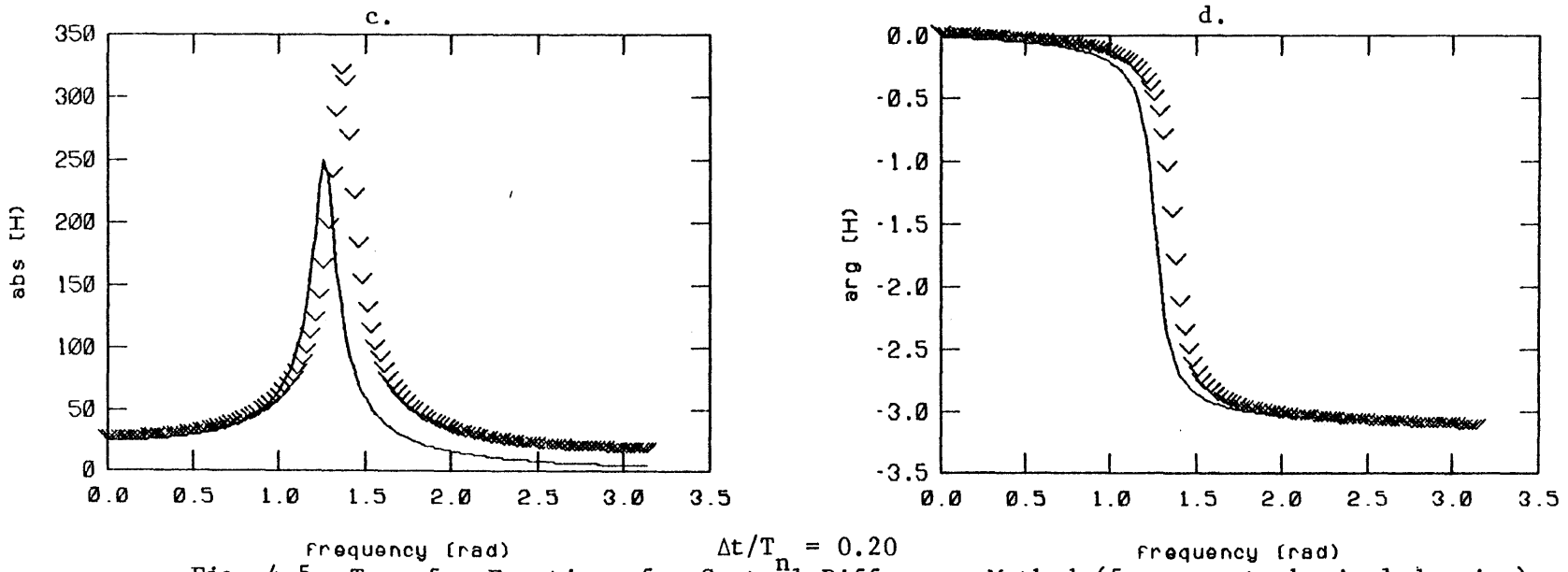

$\Delta t/T_n = 0.20$

Fig. 4.5 Transfer Functions for Central Difference Method (5 per cent physical damping)

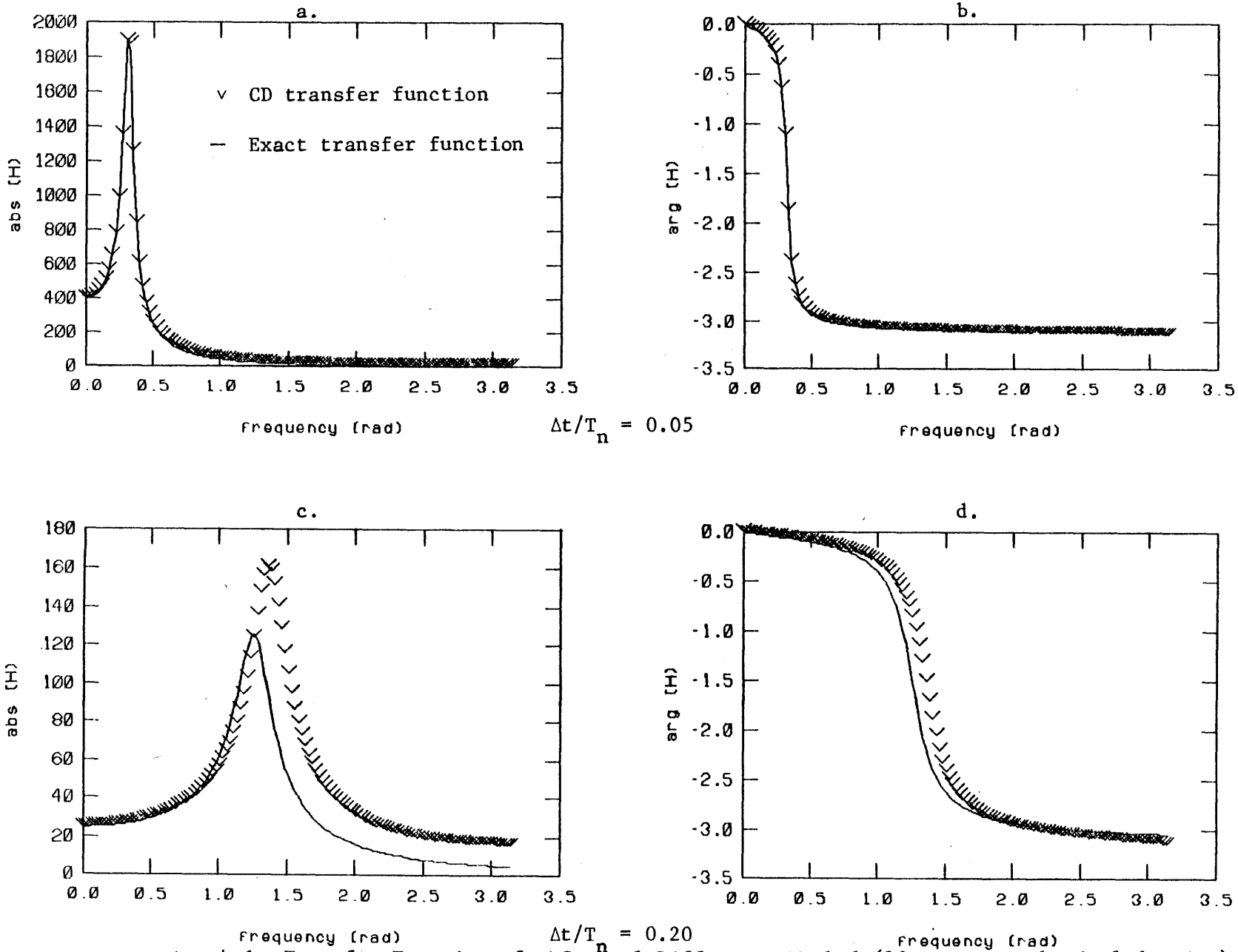

Fig. 4.6 Transfer Functions for Central Difference Method (10 per cent physical damping)

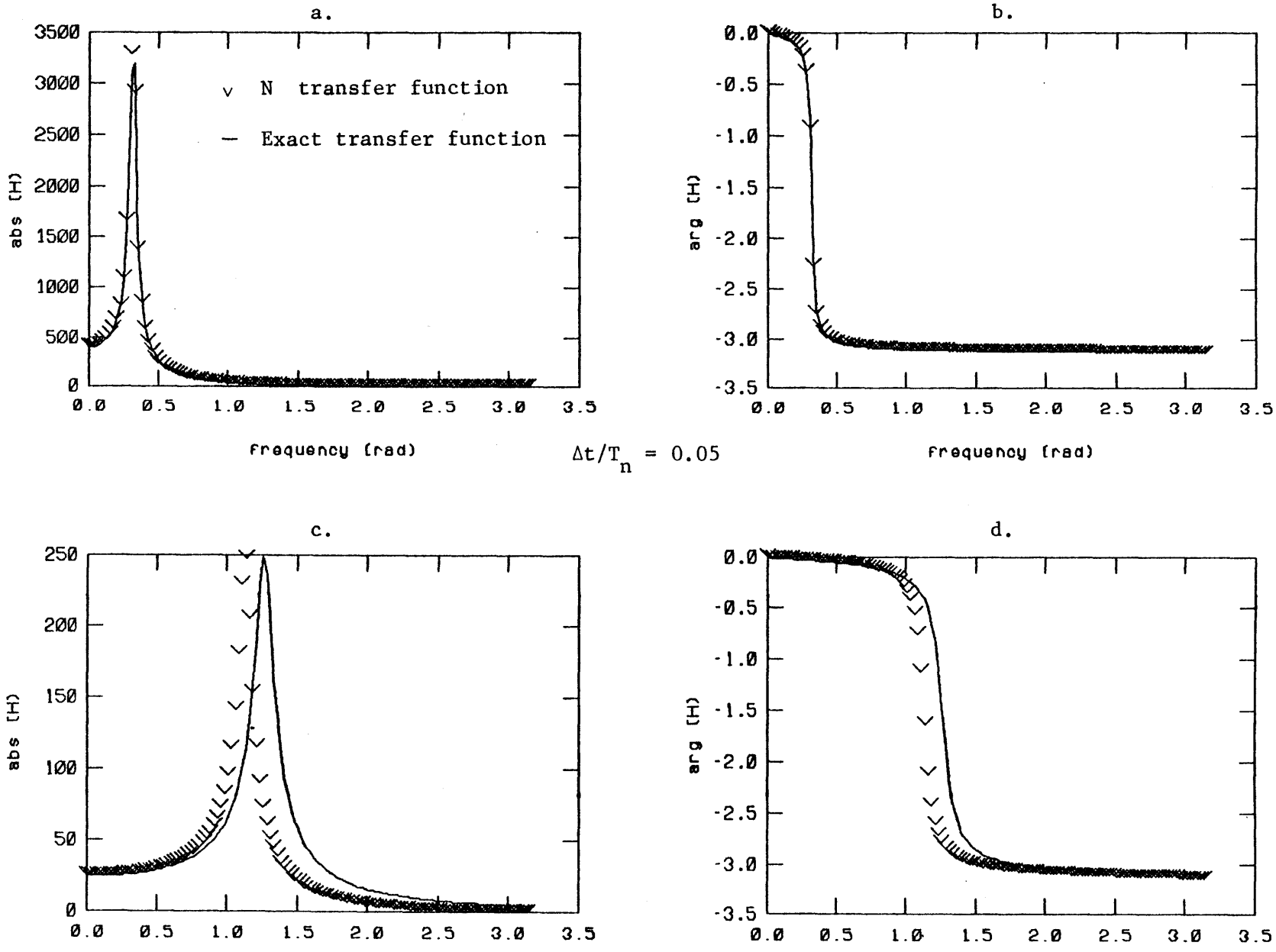

Fig. 4.7 Transfer Functions for Newmark Method (5 per cent physical damping)

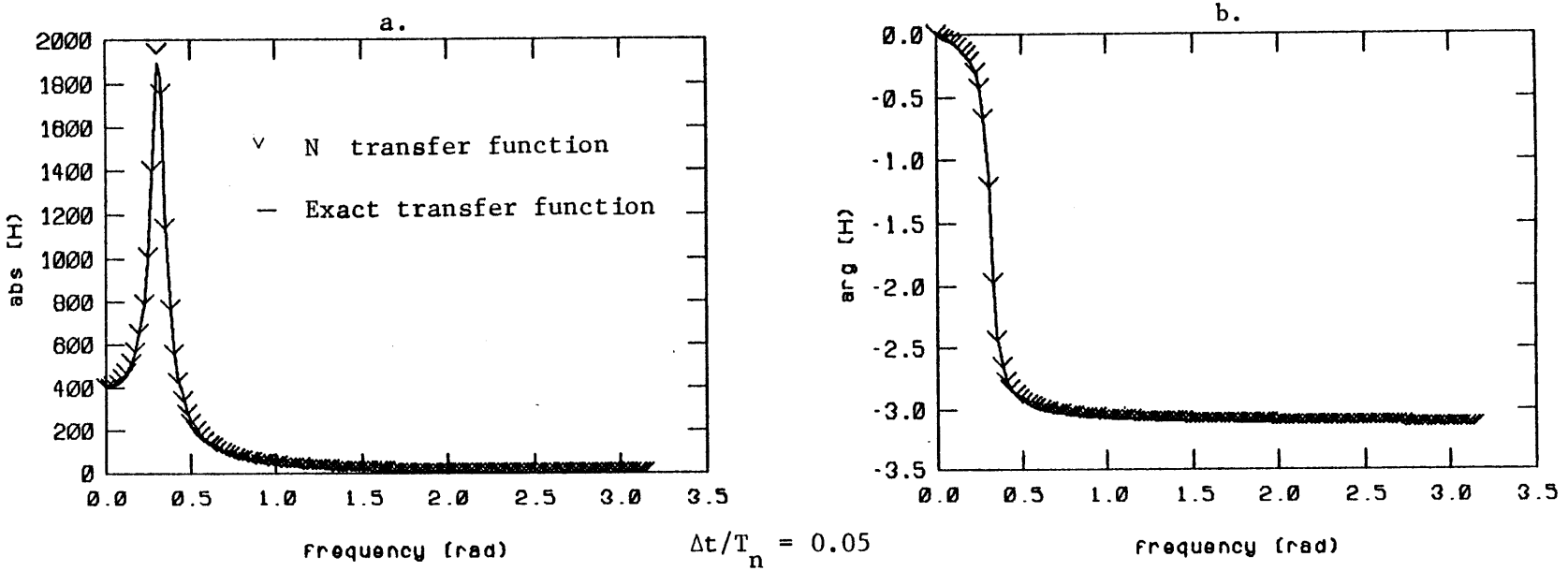

$\Delta t/T_n = 0.05$

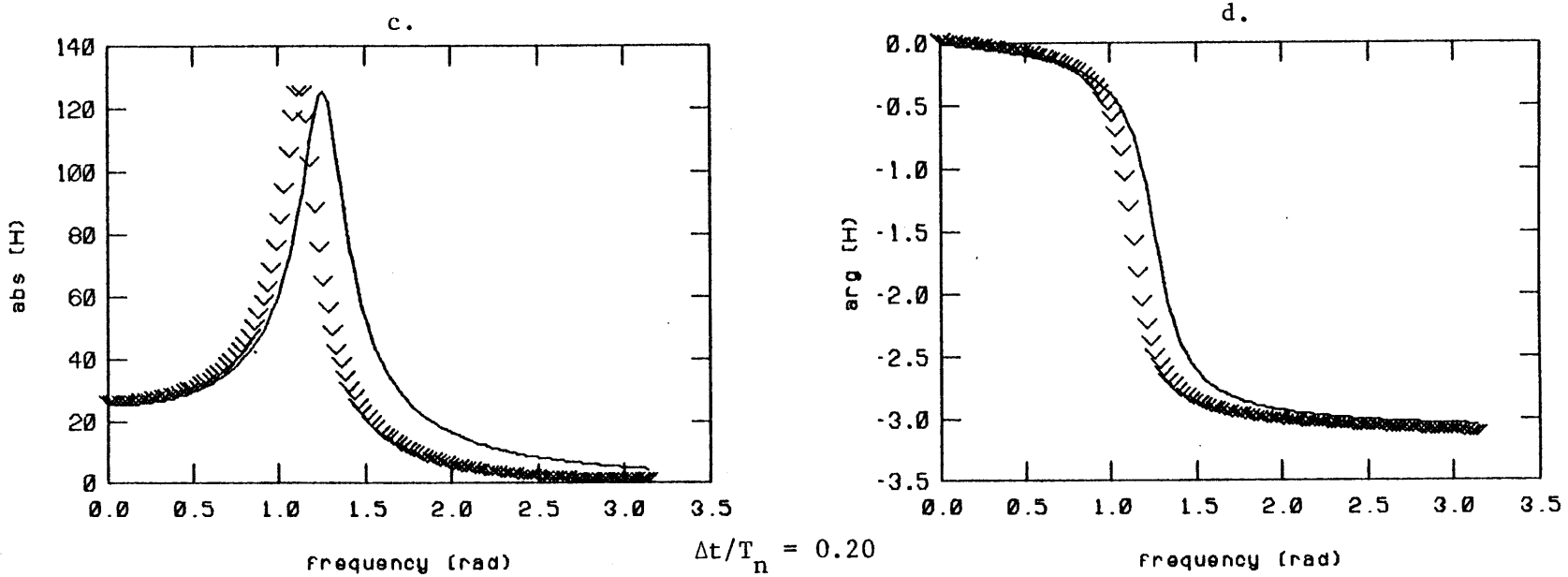

$\Delta t/T_n = 0.20$

Fig. 4.8 Transfer Functions for Newmark Method (10 per cent physical damping)

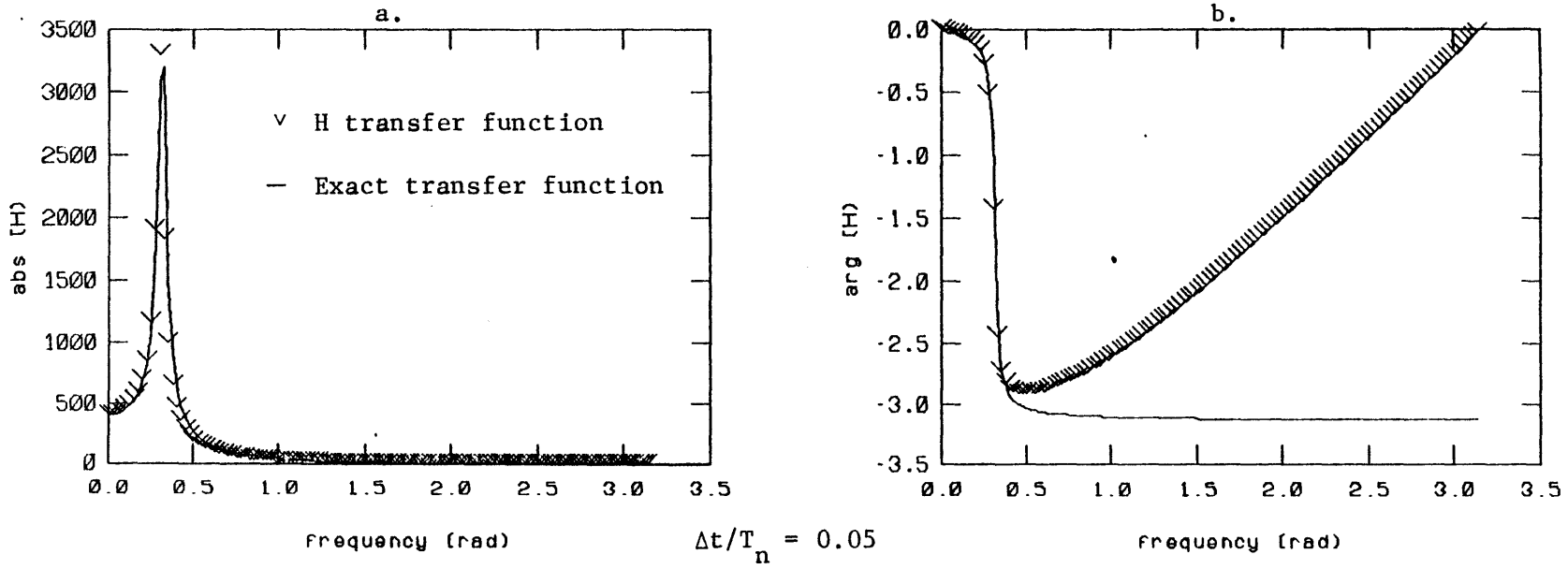

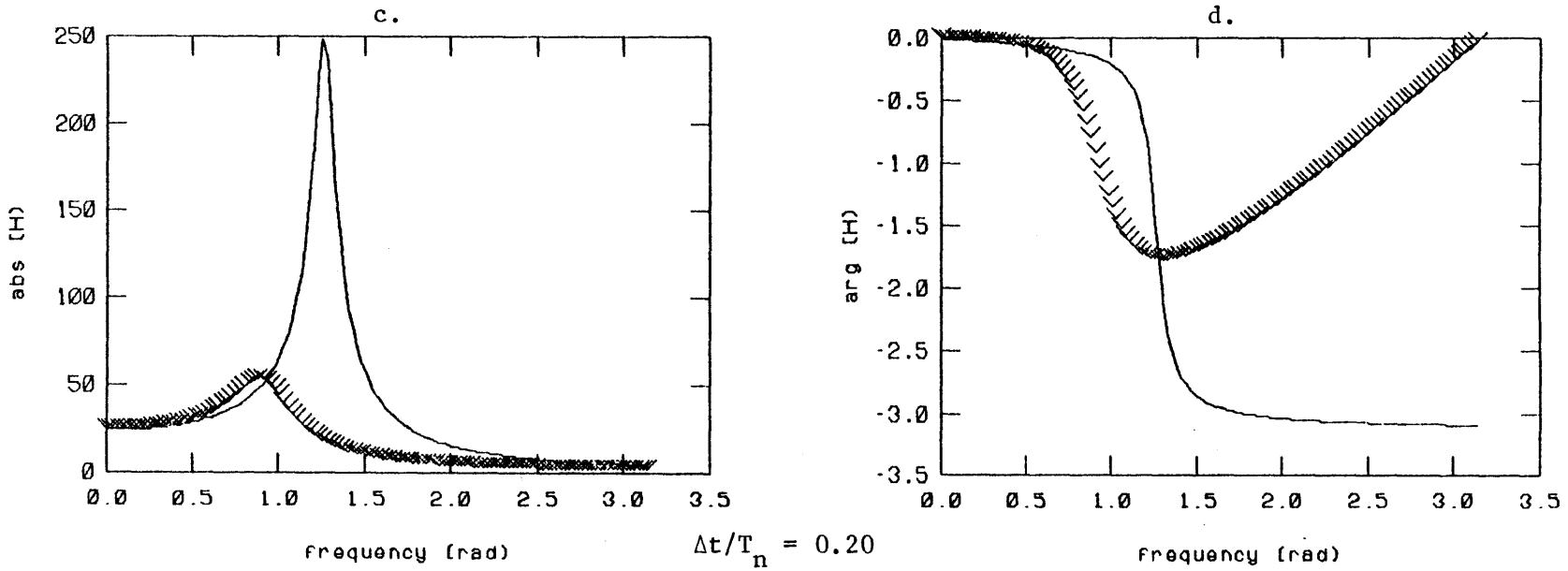

Fig. 4.9 Transfer Functions for Houbolt Method (5 per cent physical damping)

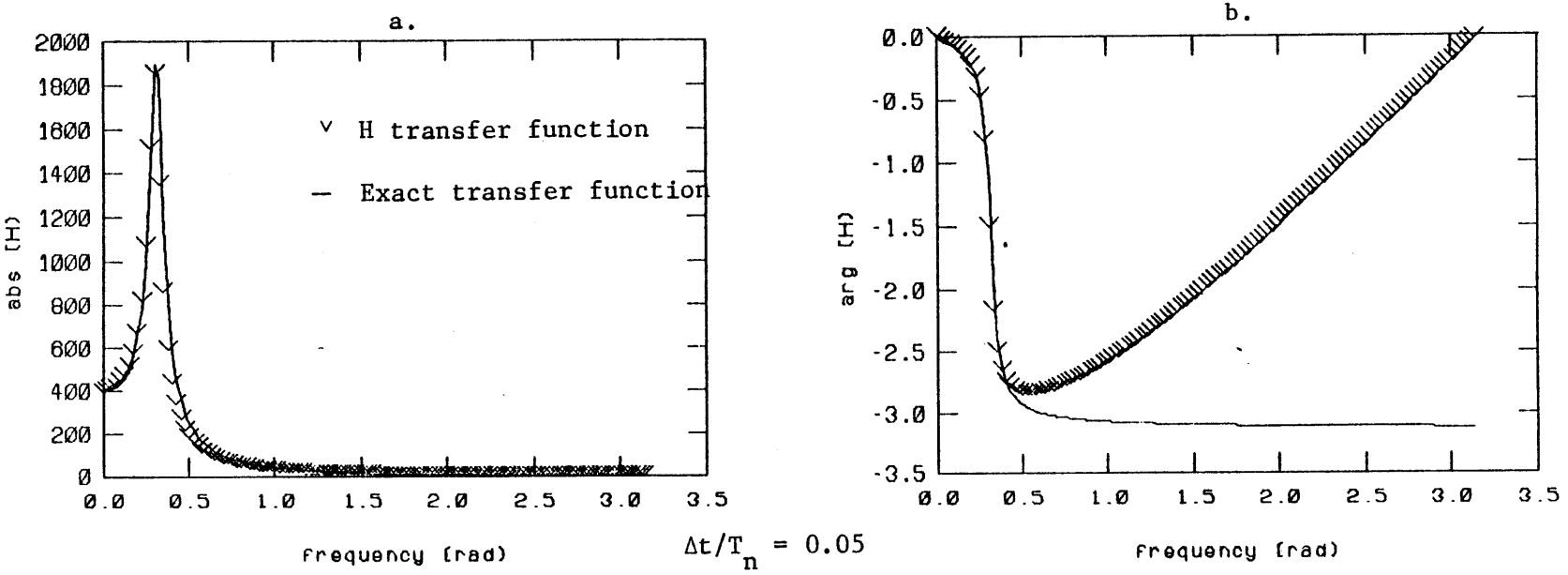

Fig. 4.10 Transfer Functions for Houbolt Method (10 per cent physical damping)

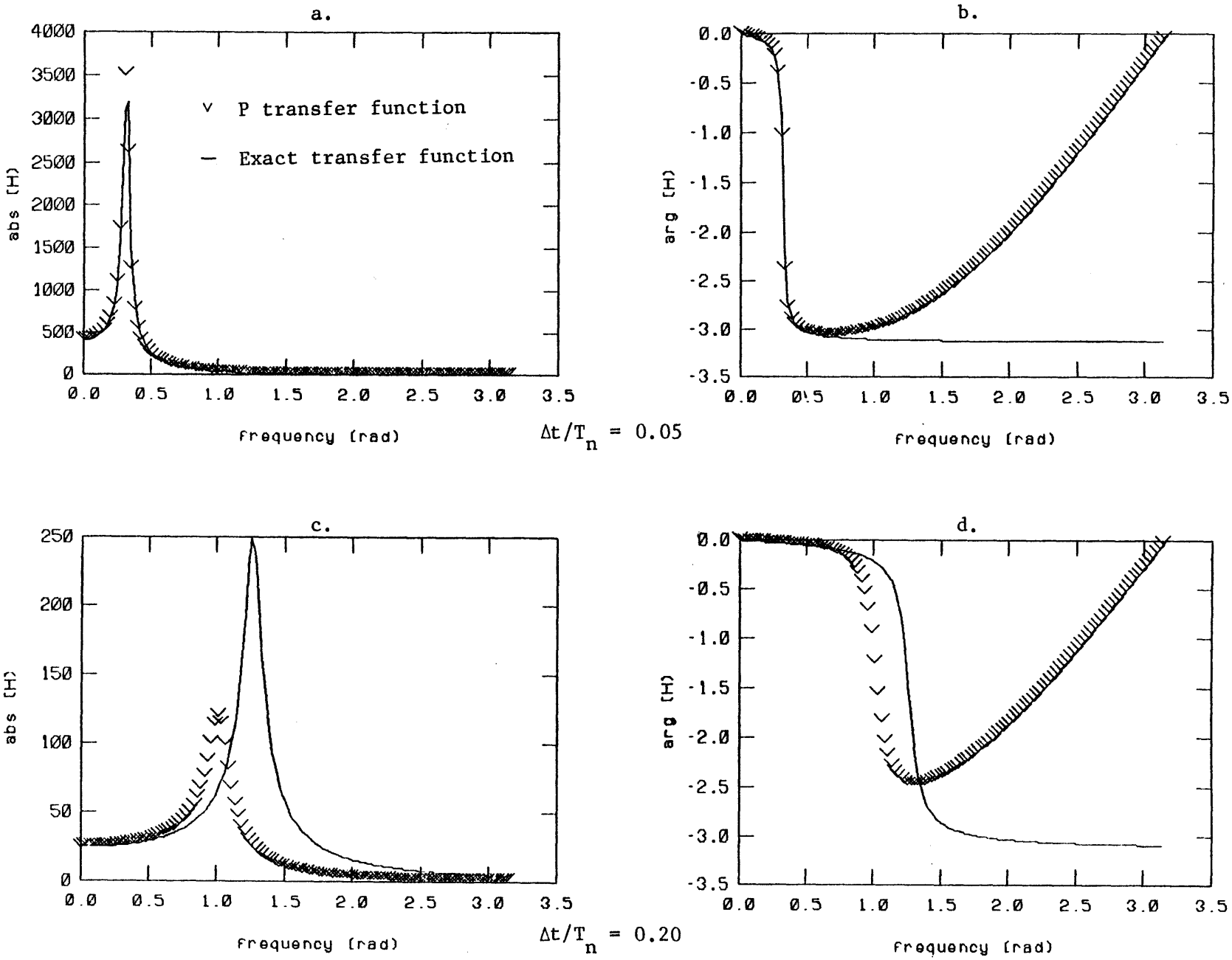

Fig. 4.11 Transfer Functions for Park Method (5 per cent physical damping)

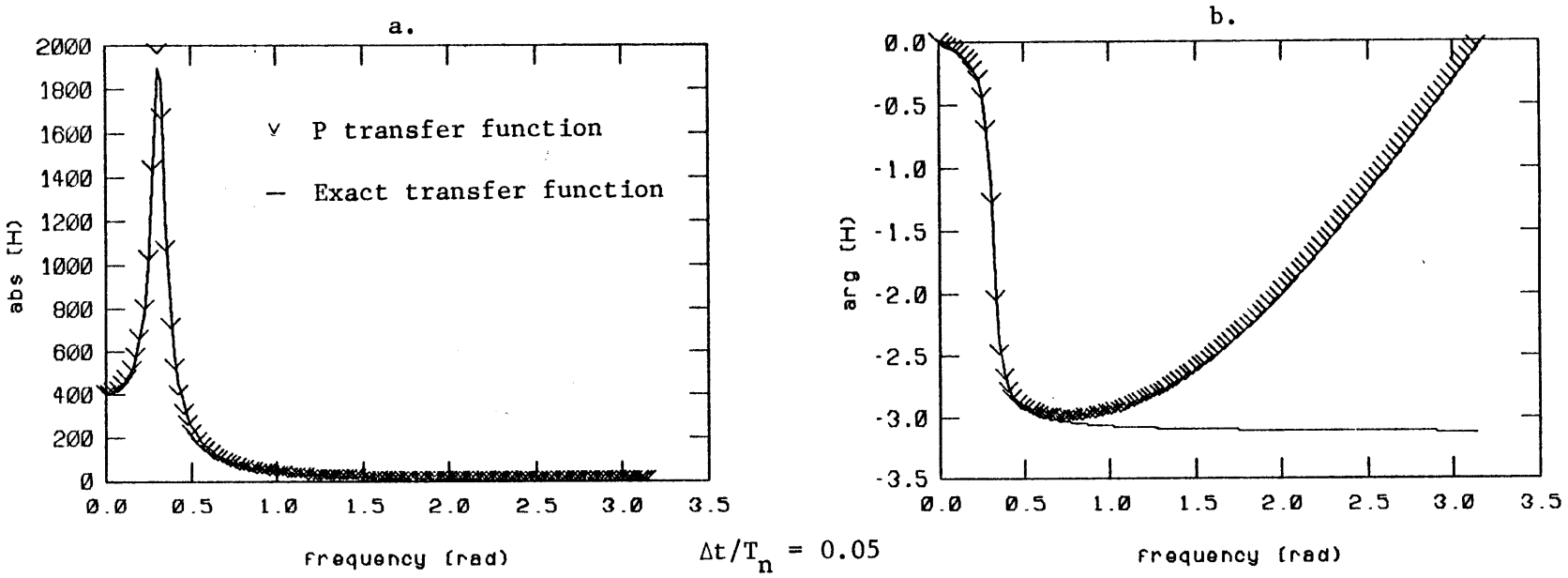

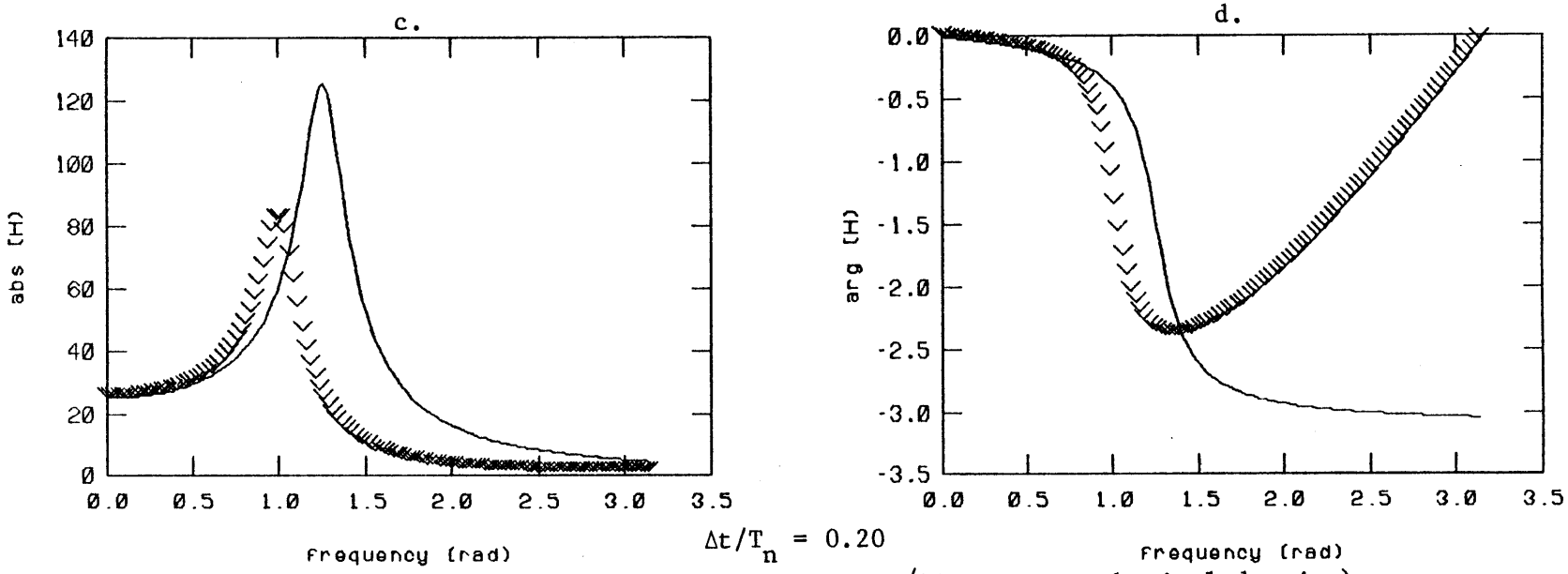

Fig. 4.12 Transfer Functions for Park Method (10 per cent physical damping)

$\Delta t/T_n$	ξ	Maximum Frequency Ω_p					$\lvert H(\Omega)\rvert_p$				
		Exact	CD	N	H	P	Exact	CD	N	H	P
0.05	0.00	0.3142	0.3155	0.3116	0.3023	0.3090	∞	∞	∞	16090	88720
0.20	0.00	1.257	1.359	1.122	0.9144	1.013	∞	∞	∞	61	221
0.05	0.05	0.3138	0.3155	0.3108	0.3007	0.3082	4004	4050	4005	3313	3987
0.20	0.05	1.255	1.359	1.120	0.8873	1.002	250	321	250	54	120
0.05	0.10	0.3126	0.3155	0.3085	0.2978	0.3059	2008	2025	2010	1857	2006
0.20	0.10	1.250	1.359	1.113	0.8608	0.9878	126	161	126	48	83

CD - central difference
N - Newmark
H - Houbolt
P - Park

Table 4.1 Resonant Frequencies and Amplitudes of Numerical Integration Transfer Functions

for frequencies greater than the resonant frequency and amplify for those less as shown in Figs. 4.7 a,c to Figs. 4.12 a,c. The central difference method depicts a reverse trend. Although these plots portray the Newmark method as a more accurate integrator than the Park method, it should be remembered that these results are limited to linear analyses. Extensions to nonlinear analyses are presented in section 4.5.

As mentioned previously, it is also possible to derive plots of the period elongation (or bias, Eq. A.16) and algorithmic damping $\bar{\xi}$ versus $\Delta t/T$. Such plots are given in Figs. 4.13-4.16 for specified damping ratios of 0.00, 0.02, 0.05, and 0.10. Notice that the central difference method exhibits no artificial damping when $\xi=0$. However, when a nonzero viscous damping is specified, the central difference method produces a negative artificial damping.

In summary we note that the linear systems theory accuracy analysis scheme provides an elegant means of examining period elongation and numerical dissipation. Contrary to the conventional time domain method where the algorithmic damping ratio and period elongation correspond to the resonant frequency, this approach gives insight as to how the response is deamplified or amplified throughout the entire frequency spectrum. Furthermore, the effect of expanding the load by a finite difference approximation is also included. Finally, notice that the

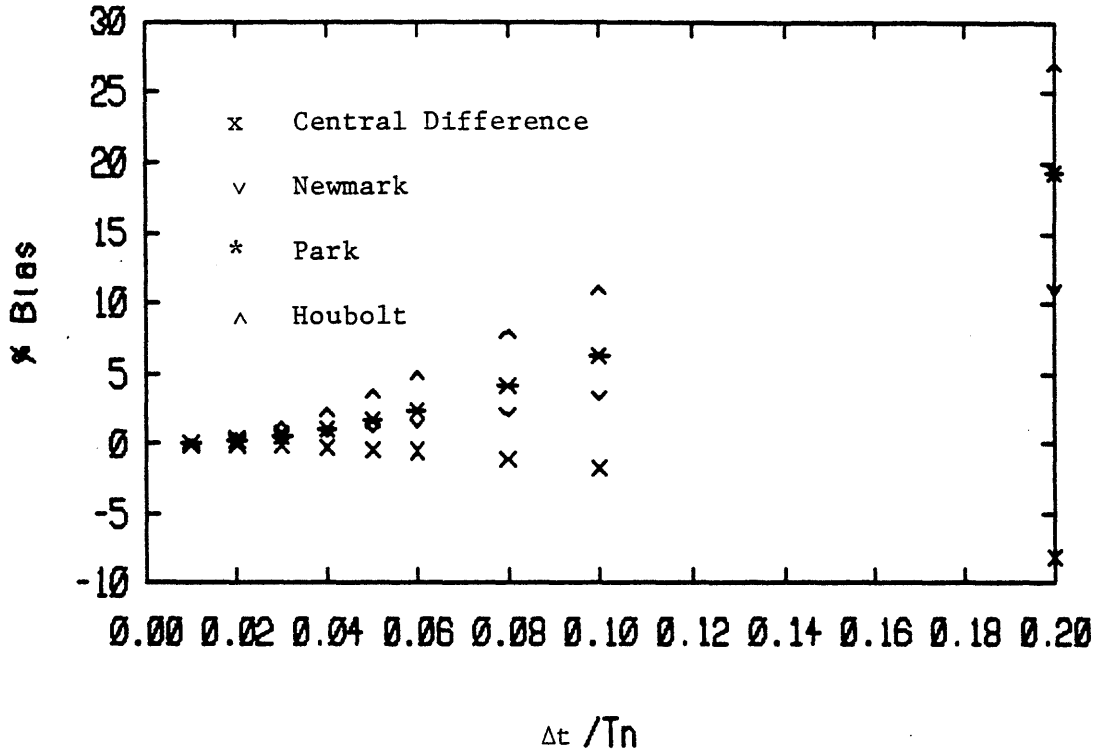

Fig. 4.13a Bias as a Function of $\bar{\omega}\Delta t$
(no physical damping)

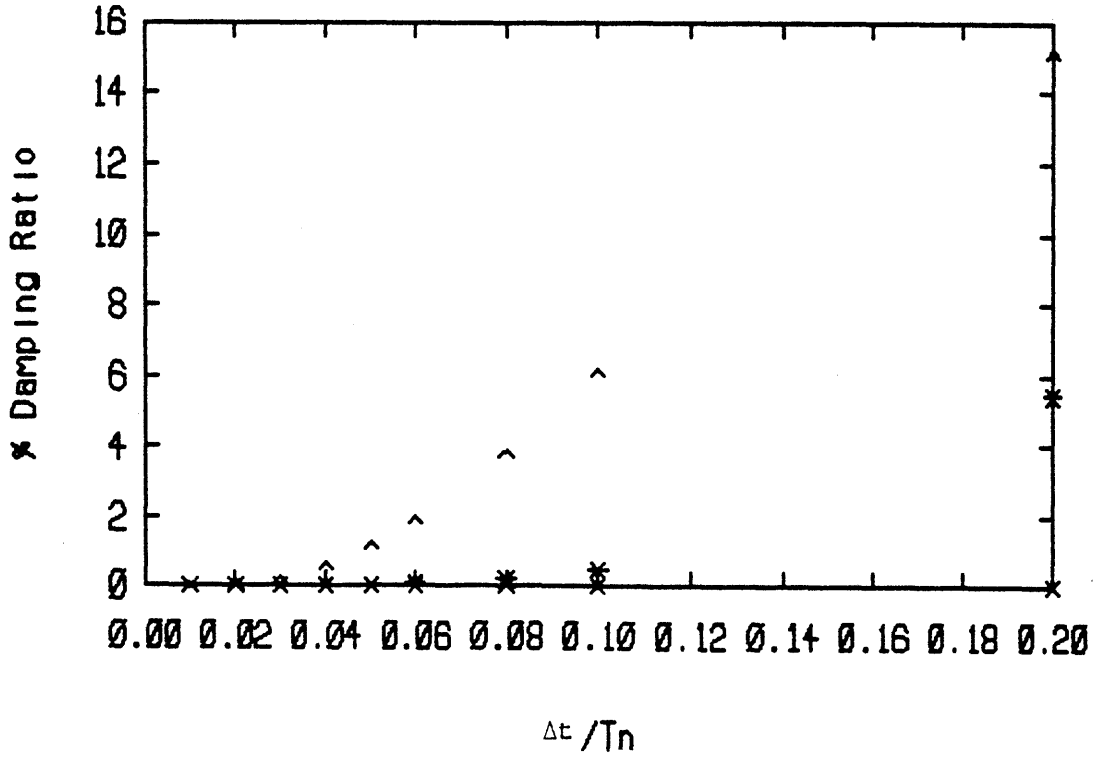

Fig. 4.13b Artificial Damping as a Function of $\bar{\omega}\Delta t$
(no physical damping)

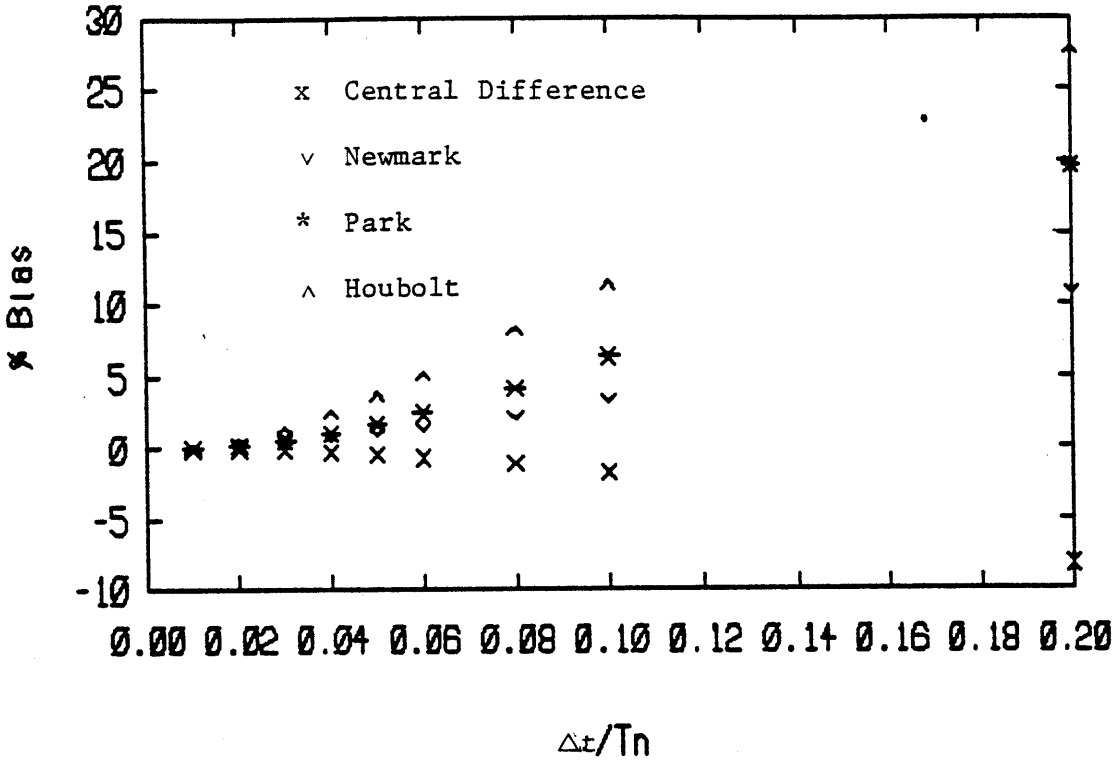

Fig. 4.15a Bias as a Function of $\bar{\omega}\Delta t$
(2 per cent physical damping)

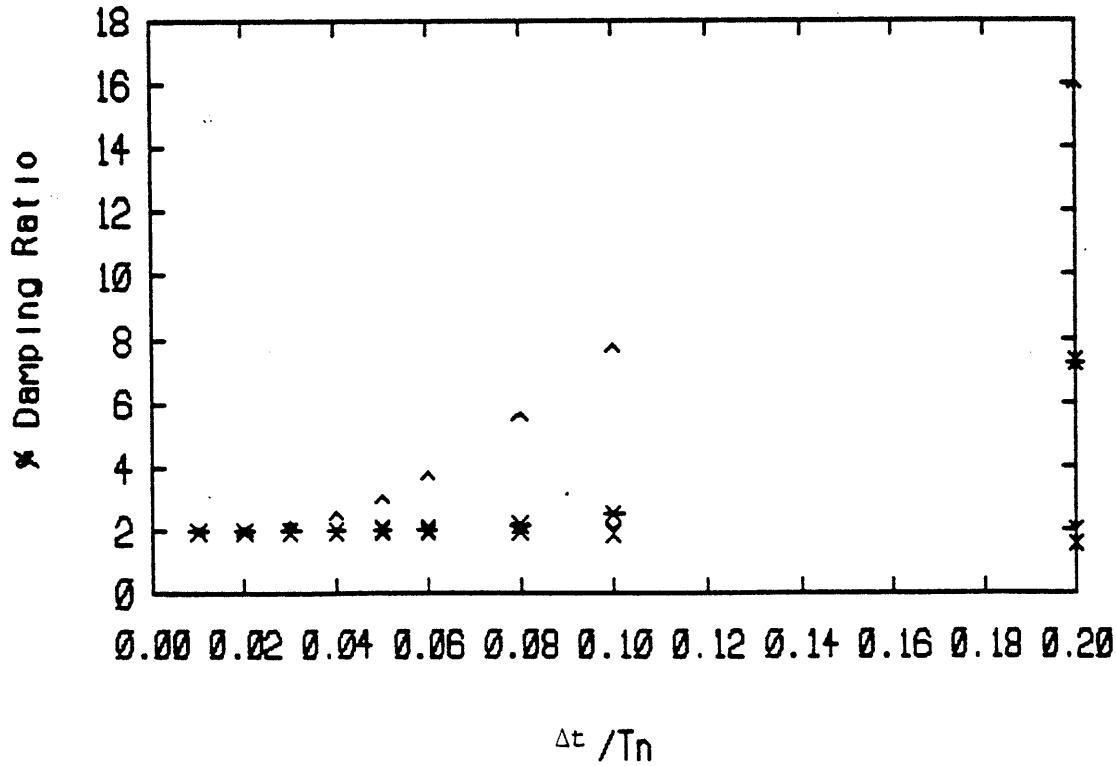

Fig. 4.15b Artificial Damping as a Function of $\bar{\omega}\Delta t$
(2 per cent physical damping)

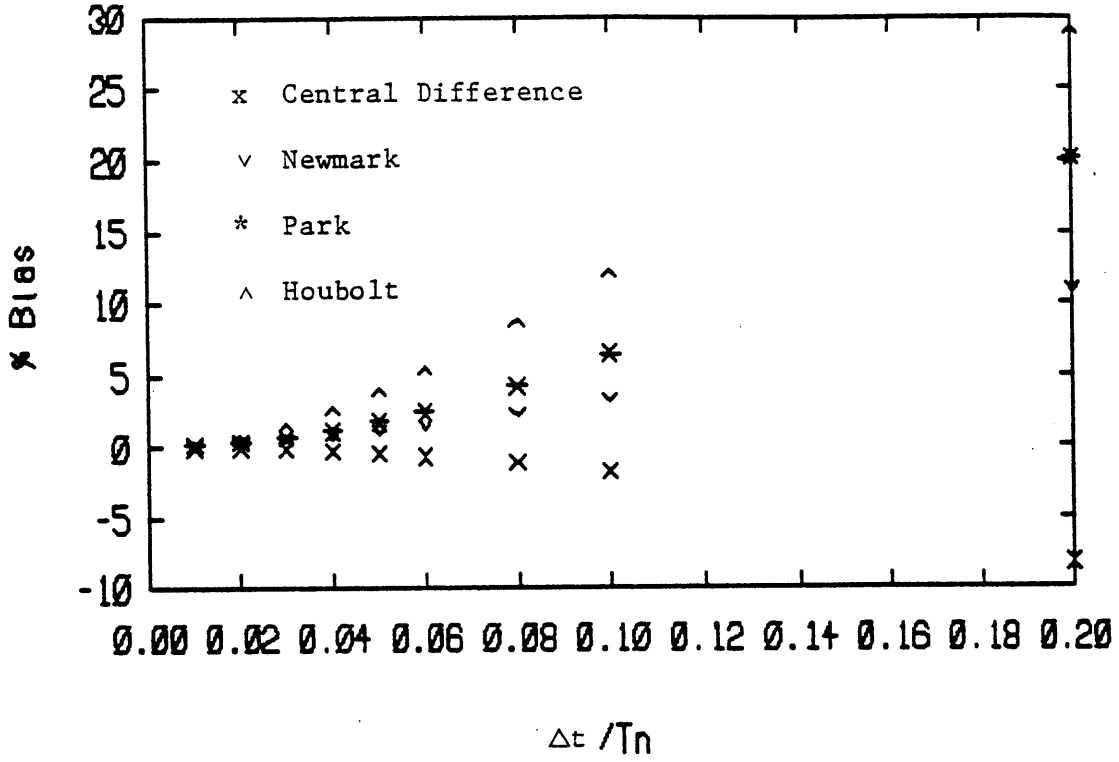

Fig. 4.14a Bias as a Function of $\bar{\omega}\Delta t$
(5 per cent physical damping)

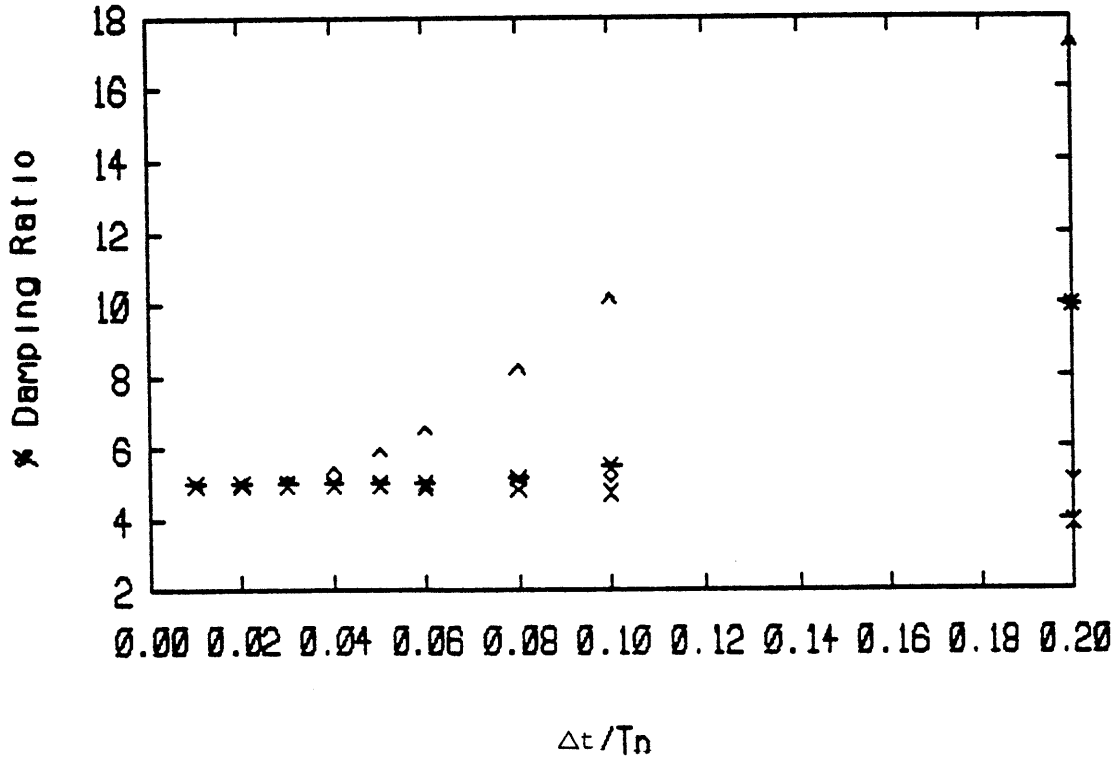

Fig. 4.14b Artificial Damping as a Function of $\bar{\omega}\Delta t$
(5 per cent physical damping)

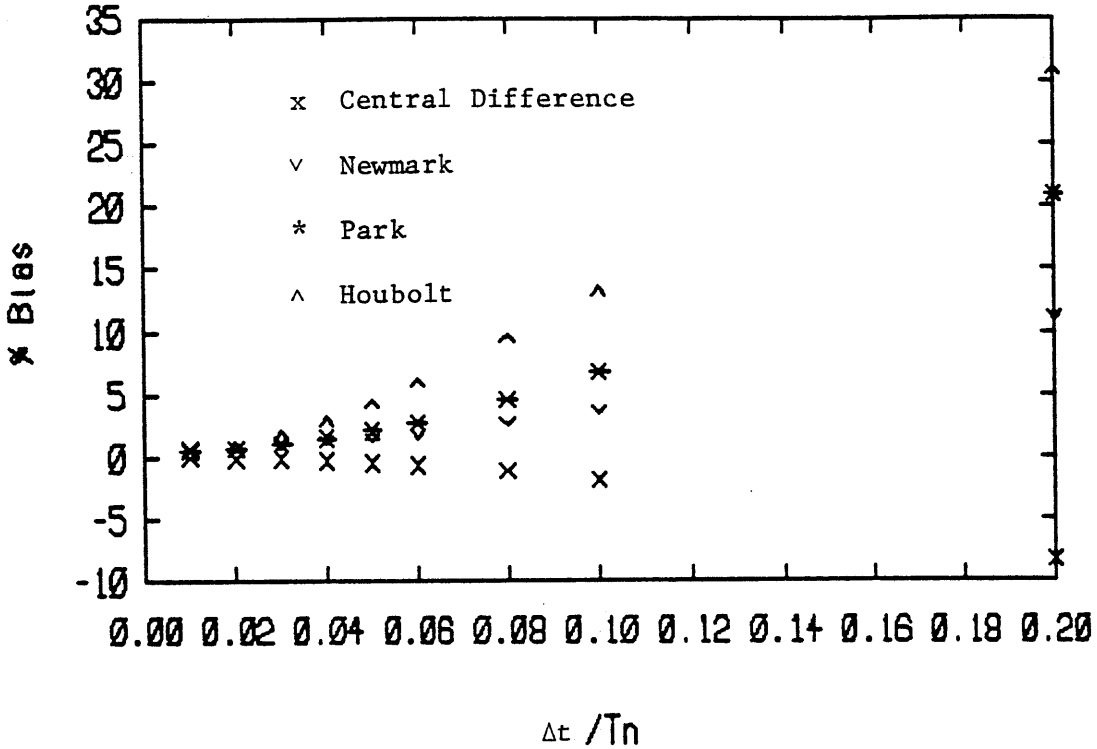

Fig. 4.16a Bias as a Function of $\bar{\omega}\Delta t$
(10 per cent physical damping)

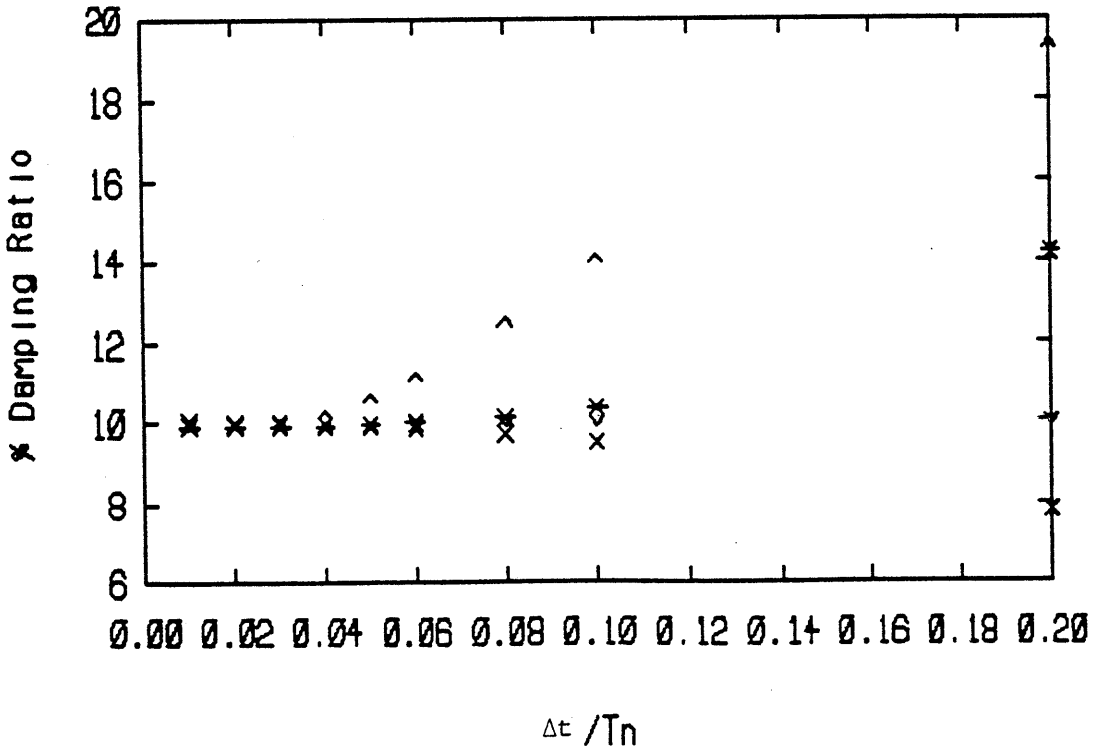

Fig. 4.16b Artificial Damping as a Function of $\bar{\omega}\Delta t$
(10 per cent physical damping)

plots given here correspond to the transfer functions by themselves. Consequently, these accuracy plots apply to the impulsive free vibration problem (the Fourier pair of $H(\omega)$ is $h(t)$ where $h(t)$ is the impulse response function). The analysis can be extended to more general loadings by transferring the load to the frequency domain, multiplying by the transfer function, and then comparing $H_e(\omega)F(\omega)$ with $\tilde{H}(\omega)\tilde{F}(\omega)$. In essence, the frequency domain representation of the load represents a weighting function, which when multiplied by the approximate transfer function, amplifies or deamplifies the inaccuracies in the approximate transfer function at each frequency.

Stability can also be investigated by using the z-transform in place of the Fourier transform (57). The z-transform $X(z)$ of a sequence $x(n)$ is given by

$$X(z) = \sum_{n=-\infty}^{\infty} x(n)z^{-n} \tag{4.42}$$

where z is a complex variable. Stability is then defined by the region of convergence of the z-transform or those sequences of z for which the z-transform converges. In particular, the region of convergence cannot contain any poles, and a stable right-sided sequence (defined only for $n \geq 0$) therefore has no poles located outside the unit circle. An illustrative stability analysis of the central difference method is given in Appendix B.

4.4 RELATION BETWEEN TIME AND FREQUENCY DOMAIN STABILITY ANALYSES

Time and frequency domain analyses are equivalent forms for analyzing the same problem. The alternate frequency domain analysis presented in section 4.3 should therefore be equivalent to the time domain analysis given in section 4.1, assuming that we are considering the free vibration problem in both cases. The conventional stability and accuracy analyses were restricted to the free vibration problem, and hence the following discussion is limited to this particular problem.

The stability analysis in the time domain begins with Eq. 4.22, corresponding to the homogeneous governing equation. Stability is ensured when the spectral radius is less than or equal to one. Let us now transfer Eq. 4.22 to the frequency domain using the z-transform, defined by Eq. 4.42. The response Q(z) is given by

$$\begin{aligned} Q(z) &= \sum_{n=0}^{\infty} d_n z^{-n} = c_1 \sum_{n=0}^{\infty} \lambda_1^n z^{-n} + c_2 \sum_{n=0}^{\infty} \lambda_2^n z^{-n} \\ &\quad + c_3 \sum_{n=0}^{\infty} \lambda_3^n z^{-n} \\ &= c_1 \frac{z}{z-\lambda_1} + c_2 \frac{z}{z-\lambda_2} + c_3 \frac{z}{z-\lambda_3} \quad \text{assuming } \left|\frac{z}{\lambda_i}\right| > 1 \\ &= \frac{z\{c_1(z-\lambda_2)(z-\lambda_3) + c_2(z-\lambda_1)(z-\lambda_3) + c_3(z-\lambda_1)(z-\lambda_2)\}}{(z-\lambda_1)(z-\lambda_2)(z-\lambda_3)} \end{aligned} \tag{4.43}$$

For the free vibration problem, the excitation F can be regarded as an impulse, implying that

$$F(z) = 1 \tag{4.44}$$

The transfer function H(z) is defined as

$$H(z) = Q(z)/F(z) \tag{4.45}$$

H(z) is the z-transform of the unit impulse response function h(n). Since h(n) is a right-sided sequence, the region of convergence of H(z) is the exterior of the unit circle centered in the z-plane, implying that all poles of H(z) must be located inside or on the unit circle to ensure stability. From Eq. 4.43, the poles of H(z) are located at λ_1, λ_2, and λ_3. As mentioned previously, stability in the time domain implies that the spectral radius is less than or equal to one. Therefore, the equivalent stability definition in the frequency domain is that all poles of H(z) lie within or on the unit circle in the z-plane. Notice in general that F need not be an impulse, and therefore the poles of $Q(z)=H(z)F(z)$ may differ from the poles of $Q(z)= H(z)\cdot 1$. In particular, a situation where both the denominator (transfer function) and numerator (load vector) equal zero may occur, and therefore it is mathematically possible for the finite difference expanded load vector to affect the system stability.

A similar argument can be presented for the accuracy analysis. Equation 4.4 corresponds to the exact free vibration response, and Eq. 4.25, the numerically integrated response. The impulse response function h by itself gives the free vibration response. Therefore, Eqs. 4.4 and 4.25 can be considered the exact and approximate impulse response functions. Rather than comparing the two

in the time domain to obtain estimates of the artificial damping and frequency distortion, we transfer both equations to the frequency domain and compare the properties of their transfer functions H. Notice that the presentation in section 4.3 was limited to the Fourier transform $H(\omega)$, and therefore corresponds to the behavior on the unit circle in the z-plane.

4.5 EXTENSION OF ACCURACY AND STABILITY ANALYSES TO NONLINEAR PROBLEMS

The amplification matrix A depends on the system properties, and consequently the stability and accuracy analysis of section 4.2 must be modified for nonlinear problems characterized by time dependent structural matrices. This section examines an analytical approach to nonlinear problems and also surveys the results of numerical experiments.

4.5.1 Analytical Approach

The stability of nonlinear problems is governed by the interaction of the numerical integrator with the approximate formulation of the governing equations of motion. Unconditionally stable integration schemes may become unstable for nonlinear analyses. Park (59,60,62) extends the stability analysis to nonlinear systems by accounting for the change in stiffness with time and then examining local instability (instability occurring in a small sequence

of time steps). His approach considers two cases: problems where the nonlinearities are evaluated exactly and those where a pseudo-force or tangent modulus approximation is involved.

The exact evaluation of the nonlinearities is discussed first. For a linear undamped system the equation describing the stability region of the trapezoidal rule, shown in Fig. 4.2, is given as (see ref. 60 for details)

$$z^2 + \frac{\bar{\omega}^2 \Delta t^2}{4} = 0 \tag{4.46}$$

When nonlinearities are included, the characteristic polynomial is derived in the same fashion as for Eq. 4.46, but for the numerically expanded governing equation where we assume that $\bar{\omega}$ varies with time. In particular, the stability equation for the trapezoidal rule becomes (60)

$$4z^2 + (\Delta t^2/2)(\bar{\omega}_n^2 - \bar{\omega}_{n-1}^2)z + (\Delta t^2/2)(\bar{\omega}_n^2 + \bar{\omega}_{n-1}^2) = 0 \tag{4.47}$$

where $\bar{\omega}_n$ is the natural frequency at time t_n. Notice from Eq. 4.47 that if $\bar{\omega}_n < \bar{\omega}_{n-1}$ at time t_n (a softening system), the coefficient of z is negative, and consequently the trapezoidal rule produces local instability. Also, if $\bar{\omega}_n$ equals $\bar{\omega}_{n-1}$, Eq. 4.46 is obtained. On the other hand, if $\bar{\omega}_n > \bar{\omega}_{n-1}$ (a hardening system), the trapezoidal rule retains local stability.

The corresponding equation for the Houbolt method is (60)

$$12z^3 + 4z^2 + \bar{\omega}_n^2 \Delta t^2 (z + 1)^3 = 0 \qquad (4.48)$$

and the Park method (60),

$$256z^6 + 576z^5 + 516z^4 + 216z^3 + 9\bar{\omega}_n^2 \Delta t^2 (z + 1)^6 = 0 \qquad (4.49)$$

Notice from Eqs. 4.48 and 4.49 that the Houbolt and Park methods are unconditionally stable when no pseudo-force or tangent modulus approximations are involved since the coefficients containing $\bar{\omega}_n$ always remain positive. Furthermore, the corresponding linear stability equations differ from the nonlinear equations only because $\bar{\omega}_n$ now varies with time. A time dependent structural stiffness, therefore, only affects the accuracy.

Comparing Eq. 4.47 with Eqs. 4.48 and 4.49, it is apparent that the instability of the trapezoidal rule arises from the admission of past-step derivatives $\bar{\omega}_{n-1}$.

Park (60) considers next the instability of numerical integrators used in conjunction with the approximate pseudo-force and tangent stiffness methods, that are based on finite difference extrapolations and differentiations of the external and internal force vectors. These finite difference approximations linearize the governing equations of motion, and as a result introduce errors in terms of past step derivatives. It is expected, consequently, that combining the Houbolt and Park methods containing no past

derivatives with solution approximations that introduce past derivatives produces a system that may be unstable.

This suspicion is indeed confirmed by examining the stability equations derived for the pseudo-force approach. The stability equations in terms of λ are given as follows (60):

Trapezoidal Rule:

$$4\lambda^4 - 8\lambda^3 - 4\lambda^2 + \bar{\omega}^2\Delta t^2\left[\lambda^4 + 2(1 + \beta_1)\lambda^3 + (4\beta_1 - \beta_2 + 1)\lambda^2 + 2(\beta_1 - \beta_2)\lambda - \beta_2\right] = 0 \tag{4.50}$$

Houbolt Method:

$$(2\lambda^3 - 5\lambda^2 + 4\lambda - 1) + \bar{\omega}^2\Delta t^2(\lambda^3 + 2\beta_1\lambda^2 - \beta_2\lambda) = 0 \tag{4.51}$$

Park Method:

$$(10\lambda^3 - 15\lambda^2 + 16\lambda - 1)^2 + 36\bar{\omega}^2\Delta t^2(\lambda^6 + 2\beta_1\lambda^5 - \beta_2\lambda^4) = 0 \tag{4.52}$$

where

$$\beta_i = (1/\bar{\omega}^2)\,\frac{\partial f(q_{n-1-i})}{\partial q}$$

$$f(q_n) = -\bar{\omega}^2 q_n + F^{NL} \tag{4.53}$$

Notice that Eqs. 4.50-4.52 contain past step derivatives in terms of the β_i, and therefore all methods exhibit a conditionally stable behavior.

Figure 4.17 depicts the stability regions plotted on the β_i plane for two different $\bar{\omega}\Delta t$ values. Regions I and III correspond to hardening and softening systems, respectively, while the other regions refer to the combined case. In particular, observe that the stability region (area inside the diagrams) in quadrant I contracts more rapidly than that for quadrant III as $\bar{\omega}\Delta t$ is increased, indicating that stiffening effects (for example, geometric nonlinearities) govern more severely the time increment than softening effects (for example, plastic material behavior).

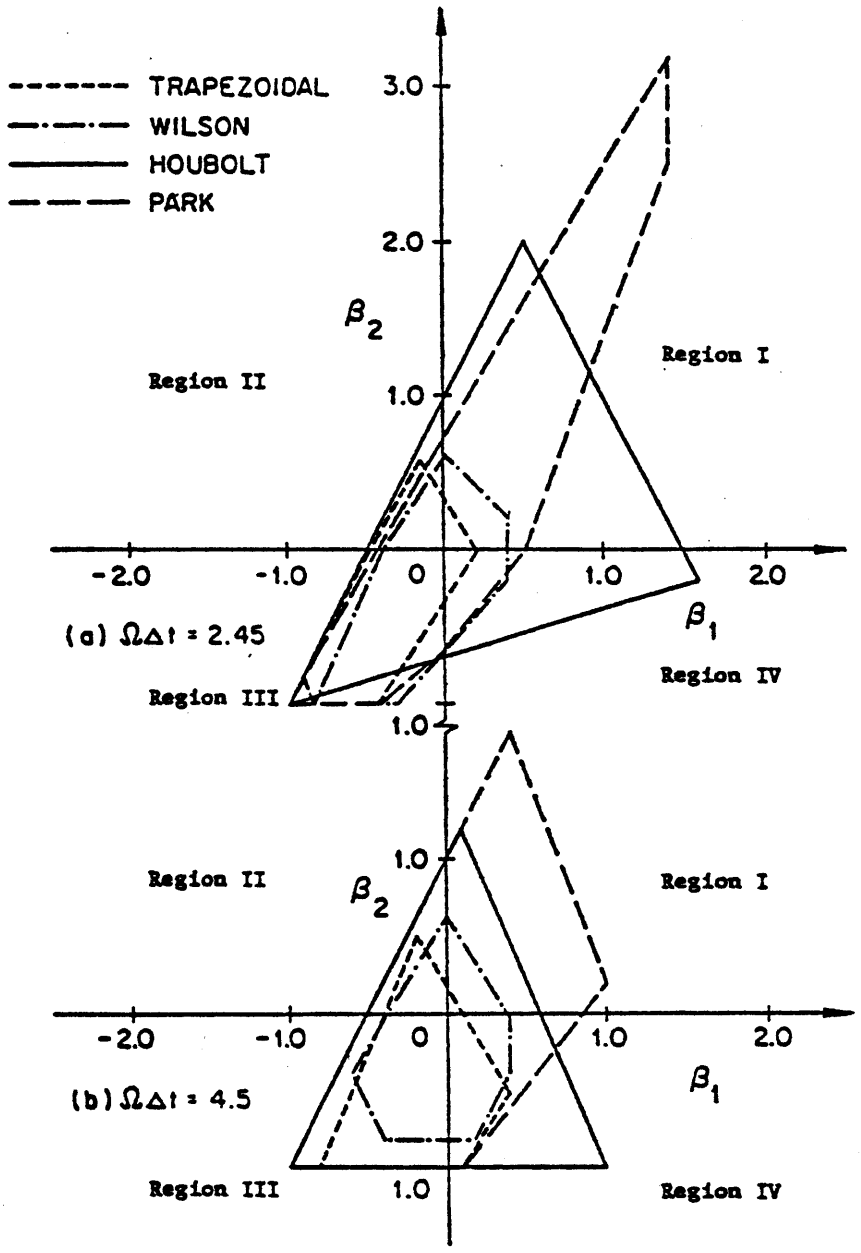

Fig. 4.17 **Conditional Stability Region of Four Methods for Linearly Extrapolated Pseudo-Force Solution Procedure.** (60)

4.5.2 Numerical Experiments

The extension of the analytical stability approach to nonlinear problems provides valuable insight into how the numerical integrators interact with the solution formulation and identifies the inclusion of past derivatives as a source of error propagation. Nonlinear problems, however, admit other sources of instability such as the material model, equilibrium iterator, and pseudo-force derivation. The current state of research, consequently, assesses instability more readily by conducting numerical experiments. This section presents a summary of these numerical experiments.

Stricklin in 1971 (81) analyzed a shell of revolution subjected to a step pressure loading. Only kinematic nonlinearities were included, and the numerical solution was derived by the 4th order Runge-Kutta, Newmark (α =0.25, δ =0.5), and Houbolt schemes applied to a conventional pseudo-force formulation of the equations of motion with linear load extrapolation. A quadratic load extrapolation scheme was also implemented, but produced numerical difficulties. The results indicated that the Houbolt method was more stable and accurate than the Newmark scheme and the Runge-Kutta method required extremely small time steps for acceptable errors.

Wu and Witmer in 1972 (93) examined structural problems with kinematic and material (elastic-plastic) nonlinearities using the 3-point central difference, Newmark (trapezoidal), and Houbolt methods. A conventional pseudo-force formulation was employed for the implicit schemes while both conventional and unconventional formulations were used for the explicit scheme. The pseudo-forces were extrapolated linearly. Based on their results, the Houbolt scheme again produced accurate results at a larger time increment than the Newmark method. Furthermore, the central difference method exhibited a smaller critical time increment for nonlinear problems compared to that for linear problems.

Also in 1972 Weeks (86) studied both the pseudo-force formulation with linear load extrapolation and the tangent stiffness formulation with Newton equilibrium iteration. The central difference, Newmark (trapezoidal), and Houbolt methods were applied to a SDOF system subjected to a rectangular load history and a cantilevered rod excited by an impulsive load. Only kinematic nonlinearities were included. In the pseudo-force formulation the Newmark method became unstable for large time increments while the Houbolt method remained stable. Both the Houbolt and Newmark methods remained stable at time increments small enough to reproduce the solution when using the tangent stiffness formulation, but the Houbolt method exhibited considerable damping. Weeks concluded that the Newmark method with load extrapolation and small time increments

produced the most accurate results at minimal computational cost.

McNamara analyzed in 1974 (46) the central difference, Newmark (trapezoidal), Houbolt, and Wilson-θ (θ=1.5) operators combined with the tangent stiffness formulation using a modified Newton iteration scheme (stiffness reformulated after each time step). A beam clamped at both ends subjected to a point step load and the same beam with an impulsive load were considered. The first case consisted only of kinematic nonlinearities while the second case also included material nonlinearities (elastic-plastic model). In both cases the Houbolt method was the best scheme. For the step load case the Houbolt method produced stable results for all time steps considered while the Newmark and Wilson-θ methods became unstable at a time increment 1/5th of the largest considered and the central difference, at a time increment 1/30th of the largest. The Newmark method was the most unstable scheme for the impulsive load problem.

Park developed in 1975 (60) a stiffly stable scheme by combining the Gear two-step and three-step methods. The scheme was compared with the Houbolt method using a conventional pseudo-force formulation with linear load extrapolation applied to a simply supported cylinder under a uniform external impulse and also a shallow spherical cap clamped at the edges and subjected to a step load at its apex. Kinematic and material (elastic-plastic)

nonlinearities were considered for the first problem while only kinematic linearities were admitted in the second case. The results indicated the Park method produced an accurate displacement response for a larger time increment. Additional studies (59) employed the tangent stiffness formulation with modified Newton iteration (reformulate stiffness at each time step). The Newmark (trapezoidal), Houbolt, and Park methods were applied to a softening spring and then to a cubically hardening spring problem. The Park scheme produced stable results in both cases and provided the most accurate displacement response. The Houbolt method also gave stable results in both problems, but exhibited a significant damping and a greater period elongation. Finally, the Newmark method began to display global instabilities for $\Delta t/T>1/4$ in the hardening case and $\Delta t/T>1/6$ in the softening case.

Adeli, Gere, and Weaver in 1978 (1) conducted a comprehensive study of popular explicit schemes in addition to the implicit schemes. The explicit central difference, trapezoidal rule with two cycle iteration, and the 4th order Runge-Kutta and the implicit Newmark (trapezoidal), Houbolt, and Park schemes were combined with the tangent stiffness formulation of the equation of motion and a modified Newton iteration method. A plane stress problem consisting of a plate uniformly loaded in its plane at the mid-line with two edges free and the other two clamped was examined. A bilinear material model was employed and kinematic

nonlinearities were included. The final results in terms of computational efficiency and accuracy indicated the central difference method to be the best of the explicit methods, while the 4th order Runge-Kutta and trapezoidal rule with two-cycle iteration were next and demonstrated similar effectiveness. Both the central difference and trapezoidal rule with two-cycle iteration exhibited instability at large time increments, and the Runge-Kutta scheme displayed excessive numerical damping. The Park method was deemed the best of the implicit schemes, with the Newmark being next, and the Houbolt, last. Comparing the central difference and Park methods, both schemes were of comparable competence for problems without kinematic nonlinearities. The inclusion of nonlinearities, however, rendered the Park method as more effective, particularly when the number of degrees of freedom was increased.

Recently in 1981 Steigmann (78) concluded a study using the tangent stiffness formulation combined with the quasi-Newton iteration schemes. Analyses employing the unconventional pseudo-force approach were also conducted. The base case was derived using the central difference method. The Newmark (trapezoidal), Houbolt, and Park methods were applied to a doubly clamped beam subjected to an impulsive load at a central region of the span. Kinematic nonlinearities were included, and elastic-perfectly plastic, elastic-strain hardening, and elastic - strain hardening - strain rate dependent material models were employed.

Results of the study indicated that for the quasi-Newton schemes, the DFP method was most appropriate for strain rate independent behavior and the BFGS was most effective for rate dependent material models. The Houbolt and Park schemes were unconditionally stable when using the tangent stiffness - equilibrium iteration approach. For small and moderate time step sizes (up to 30 times the time increment required for the central difference scheme) the Newmark method was most effective for strain rate independent material, while for large time increments (50-100 times the central difference time increment) the Park and Houbolt methods were preferred. The Park method tended to estimate the transient displacement response accurately while the Houbolt method better reproduced the peak transient strain response. In general, for the tangent stiffness - quasi-Newton iteration approach applied to strain rate dependent material, the Houbolt method combined with the BFGS iterator was best and the Newmark/BFGS combination was next best. Furthermore, the Park method gave the best results when using a pseudo-force linear-extrapolation non-iterative procedure.

4.6 SELECTING A TIME INCREMENT

The procedure for selecting an appropriate time step is reviewed in this section. Different criteria are applied depending on whether a wave propagation or structural type problem is under consideration. Any problem must consider

the type of numerical integrator, the accuracy characteristics of the integrator, the mathematical model of the structure, and the frequency content of the excitation. The extension to nonlinear analyses entails additional considerations such as the formulation of the equations of motion, pseudo-force extrapolation procedure, equilibrium iteration technique, and material modelling.

In wave propagation problems practically all structural frequencies are excited, and consequently the structural model must be selected such that it accurately captures the propagation of stress waves through the structure. The time step size for such a problem is based on the smallest geometric element size, or analagously the highest structural frequency embedded in the mathematical model of the structure. Using this as the governing criterion, explicit integration schemes are employed since the small time increment chosen for accuracy requirements inevitably satisfies the stability requirement. Implicit schemes may also be used for solving wave propagation problems, but their property of unconditional stability is no longer an advantage, and therefore their higher computational cost excludes them from consideration.

The critical time increment for a linear undamped problem using the central difference method is

$$\Delta t_{cr} = 2/\bar{\omega}_{max} \tag{4.54}$$

where $\bar{\omega}_{max}$ is the highest linear-system structural frequency. In nonlinear analyses, however, the structural frequencies change with time, and $\bar{\omega}_{max}$ in Eq. 4.54 must be regarded as the largest instantaneous frequency of the system for instantaneous stability. Witmer (92) recommends as a convenient rule-of-thumb the following critical time increment for nonlinear analyses of structures with large deflections and material nonlinearities:

$$\Delta t_{cr} = 0.8 \times (2/\bar{\omega}_{max}) \tag{4.55}$$

Other explicit schemes require smaller time steps than that of the central difference method.

Structural dynamic problems are characterized by only the lowest modes being excited. The structural model in such cases usually provides an appropriate geometric reproduction of the structure. This approach to modelling the structure, however, may include areas of localized high stiffness or small mass. Although the loading may not excite these localized areas, the structural frequencies corresponding to extremely stiff or light members are very high. Explicit integrators, consequently, are rarely used for extremely large structural dynamic problems since the time increment is governed by the highest frequency, even though only the lowest modes contribute to the response. Furthermore, the highest modes usually have no physical

resemblance to the actual structure.

Structural dynamic problems, therefore, often employ implicit integration schemes combined with a pseudo-force or tangent stiffness formulation. Bathe recommends the following procedure for selecting a time increment (6):

1. Transform the load history to the frequency domain and evaluate its highest frequency ω_{max}
2. Define $\omega_c = 4\omega_{max}$
3. Assuming that for $\omega/\bar{\omega}<0.25$ the response is static (ω is the loading frequency and $\bar{\omega}$, the structural frequency), the dynamic response can be obtained using a Δt based on ω_c
4. Discretize the structure such that it adequately captures all frequencies up to ω_c
5. Select a time increment satisfying

$$\Delta t = c_1 \cdot \frac{2\pi}{\omega_c}$$

where c_1 has a minimum value of 1/20 and is based upon the accuracy plots given in Fig. 4.3.

From section 4.5 we note that c_1 is also a function of the solution formulation and the equilibrium iteration scheme. Furthermore, complex path dependent material behavior may restrict the time step size. In nonlinear modal analyses the ω_c would correspond to the highest mode employed.

CHAPTER 5

FOURIER TRANSFORMS AND THE HYBRID FREQUENCY-TIME DOMAIN ANALYSIS SCHEME

Nonlinear structural dynamic problems are often solved by direct time integration techniques combined with equilibrium iteration schemes. This approach has generated an impressive algorithm for selecting time increments, equilibrium iterators, numerical integrators, convergence criteria, convergence accelerators, and divergence detectors, providing solutions whose accuracy is limited only by simplifications in the material modelling, structural discretization, and the theoretical basis. The computational cost for producing accurate results, however, may be excessive and preclude the execution of a considerable number of analyses. As a result, applications requiring extensive parameter studies to evaluate the effect of modelling uncertainties usually resort to other solution

techniques such as the response spectra or equivalent static load approaches. Although these schemes are remarkably efficient, and indeed may provide a good estimate of the structural behavior, they involve simplifications in the material modelling and numerous assumptions on the actual behavior, and hence detailed direct time integration analyses must be conducted initially to ascertain the extent of the error in the results.

This chapter presents an alternate hybrid frequency-time (HFT) domain approach for solving nonlinear problems. Unlike the case of the direct time integration scheme, the hybrid frequency-time domain method provides an accurate timewise solution without false damping or frequency distortion and, hence, is limited in accuracy only by modelling considerations. The scheme combines a mode superposition analysis with a theoretically "exact" numerical integrator, allowing the selection of time steps not constrained by numerical integration considerations. Furthermore, the solution in the frequency domain offers the analyst the option of examining response quantities in their energy spectrum form, and also frequency dependent stiffness and damping values can be selected, as is appropriate for soil-structure interaction problems. The chapter begins with a review of the standard frequency domain solution scheme and its numerical implementation and then concludes with a description of the HFT method.

5.1 FREQUENCY DOMAIN ANALYSIS

A solution scheme in the frequency domain applies strictly to linear time-invariant systems. The linear governing equation of motion for a SDOF system is given as

$$m\ddot{q}(t) + c\dot{q}(t) + kq(t) = f(t) \tag{5.1}$$

whose solution in the frequency domain is easily grasped conceptually by letting

$$f(t) = f(\omega)\, e^{i\omega t} \tag{5.2}$$

and defining a transfer function $H(\omega)$ such that

$$q(t) = H(\omega)f(t) = H(\omega)f(\omega)\, e^{i\omega t} \tag{5.3}$$

Substituting Eq. 5.3 into Eq. 5.1 we obtain

$$-\omega^2 mH(\omega)F(\omega)\, e^{i\omega t} + i\omega cH(\omega)f(\omega)e^{i\omega t} + kH(\omega)f(\omega)e^{i\omega t} = f(\omega)\, e^{i\omega t} \tag{5.4}$$

implying

$$(-\omega^2 m + i\omega c + k)H(\omega) = 1 \tag{5.5}$$

Therefore

$$H(\omega) = (-\omega^2 m + i\omega c + k)^{-1} \tag{5.6}$$

In general for MDOF systems we have

$$\underline{H}(\omega) = (-\omega^2 \underline{M} + i\omega \underline{C} + \underline{K})^{-1} \tag{5.7}$$

The procedure, therefore, consists of transferring the force history to the frequency domain by evaluating its Fourier transform; multiplying the Fourier transform of the force history by the transfer function; and transferring the product back to the time domain using an inverse Fourier transform to obtain the response history.

The following subsections examine the mathematical basis for the frequency domain solution scheme. An analytical approach producing the response continuously in time is presented first, and then a numerical approach providing the response at discrete times is described.

5.1.1 Continuous Fourier Series and Transforms

In the continuous time approach the forcing function f is expressed in terms of its Fourier series

$$f(t) = a_o/2 + \sum_{m=1}^{\infty} \left(a_m \cos \frac{2m\pi t}{T} + b_m \sin \frac{2m\pi t}{T}\right) \tag{5.8}$$

where t is the current time; T, the period of the forcing function; and a_m and b_m are constants. The coefficient a_m is evaluated by multiplying Eq. 5.8 by $\cos \frac{2m\pi t}{T}$ and then integrating from -T/2 to T/2 with respect to t. Using the orthogonality relations of the cosine and sine functions we

obtain

$$a_i = (2/T)\int_{-T/2}^{T/2} f(t)\cos\frac{2n\pi t}{T}\,dt, \qquad n = 0,1,2, \ldots \tag{5.9}$$

and similarly

$$b_i = (2/T)\int_{-T/2}^{T/2} f(t)\sin\frac{2n\pi t}{T}\,dt, \qquad n = 1,2,3, \ldots \tag{5.10}$$

Convergence of Eq. 5.8 is guaranteed when f and f′ are piecewise continuous for $-T/2<t<T/2$ and f is periodic with period T. The Fourier series converges to f(t) at its points of continuity and to $(f(t^+)+f(t^-))/2$ at its discontinuities. Note that the above conditions for convergence are sufficient, but not necessary.

Equation 5.8 can also be rewritten in terms of complex exponentials by using the following identities

$$\begin{aligned}\cos\frac{2\pi mt}{T} &= 0.5(e^{i2\pi mt/T} + e^{-i2\pi mt/T})\\ \sin\frac{2\pi mt}{T} &= 0.5(e^{i2\pi mt/T} - e^{i2\pi mt/T})\end{aligned} \tag{5.11}$$

Hence,

$$f(t) = \sum_{n=-\infty}^{\infty} c_n e^{i2\pi nt/T} \tag{5.12}$$

where

$$\begin{aligned}c_n &= 0.5(a_n - ib_n), \qquad n = 0, \pm1, \pm2, \ldots\\ &= (1/T)\int_{-T/2}^{T/2} f(t)e^{-i2\pi nt/T}\,dt\end{aligned} \tag{5.13}$$

Equation 5.12 will be referred to later when the discrete time approach is examined. The remainder of this discussion considers Fourier transforms that apply to aperiodic functions.

The Fourier transform $F(\omega)$ of a function $f(t)$ is derived by extending T to infinity in Eq. 5.12, resulting in

$$F(\omega) = \int_{-\infty}^{\infty} f(t) e^{-i2\pi t/T} \, dt \tag{5.14}$$

and the inverse Fourier transform by

$$f(t) = (1/2\pi) \int_{-\infty}^{\infty} F(\omega) \, e^{i2\pi t/T} \, d\omega \tag{5.15}$$

Equations 5.14 and 5.15 imply that $f(t)$ and $F(\omega)$ are a Fourier transform pair. The existence of $F(\omega)$ is assured when

$$\int_{-\infty}^{\infty} \left| f(t) \right| \, dt < \infty \tag{5.16}$$

Once again, Eq. 5.16 is a sufficient, but not a necessary condition.

The Fourier transform of impulse functions also exists if we use the theory of distributions (17). For such applications the Dirac delta function δ is defined by

$$\delta(t-t_o) = \begin{cases} \infty, & t = t_o \\ 0, & \text{otherwise} \end{cases} \tag{5.17}$$

$$\int_{-\infty}^{\infty} \delta(t-t_o) \, dt = 1$$

Extending these concepts to structural problems, the solution of a dynamic system is given analytically in the time domain by Duhamel's integral (18,38)

$$q(t) = \int_0^t f(\tau)\, h(t-\tau)\, d\tau \tag{5.18}$$

where

$$h(t-\tau) = (1/m\bar{\omega}_D)e^{-\bar{\xi}\bar{\omega}(t-\tau)} \sin\bar{\omega}_D(t-\tau) \tag{5.19}$$

Equation 5.18 is referred to mathematically as the convolution integral and can be rewritten as

$$q(t) = f(t)*h(t) \tag{5.20}$$

Using Eq. 5.14 the response in the frequency domain is given by

$$Q(\omega) = \int_{-\infty}^{\infty} q(t)\, e^{-i2\pi t/T}\, dt \tag{5.21}$$

Substituting Eq. 5.18 into Eq. 5.21 we obtain

$$\begin{aligned} Q(\omega) &= \int_{-\infty}^{\infty}\left(\int_{-\infty}^{\infty} f(\tau)h(t-\tau)\, d\tau\right)e^{-i2\pi t/T}\, dt \\ &= \int_{-\infty}^{\infty} f(\tau)\int_{-\infty}^{\infty} h(t-\tau)e^{-i2\pi t/T}\, dt\, d\tau \\ &= \int_{-\infty} f(\tau)\int_{-\infty} h(t-\tau)e^{-i2\pi(t-\tau)/T}\, dt\, e^{-i2\pi\tau/T}\, d\tau \\ &= \int_{-\infty}^{\infty} f(\tau)H(\omega)\, e^{-i2\pi\tau/T}\, d\tau \\ &= F(\omega)\, H(\omega) \end{aligned} \tag{5.22}$$

Therefore, $h(t)*f(t)$ and $H(\omega)F(\omega)$ are Fourier transform pairs and moreover $h(t)$ and $H(\omega)$ are Fourier transform pairs. Notice that the convolution in the time domain corresponds to a simple multiplication in the frequency domain, and hence, the presentation for Eqs. 5.1-5.7 agrees with the mathematical formulation.

5.1.2 Fourier Transforms of Discrete Time Series

The actual solution of Eq. 5.1 involves a force history given at discrete times, and hence the previous presentation on Fourier series and transforms does not apply. For discrete time series we must resort to the discrete-time Fourier transform. The Fourier series and transforms provide a basis for understanding the discrete Fourier transform, but it is emphasized that the discrete-time Fourier transform is not an approximation to the continuous Fourier transform. Although it is possible to begin with the continuous Fourier transform when deriving the discrete-time Fourier transform, the theoretical foundation of the discrete-time Fourier transform exists independently of the continuous Fourier transform, and furthermore the discrete-time Fourier transform produces exact results for discrete time series.

We begin our discussion of the discrete-time Fourier transform by defining the discrete time series as a sequence x where $x(n)$ is the nth term in the sequence. The response of the linear system represented by Eq. 5.1 is given as

$$q(n) = T(f(n)) \tag{5.23}$$

where T is a linear transformation such that

$$T\left[af_1(n) + bf_2(n)\right] = aT\left[f_1(n)\right] + bT\left[f_2(n)\right] = aq_1(n) + bq_2(n) \tag{5.24}$$

for arbitrary constants a and b. The unit-sample sequence, $\delta(n)$, is defined by

$$\delta(n) = \begin{cases} 1, & n = 0 \\ 0, & \text{otherwise} \end{cases} \tag{5.25}$$

If $h_k(n)$ is defined as the system response to $\delta(n-k)$, we have

$$\begin{aligned} q(n) &= T\left[\sum_{k=-\infty}^{\infty} f(k)\delta(n-k)\right] \\ &= \sum_{k=-\infty}^{\infty} f(k)T\left[\delta(n-k)\right] = \sum_{k=-\infty}^{\infty} f(k)h_k(n) \end{aligned} \tag{5.26}$$

Since we have assumed a linear time invariant system, Eq. 5.26 can be rewritten as

$$q(n) = \sum_{k=-\infty}^{\infty} f(k)h(n-k) \tag{5.27}$$

where Eq. 5.27 is the convolution sum or

$$q(n) = f(n)*h(n) \tag{5.28}$$

A stable system is defined by

$$\sum_{k=-\infty}^{\infty} \left|h(k)\right| < \infty \tag{5.29}$$

The discrete-time Fourier transform of a sequence x(n) is defined by

$$X(e^{i\Omega}) = \sum_{n=-\infty}^{\infty} x(n)e^{-i\Omega n} \tag{5.30}$$

and the inverse Fourier transform by

$$x(n) = (1/2\pi)\int_{-\pi}^{\pi} X(e^{i\Omega})\ e^{i\Omega n}\ d\Omega \tag{5.31}$$

The convergence of Eq. 5.30 is guaranteed when

$$\sum_{n=-\infty}^{\infty} \left|x(n)\right| < \infty \tag{5.32}$$

Equation 5.27 is represented in the frequency domain using Eq. 5.30 to obtain

$$Q(e^{i\Omega}) \equiv H(e^{i\Omega})F(e^{i\Omega}) \tag{5.33}$$

where

$$H(e^{i\Omega}) = \sum_{n=-\infty}^{\infty} h(n)e^{-i\Omega n} \tag{5.34}$$

and $H(e^{i\Omega})$ is the frequency response of the system when the unit-sample response is h(n).

The development of the discrete-time Fourier transform has been presented independently of the continuous Fourier transform. In actual practice, however, the discrete-time Fourier transform is applied to structural systems that are excited by a continuous load history and respond continuously in time. Therefore, the relation between the discrete response and the continuous response will now be examined.

Let $x_a(t)$ be the continuous history and $X_a(i\omega)$ its Fourier transform. Then by Eqs. 5.14 and 5.15 we have

$$x_a(t) = (1/2\pi)\int_{-\infty}^{\infty} X_a(i\omega)e^{i\omega t}d\omega \tag{5.35}$$

$$X_a(i\omega) = \int_{-\infty}^{\infty} x_a(t)e^{-i\omega t}dt \tag{5.36}$$

Also let $x(n)$ be the sequence derived from $x_a(t)$ at time increments Δt. We now compare $X_a(i\omega)$ with $X(e^{i\Omega})$. From Eq. 5.31 we have

$$x(n) = (1/2\pi)\int_{-\pi}^{\pi} X(e^{i\Omega})e^{i\Omega n}d\Omega \tag{5.37}$$

and from Eq. 5.35

$$x(n) = x_a(n\Delta t) = (1/2\pi)\int_{-\infty}^{\infty} X_a(i\omega)e^{i\omega n\Delta t}d\omega \tag{5.38}$$

Equation 5.38 is expanded further as follows:

$$\begin{aligned} x(n) &= (1/2\pi)\sum_{r=-\infty}^{\infty}\int_{(2r-1)\pi/\Delta t}^{(2r+1)\pi/\Delta t} X_a(i\omega)\, e^{i\omega n\Delta t}\, d\omega \\ &= (1/2\pi)\sum_{r=-\infty}^{\infty}\int_{-\pi/\Delta t}^{\pi/\Delta t} X_a\left(i\omega + i\,\frac{2\pi r}{\Delta t}\right) e^{i\omega n\Delta t}e^{i2\pi rn}\, d\omega \end{aligned} \tag{5.39}$$

$$= (1/2\pi) \int_{-\pi/\Delta t}^{\pi/\Delta t} \left(\sum_{r=-\infty}^{\infty} X_a(i\omega + i \frac{2\pi r}{\Delta t}) \right) e^{i\omega n \Delta t} \, d\omega$$

$$= (1/2\pi) \int_{-\pi}^{\pi} (1/\Delta t) \sum_{r=-\infty}^{\infty} X_a(i\omega + i \frac{2\pi r}{\Delta t}) \, e^{i\Omega n} \, d\Omega \qquad (5.39)$$

From Eqs. 5.37 and 5.39 we conclude that

$$X(e^{i\Omega}) = (1/\Delta t) \sum_{r=-\infty}^{\infty} X_a(\frac{i\Omega}{\Delta t} + i \frac{2\pi r}{\Delta t}) \qquad (5.40)$$

or

$$X(e^{i\omega\Delta t}) = (1/\Delta t) \sum_{r=-\infty}^{\infty} X_a(i\omega + i \frac{2\pi r}{\Delta t}) \qquad (5.41)$$

Suppose $X_a(i\,\omega)$ has nonzero values for $-\omega_o < \omega < \omega_o$ and is zero elsewhere. Then from Eq. 5.40 or 5.41 we conclude that if $2\pi / \Delta t$ is greater than $2\omega_o$,

$$X_a(i\omega + i \frac{2\pi r}{\Delta t}) = 0 \qquad (5.42)$$

for all $r \neq 0$. Otherwise, if $2\pi / \Delta t$ is less than $2\omega_o$, $X(e^{i\Omega})$ will include spurious overlaps of high and low frequency components of $X_a(i\,\omega)$, and x(n) rederived from $X(e^{i\Omega})$ will be incorrect. This overlapping phenomenom when the time increment, or equivalently the sampling period, is too large is called aliasing. The minimum sampling rate that reproduces the actual history is referred to as the Nyquist frequency given as

$$f_N = 1/2\Delta t = \omega_o/2\pi \qquad (5.43)$$

where ω_o corresponds to the highest frequency in the time history. A schematic representation of the aliasing effect is given in Fig. 5.1. Figure 5.1a shows the continuous Fourier transform; Fig. 5.1b, the discrete-time Fourier

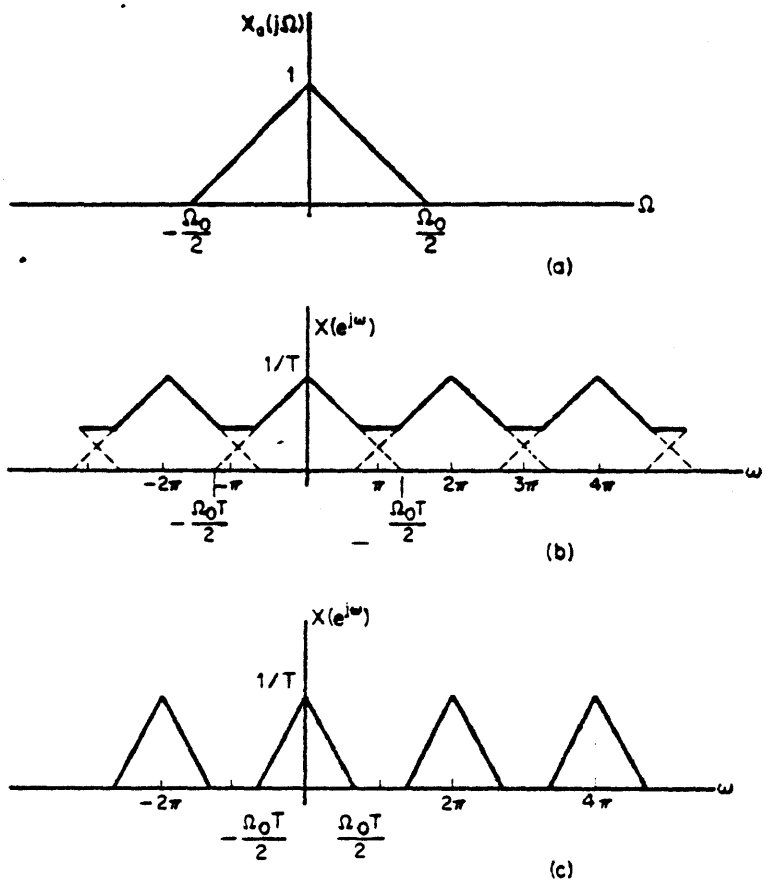

(a) Fourier transform of a continuous-time signal. (b) Fourier transform of the discrete-time signal obtained by periodic sampling. The sampling period is large, so the periodic repetitions of the continuous-time transform overlap. (c) Same as (b), but with the sampling period small enough so that the periodic repetitions of the continuous-time transform do not overlap.

Fig. 5.1 Fourier Transforms of Continuous and Discrete Time Signals (57)

transform when the sampling rate is less than the Nyquist frequency; and Fig. 5.1c, when the sampling rate is greater than the Nyquist frequency. Notice that the Nyquist frequency tends to infinity as the bandwidth of the signal extends to infinity, and hence only bandlimited signals can be reproduced exactly. For bandlimited signals the continuous-time signal $x_a(t)$ is recovered from its discrete values $x_a(n\Delta t)$ using the following interpolation formula:

$$x_a(t) = \sum_{k=-\infty}^{\infty} x_a(k\Delta t) \frac{\sin((\pi/\Delta t)(t-k\Delta t))}{(\pi/\Delta t)(t-k\Delta t)} \tag{5.44}$$

In summary, discrete-time Fourier transforms provide exact results for discrete-time series. The application to continuous-time signals requires that the sampling rate Δt be less than one-half the Nyquist frequency

$$\Delta t < \frac{1}{2f_N} \tag{5.45}$$

where f_N corresponds to the highest frequency present in the continuous time signal. Actual applications may involve f_N approaching infinity, and therefore a cutoff frequency f_o must be selected such that negligible energy exists for $f>f_o$ and Δt equals $1/2f_o$.

5.1.3 Discrete Fourier Series and Transforms

The discrete-time Fourier transform presented previously is based on a discrete time input and a continuous frequency output. A numerical implementation of the Fourier transform requires discrete sequences both in the time and frequency domains. Therefore, the Fourier series and discrete-time Fourier transform are extended subsequently to derive the discrete Fourier transform (DFT) that operates with discrete time and frequency series.

Consider the Fourier series of a periodic sequence x(n) such that $x(n)=x(n+kN)$ where N is the period and k an integer. There now exist only N distinct complex exponentials $e^{i(2\pi/N)nk}$ as opposed to the infinite number of exponentials in Eq. 5.12. Therefore,

$$x(n) = (1/N)\sum_{k=0}^{N-1} X(k)\ e^{i(2\pi/N)nk} \tag{5.46}$$

Multiplying both sides of Eq. 5.46 by $e^{-i(2\pi/N)nr}$ and summing from n=0 to N-1, we can show that

$$X(k) = \sum_{n=0}^{N-1} x(n)e^{-i(2\pi/N)nk} \tag{5.47}$$

Notice that in addition to x(n) being periodic, X(k) is also periodic with period N. By defining $W_N=e^{-i(2\pi/N)}$, Eqs. 5.46 and 5.47 can be rewritten as

$$x(n) = (1/N)\sum_{k=0}^{N-1} X(k)W_N^{-kn} \tag{5.48}$$

$$X(k) = \sum_{n=0}^{N-1} x(n)W_N^{kn} \tag{5.49}$$

Equations 5.48 and 5.49 are the discrete Fourier series (DFS) of the periodic sequence x(n).

The extension of the discrete Fourier series to finite-duration sequences produces the discrete Fourier transform (DFT) given by

$$x(n) = \begin{cases} (1/N)\sum_{k=0}^{N-1} X(k)\, W_N^{-kn}, & 0 \le n \le N-1 \\ 0, & \text{otherwise} \end{cases} \tag{5.50}$$

$$X(k) = \begin{cases} \sum_{n=0}^{N-1} x(n)\, W_N^{kn}, & 0 \le k \le N-1 \\ 0, & \text{otherwise} \end{cases} \tag{5.51}$$

We now examine the linear convolution using the discrete Fourier transform. Let $x_3(n)$ be the linear convolution of two N-point sequences, $x_1(n)$ and $x_2(n)$. Therefore

$$x_3(n) = \sum_{m=0}^{N-1} x_1(m)\, x_2(n-m) \tag{5.52}$$

Notice that $x_3(n)$ has length 2N-1, and therefore the DFT's $X_1(k)$ and $X_2(k)$ are computed on the basis of 2N-1 points. Substituting Eqs. 5.50 and 5.51 for 2N-1 points into Eq. 5.52, we obtain

$$x_3(n) = \begin{cases} 1/(2N-1)\left[\sum_{k=0}^{2N-2} (X_1(k)X_2(k))\, W_{2N-1}^{-nk}\right], & 0 \le n \le 2N-1 \\ 0, & \text{otherwise} \end{cases} \tag{5.53}$$

In the application of the linear convolution to structural dynamic problems, where x_1 is the impulse response function h, x_2 the load history f, and x_3 the response q, the convolution must theoretically be evaluated for an infinite number of points because rather than evaluating x_1 in the time domain and then transferring to the frequency domain, $X_1(\omega)$ is given directly in its analytical form in the frequency domain. The actual application, however, involves a finite number of points because system damping attenuates the response as it progresses in time. Therefore, the actual load history of N points is extended M points by adding zeroes such that the response at time $t=M\Delta t$ is negligible.

5.1.4 Numerical Evaluation of the Discrete Fourier Transform

The computation of the discrete Fourier transform and similarly the inverse DFT, is examined next. A direct evaluation of Eqs. 5.50 and 5.51 requires approximately N complex multiplications and N(N-1) complex additions or 4N real multiplications and N(4N-2) real additions. The number of numerical operations, therefore, increases rapidly as N increases, and the direct evaluation of the DFT is feasible only for small values of N.

Numerous approaches have been devised for reducing the computational effort for the DFT (16,20,54,55,69,77,90,91). Many of these algorithms gain their efficiency by taking advantage of the periodicity and symmetry properties of the

trigonometric functions. In particular

$$W_N^{kn} = W_N^{k(n+N)} = W_N^{(k+N)n} \tag{5.54}$$

and

$$W_N^{k(N-n)} = (W_N^{kn})^* \tag{5.55}$$

where supercase * in Eq. 5.55 refers to the complex conjugate.

The most popular algorithm currently available for increasing the computational efficiency is the fast Fourier transform (FFT) presented by Cooley and Tukey in 1965 (20). The basic concept behind the FFT consists of successively decomposing the sequence x of length N into smaller sequences until N/2 two-point sequences remain, such that the final computation only involves a two-point DFT. The two-point DFT's are then recombined to yield the full DFT of x(n). Since the final stage computes the DFT of a two-point sequence, N must be a power of two. The total number of complex multiplications and additions for the FFT is approximately $N\log_2 N$, obviously a significant decrease from that for a direct evaluation of the DFT. Notice that the actual finite duration sequence x(n) may not have a total number of terms equal to a power of 2. In such cases zeroes are appended to the end of the record to bring the total number of points up to a power of two. The DFT of the extended history provides a finer resolution since the

number of frequency components have increased while the sampling rate remains the same.

Various forms of the FFT are available and can generally be classified into decimation-in-time algorithms, that rearrange the sequence x(n) into smaller subsequences, and decimation-in-frequency algorithms, that decompose X(k) into smaller subsequences. Some algorithms are based on N not a power of 2. For example N may be a power of 8 or a prime number (16,69). More recent approaches include the Winograd fast Fourier transform (90,91) which is more efficient than the FFT theoretically, but demonstrates less efficiency in actual applications (47,76). Regardless of the form of FFT employed, the application of the FFT in conjunction with the digital computer has rendered the frequency domain approach a viable alternative to the traditional time domain schemes for solving linear dynamic systems.

5.1.5 Frequency Domain Analysis and Nonlinear Systems

Nonlinear systems often display completely unexpected patterns of behavior. A linear system with frequency $\bar{\omega}$ excited at frequency ω will respond harmonically at frequency ω and also contain initial transients with frequency $\bar{\omega}$ that eventually die out in damped systems. A nonlinear system, however, may respond at other frequencies ω_1, ω_2, ω_3, and so forth that persist in time. This section addresses the analytical solution of Duffing's problem

(65,79) and provides an introductory background to the distinguishing features of nonlinear problems. Essential differences between time domain and frequency domain solutions are identified, and the underlying motive for exploiting the frequency domain solution, and in particular the HFT scheme, is presented.

Duffing's problem consists of the system defined by the following equation:

$$m\ddot{q} + c\dot{q} + \alpha q + \beta q^3 = f(t) \tag{5.56}$$

where in a structural problem, m corresponds to the mass; c, the damping; α, the linear stiffness; and f, the excitation. Nonlinearities are introduced by the addition of the βq^3 component. The system can be regarded as a nonlinear material problem, where the material is an elastic stiffening type if β is greater than zero and elastic softening if less than zero. In another sense, the βq^3 term can be viewed as a geometric type nonlinearity.

Let us first consider the linear problem, $\beta = 0$. A solution in the time domain can be obtained analytically using Duhamel's integral

$$q(t) = \int_0^t h(\tau) f(t-\tau)\, d\tau \tag{5.57}$$

$$= h(t) * f(t) \qquad \text{(convolution)}$$

where h is the impulse response function. Notice that we have assumed a causal system. Equation 5.57 must be integrated for a few response cycles to obtain the steady state forced response.

Evaluating Duhamel's integral is often cumbersome, even numerically, and therefore an alternate solution scheme is desired. A possible alternative is to substitute into Eq. 5.56 (β=0) the Fourier transforms of q and f (use the Fourier series for periodic forcing functions)

$$q(t) = (1/2\pi) \int_{-\infty}^{\infty} Q(\omega)\ e^{i\omega t}\ d\omega$$
$$f(t) = (1/2\pi) \int_{-\infty}^{\infty} F(\omega)\ e^{i\omega t}\ d\omega \qquad (5.58)$$

to obtain

$$m \int_{-\infty}^{\infty} -\omega^2 Q(\omega) e^{i\omega t}\ d\omega + c \int_{-\infty}^{\infty} i\omega Q(\omega) e^{i\omega t}\ d\omega + \alpha \int_{-\infty}^{\infty} Q(\omega)\ e^{i\omega t}\ d\omega = \int_{-\infty}^{\infty} F(\omega)\ e^{i\omega t}\ d\omega \qquad (5.59)$$

and after simplifying

$$\int_{-\infty}^{\infty} (-\omega^2 m + i\omega c + \alpha) Q(\omega) e^{i\omega t}\ d\omega = \int_{-\infty}^{\infty} F(\omega)\ e^{i\omega t}\ d\omega \qquad (5.60)$$

or

$$Q(\omega) = (-\omega^2 m + i\omega c + \alpha)^{-1}\ F(\omega) \qquad (5.61)$$
$$= H(\omega)\ F(\omega)$$

where H is the transfer function.

Equation 5.61 corresponds to a frequency domain solution and implies that rather than evaluating the convolution in the time domain, we can obtain the same solution in the frequency domain by a simple algebraic multiplication of H and F. The conceptual simplicity of evaluating a solution in the frequency domain provides an incentive to exploit this approach. A tradeoff exists, of course, since the Fourier transforms must be evaluated, but the numerical computation is minimized by using the FFT.

Let us now consider the nonlinear problem, $\beta \neq 0$. A time domain solution by Duhamel's integral is no longer straightforward since the impulse response function depends on the system frequency which now varies with the response amplitude. Analytical approximations have been derived using iteration and perturbation techniques, with any degree of accuracy attainable. In general, these solution schemes indicate that the steady state response does not necessarily consist only of the frequency component ω, but may also have lower (subharmonic) and higher (ultraharmonic) components, illustrated in Fig. 5.2. This subharmonic and ultraharmonic behavior implies that a simple transfer function given by Eq. 5.61 where an input frequency ω only generates an output frequency ω, is no longer valid. In particular, we may have

$$Q(\omega_1) = \sum_i H(\omega_1, \omega_i)\ F(\omega_i) \tag{5.62}$$

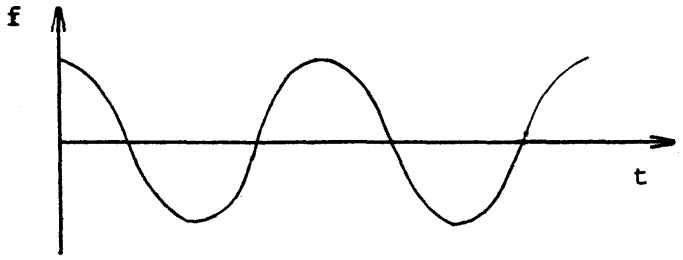

a. excitation

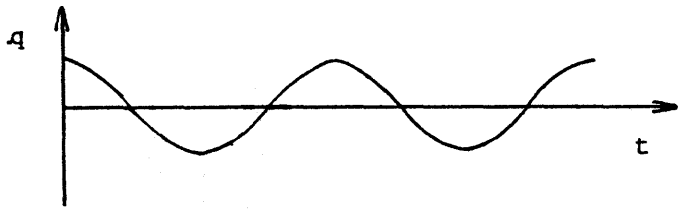

b. harmonic response

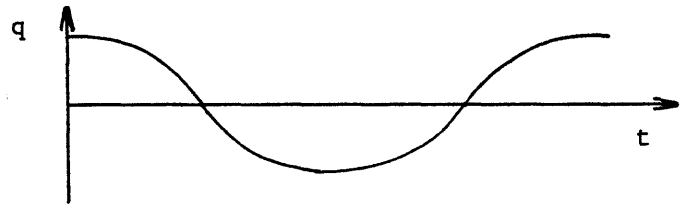

c. subharmonic response

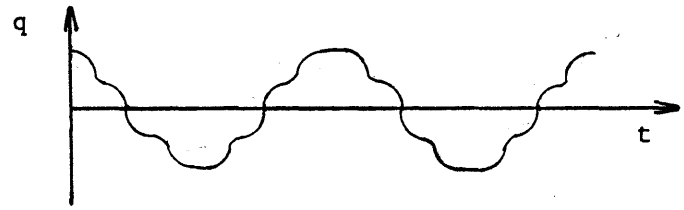

d. ultraharmonic response

Fig. 5.2 Nonlinear Response to a Harmonic Excitation

Following the same procedure as before, let us transfer Eq. 5.56 to the frequency domain. All terms remain the same except for βq^3. We can show (see Appendix C) that the Fourier transform pair of q^3 is given by

$$\int_{-\infty}^{\infty} \int_{-\infty}^{\infty} Q(\omega_1 - \omega_2)\, Q(\omega_2 - \omega_3)\, Q(\omega_3)\, d\omega_2\, d\omega_3 \qquad (5.63)$$

The solution of Eq. 5.56 in the frequency domain is now an iterative process and, moreover, involves the evaluation of the integral given by Eq. 5.63, contrasted to the simple multiplication denoted by Eq. 5.61. As a result, we are once again confronted with the same integration problem (convolution) posed by the time domain solution of the linear system.

The proposed solution is to eliminate the integral evaluation by reverting to a time domain evaluation of the βq^3 component and solving the remaining system in the frequency domain. In other words, we introduce the hybrid frequency-time domain scheme where all nonlinearities are evaluated in the time domain, and the solution is executed in the frequency domain with only simple multiplications.

5.2 HYBRID FREQUENCY-TIME DOMAIN ANALYSIS

The standard frequency domain solution scheme presented in the previous section is limited to linear time invariant systems. Various extensions to nonlinear analyses have been proposed recently, with specialized applications to the

response of offshore structures (5,24,70,82). These applications derive the structural response to a steady state excitation, the wave loading, and hence the converged solution represents the steady state nonlinear behavior, where the nonlinearities are due to the hydrodynamic drag damping effect. The proposed solution schemes consist of an iterative process whereby the nonlinearities are evaluated in the time domain and expressed by load vectors on the RHS of the equations of motion and the solution is obtained in the frequency domain. By exploiting the inherent harmonic basis of the Fourier transform, these schemes avoid the problem of eliminating the initial transients, characteristic of time domain solution schemes.

Most nonlinear frequency domain solution schemes are developed for steady state response problems with response dependent system matrices while transient response problems are usually addressed by time integration solution schemes. Various structural dynamic problems, however, require an excessively small time increment determined by the accuracy of the numerical integrator, rather than the material behavior or actual structural response. Moreover, soil-structure interaction problems characterized by frequency dependent stiffness and damping terms are solved exactly only in the frequency domain. Other structural problems are tremendously large in size and preclude conducting any significant parameter studies.

An alternate solution scheme, the hybrid frequency-time domain (HFT) method, presented in this section has, consequently, been developed to evaluate the transient dynamic response of large scale structural systems. In contrast to the previously proposed frequency domain analysis schemes, the HFT method also admits the effect of initial transients, and hence accounts for the development of kinematic and material nonlinearities from the initial linear system to the nonlinear system. The scheme embraces all nonlinearities and is applicable to both transient and steady state type problems. This section first describes the HFT solution scheme, examines associated numerical considerations, and concludes with a review of its applicability and limitations.

5.2.1 Formulation of the HFT Approach

The hybrid frequency time domain solution scheme employs the unconventional pseudo-force approach given by Eq. 3.24 and rewritten here as

$$\underline{M}\ddot{\underline{q}} + \underline{K}\underline{q} = \underline{F} + \underline{F}^{NL} \tag{5.64}$$

where $\underline{M}$ and $\underline{K}$ represent the linear mass and stiffness matrices; $\underline{F}$, the external load vector; $\underline{F}^{NL}$, the force vector containing all nonlinear terms; and $\underline{q}$ is redefined as the global nodal displacement. In conjunction with a mode superposition approach, Eq. 5.64 is rewritten as Eq. 3.83 in its generalized form including damping

$$\tilde{\underline{M}}\ddot{\underline{y}} + \tilde{\underline{C}}\dot{\underline{y}} + \tilde{\underline{K}}\underline{y} = \tilde{\underline{F}} + \tilde{\underline{F}}^{NL} \tag{5.65}$$

where the tilda (~) denotes generalized matrices and $\underline{y}$ is the generalized displacement response. The corresponding transfer matrix $\underline{H}$ is

$$\underline{H}(\omega) = (-\omega^2\tilde{\underline{M}} + i\omega\tilde{\underline{C}} + \tilde{\underline{K}})^{-1} \tag{5.66}$$

Assuming the eigenproblem has been completed and the generalized matrices in Eq. 5.65 and transfer matrix $\underline{H}(\omega)$ are available, the basic procedure for conducting the HFT analysis is as follows:

1. Evaluate Fourier transform of $\underline{F}(t)$ using the FFT, and therefore obtain the frequency domain representation of the force history, $\underline{F}(\omega)$.
2. Compute the response in the frequency domain $\underline{Y}(\omega)$ by simply multiplying $\underline{H}(\omega)$ and $\underline{F}(\omega)$.
3. Transfer $\underline{Y}(\omega)$ to the time domain by evaluating its inverse Fourier transform
4. Derive the geometric response $\underline{q}(t)$ from the generalized response $\underline{y}(t)$, and determine all nonlinearities. Store the nonlinearities as a force time history $\underline{F}^{NL}(t)$.
5. Transfer $\underline{F}^{NL}(t)$ to the frequency domain using the FFT
6. The forcing function is now $\underline{F}(\omega)+\underline{F}^{NL}(\omega)$. Multiply

the forcing function by $\underline{H}(\omega)$ to obtain the new frequency domain response $\underline{Y}(\omega)$.

7. Repeat steps 3-6 until a convergence criterion is satisfied

The HFT solution scheme is conceptually simple and easily executed. Furthermore, adapting the HFT scheme to existing direct time integration computer programs requires minimal effort. The only program dependent attribute is the evaluation of the nonlinearities, step 4. Even this aspect is easily implemented since time integration schemes already evaluate the nonlinearities during the equilibrium iteration phase for the incremental formulation and as part of the load vector for explicit and pseudo-force formulations. An efficient application of the HFT method producing accurate results, however, entails numerous additions to the basic procedure outlined in steps 1-7. These modifications are addressed in the next subsection.

5.2.2 Numerical Considerations for Applying an HFT Analysis

The development of the HFT solution scheme involves no ingenious stretches of the mind, nor does its application require extremely complex and powerful recondite numerical methods. The HFT method evaluates the nonlinearities in the same manner as a time integration approach and resorts to the FFT for acquiring the solution. Despite its simple formulation, the HFT solution scheme has never been applied to the practical solution of structural dynamic problems

(based on a review of the literature) possibly because many engineers are unacquainted or uncomfortable with the frequency domain concept and others familiar with the concept believe the scheme is unfeasible, based on cursory theoretical considerations.

The HFT method presented here has been developed to solve nonlinear dynamic structural problems with accurate results. Modifications and additions to the basic procedure for achieving a practical solution scheme can be classified under the categories of efficiency and stability (accuracy). These changes are examined in the following subsections.

5.2.2.1 Solution Formulation

Steps 1-7 of the solution process can be approached in two different forms. The first approach, referred to here as the dual displacement formulation, obtains the linear response $\underline{y}_1$ from steps 1 and 2, and then iterates from steps 3 through 7 to derive a correction response $\underline{y}_2$, which when added to the linear response produces the nonlinear response

$$\underline{y} = \underline{y}_1 + \underline{y}_2 \tag{5.67}$$

The governing equation for the first cycle is

$$\tilde{\underline{M}}\ddot{\underline{y}}_1 + \tilde{\underline{C}}\dot{\underline{y}}_1 + \tilde{\underline{K}}\underline{y}_1 = \tilde{\underline{F}} \tag{5.68}$$

and during the successive iterative cycles

$$\tilde{\underline{M}}\ddot{\underline{y}}_2 + \tilde{\underline{C}}\dot{\underline{y}}_2 + \tilde{\underline{K}}\underline{y}_2 = \tilde{\underline{F}}^{NL} \tag{5.69}$$

This formulation calculates the linear response $\underline{y}_1$ during the first cycle, and consequently provides the analyst an estimate of the nonlinear response. Notice that since the nonlinear correction is evaluated independently of the linear response, numerical round-off errors are minimized and, furthermore, the evaluation of the Fourier transform of the force history $\underline{F}^{NL}$ may require less points in the frequency domain than that for $\underline{F}$, thus reducing the computational cost.

The dual displacement formulation possesses favorable computational accuracy features. However, the solution converges slowly when the nonlinear response departs significantly from the linear response, and may even diverge and become unstable. Furthermore, since the actual load history is employed only in the first cycle to obtain the linear response and since $\underline{F}^{NL}$ is based on $\underline{y}_1+\underline{y}_2$, during succeeding cycles the response correction $\underline{y}_2$ may never approach its true value. In other words, if $\underline{y}_1$ differs appreciably from the actual nonlinear response, then $\underline{y}_2$ cannot be calculated with any reasonable accuracy to produce the correct response $\underline{y}$. Inaccuracies in $\underline{y}_1$ may stem from an insufficient number of modes being included in the mode superposition analysis, the number of appended zeroes being

deficient to adequately resolve the histories, or the selection of an excessive time increment producing a significant Nyquist frequency component.

Considering the various difficulties of the dual displacement formulation, the second solution formulation, referred to here as the total displacement formulation, operates on the total displacement, and hence solves Eq. 5.65 directly. Since the total displacement formulation always evaluates the response to the total force history, $\underline{\tilde{F}}+\underline{\tilde{F}}^{NL}$, this approach is more forgiving in the sense that initial approximations are corrected during succeeding iterations. In addition, it will be shown later that the total displacement formulation may converge faster because a "better" initial guess to the nonlinear response can be produced by employing artificial damping. Notice also that the storage requirements are reduced considerably since only one response quantity $\underline{y}$ is stored, rather than both $\underline{y}_1$ and $\underline{y}_2$.

5.2.2.2 Zero Minimization Problem

Subsections 5.1.3 and 5.1.4 demonstrated that evaluating the Fourier transform requires extra zeroes appended to the end of the sequence x(n), where x(n) represents the excitation or nonlinear force history. The additional zeroes extend the sequence x(n) such that it contains N terms, a power of two, allowing the use of the radix-2 FFT, increase the resolution by decreasing the

frequency increment, and prevent transient effects at the end of the response history from entering the beginning.

The last item in a physical sense is due to the initial conditions at the end of the load history creating a damped free vibration that requires a finite amount of time to decay to a negligible amplitude. This finite decay time is provided by the additional zeroes. If an insufficient number of zeroes is appended, the free vibration will have a significant amplitude at time $t=N\Delta t$, and hence the use of the inverse Fourier transform to reproduce the response history implies that the final transient conditions will alter the initial response. This process is shown schematically in Fig. 5.3.

The actual number of appended zeroes can be derived for linear systems using an analytical approach. Consider the free vibration of a SDOF system with viscous damping ratio ξ, natural frequency $\bar{\omega}$, and damped natural frequency $\bar{\omega}_D$. Let u_o and $\dot{u}_o$ be the initial conditions. The free vibration response is then given as

$$u(t) = e^{-\xi\bar{\omega}t}\left(\frac{\dot{u}_o + u_o\xi\bar{\omega}}{\bar{\omega}_D} \sin\bar{\omega}_D t + u_o \cos\bar{\omega}_D t\right) \qquad (5.70)$$

Using Eq. 5.70, it is possible to determine how much the amplitude decreases in one cycle for a specified damping ratio. A plot derived with such an approach is shown in Fig. 5.4. The analyst, therefore, selects an allowable ratio of the final amplitude to the initial response

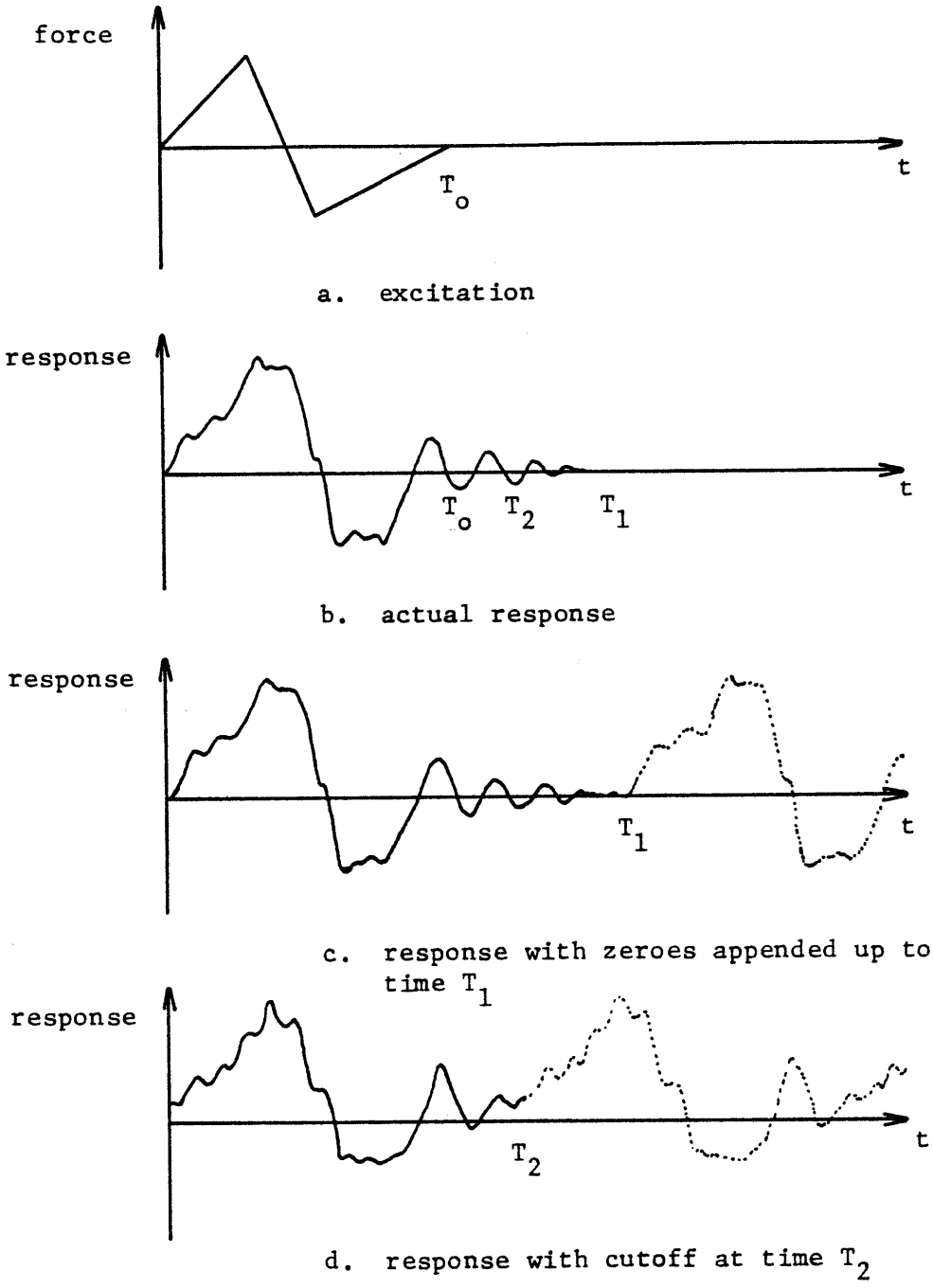

Fig. 5.3 Effect of Appended Zeroes in a Frequency Domain Analysis

amplitude, obtains from Fig. 5.4 the number of cycles S to produce such an amplitude attenuation, and calculates the number of points (zeroes) contained in those cycles, which equals $S/\Delta t$.

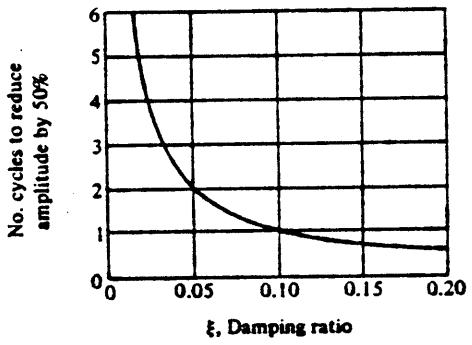

Fig. 5.4 **Damping ratio vs. number of cycles required to reduce amplitude by 50 percent.** (18)

It is evident that the number of extra zeroes may become prohibitively large for systems with high fundamental periods. Furthermore, in nonlinear analyses the system may soften, causing the structural periods to increase, and therefore, necessitating the use of even more zeroes. This large number of zeroes may significantly reduce the efficiency of the frequency domain solution.

In response to the extra zeroes problem, a zero minimization technique was developed such that the number of appended zeroes in the ideal case brought the total number of points N up to the next smallest power of 2 greater than the actual load history. More zeroes can obviously be

appended if the resolution is insufficient, but it is noted that the proposed zero minimization technique eliminates the analyst's task of choosing the number of zeroes based on free vibration considerations.

The procedure for implementing the zero minimization scheme is as follows:

1. Let N be the number of points representing the excitation history $\underline{F}(t)$ and NB the total number of points used in the frequency domain ($N<NB$).
2. NB is chosen such that $N<NB<2N$. In other words, NB is the smallest power of two greater than N.
3. Using such an NB, evaluate the Fourier transform $\underline{F}(\omega)$ of the load history. This transform is exact for the given time increment and NB.
4. Multiply $\underline{F}(\omega)$ by its transfer function $\underline{H}(\omega)$ to obtain the frequency domain representation of the response $\underline{Y}(\omega)$
5. Evaluate the inverse Fourier transform of $\underline{Y}(\omega)$ to obtain the response history $\underline{y}(t)$
6. $\underline{y}(t)$ is an incorrect response because the linear convolution executed with NB produces a significant free vibration component at $t=NB\Delta t$ that modifies the beginning of the response.
7. Obtain the correct response by realizing that the initial conditions $\underline{y}_o$ and $\dot{\underline{y}}_o$ should be zero (or whatever the analyst specified). Therefore, purge $\underline{y}(t)$ of the free vibration component by subtracting out this

component using Eq. 5.70.

A schematic representation of the zero minimization technique is given in Fig. 5.5.

Using this technique, the number of total points NB can be easily reduced by a factor of two to four. The procedure is theoretically sound since the only difference between the exact response $\underline{y}$ and the incorrect response $\underline{\tilde{y}}$ is the presence of the free vibration component. $\underline{y}$ is rederived from $\underline{\tilde{y}}$ by imposing the known actual initial conditions on $\underline{\tilde{y}}$ (see Appendix D for a mathematical explanation of the zero minimization technique). This correction implemented numerically, however, is approximate. Based on economic considerations $\underline{\tilde{y}}$ is available, but $\underline{\dot{\tilde{y}}}$ is derived from $\underline{\tilde{y}}(t)$ using a finite difference approximation. Furthermore, even if the initial conditions are adjusted to zero by flushing out the final free vibration, some components of the free vibration may still be present. Since the damped free vibration consists numerically of a finite number of harmonic components, it is possible that some of these components when combined yield zero initial conditions. A better approach, therefore, would use the initial conditions at $t=N\Delta t$ to evaluate the free vibration. In most cases, however, the probability of some free vibration components combining such that they produce zero initial conditions at time $t=0$ is negligible, and the procedure outlined in Fig. 5.5 is acceptable. Notice that the zero minimization technique applies to both linear and nonlinear analyses,

a. excitation with minimum number of appended zeroes

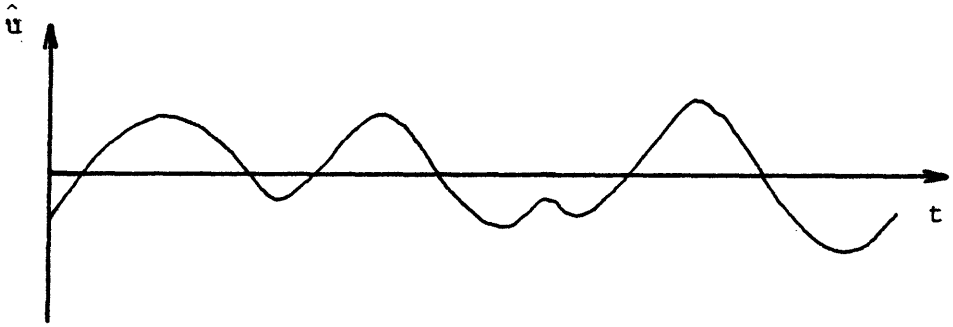

b. incorrect response obtained by a frequency domain solution with minimum zeroes

+

c. $$u(t) = -e^{-\xi\bar{\omega}t}\left(\frac{\dot{u}_f + u_f\xi\bar{\omega}}{\bar{\omega}_D}\sin\bar{\omega}_D t + u_f\cos\bar{\omega}_D t\right)$$

=

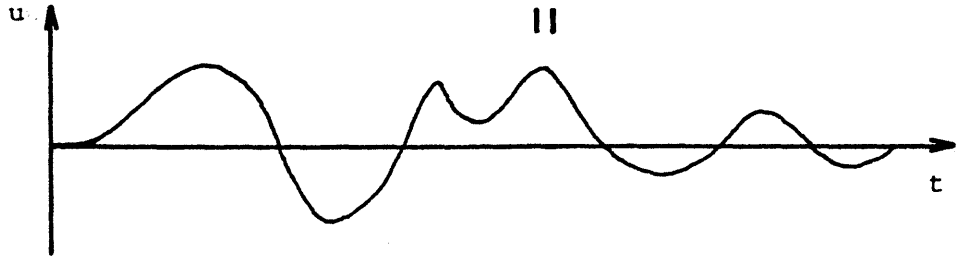

d. correct response

Fig. 5.5 Zero Minimization Technique

with no iterative process involved for the linear analysis.

5.2.2.3 Relaxation

In addition to the zero minimization technique, relaxation procedures were investigated as a means of accelerating the convergence process. The relaxation procedure is defined as follows:

$$y^i = \alpha\bar{y}^i + (1-\alpha)y^{i-1} \tag{5.71}$$

where the right superscript refers to the iteration cycle number; α is the acceleration coefficient; y, the response after applying relaxation; and $\bar{y}$, the response before applying relaxation. For $\alpha>1$ the procedure is called over-relaxation; $\alpha<1$, under-relaxation; and $\alpha=1$, no relaxation. In general, when $\alpha>1$ a larger weighting factor is applied to $\bar{y}^i$ than y^{i-1}, and when $\alpha<1$ the reverse statement holds.

Relaxation was applied to both the displacement and the pseudo-force histories. In both applications of over-relaxation the response demonstrated an accelerated convergence in the early cycles, and moreover the simultaneous over-relaxation of the response and the pseudo-force histories accelerated the convergence process at an even greater rate. During the latter cycles, however, the response began to diverge and eventually displayed a significant instability. A similar application of

under-relaxation demonstrated a slower convergence rate with no instability.

The inability of the over-relaxation scheme to accelerate the convergence stems from the HFT approach being based on the pseudo-force formulation combined with a frequency domain solution scheme. Since the pseudo-force vector at time $t_n = n\Delta t$ is evaluated from the response at time $t < t_n$, the end of the response history is the last to converge. In other words, the solution correction progresses forward in time. As a result, the pseudo-force history after time t_n, where time t_n is the time up to which the response is correct, resembles the actual pseudo-force for only a short time interval after t_n and may differ significantly from the exact pseudo-force history for an appreciable time after t_n. The use of an over-relaxation scheme, consequently, amplifies the incorrect pseudo-force history, producing a response drastically different from the true response, in turn exacerbating the problem by creating an even worse approximation to the pseudo-force history for the next cycle. When no relaxation is used, the iterative process may still create these significant differences in the pseudo-force history after time t_n, but these differences are not amplified in succeeding cycles, and hence the solution eventually converges.

Based on the results of the relaxation study, it appears that any scheme producing a pseudo-force history differing significantly from the actual force history and amplifying these differences in latter cycles cannot accelerate the convergence rate of the HFT solution scheme.

5.2.2.4 Other Acceleration Schemes

Alternate approaches for increasing the solution efficiency include using other than radix-2 FFT's, evaluating the Fourier transform of two N-point real arrays simultaneously or an N-point real array by an N/2-point transform, and segmenting the force history. The first method exploits, for example, 4-point and 8-point transforms, but is probably impractical since a different FFT will be optimally chosen for each history length. Recent FFT variations include schemes that are particularly suited to structural dynamics. An improved algorithm presented by Hall (32) offers greater versatility in choosing the transform size ($N = 2^M \cdot L$, $L = 2$ or 3), thus reducing the computation time.

The second approach takes advantage of the FFT evaluating the Fourier transform of a complex array. In particular, two real arrays of length N can be rearranged and stored in a complex array of length N, the Fourier transform of the complex array is evaluated, and then the terms of the complex array recombined to obtain the actual Fourier transforms of the real arrays. The FFT, therefore,

is executed once for two real arrays. This approach increases the solution efficiency in some cases, but in the particular application to structural dynamic problems the FFT also evalutes the inverse Fourier transform of the response spectrum $Y(\omega)$, a complex array, to obtain the response history $y(t)$, and hence the approach applies only when transferring the load history to the frequency domain. In addition, the algebraic rearrangement of the real arrays and the subsequent recombination of terms in the complex array may exclude any overall gains in efficiency. The scheme proposed by Hall, however, is particularly adapted to problems with real and complex symmetric arrays, requiring half the computer storage and computation time.

The final efficiency scheme of segmenting the force history and evaluating the response to each segment separately is based on the observation that the pseudo-force history corrects itself in a time progressing manner. The latter portions of the pseudo-force history are evaluated in all cycles, but only in the final cycles do they begin to converge to the exact history. It appears, therefore, that if the load history were segmented, for example, into two parts, the initial half would be evaluated first and convergence would occur in the same number of cycles as if the entire history were being evaluated. The second half would be considered next, and convergence may be more rapid because the first half response is already established. This approach will be examined again later in relation to

nonlinear mode updating schemes.

5.2.2.5 Stabilization by Artificial Damping and Incremental Load Application

Schemes for stabilizing the HFT solution process are described in this section. The basic procedure presented in subsection 5.2.1 should work theoretically. Its application, however, involves numerical approximations such as evaluating the velocity at time zero by a finite difference expansion (used for the zero minimization process) and extracting the Fourier transform of series that may actually possess an infinite frequency content. In particular, the actual displacement in the neighborhood of time zero may be oscillating to such an extreme degree that the use of a 4th, 5th, or even tenth order finite difference approximation will not yield the correct velocity at time zero, and hence the zero minimization technique works improperly and the free vibration at the end of the response contaminates the entire response. This "leakage" results in the unconverged pseudo-force vector toward the end of the response history creating an incorrect pseudo-force vector at the beginning of the previously converged response history, eventually causing the entire solution to destabilize. The second numerical approximation of using the discrete Fourier transform occurs when an excessively large time increment is selected such that a component with significant magnitude exists at the corresponding

Nyquist frequency, producing aliasing. This aliasing may cause an improper transform of the pseudo-force history, and eventually contribute to an unconverging solution.

Furthermore, the use of a digital computer with finite word length and, hence, the presence of truncation error and upper and lower limits on number sizes may prevent the solution process from converging. This divergence may only be numerical in the sense that the analytical iterative solution process would also induce large numbers during the solution process, but these numbers would remain finite.

Due to the inherent numerical nature of the HFT solution scheme, stabilization schemes were developed that do not necessarily accelerate the convergence process, but prevent divergence when used properly. The first stabilization scheme employs artificial viscous damping. Stated mathematically, a damping matrix (force) is added to both sides of the equation of motion as follows:

$$\tilde{\underline{M}}\ddot{\underline{y}} + (\tilde{\underline{C}} + \tilde{\underline{C}}_v)\dot{\underline{y}} + \tilde{\underline{K}}\underline{y} = \tilde{\underline{F}} + \tilde{\underline{F}}^{NL} + \tilde{\underline{F}}^{V} \tag{5.72}$$

where $\tilde{\underline{C}}_v$ is the artificial viscous damping matrix and $\tilde{\underline{F}}^{V}$ is the artificial viscous damping force equal to $\tilde{\underline{C}}_v\dot{\underline{y}}$. Notice that both $\tilde{\underline{F}}^{NL}$ and $\tilde{\underline{F}}^{V}$ are unknowns on the RHS of Eq. 5.72. In general, $\tilde{\underline{C}}_v$ is not given explicitly, since the HFT scheme is based on a mode superposition approach, but rather it is expressed in terms of artificial viscous damping ratios ξ_v such that $\underline{\phi}^T\tilde{\underline{C}}_v\underline{\phi}$ is equal to $2\xi_v\bar{\omega}$.

In addition, artificial hysteretic damping may be used. The concept of hysteretic damping is only defined theoretically in the frequency domain, and hence Eq. 5.72 is examined in the frequency domain. The stiffness now becomes $\tilde{k}+\tilde{k}_h$ where $\tilde{k}$ is the generalized stiffness ($\underline{\phi}^T\underline{\tilde{K}}\underline{\phi}$) and $\tilde{k}_h$ is the hysteretic term given by $i2\xi_h \tilde{k}$ where $i=\sqrt{-1}$ and ξ_h is the artificial hysteretic damping ratio. The hysteretic damping force $f_h(\omega)$ equals $i2\xi_h\tilde{k}Y(\omega)$ where $Y(\omega)$ is the displacement response in the frequency domain. Equation 5.72 in the frequency domain for one mode becomes

$$\ddot{Y} + (\tilde{c} + 2\xi_v\bar{\omega})\dot{Y} + \tilde{k}(1 + i2\xi_h)Y = f + f^{NL} + f^v + f^h \qquad (5.73)$$

where Y is the generalized response; $\tilde{c}$ equals $\underline{\phi}^T\underline{\tilde{C}}\underline{\phi}$; and other terms are as defined previously.

The choice of using ξ_v or ξ_h or both depends on the actual damping dominating the structural response. Artificial hysteretic damping tends to be more appropriate for structural dynamic type problems since such problems usually exhibit a frequency independent energy dissipation in the material behavior. A viscous type damping may be more appealing conceptually since it is well defined in the time domain. Notice that the zero minimization technique, in other words, the use of Eq. 5.70 is still valid. This equivalent application for both types of damping is easily demonstrated by deriving the corresponding transfer functions for the undamped problem. We have

$$H_v(\omega) = (-\omega^2 + i\omega 2\xi_v \bar{\omega} + \bar{\omega}^2)^{-1} \tag{5.74}$$

for artificial viscous damping and

$$H_h(\omega) = \left[-\omega^2 + \bar{\omega}^2(1 + i2\xi_h)\right]^{-1} \tag{5.75}$$

for artificial hysteretic damping. Therefore, when $\xi_v = \xi_h$, $H_v(\omega)$ equals $H_h(\omega)$ for $\omega = \bar{\omega}$. In turn, $Y_v(\omega)$ equals $Y_h(\omega)$ if $F(\omega)=1$. This situation corresponds to the free vibration problem (the Fourier transform pair of $H(\omega)$ is $h(t)$, the impulse response function), and hence Eq. 5.70 still applies.

Artificial damping as a stabilization method simply stabilizes the solution by preventing excessive vibration amplitudes during the iterative process. The damping matrix on the LHS of the governing equation is balanced by the damping force on the RHS, implying that the approach is theoretically sound. As mentioned previously, if the initial iterative cycles produce poor approximations to the actual response, the succeeding cycles may be subjected to pseudo-force histories differing significantly from the actual history, resulting in a numerical divergence. Artificial damping alleviates this problem by providing the analyst a means of attenuating considerably the initial response and the consequent pseudo-force history. The result is a pseudo-force history containing small incorrect amplitudes until the solution converges. Furthermore, since the HFT scheme evaluates the pseudo-force history only to the end of the loading, the artificial damping approach aids

the zero minimization technique by damping out the free vibration at the end of the loading. Notice that when only hysteretic damping is present, the initial cycle will produce the damped linear response where the damping is provided by, for example, artificial hysteretic damping. As the iterative cycle progresses, the actual hysteretic damping is manifested in the pseudo-force vector $\underline{F}^{NL}$ such that by the last iteration, $\underline{F}^{NL}$ contains all hysteretic damping contributions and $\underline{F}^{h}$ is zero.

The actual implementation of the artificial damping concept involves numerical approximations. As shown by Eq. 5.73, f^{v} depends on the velocity $\dot{y}$. However, $\dot{y}$ is never actually evaluated in the solution process and must be approximated from y ($\dot{y}(t)$ can be obtained from $Y(\omega)$ by evaluating the inverse Fourier transform of $i\omega Y(\omega)$, but an additional cost of applying the FFT is incurred). A finite difference scheme, therefore, approximates $\dot{y}(t)$ from y(t), and the problems mentioned previously are present again. Furthermore, $c_v(\omega)=i2\xi_v\bar{\omega}\omega Y(\omega)$ depends on the frequency ω in the frequency spectrum. As a result, if during the iterative process incorrect significant pseudo-force components are evaluated at large ω, a large high frequency component in the response may be generated, in turn creating a larger high frequency viscous damping force, and possibly producing instability before the solution converges. The use of artificial viscous damping should, consequently, be applied carefully.

Artificial hysteretic damping demonstrates a better numerical behavior since the damping is directly proportional to $Y(\omega)$ and also independent of the frequency ω. The two problems associated with artificial viscous damping are avoided. Its implementation, however, is not straightforward since the hysteretic damping force cannot be evaluated in the time domain. This disadvantage would pose no problems if the zero minimization technique were not employed, since in such a case the hysteretic damping force would be obtained easily in the frequency domain by multiplying the response $Y(\omega)$ by $i2\xi_h$. In conjunction with the zero minimization technique, however, $Y(\omega)$ contains incorrect free vibration components that are removed in the time domain. The hysteretic damping force for the succeeding cycle, therefore, can be evaluated only by transferring the corrected response $y(t)$ back to the frequency domain and then multiplying by $i2\xi_h$. This process involves two applications of the FFT, one to transfer the force vector $f(t)+f^{NL}(t)$ to the frequency domain and the other to transfer $y(t)$. The apparent inefficiences of using artificial hysteretic damping are avoided by realizing that both $y(t)$ and $f(t)+f^{NL}(t)$ are real histories, and hence only one FFT need be implemented if advantage is taken of a complex array storing, for example, $y(t)$ as its real part and $f(t)+f^{NL}(t)$ as its imaginary part. The actual procedure for transferring two real arrays simultaneously is given in the references (17).

Case studies demonstrating the behavior of the solution when artificial damping was included were conducted and are discussed in Ch. 6.

Another stabilization method is the incremental load application approach. Rather than loading the structure immediately with the actual load history, the load is scaled down and applied incrementally. This stabilization technique is based on the same concept of artificial damping where the incorrect response during the initial cycles is diminished considerably such that the resulting pseudo-force history does not generate an excessive incorrect response in the course of succeeding cycles. The procedure resembles the solution of nonlinear static problems, and indeed is identical if the frequency domain solution is regarded from the perspective of a complex stiffness approach

$$k_c(\omega)Y(\omega) = f(\omega) + f^{NL}(\omega) + f^{v}(\omega) + f^{h}(\omega) \tag{5.76}$$

where

$$k_c = -\omega^2 + i\omega 2\bar{\omega}(\xi + \xi_v) + \bar{\omega}^2(1 + i2\xi_h) \tag{5.77}$$

5.2.2.6 Nonlinear Mode Updating in the Frequency Domain

The numerical considerations given up to this point concern the solution of the independent SDOF problems. This subsection discusses the problem in its entirety, or more specifically, the development of nonlinear mode updating schemes in the frequency domain. In general, the problem consists of evaluating modal updates to the linear structure

as it becomes nonlinear and applying these new mode shapes to the geometric structural matrices to obtain the generalized matrices.

Beginning with the second problem, suppose that n linear mode shapes, where n is less than the total number of degrees of freedom, are used in the first few iterative cycles. The solution process is stopped, and m nonlinear mode shapes orthogonal to the original n mode shapes are obtained. The eigenvector matrix $\underline{\Phi}$ is given as

$$\underline{\Phi} = \begin{Bmatrix} \underline{\Phi}^T_{\text{linear}} \\ \\ \underline{\Phi}^T_{\text{nonlinear}} \end{Bmatrix}^T \begin{matrix} \text{n shapes} \\ \\ \text{m shapes} \end{matrix} \tag{5.78}$$

These mode shapes are then applied to the original governing equation of motion to obtain the generalized equation of motion. The generalized structural matrices, however, are only partially diagonal. Although the linear mode shapes $\underline{\Phi}_1$ were derived from the eigenproblem using the linear stiffness matrix

$$(\underline{K}_1 - \bar{\omega}_1^2 \underline{M})\underline{\phi}_1 = \underline{0} \tag{5.79}$$

implying that

$$\underline{\phi}_1^T \underline{K}_1 \underline{\phi}_1 - \bar{\omega}_1^2 \underline{\phi}_1^T \underline{M} \underline{\phi}_1 = 0 \tag{5.80}$$

or

$$\underline{\Phi}_1^T \underline{K}_1 \underline{\Phi}_1 = \underline{I\omega}_1^2 = \text{diagonal matrix} \tag{5.81}$$

the nonlinear mode shapes $\underline{\Phi}_{n1}$ were derived from eigenproblems using nonlinear stiffness matrices

$$(\underline{K}_{n1} - \tilde{\omega}_{n1}^2 \underline{M}) \underline{\phi}_{n1} = \underline{0} \tag{5.82}$$

and hence $\underline{\Phi}_{n1}^T \underline{K}_1 \underline{\Phi}_{n1}$ is not necessarily a diagonal matrix. Since the generalized structural matrices are no longer diagonal, the transfer matrix $\underline{H}$, given by Eq. 5.66, cannot be evaluated simply by computing the reciprocals of the diagonal terms in $\underline{H}^{-1}$.

One possibility for circumventing the nondiagonal $\underline{H}^{-1}$ problem is to obtain $\underline{H}$ directly by evaluating $[\underline{H}^{-1}]^{-1}$. This approach, however, is extremely costly since the matrix inversion must be executed for all frequencies in the spectrum (10,000 times if the excitation has 10,000 time steps) and, moreover, entails additional storage requirements since the off-diagonal terms of $\underline{H}$ must be stored in addition to the diagonal terms.

The impracticality of the first approach suggests an alternate iterative scheme for managing the off-diagonal terms in the transfer matrix. Rather than employing $\underline{H}$ in the solution process, an approximate diagonal transfer matrix is used. This approach transfers all off-diagonal

terms in the generalized matrices to the RHS of the equations of motion. The remaining diagonal terms are used to evaluate the approximate $\underline{H}^{-1}$, and hence $\underline{H}$ is easily obtained from $\underline{H}^{-1}$ by computing the reciprocals of the diagonal terms. This procedure obviously engenders an iterative solution scheme, but does not pose any new problems since the solution process is already iterative. The governing equations of motion for the system is now

$$\underset{\sim}{M}\ddot{y} + (\overset{\cup}{\underline{C}} + \overset{\cup}{\underline{C}}_v)\dot{y} + \overset{\cup}{\underline{K}}y = \underset{\sim}{F} + \underset{\sim}{F}^{NL} + \underset{\sim}{F}^{V} + \underset{\sim}{F}^{OD} \tag{5.83}$$

where the superscript $\cup$ refers to a generalized matrix containing only its diagonal terms and $\underset{\sim}{F}^{OD}$ is the off-diagonal force vector

$$\underset{\sim}{F}^{OD} = (\overset{\cap}{\underline{C}} + \overset{\cap}{\underline{C}}_v)\dot{y} + \overset{\cap}{\underline{K}}y \tag{5.84}$$

where the superscript $\cap$ denotes a generalized matrix containing only off-diagonal terms. Therefore

$$\begin{aligned} \underset{\sim}{C} &= \overset{\cup}{\underline{C}} + \overset{\cap}{\underline{C}} \\ \underset{\sim}{C}_v &= \overset{\cup}{\underline{C}}_v + \overset{\cap}{\underline{C}}_v \\ \underset{\sim}{K} &= \overset{\cup}{\underline{K}} + \overset{\cap}{\underline{K}} \end{aligned} \tag{5.85}$$

A final approach is to use only the nonlinear mode shapes. In other words, new eigenvectors are evaluated from a nonlinear stiffness matrix $\underline{K}_{nl}$ and only these eigenvectors are employed in the succeeding iterations. The equation of

motion is

$$\tilde{\underline{M}}\ddot{\underline{y}} + \tilde{\underline{C}}_{nl}\dot{\underline{y}} + \tilde{\underline{K}}_{nl}\underline{y} = \tilde{\underline{F}} + \tilde{\underline{F}}^{NL} \tag{5.86}$$

where all generalized structural matrices are diagonal because the mode shapes $\underline{\phi}_{nl}$ were derived from $\underline{K}_{nl}$. Notice that the pseudo-force vector $\underline{F}^{NL}$ is now derived by evaluating the difference between $\underline{K}_{nl}\underline{q}$ and $\underline{I}$, the actual member forces. This last approach is suitable when the nonlinear response is fairly uniform such that $\underline{K}_{nl}$ represents the stiffness during a significant portion of the history. The eigenproblem, however, may be more expensive computationally than the other approaches because an entire new set of eigenvectors must be derived. Applications of these schemes are presented in Chapter 6.

With various approaches available for handling non-diagonal transfer matrices, we now proceed to the first problem of updating the mode shapes. Nonlinear mode updating schemes in the frequency domain, in contrast to the nonlinear mode updating schemes discussed in section 3.2.2, cannot proceed in time and be implemented whenever the nonlinearities begin to change substantially. The very nature of a frequency domain solution implies that the solution at all time steps is obtained simultaneously, and hence all mode shapes must be selected before the solution commences. Updating is possible only after an iterative cycle. Furthermore, the stiffness matrix $\underline{K}_{nl}$ is never

evaluated, and only the pseudo-force history is extracted. These considerations significantly restrict the means for updating the mode shapes.

Of the updating schemes presented in section 3.2.2, the second approach involving mode shapes selected from the eigenproblem of an imposed deformed shape appears the most promising. The HFT scheme due to its iterative process offers the additional advantage of providing insight to the nonlinear response. This updating approach adapted to the HFT would be as follows:

1. Iterate the first few cycles with the linear mode shapes
2. Stop the Analysis
3. Derive an equivalent static load distribution from the pseudo-force histories
4. Apply this static load distribution to the structure and thus, obtain a tangent stiffness matrix $\underline{K}_t$
5. Evaluate the first few eigenpairs corresponding to $\underline{K}_t$
6. Gram-Schmidt orthogonalize these nonlinear eigenvectors with respect to the previous eigenvectors
7. Restart the analysis using the new basis vectors
8. Repeat steps 2-7 until the solution demonstrates acceptable convergence

The procedure as described appears fairly straightforward. Step 3, however, involves considerable insight on the part of the analyst. For simple pseudo-force histories, such as those exhibiting one peak occurring at the same time for all members, the equivalent static load distribution is easily selected. Most analyses, however, involve extremely complicated pseudo-force histories differing for all members, and the selection of a static load distribution, or even a set of distributions, that adequately recreates the nonlinear deformed structure requires considerable judgement and, more importantly, luck.

A second updating approach involving less luck and insight and demanding minimal preparation time was subsequently developed. This scheme exploits the pseudo-force history from a more rational and systematic perspective. In particular, since the pseudo-force history is derived from the member forces, obtained from the current stress-strain states, the exact tangent and secant stiffness histories are available indirectly, permitting the evaluation of the exact global tangent and secant structural stiffness matrices. An HFT solution scheme, however, employs one set of eigenvectors during each iterative cycle, thus requiring a method for selecting a structural stiffness or stiffnesses characterizing most of the response history. Only one stiffness matrix and its set of eigenvectors can be used if an exact diagonal transfer matrix approach is chosen. If the approach of transferring off-diagonal terms

to the RHS of the governing equation is selected, a host of eigenvectors corresponding to different stiffnesses may be used, but again only one stiffness matrix can be used in the evaluation of $\underline{H}$.

In either case, the second updating scheme is valid and is given as follows:

1. Obtain E_{sec} for each member from the stress-strain pairs evaluated during the generation of the pseudo-force histories
2. During the process of deriving E_{sec}, store ΣE_{sec} and ΣE_{sec}^2 where the summation is over time
3. After the entire pseudo-force history is evaluated, obtain a least squares approximation of E_{sec} for each degree of freedom using the results from step 2
4. Reconstruct the secant stiffness matrix $\underline{K}_{nl}$ corresponding to the E_{sec}'s of step 3
5. Evaluate m eigenvectors $\underline{\Phi}_{nl}$ of $\underline{K}_{nl}$
6. Use $\underline{\Phi}_{nl}$ directly in the next iteration (exact diagonal matrix transfer function) or Gram-Schmidt orthogonalize $\underline{\Phi}_{nl}$ with respect to the previous set of eigenvectors and proceed with the analysis (off-diagonal term transfer approach)

This updating scheme can be executed without stopping the analysis, and hence requires no participation from the analyst during the solution process. The updating efficiency can be increased by implementing the process only

after every i cycles. Furthermore, least squares fitted secant stiffness matrices can be evaluated for specified intervals of the history, eigenvectors corresponding to each secant stiffness matrix are then derived, and the eigenvectors are recombined. This approach produces a total eigenvector matrix consisting of eigenvectors representing the dominant behavior of different portions of the response history.

The actual implementation of both modal updating schemes is discussed in Chapter 6.

Regardless of the mode updating scheme, a substantial portion of the solution cost for large systems may be contributed by the eigenvalue problem. Although an eigenvalue analysis is usually conducted initially for both time integration and frequency domain solutions to determine structural properties such as the lowest periods and mode shapes, an additional cost is incurred in the HFT analysis as the mode shapes are updated. An efficient eigensolver is therefore essential.

The subspace interation technique is often employed for large structural systems (9). With respect to the HFT mode updating schemes, the subspace iteration approach also appears attractive since the previous mode shapes can be used as the initial shapes in determining the updated shapes. A more efficient eigensolver has been investigated recently by Wilson, et. al. (88,89). The scheme is

particularly suited to problems where the excitation can be decomposed into a spatial vector multiplied by a temporal vector, such as in seismic excitation problems. Rather than evaluating the exact eigenvectors of the system, the new scheme generates orthogonal Ritz vectors, which are then used in the succeeding mode superposition analysis. The generated Ritz vectors only correspond to those shapes actually participating in the response, as opposed to eigenvectors which may not participate in the response if their shape is orthogonal to the loading, even though their natural frequency may be near dominating load frequencies. Studies by Wilson, et. al., indicate that generating the Ritz vectors involves one-tenth the effort to generate the exact eigenvectors. Furthermore, computation times for mode superposition analyses were less when using Ritz vectors, because a smaller basis could produce a more accurate response.

In conjunction with the second mode updating scheme, we now reexamine the segmenting method introduced in section 5.2.2.4. The segmenting scheme was motivated from the pseudo-force history correcting itself in time. The incentive here is to model portions of the response history by different $\underline{K}_{n1}$ and $\underline{\Phi}_{n1}$ such that an exact diagonal transfer function approach is maintained and the $\underline{K}_{n1}$ produces a good representation of its portion of the response. An overlap-add or overlap-save (17) method would appropriately link the response of the different segments.

In particular, $\underline{K}_1$ may be used for time t_1 to t_j and $\underline{K}_{n1}$ for time t_j to t_k. The procedure is shown schematically in Fig. 5.6.

5.2.2.7 Selecting a Time Increment

As the final part of the numerical considerations section, we discuss a procedure for selecting an appropriate time increment. A first guess is obtained from the external load history by choosing the time increment Δt_1 such that at the Nyquist frequency f_N, the load component has negligible magnitude. This time increment is then compared with the period T_n corresponding to the highest mode used in the analysis. If $\Delta t_1 < T_n/2$, a larger time increment may be appropriate. Time increment Δt_1, however, may be too large for problems with path-dependent material behavior. A smaller time increment, therefore, must be chosen such that the material response is adequately followed. The time selection procedure is outlined as follows:

1. Obtain Fourier transform of load history
2. Let ω_{max} be highest frequency in load spectrum
3. Choose $\Delta t_1 = 1/2f_n = \pi/\omega_{max}$
4. Compare Δt_1 with the period of the highest structural mode T_n
5. If Δt_1 is significantly smaller than $T_n/2$, a larger time increment may be appropriate, and the external load history should have its higher frequency components set to zero if a larger Δt is chosen. Also,

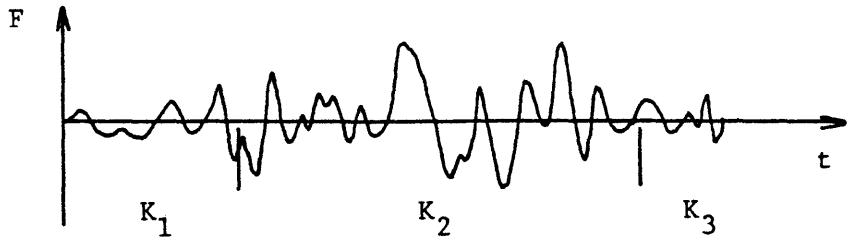

a. excitation history

b. response using K_1 for interval 1

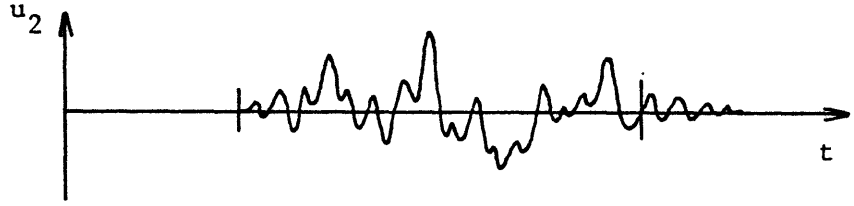

c. response using K_2 for interval 2

d. response using K_3 for interval 3

e. total response

Fig. 5.6 Segmented History Analysis

if the material behavior is path dependent and demonstrates considerable changes for consecutive time steps, a smaller time increment may be necessary

Notice that the pseudo-force history was never considered when selecting a time increment. This approach is theoretically consistent with steps 1, 2, and 3 since in a linear analysis a response will never be generated with higher frequency components than the input (load history). In other words, since $Y(\omega)=H(\omega)F(\omega)$, if $F(\omega)$ has highest frequency ω_o, $Y(\omega)$ also has a highest frequency component at ω_o. In a nonlinear analysis, however, ultraharmonic components corresponding to multiples of the external load frequency can be generated (65,79). These ultraharmonic components in the HFT analysis will originate from the pseudo-force history, and hence steps 4 and 5 should be exercised carefully.

5.2.3 Qualitative Evaluation of the HFT Solution Scheme

Any new analytical technique adapted for solving practical engineering problems must offer considerable advantages over accepted solution techniques. The salient characteristics of the HFT solution scheme are accentuated in this section to provide the analyst a basis for evaluating its applicability to the solution of nonlinear dynamic structural problems.

By combining the nonlinear mode superposition technique with a frequency domain solution, the HFT solution approach exploits the economics offered by a reduced vector space and the accuracy of a theoretically exact numerical integrator. The mode superposition approach easily accommodates structural dynamic problems, but precludes the practical solution of wave propagation problems where all modes are excited. Potential applications, therefore, include the transient response to seismic excitations, intense wave loadings, and wind forces. Applications to wave propagation type problems are excluded. Extensions to steady state problems such as the response to wave spectrums are partially restricted in the sense that the global nonlinear response behavior can be evaluated, but localized effects such as fatigue degradation may require a substantial number of modes, producing an inefficient solution (85).

The frequency domain solution employs a transfer function that behaves as an exact numerical integrator if the Nyquist frequency is properly chosen and the resolution is sufficient to capture the peaks in the frequency spectrum. Numerical accuracy problems of period elongation and artificial damping, consequently, are eliminated, and the appropriate time increment of an HFT approach is often 5-10 times larger than the time increment of a direct time integration approach.

Furthermore, the solution in the frequency domain presents the response in terms of generalized displacement (or velocity and acceleration) and pseudo-force spectra, and hence offers a quantitative measure of the modes dominating the response and readily portrays the transition from a linear to a nonlinear response. The accuracy of the solution is more easily examined by comparing the response spectra of consecutive cycles.

The HFT solution approach also allows an updating of the solution parameters after each iteration. Particular examples include changing the time increment, modifying the number of frequency components (total number of points in the frequency domain), and reselecting the mode shapes. By examining the response spectra, the analyst can ascertain if the component at the Nyquist frequency has an appreciable magnitude and evaluate the contribution of each mode to the response, and subsequently choose a larger time increment or eliminate the non-participating modes. As a final check for verifying the solution accuracy, during the last iteration the time increment can be decreased, more modes can be added, and the number of zeroes extended, and then the resulting response compared with the response at the previous iteration.

This attribute of updating the solution parameters, however, originates from the frequency domain approach storing the entire response history, and hence implies that

the HFT scheme demands a substantial storage space. The HFT storage requirements are easily deduced by examining its computer program flow chart, presented in Fig. 5.7 for the total displacement formulation. Notice that two main loops are embedded inside the iterative loop 100. The first loop over the response history operates in the time domain and evaluates the total force history. The second loop contained in subroutine RESPON is over the number of generalized degrees of freedom and evaluates the generalized response. Two complex arrays TRANSF and CA are required. TRANSF stores the transfer functions for all modes and frequency components and CA is used in the application of the FFT. Therefore, TRANSF has size NMODE*(NB/2+1) and CA, size NB where NMODE is the number of modes and NB the number of points in the frequency domain (TRANSF can be eliminated if the transfer function is reevaluated each time it is used).

Since the response loop succeeds the force evaluation loop, the generalized force vector must be stored for all degrees of freedom and the entire history. The iterative loop requires this sequence because the frequency domain approach entails transferring the entire history. Furthermore, an alternate procedure evaluating the generalized total force history and then response for one mode and repeating the process for the next mode cannot be implemented since the generalized force is derived from the entire geometric force, and hence the entire geometric force

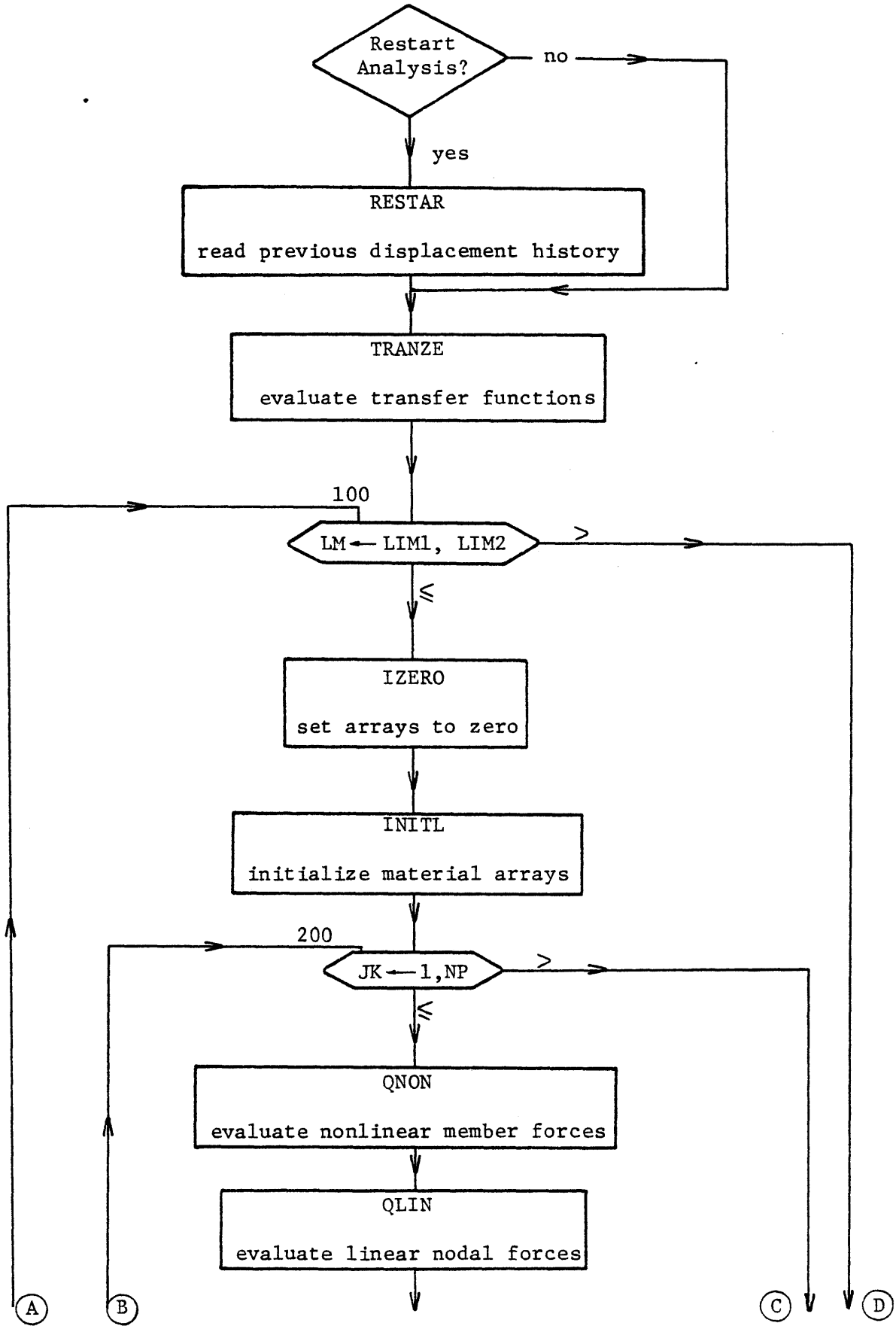
Restart Analysis?
no
yes
RESTAR
read previous displacement history
TRANZE
evaluate transfer functions
100
LM ← LIM1, LIM2
>
≤
IZERO
set arrays to zero
INITL
initialize material arrays
200
JK ← 1,NP
>
≤
QNON
evaluate nonlinear member forces
QLIN
evaluate linear nodal forces
A
B
C
D

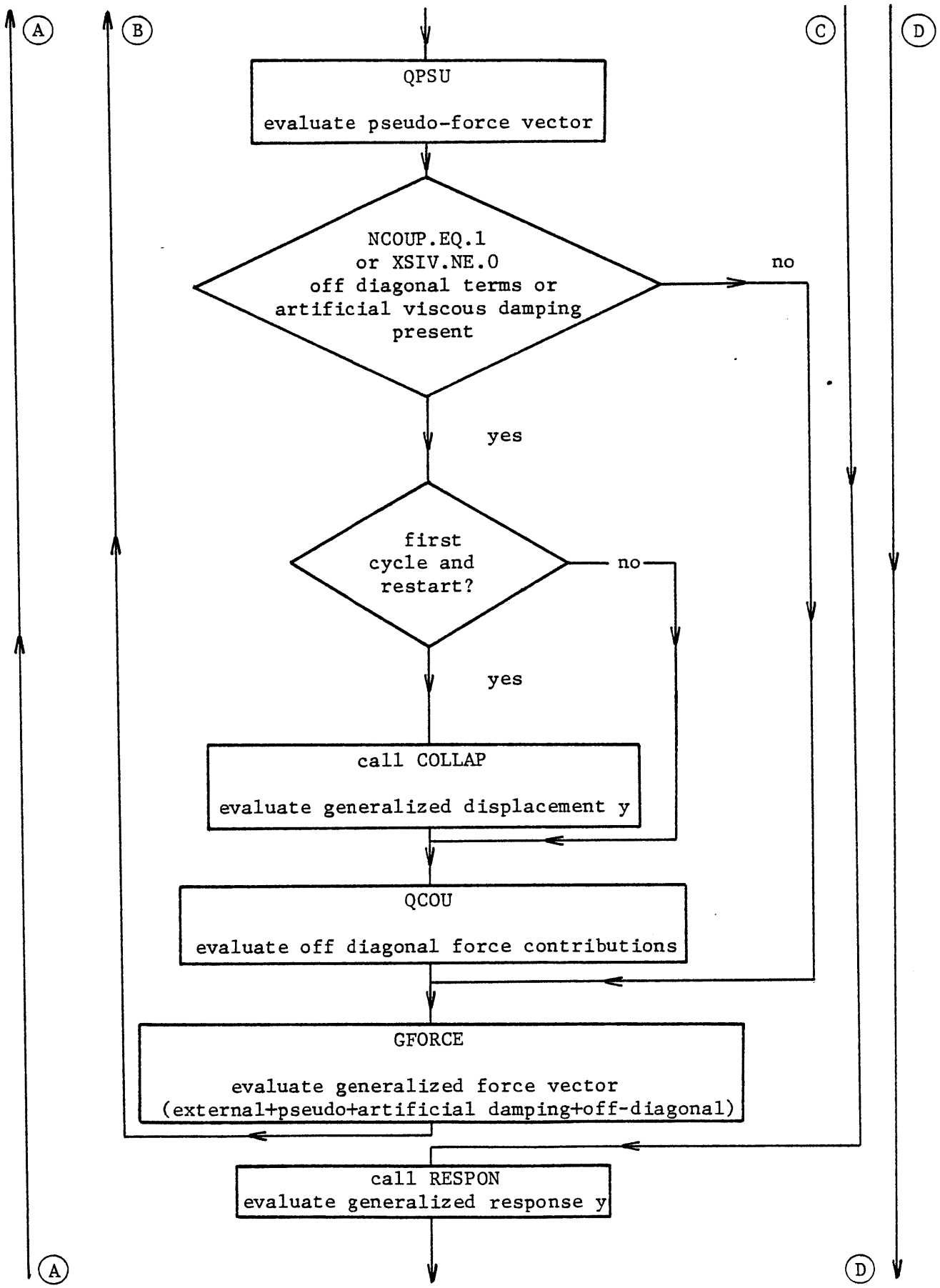
A
B
C
D
QPSU
evaluate pseudo-force vector
NCOUP.EQ.1
or XSIV.NE.0
off diagonal terms or
artificial viscous damping
present
no
yes
first
cycle and
restart?
no
yes
call COLLAP
evaluate generalized displacement y
QCOU
evaluate off diagonal force contributions
GFORCE
evaluate generalized force vector
(external+pseudo+artificial damping+off-diagonal)
call RESPON
evaluate generalized response y
A
D

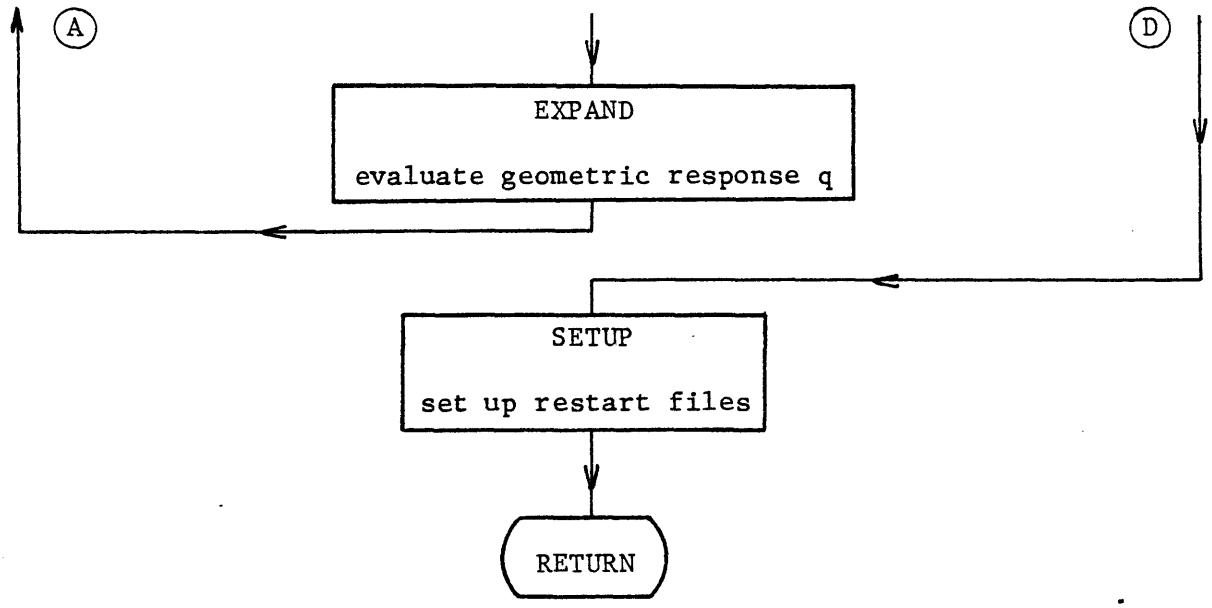

Fig. 5.7 Flow Chart for Hybrid Frequency-Time Domain Analysis Package

history must be acquired before evaluating the generalized forces of each mode. The result is an array GPF storing the generalized force history of all included modes. GPF has size NMODE*NP where NP is the number of points in the load history.

The HFT storage requirements, therefore, are determined mainly by CA, TRANSF, and GPF, amounting to a minimum storage size of NB+NMODE*(NB/2+1)+NMODE*NP. For a typical problem with 50 modes and 8000 time steps (NP), implying NB=8192, the required storage space is 613,042. If TRANSF is not stored but recalculated each time, the storage space becomes NB+NMODE*NP, or 408,192 for our particular problem. The storage requirements, consequently, are relatively large compared to those of typical direct time integration programs.

With these considerations in mind, the analyst can judiciously select an appropriate solution scheme for nonlinear problems. The HFT approach, however, does not possess the extensive background of established direct time integration studies that can provide valuable insight when implementing the solution process. Considerable studies on a variety of problems are necessary before the HFT scheme can be employed with confidence.

CHAPTER 6

SAMPLE STUDIES

Chapter 2 of this thesis presented the theoretical foundation for nonlinear continuum mechanics, while Chapters 3, 4, and 5 discussed the actual numerical implementation of the solution techniques. The process of obtaining a solution numerically from well established theoretical formulations has become possible only during the last two decades with the introduction of the digital computer. Even then, although the problem may be well formulated theoretically and numerically, the actual nonlinear solution process often involves a trial and error learning period consisting of a multitude of unforeseen and often unpredictable "bugs" stemming from numerical limitations such as finite length numbers and discrete modelling or even theoretical restrictions such as the existence and uniqueness of the solution.

The development considerations for the hybrid frequency-time domain solution scheme described in Chapter 5 are illustrated in this chapter by a collection of sample studies. Efficiency and stability characteristics are demonstrated first by SDOF system studies, and then additional refinements are examined in MDOF system examples. Particular emphasis is placed on the formulation of the solution scheme, zero minimization, acceleration by relaxation, stabilization by artificial damping, and nonlinear mode updating. Most sample studies display several development ideas. The studies are not presented in chronological order, but rather in a sequence emphasizing the evolution of the HFT scheme as it is applied to more complex problems.

6.1 FEASIBILITY STUDY, SDOF SYSTEM

This section discusses studies conducted during the initial development of the HFT scheme to ascertain its ability to reproduce the nonlinear response of SDOF systems. The SDOF structure had a period of 1.72 seconds and 5% viscous damping. Both an elastic-perfectly plastic and a tubular brace material model (39,43,66,94), shown in Fig. 6.1, were employed. Although the tubular brace model in a SDOF does not represent any realistic structure, this model was used to demonstrate the convergence capabilities of the HFT scheme for a complex material model containing buckling and a degrading stiffness. Two acceleration histories were

employed -- a two second single cycle sine wave with amplitude 10 and a 5 second history extracted from the SN component of the March 1977 Bucarest earthquake with peak acceleration scaled to 0.25 g, shown in Fig. 6.2.

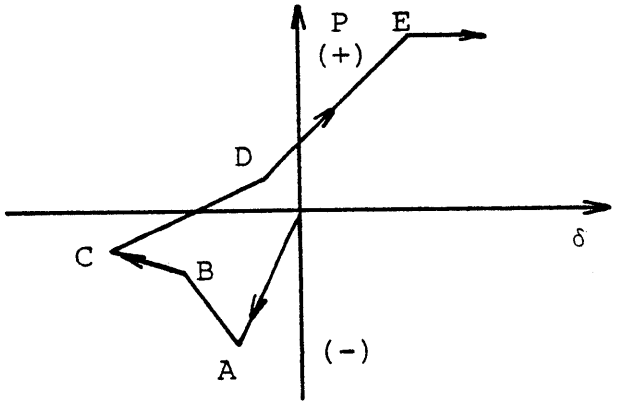

Fig. 6.1 Tubular Brace Model

The first SDOF study consisted of the elastic-perfectly plastic material model and single cycle sine wave excitation. The direct time integration results were obtained with the Newmark integration method, α=0.25 and δ =0.50, using a time increment of 0.1 seconds and combined with the Newton equilibrium iteration scheme. An identical time increment was specified in the HFT analysis. No zero minimization or artificial damping was employed. 512 points were required in the frequency domain to eliminate transient effects (20 to represent the load and an additional 492

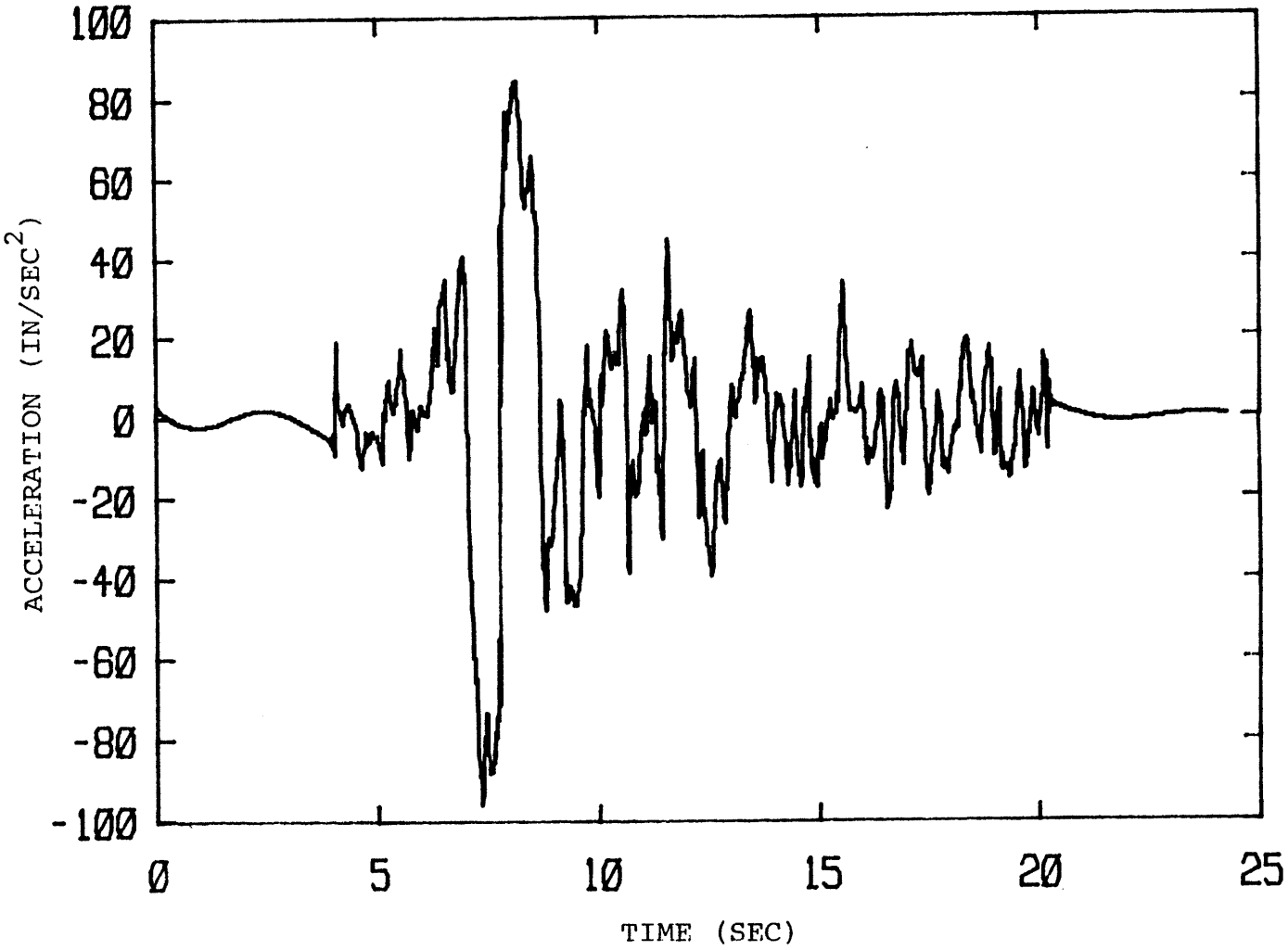

Fig. 6.2 - Bucarest Acceleration History

appended zeroes). A dual displacement formulation was used in all HFT analyses.

The results for the linear case are given in Fig. 6.3. Figure 6.4 shows the time domain and hybrid frequency-time domain results for a yield stress of 5 ksi, corresponding to a yield displacement of 1.39 inches. After five iterations the responses are almost identical.

To identify critical problem areas associated with the hybrid frequency-time domain analysis, the study was extended to an extreme case where the yield stress was 2 ksi, corresponding to a yield displacement of 0.56 inches. Figure 6.5 presents the results for this case. A substantial amount of yielding occurred, compared to the 5 ksi yield stress case. The frequency domain response, even after ten iterations, is inaccurate, particularly after t=1.5 seconds. In fact, when Figs. 6.6 and 6.7 are perused carefully, we notice that the solution diverges. These results in the frequency domain were obtained by evaluating the pseudo-force history for a time interval of 6 seconds, or 4 seconds after the loading terminated.

Given the poor results obtained for the 2 ksi case, an additional study with the pseudo-force calculated only to the end of the loading was conducted. Figure 6.8 shows the response up to two seconds using direct time integration and the response obtained in the frequency domain after one and ten iterations. Notice that the HFT analysis converges when

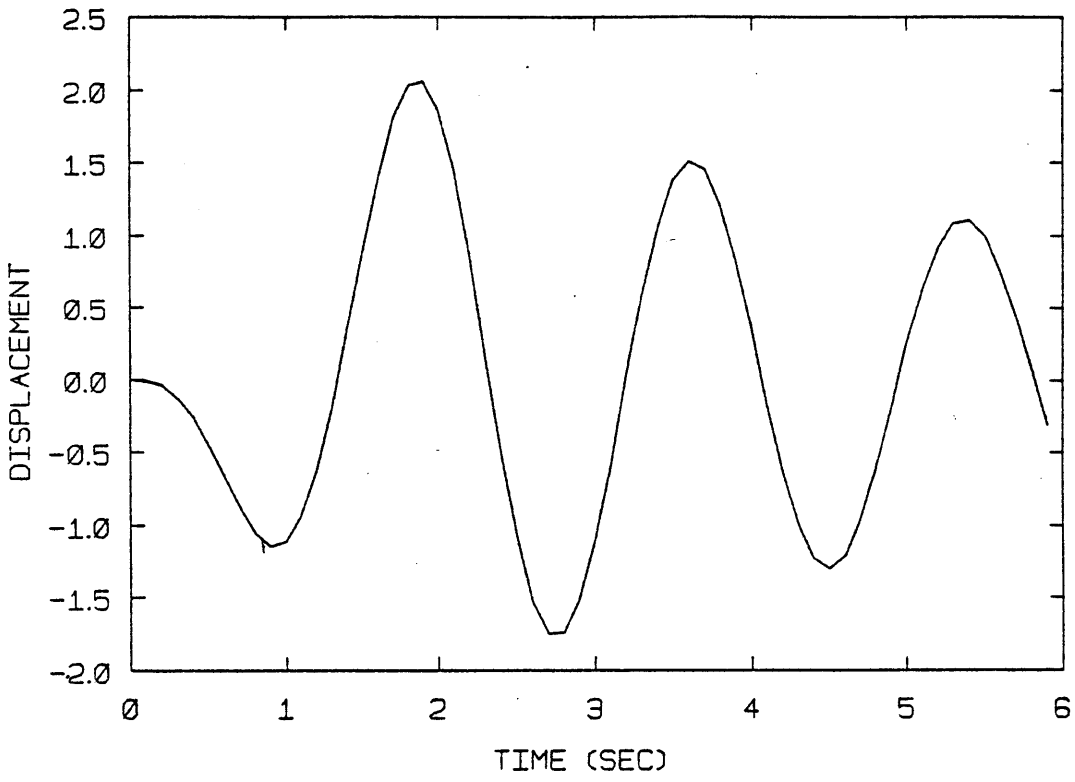

Fig. 6.3 **Linear-Elastic Response to a Sine Wave Loading**

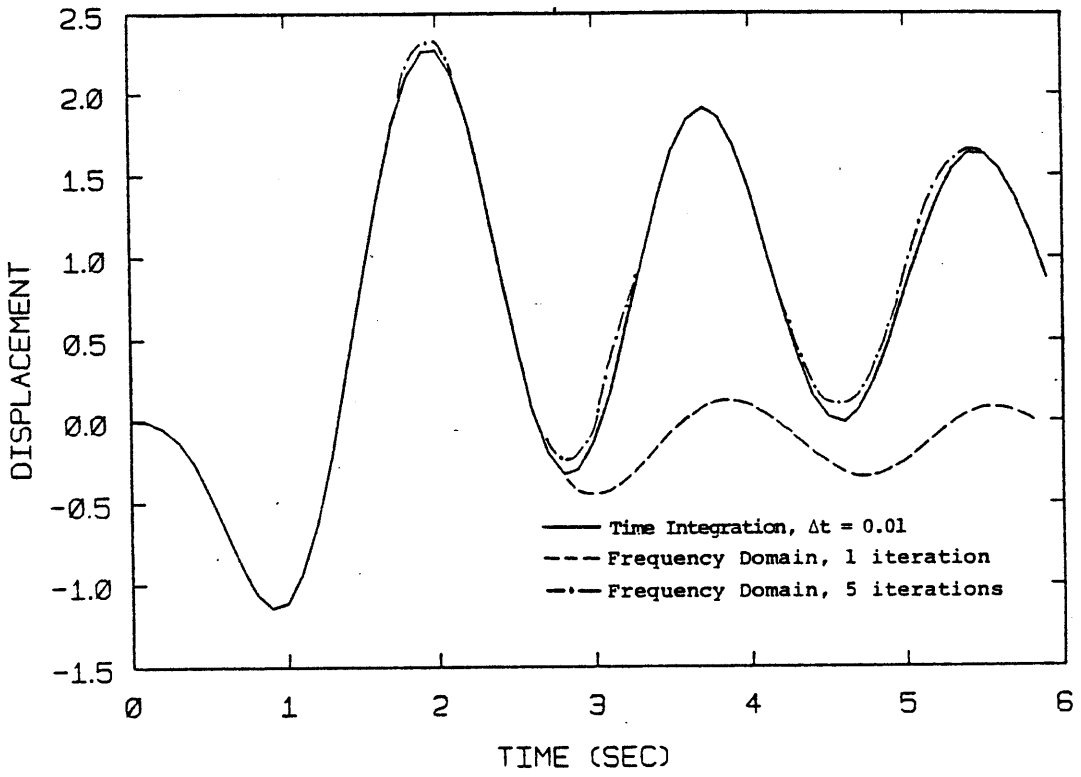

Fig. 6.4 Elastic-Plastic Response (Fy = 5 ksi)

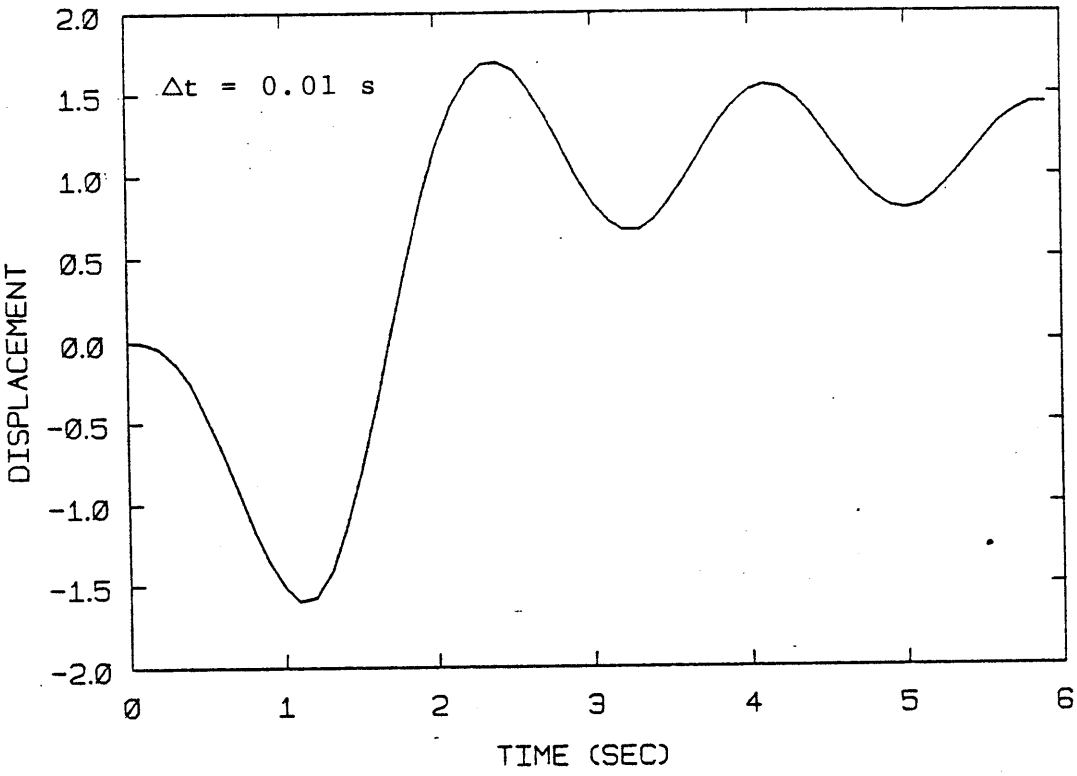

Fig. 6.5 **Elastic-Plastic Response Using a Time Domain Analysis (Fy = 2 ksi)**

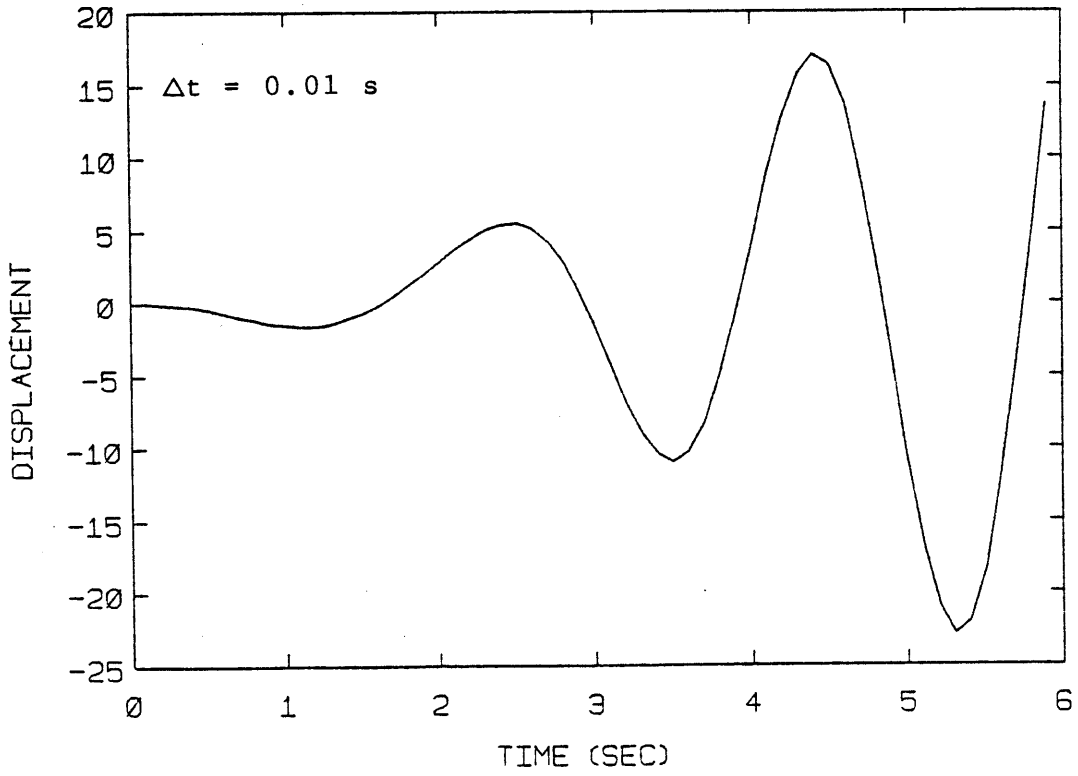

Fig. 6.6 **Elastic-Plastic Response Using a Frequency Domain Analysis, One Iteration (Fy = 2 ksi)**

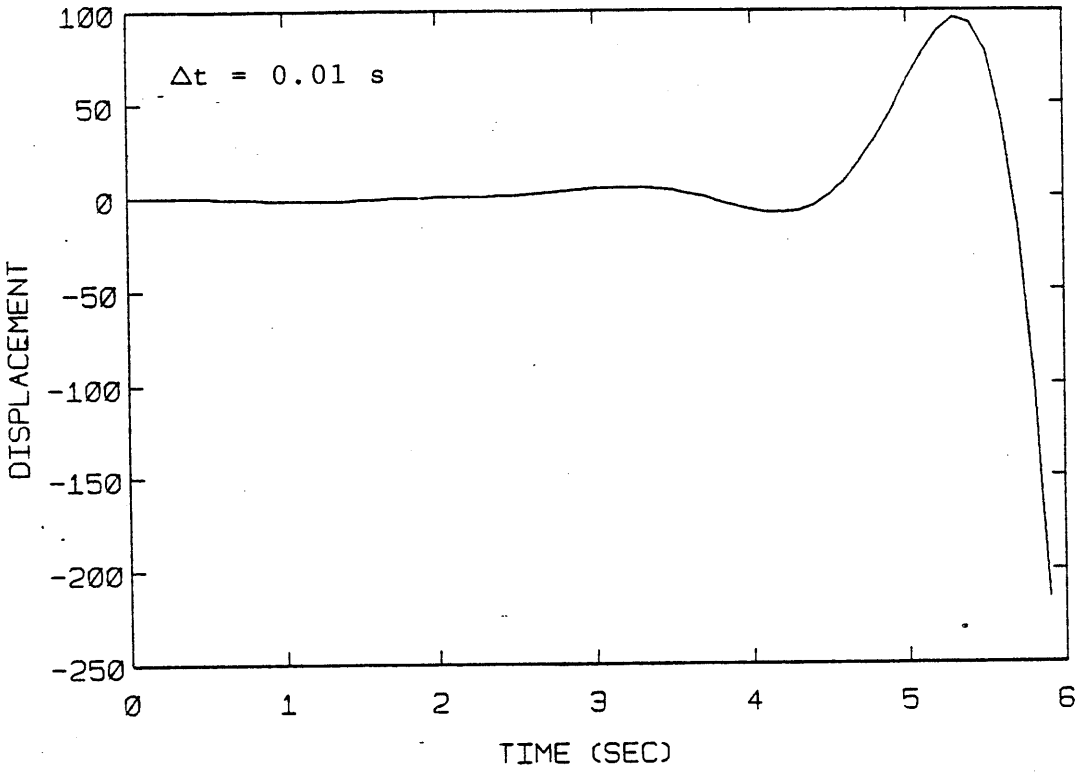

Fig. 6.7 Elastic-Plastic Response Using a Frequency Domain Analysis, 10 Iterations (Fy = 2 ksi)

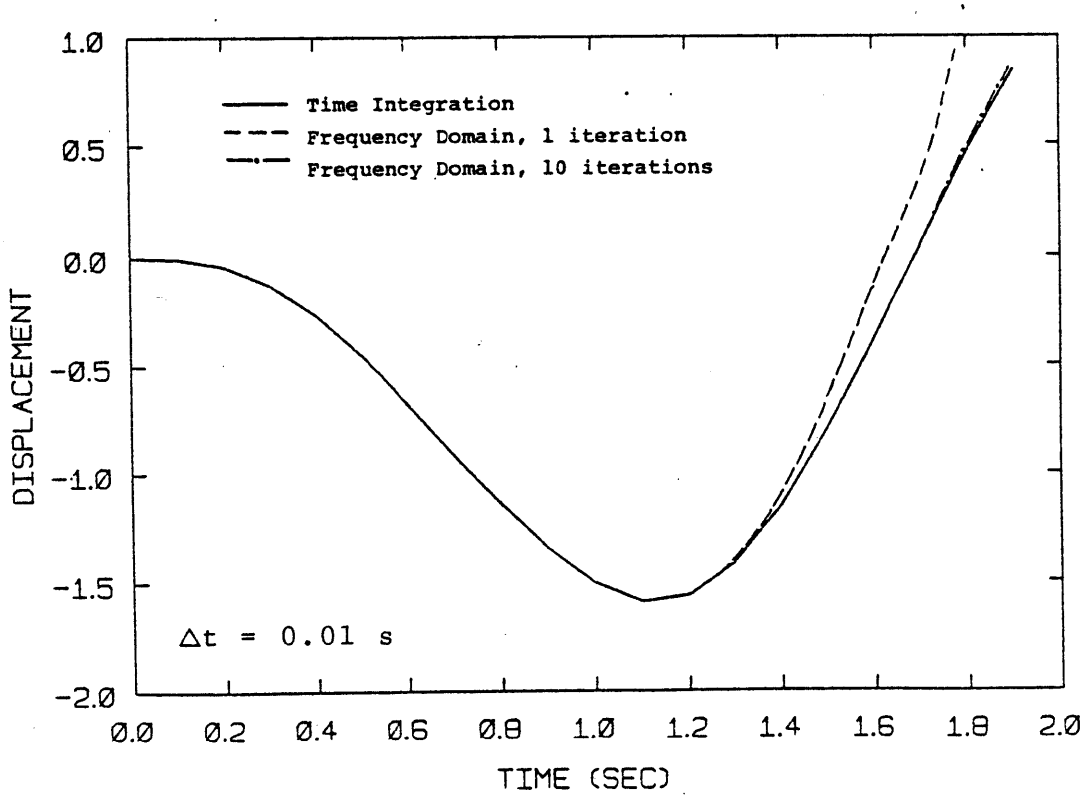

Fig. 6.8 Elastic-Plastic Response with Pseudo-force Correction to T = 2.0s.

the free vibration part is neglected (after time 2 seconds).

This apparent anomaly where the response in the frequency domain converges only when the free vibration part is neglected can be explained by observing Figs. 6.9, 6.10, and 6.11. . Figure 6.9 depicts the pseudo-force history during the first iteration. Notice how closely the pseudo-force history resembles the linear elastic response shown in Fig. 6.3. The plateaus in Fig. 6.9 correspond to elastic stress reversals from plastic yielding and the sloped portions correspond to plastic yielding regions. The flat portion from 0 to 0.5 seconds corresponds to the initial linear elastic response (refer to Fig. 6.12 for an explanation of how the pseudo-force history is obtained). Figures 6.10 and 6.11 show the pseudo-force histories for successive iterations. All three figures depict periodic pseudo-force histories with periods of vibration almost identical to that of the structure. In other words, the pseudo-force histories, which are imposing corrections upon the linear response to obtain the nonlinear response, are exciting the structure at periods close to its fundamental period during the free vibration stage, and consequently cause the structure to approach resonance, yielding displacement corrections that are extremely large. The hybrid frequency-time domain analysis is therefore limited to the excited portion of the response and cannot reproduce the free vibration response for an elastic-perfectly plastic system whenever the free vibration stage consists of

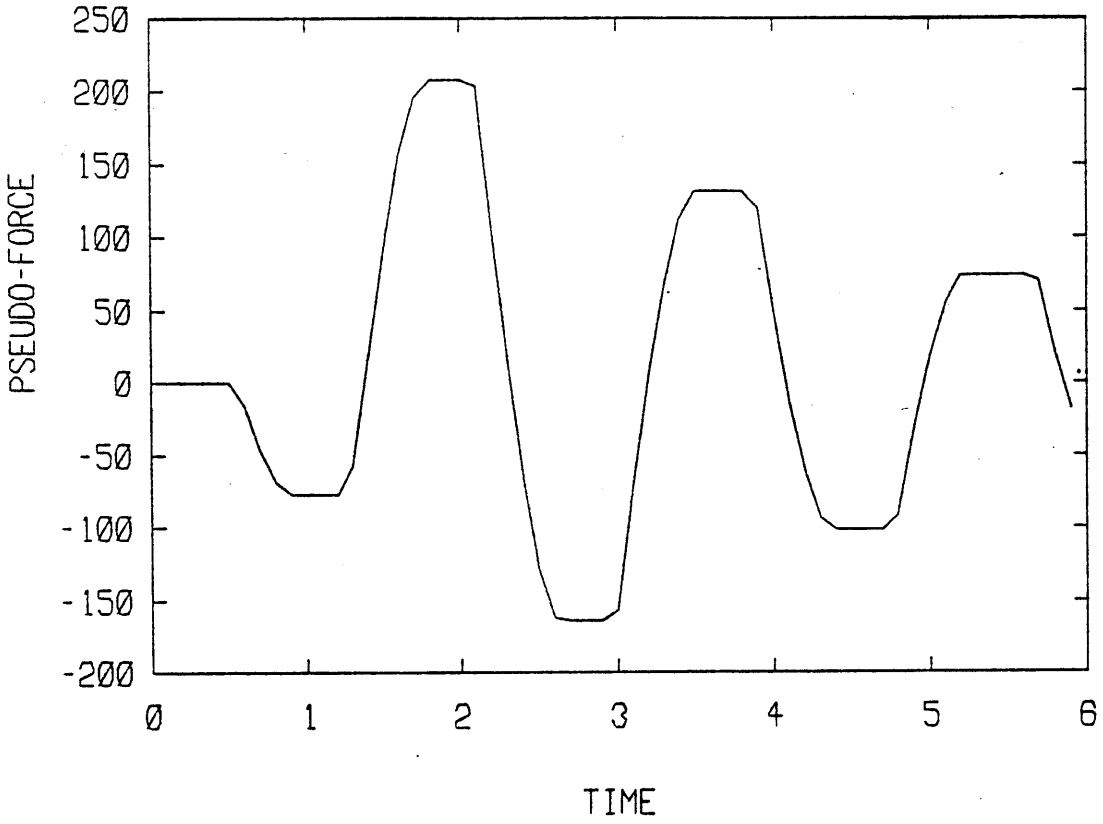

Fig. 6.9 Pseudo Force History, 1 iteration

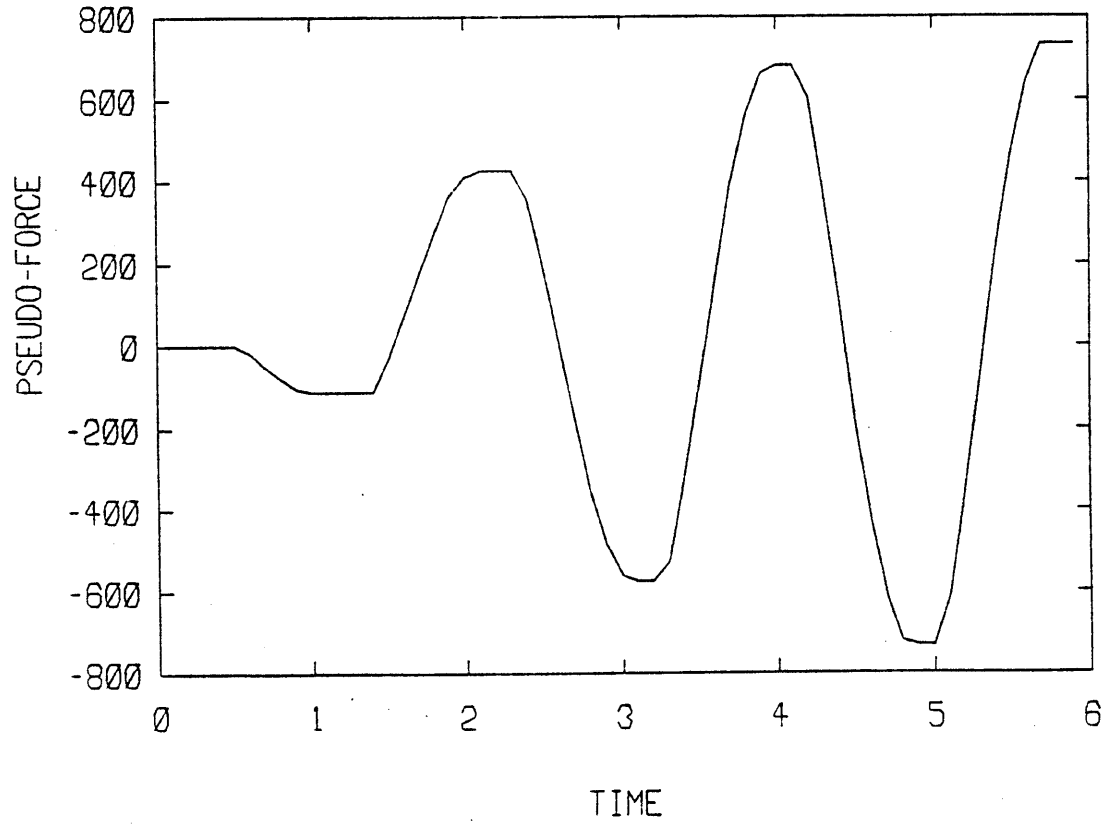

Fig. 6.10 Pseudo Force History, 2 iterations

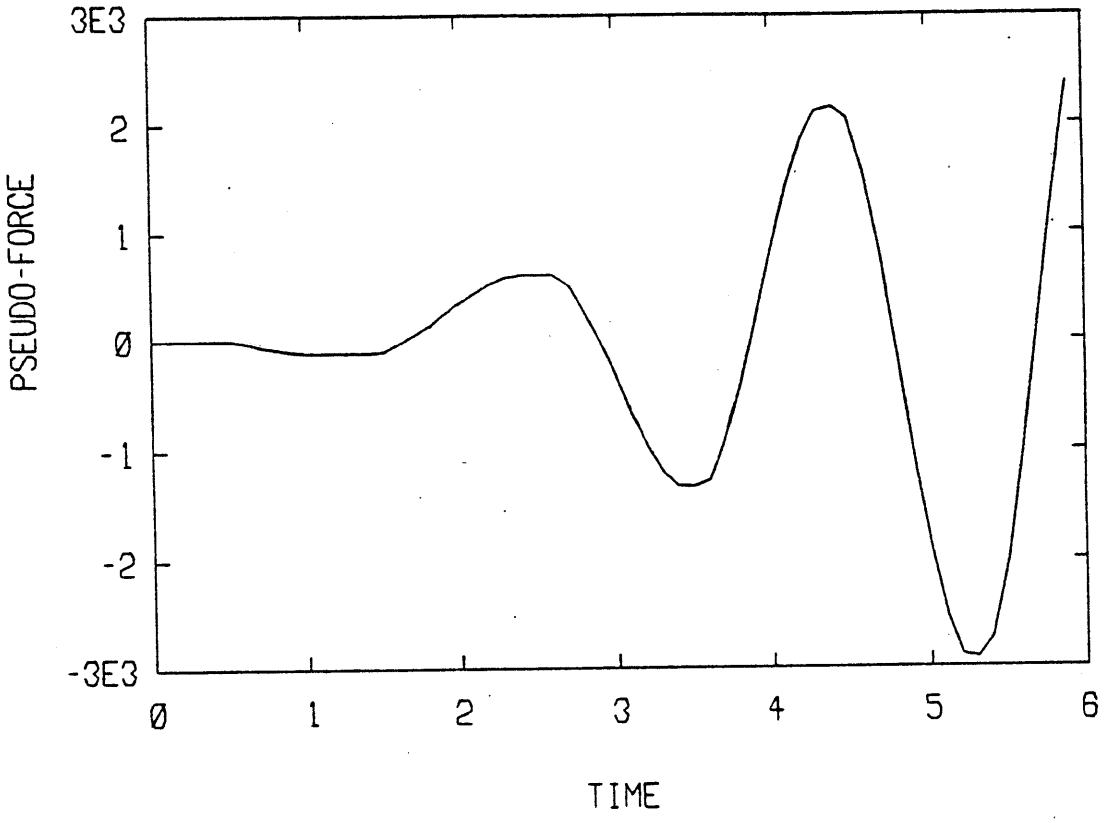

Fig. 6.11 Pseudo Force History, 3 iterations

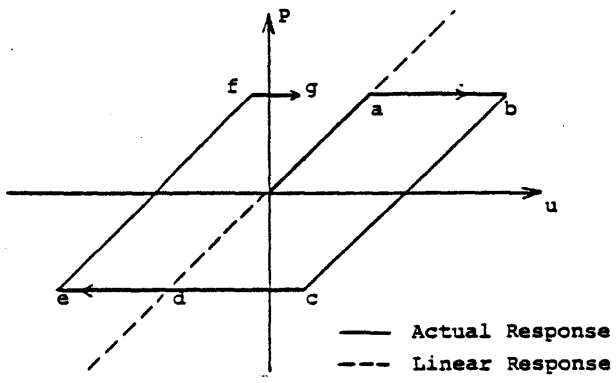

a. Force-Displacement Diagram

P_s = Pseudo-force = linear load - nonlinear load

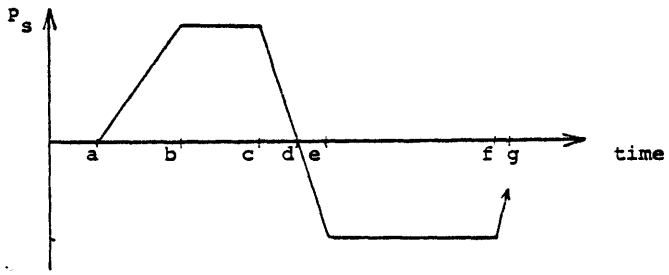

b. Pseudo-force History

Fig. 6.12 Pseudo-force History for an Elastic-Perfectly Plastic Material Model

inelastic deformations.

The next study considered the same structure with a yield stress of 36 ksi subjected to 5 seconds of the Bucarest earthquake (peak acceleration of 0.25 g) beginning at time 6 seconds and ending at 11 seconds, with a time increment of 0.01 seconds. A string of approximately 7700 zeroes was added to the end of the excitation to ensure that all transient effects were eliminated and that a sufficient number of harmonics represented the loading and response.

Figure 6.13 shows the displacement response for the direct time integration and HFT analyses. After eleven iterations using 2^{13} points in the frequency domain, the residual of the nonlinear displacement ($\underline{y}_2$) is 4.24×10^{-4} inches such that no differences can be visually observed between the two figures. The HFT analysis required 90 seconds of CPU time while the time domain analysis using equilibrium iteration at each time step required only 5 seconds.

It is quite evident that the hybrid frequency-time domain technique provides accurate results during the loading stage and even during the free vibration stage after the loading terminates if the free vibrations oscillate within the elastic regime, which is usually the case. However, the expended CPU time is much larger, and consequently the study was extended to optimize the solution scheme. Further analyses determined the minimum number of

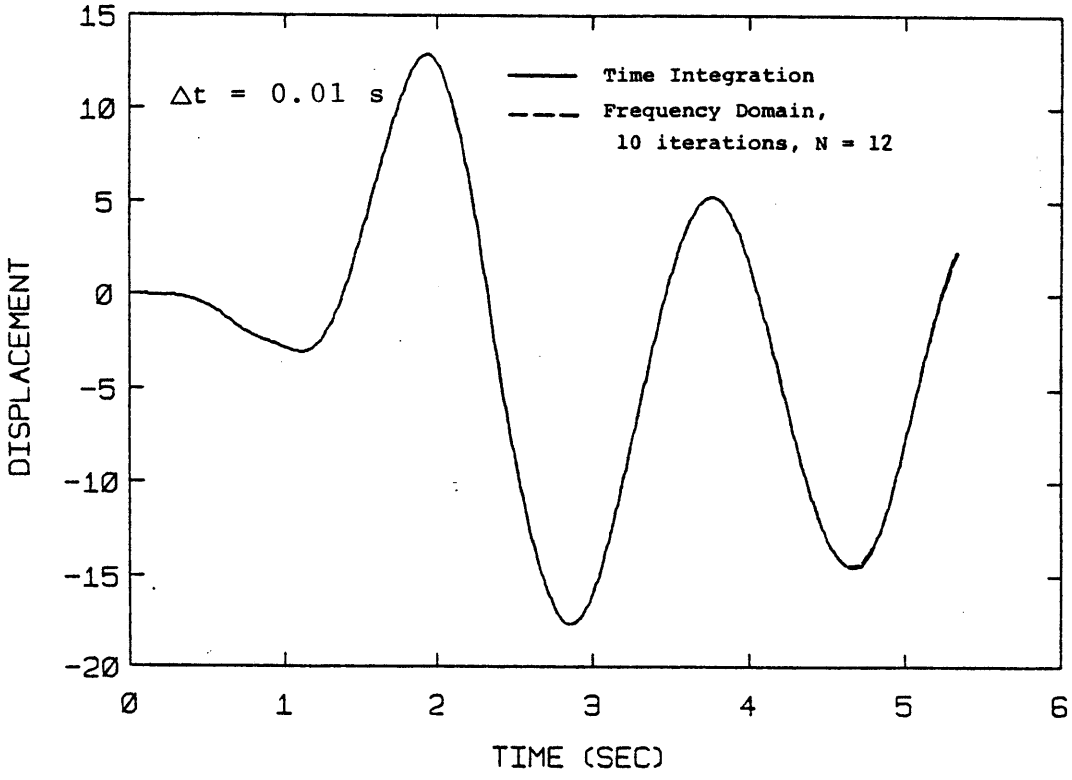

Fig. 6.13 Elastic-Plastic Response to the Bucarest Earthquake (Fy = 36 ksi)

trailing zeroes required in the loading and the number of iterations at which the responses were sufficiently similar. The results are given in Table 6.1. As can be seen from the tabulated results, a minimum of 2^{12} points are required. A residual displacement of 157" after six iterations produces the best results at minimal cost (CPU time of 26 seconds). The corresponding displacement plot is shown in Fig. 6.14. Notice that the displacement response is practically identical to that given in Fig. 6.13, except for discrepancies toward the end of the analysis. Figure 6.15 depicts the displacement response for a residual of 342 inches after 5 iterations. Although the maximum response corresponding to the last time step is extremely large, the response at time 2.9 seconds is approximately 18" which compares well with the exact response. This large error in response toward the end of the history characterizes the forward progressing corrective behavior of the HFT solution scheme.

As a final study of this section, the HFT solution scheme was applied to a SDOF system composed of the tubular brace material model and subjected to the same Bucarest earthquake history. The time integration results are shown in Fig. 6.16. Using 2^{12} points in the HFT scheme the response after three iterations, shown in Fig. 6.17, diverges. With 2^{13} points the response after 12 and 15 iterations are shown in Figs. 6.18 and 6.19, respectively. Response values and computation times are listed in Table

Solution Scheme	No. of Points	Iterations	Residual	Maximum Displacement (inches)	CPU Time (sec)
Time Integration (nonlinear)	----	----	----	17.64	5
HFT	8192	11	.0004	17.64	90
	8192	6	163	17.64	52
	4096	11	1	17.64	42
	4096	8	10	17.72	33
	4096	7	20	17.74	29
	4096	6	157	17.53	26
	4096	5	342	54.97*	23
	2048	11	4132	34.73	22

time increment = 0.01 seconds for all analyses

* occurred during last time step

Table 6.1 Computation Times for Elastic-Perfectly Plastic SDOF Model

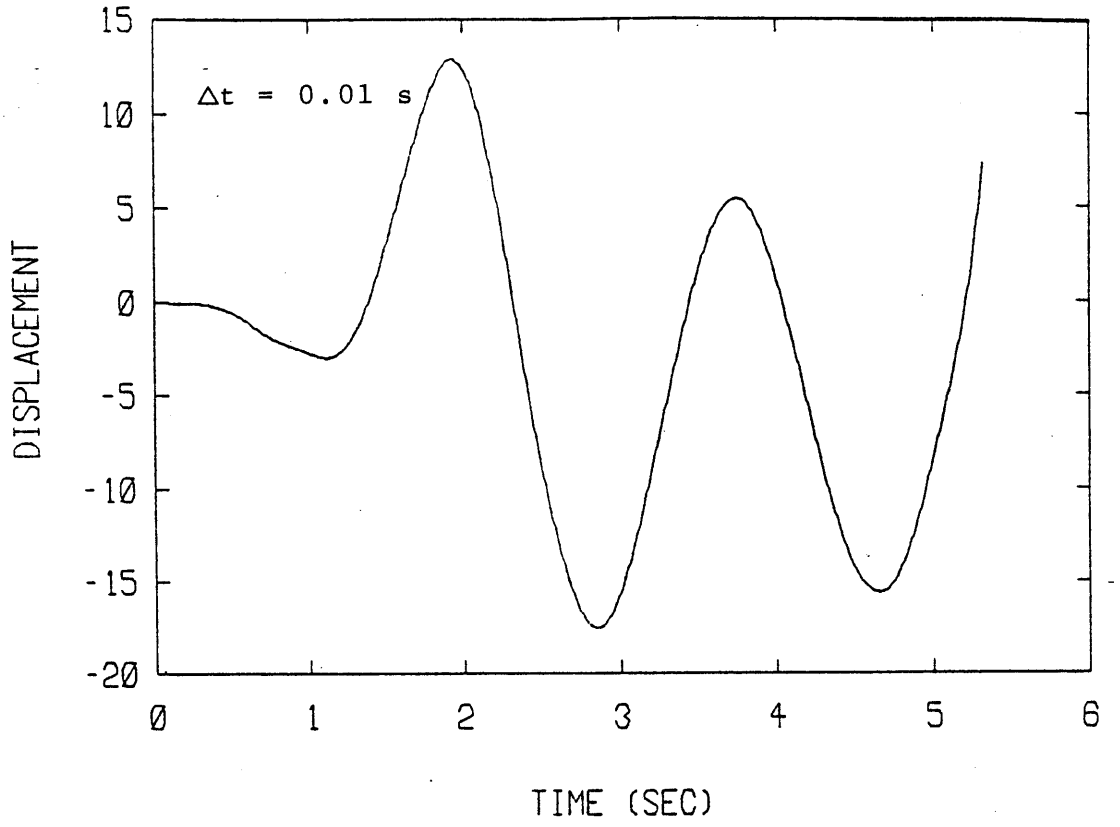

Fig. 6.14 **Elastic-Plastic Response to the Bucarest Earthquake, 6 iterations, N = 12.**

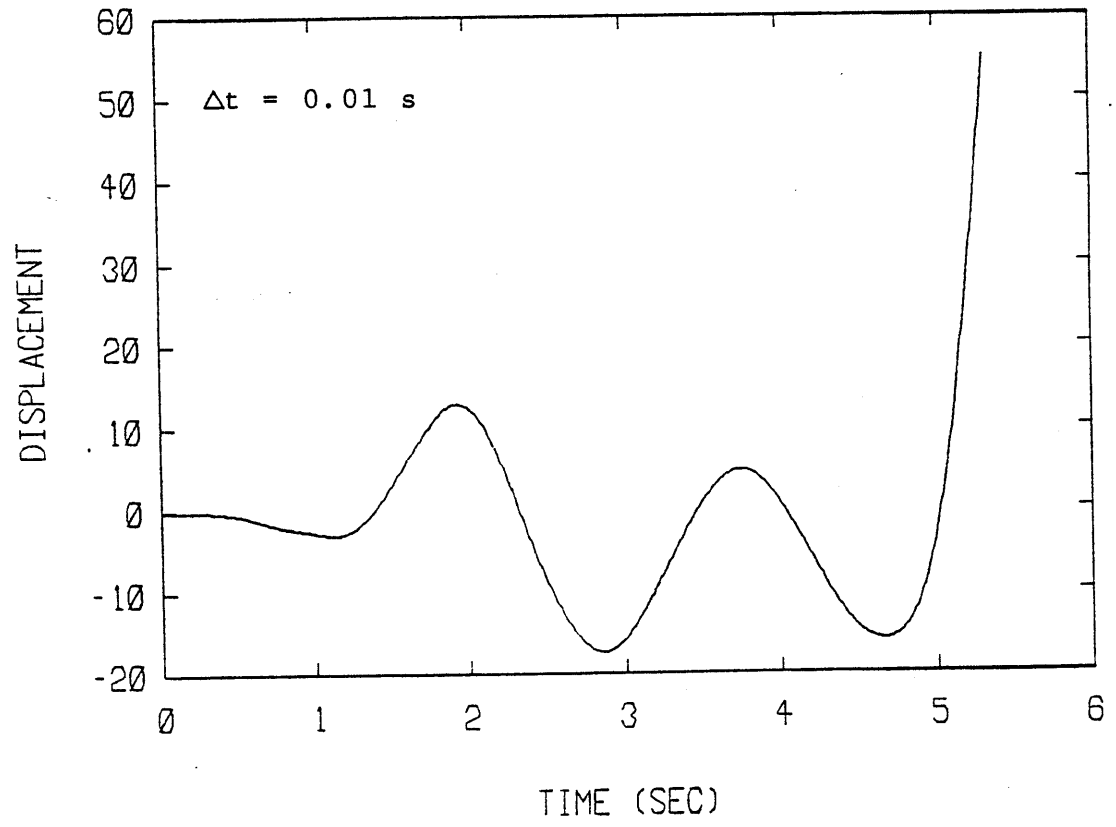

Fig. 6.15 **Elastic-Plastic Response to the Bucarest Earthquake, 5 iterations, N = 12.**

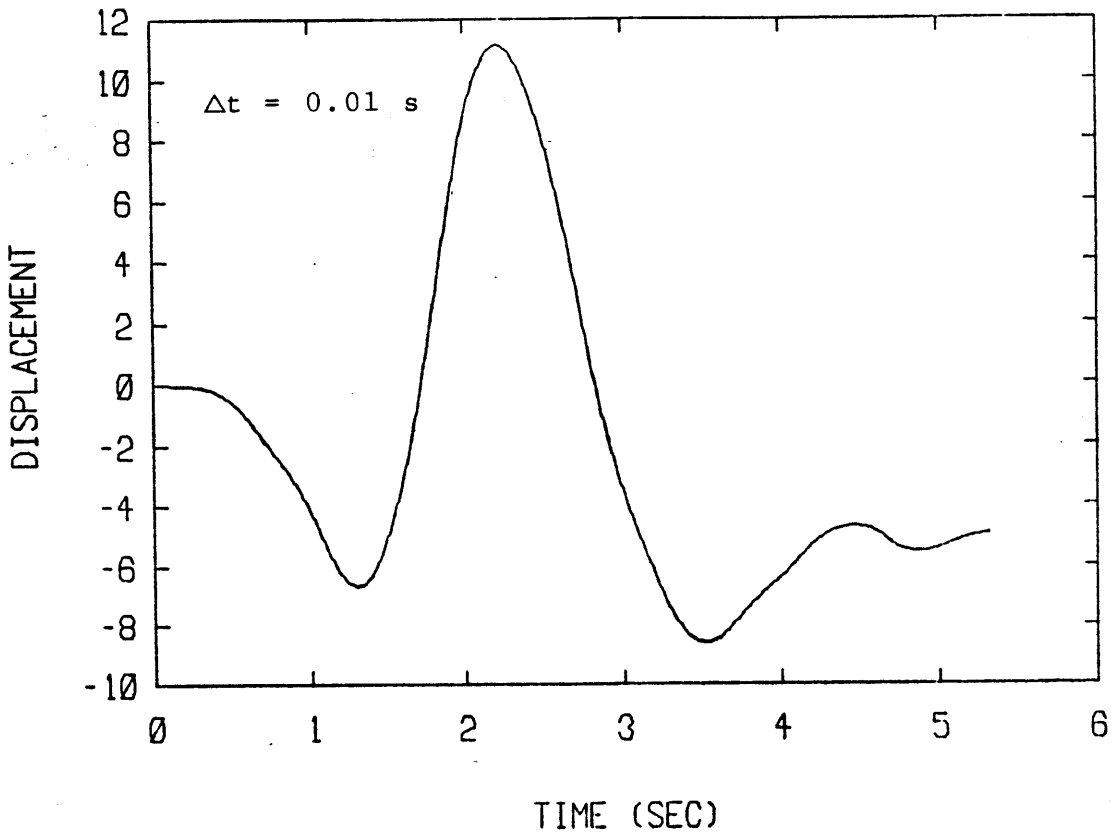

Fig. 6.16 Tubular Member Response to the Bucarest Earthquake, Time Integration

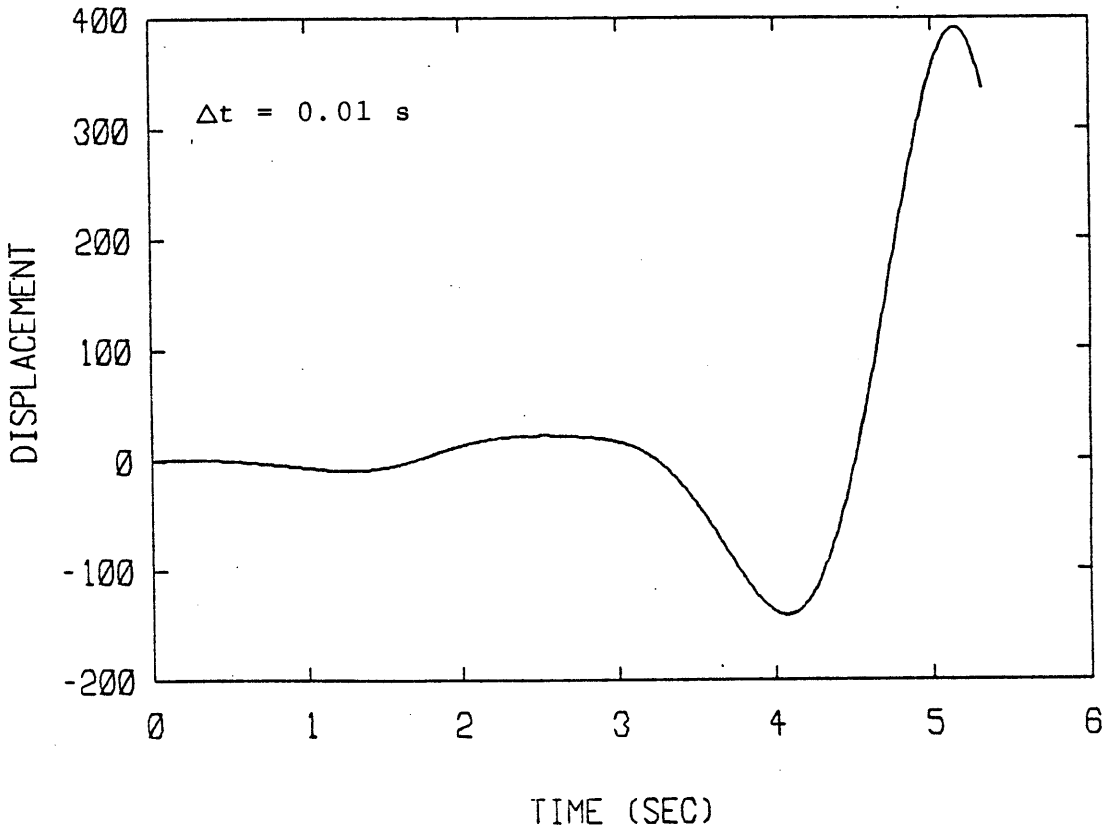

Fig. 6.17 Tubular Member Response to the Bucarest Earthquake, 3 Iterations, N = 12

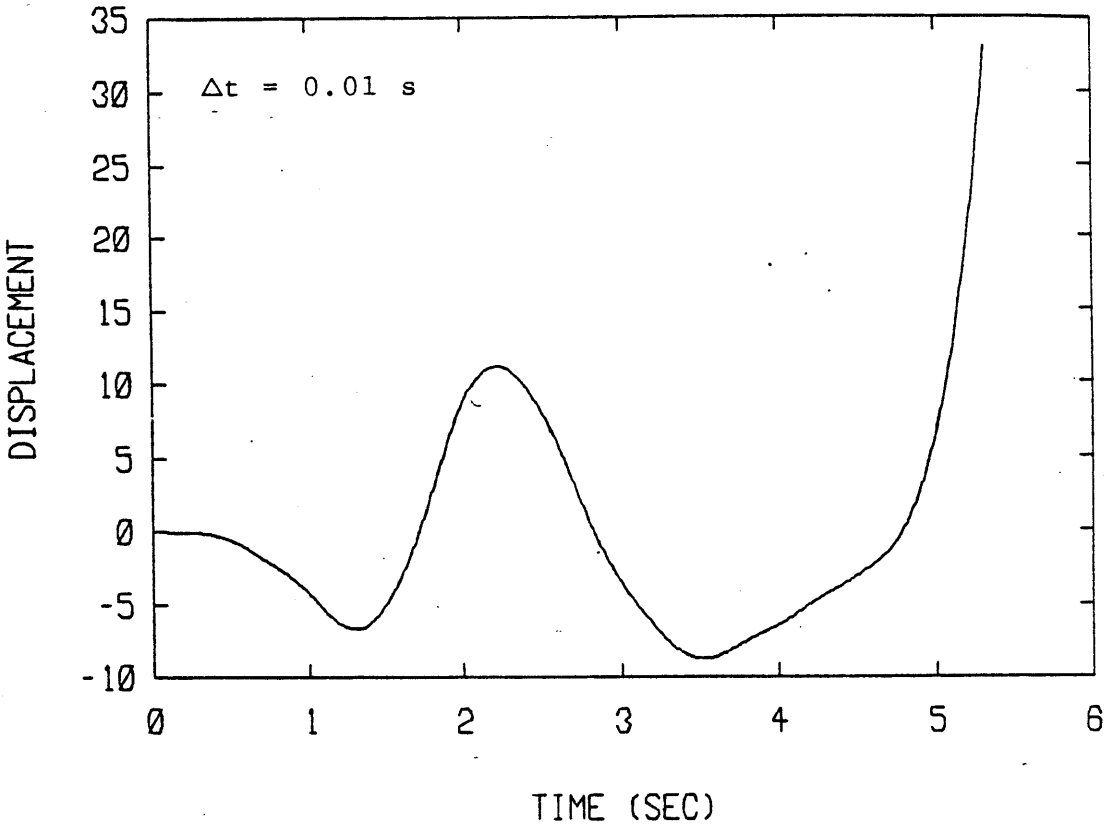

Fig. 6.18 Tubular Member Response to the Bucarest Earthquake 12 Iterations, N = 13

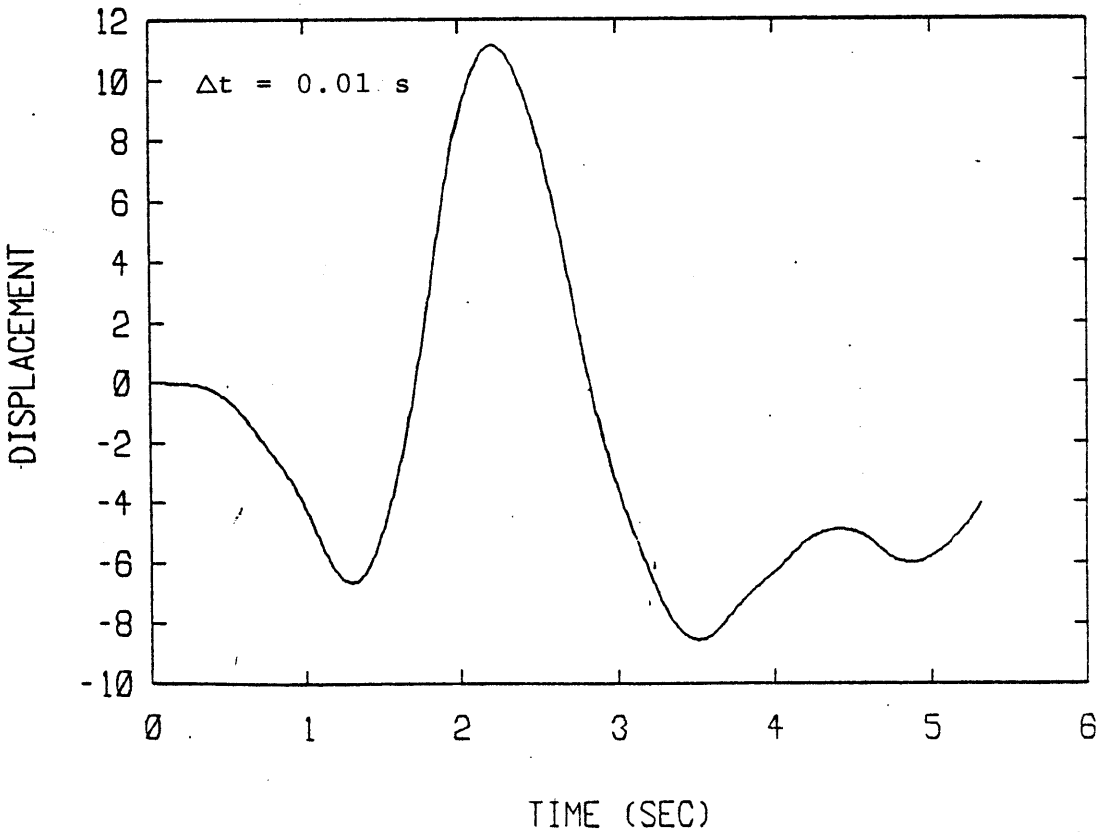

Fig. 6.19 Tubular Member Response to the Bucarest Earthquake, 15 Iterations, N = 13

6.2.

These studies demonstrate that the hybrid frequency-time domain solution scheme is capable of reproducing the response for SDOF systems subjected to complex load histories and represented by complicated material models. The solution scheme as presented, however, is extremely inefficient, and the succeeding discussion considers possible means of improving the efficiency.

The two cases where the excitation consisted of the Bucarest earthquake readily illustrate the computation cost contributed by the appended zeroes. Although only 500 points are necessary to model the 5 second load history, a solution in the frequency domain required an additional 3596 and 7692 zeroes for the elastic-perfectly plastic and tubular brace models, respectively. Tables 6.1 and 6.2 indicate that the computation time doubles for each additional factor of two. As a consequence of this inefficiency stemming from the appended zeroes, a zero minimization technique was developed, as described in Chapter 5.

Applying the zero minimization scheme to the elastic-perfectly plastic SDOF system subjected to the Bucarest earthquake yielded the results displayed in Table 6.3. Notice in general that the number of required points has been reduced by a factor of 4 (optimum case has 1024 points - 500 for the load history and 524 zeroes). The

Solution Scheme	No. of Points	Iterations	Residual	Maximum Displacement (inches)	CPU Time (sec)
Time Integration (nonlinear)	----	----	----	11.2	6
HFT	8192	15	16	11.2	115
	8192	12	206	33.0*	95
	4096	30	1.8×10^{5}	2.3×10^{4}	105

time increment = 0.01 seconds for all analyses

* occurred during last time step

Table 6.2 Computation Times for Tubular Brace SDOF Model

Solution Scheme	No. of Points	Iterations	Residual	Maximum Displacement (inches)	CPU Time (sec)
Time Integration (nonlinear)	----	----	----	20.75	5
Time Integration (linear)	----	----	----	17.64	6
HFT	512	10	5795	234	11
	1024	6	202	18.53	10
	1024	8	80	18.86	13
	1024	10	100	17.40	15
	2048	6	41	17.62	16
	2048	7	15	17.50	17

time increment = 0.01 seconds for all analyses

Table 6.3 Computation Times for Elastic-Perfectly Plastic SDOF Model Using the Zero Minimization Technique

response after 10 iterations using 1024 points is shown in Fig. 6.20.

A simple relaxation scheme was also investigated as a means of accelerating the convergence. Details of the procedure were given in Chapter 5. Results of the study indicated that the system was highly sensitive to any form of over-relaxation or under-relaxation, usually producing a slower convergence rate, if not divergence. Table 6.4 shows typical convergence characteristics for the elastic-perfectly plastic SDOF system subjected to the Bucarest earthquake. Tabulated results are for acceleration coefficients of 1.0, 1.10, 1.01, and 0.99.

This section demonstrated the feasibility of the HFT scheme applied to SDOF systems. Accurate results are derivable and although the efficiency may be less than that of direct time integration analyses, even when using the zero minimization scheme, it is noted that a mode superposition approach can not be applied to SDOF systems and that the use of a possibly smaller time increment in the HFT analysis was not exploited.

6.2 SDOF SOIL AMPLIFICATION PROBLEM

This study applied the HFT scheme to a soil amplification problem analyzed by Constantopoulos in 1973 (19). The problem exhibited a fairly complex response with significant nonlinearities and, moreover, had no viscous

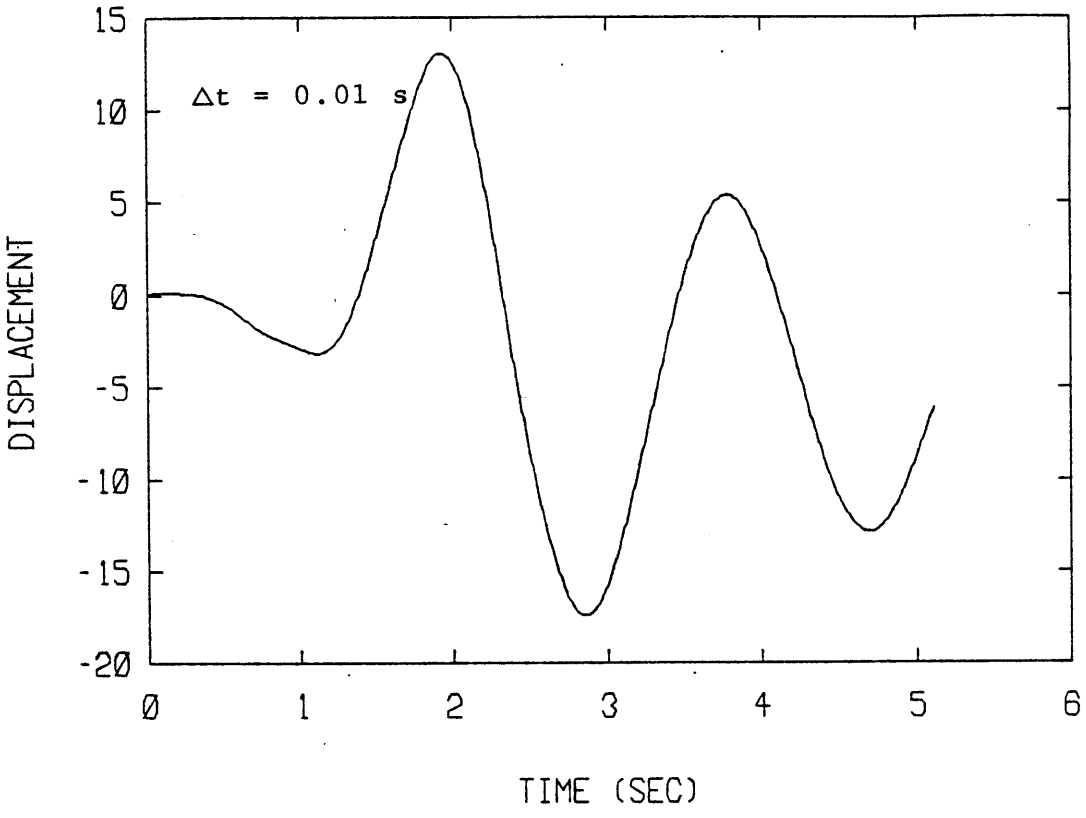

Fig. 6.20 Elastic-Plastic Response to the Bucarest Earthquake, 10 Iterations, N = 10

Acceleration Coefficient Alpha	Iteration	Residual
1.00	1	497
	2	758
	3	777
	4	627
	5	460
	6	202
	7	115
	8	79
	9	138
	10	100
1.10	1	399
	2	1360
	3	2868
	4	5421
	5	8101
	6	13261
	7	23395
	8	37698
	9	70330
	10	142800
1.01	1	640
	2	1039
	3	985
	4	952
	5	986
	6	1223
	7	1466
	8	1528
	9	2022
	10	2256
0.99	1	382
	2	706
	3	993
	4	821
	5	852
	6	742
	7	500
	8	621
	9	457
	10	290

Table 6.4 Residual Displacements When Using Relaxation Schemes

damping. These two aspects posed convergence problems for the basic HFT scheme used in section 6.1.

The soil amplification problem in general consists of determining the surface response to a seismic excitation applied at the base of a soil deposit. In this example the soil was represented by a SDOF system with a period of 0.25 s. A Ramberg-Osgood material model (u_y =0.001, f_y=1.264, α=0.05, r=2) characterized the soil behavior. The relationship governing the Ramberg-Osgood model is

$$\frac{u - u_i}{cu_y} = \frac{f - f_i}{cf_y} + \alpha\left[\frac{f - f_i}{cf_y}\right]^r \qquad (6.1)$$

where the u's correspond to displacements and f's to forces, producing the load-deflection curve shown in Fig. 6.21. The excitation was the first ten seconds of the N69W component of the Taft record of the 1952 Kern county earthquake, with peak acceleration scaled to 0.01 g, shown in Fig. 6.22. No viscous damping was specified. Relevant structural parameters are provided in Fig. 6.23.

The extension of the frequency domain analysis to problems with no damping is theoretically inconsistent since an undamped problem exhibits a periodic response which does not decay with time. Assuming that all significant loading frequencies do not correspond to the natural structural frequencies or that the discretized frequency spectrum avoids these singularities, a resonance effect will not develop, and it is possible to evaluate numerically the

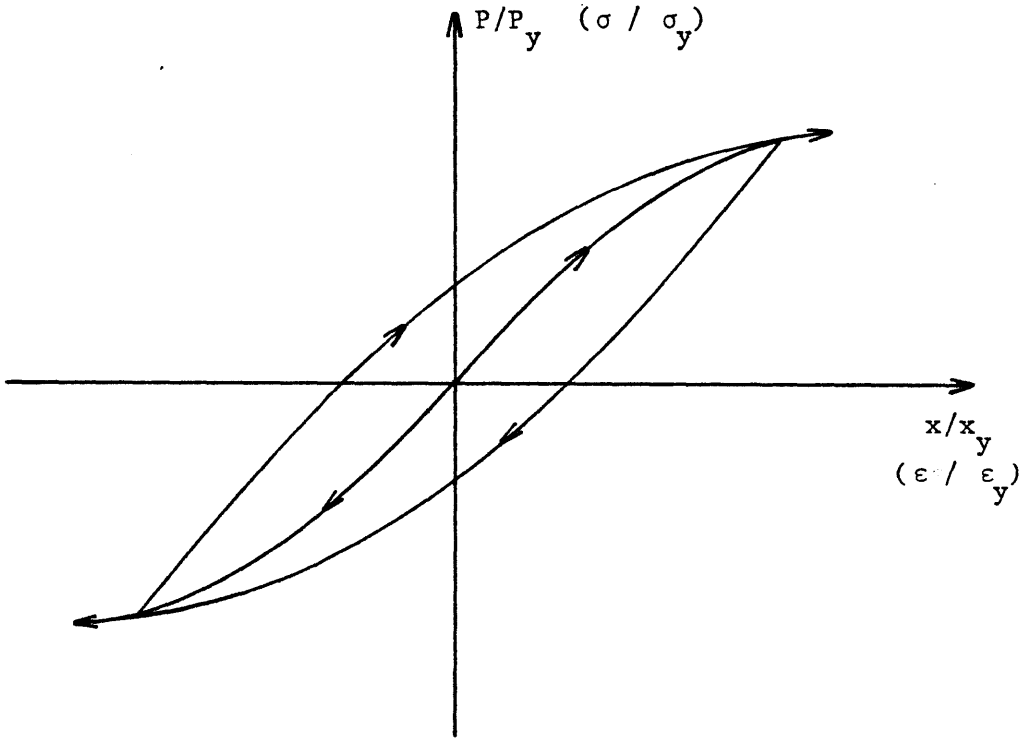

Fig. 6.21 Ramberg-Osgood Material Model

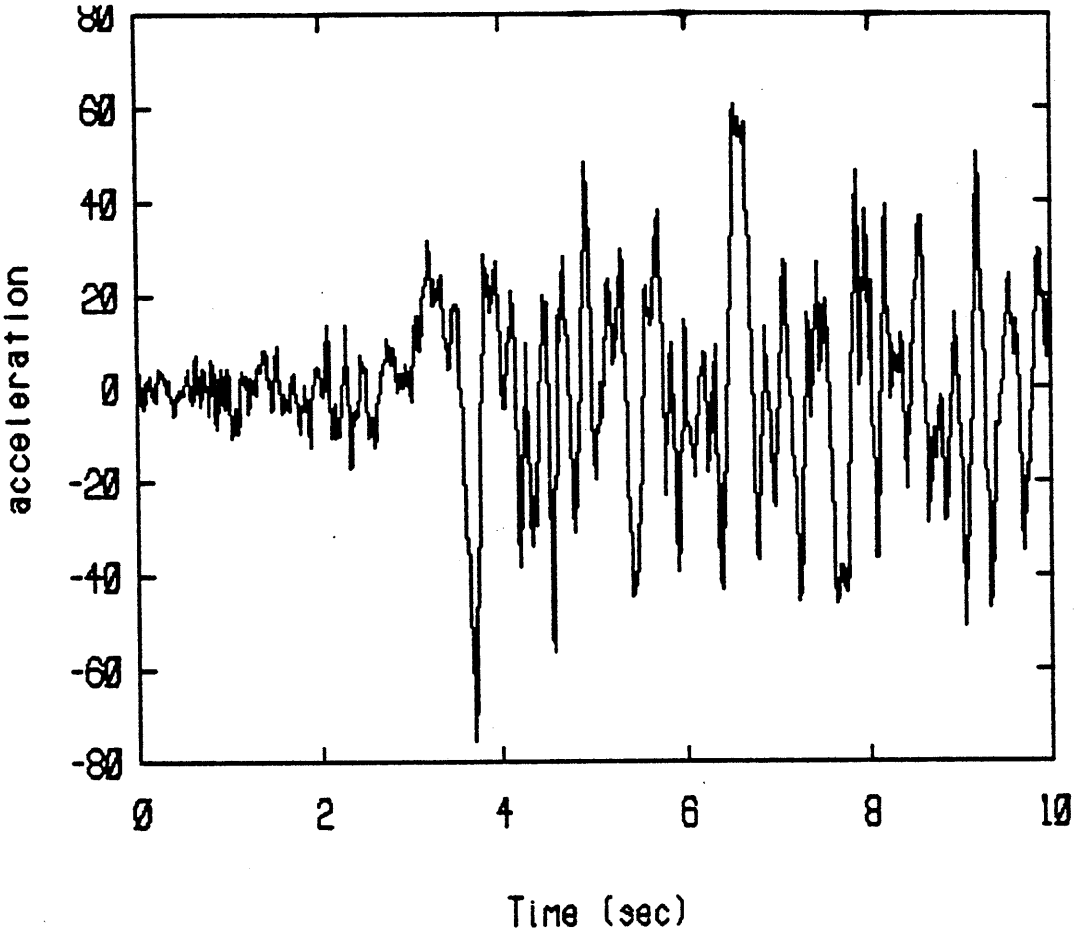

Fig. 6.22 Taft Acceleration History

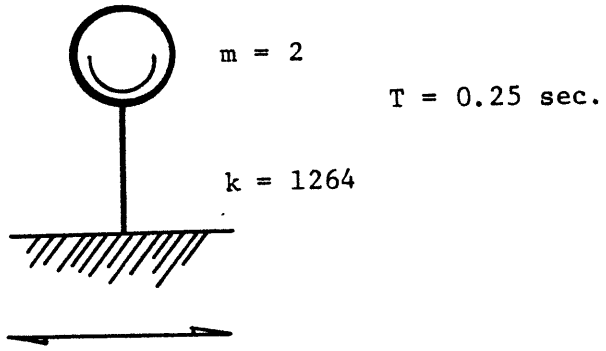

Fig. 6.23 SDOF Soil Model

response with the standard frequency domain approach. In a nonlinear analysis, however, the natural frequencies will shift, and a previously stable problem will become intractable if the pseudo-force histories begin to contribute loads at the natural frequencies. This resonance problem is particularly acute for seismic analyses where the energy spectrum may contain a significant range of frequencies.

As a result, preliminary runs using the solution scheme in section 6.1 produced a diverging solution. Although this problem contains hysteretic damping provided by the soil model, initial iterations using the same approach as in section 6.1 progress without any damping. The hysteretic damping appears during the latter cycles of the solution process in the form of pseudo-force load vectors. As a consequence, artificial viscous damping was employed in the subsequent soil amplification studies to act as a buffer to extremes in the converging response. In essence, the artificial damping approximates the actual hysteretic damping effect upon the response.

Furthermore, preliminary studies indicated that the linear response (no viscous damping) differed significantly from the actual nonlinear response. The formulation of the governing equations of motion was consequently modified such that rather than evaluating the linear response to the earthquake and then iterating with the resulting

pseudo-forces to obtain a correction displacement term which when added to the linear response gave the actual response, all iterations included the earthquake loading, and the actual response was evaluated directly (total displacement formulation).

In the time integration analyses time increments of 0.01 s and 0.005 s were used. The results for $\Delta t=0.01$ s differed slightly from those for $\Delta t=0.005$ s, and it was concluded that $\Delta t=0.01$ s was adequate. Notice that since the soil model contains hysteretic damping, no numerical artificial damping should be imposed on the response. Consequently, the Newmark method with $\alpha=0.25$ and $\delta=0.50$ (no artificial damping) was used in conjunction with a Newton equilibrium iteration scheme. In addition a displacement tolerance of 10^{-8} and iteration limit of 15 was specified in the equilibrium iteration.

For the HFT analysis a time increment of 0.01 seconds was selected. The peaks of the response could not be captured for $\Delta t=0.02$ s and no further information would be obtained for $\Delta t<0.01$s since the Nyquist frequency corresponds to 50 Hz for the given earthquake history. Based on preliminary studies, an artificial viscous damping ratio of 0.50 was selected since the response would eventually diverge during the iterative process for an artificial damping ratio less than 0.25.

Figure 6.24 depicts the results using a time integration analysis, and Figs. 6.25, 6.26, and 6.27 show the response after 20, 60, and 75 iterations. The response converges between 60 and 75 iterations. Comparing the efficiencies of the methods, 47 s CPU time were required for the direct time integration analyses while 172 s CPU time were required for 75 iterations using the HFT analysis. It should be mentioned that artificial damping was included not simply because no viscous damping was specified, but also because the problem was highly nonlinear, causing convergence difficulties for the HFT analysis. Even with a specified ordinary viscous damping ratio of 5%, as in the previous SDOF study, the solution would diverge by the 10th iterative cycle.

The use of artificial damping and the total displacement formulation were demonstrated in this study. Both schemes stabilized the solution process by producing a better initial estimate of the nonlinear response and preventing excessive inaccuracies in the pseudo-force history during the iterative process. The HFT scheme once again proved less efficient than a direct time integration analysis.

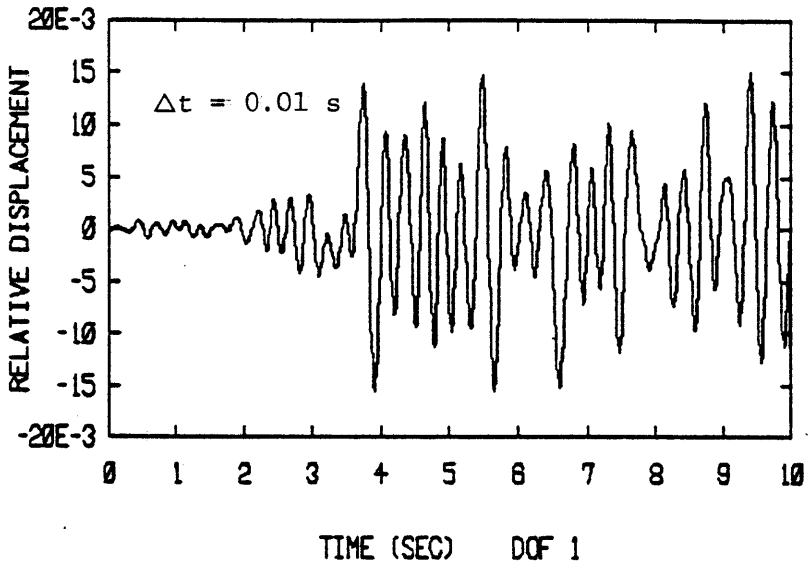

Fig. 6.24 Soil Amplification Results Using a Direct Time Integration Analysis

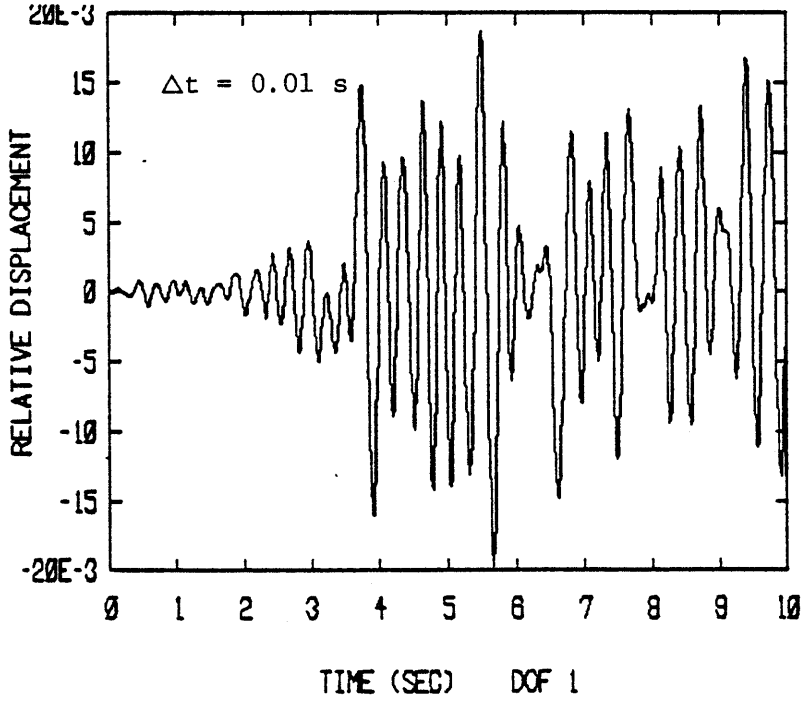

Fig. 6.25 Soil Amplification Results Using an HFT Analysis (20 iterations, artificial viscous damping ratio of 0.50)

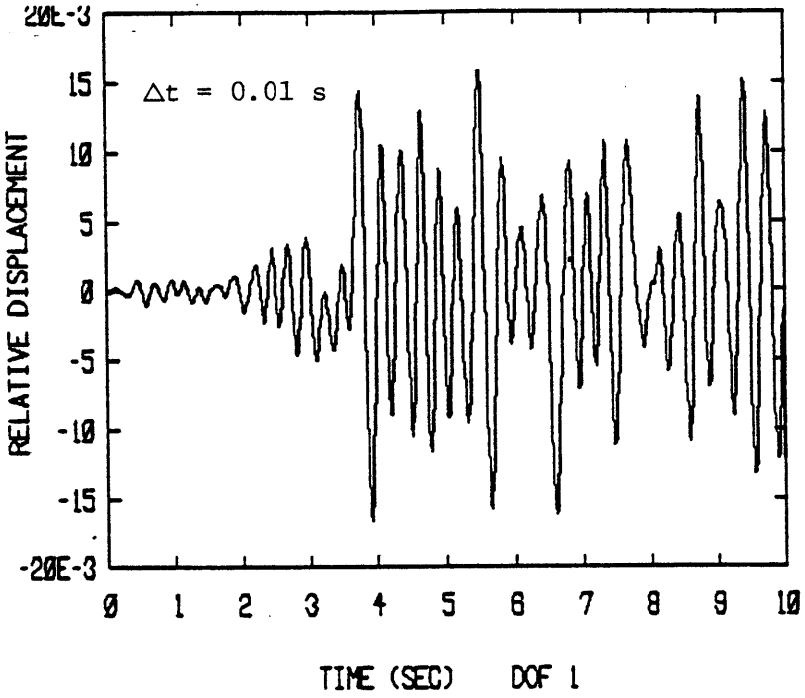

Fig. 6.26 Soil Amplification Results Using an HFT Analysis (60 iterations)

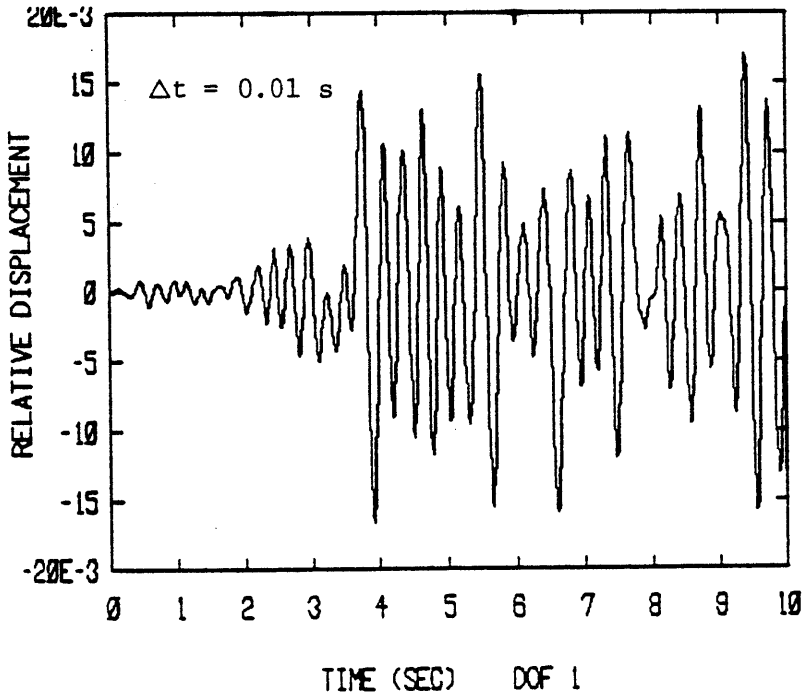

Fig. 6.27 Soil Amplification Results Using an HFT Analysis (75 iterations)

6.3 TEN DOF SHEAR BEAM STRUCTURE

The response of a ten degree of freedom shear beam type structure described by elastic-perfectly plastic material models was examined in this study. The fundamental period was 3.65 seconds and the 10th period, 0.28 seconds. A seismic excitation represented by a single cycle sine wave of duration two seconds was used as the loading. To induce a localized nonlinear behavior and participation of higher modes in the structure, a yield stress of 100 ksi was specified for each member, except at level four where the yield stress was 1 ksi. Rayleigh damping was employed by specifying a damping ratio of 5% for the 1st and 4th frequencies. Relevant structural parameters are given in Fig. 6.28.

The Newmark integration method with α=0.25 and δ=0.50 and the Newton equilibrium iteration scheme were used for the direct time integration case. The governing equations of motion were solved in an incremental form. A time increment of 0.02 seconds was specified.

In the hybrid frequency-time domain analysis a time increment of 0.1 seconds was specified. 64 points were used. Notice that in the optimum case we would use only 32 points. However, for this particular problem, 32 points in the frequency domain were insufficient to adequately resolve the shape of the displacement response and pseudo-force histories. No artificial damping was employed, and the dual

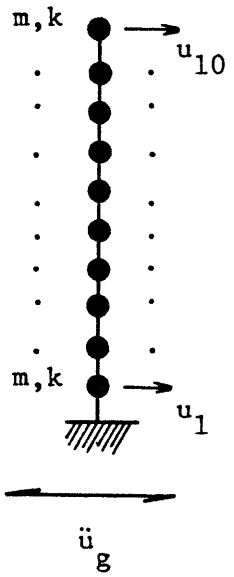

$k = 133, \quad m = 1$

$\xi = 0.05 \quad @ \quad \omega_1 = 1.72$ and $\omega_4 = 11.52$ rad/sec

$T_1 = 3.65$ sec.

$T_{10} = 0.28$ sec.

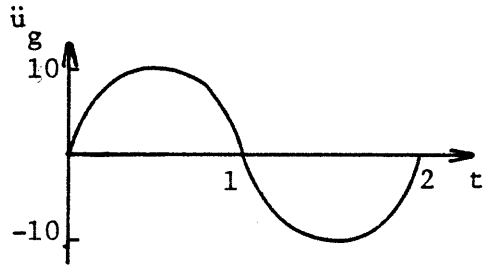

Elastic-perfectly plastic material model

$$F_y = \begin{cases} 1, & \text{at level 4} \\ 100, & \text{elsewhere} \end{cases}$$

Fig. 6.28 Ten Degree of Freedom Shear Beam Study

displacement formulation was used.

The problem of nonlinear mode updating in the frequency domain and the consequent problem of handling the off-diagonal terms in the new generalized structural matrices were first addressed in this study. Linear and nonlinear mode shapes were used simultaneously, and hence all off-diagonal terms were managed by transferring them to the RHS of the equations of motion. Mode updating was implemented with the first scheme outlined in section 5.2.2.6.

An HFT analysis with all ten linear modes was conducted first to determine the convergence behavior of this particular problem. As can be seen from the response histories of dof's 1 and 10, shown in Figs. 6.29 and 6.30, the solution converges within 20 iterations. The response histories after the first iteration correspond to the linear response (dual displacement formulation). Notice that the 10th degree of freedom converges quickly because its nonlinear response resembles its linear response. Figure 6.31 depicts the corresponding deflected shapes of the converged solution from time t=1.0 s to t=1.5 s. From Fig. 6.31 it is apparent that the nonlinearities are concentrated in element 4 (from the base), resulting in a fairly simple pseudo-force distribution existing only at nodes 3 and 4. The first proposed mode updating scheme, consequently, is readily adapted to this problem.

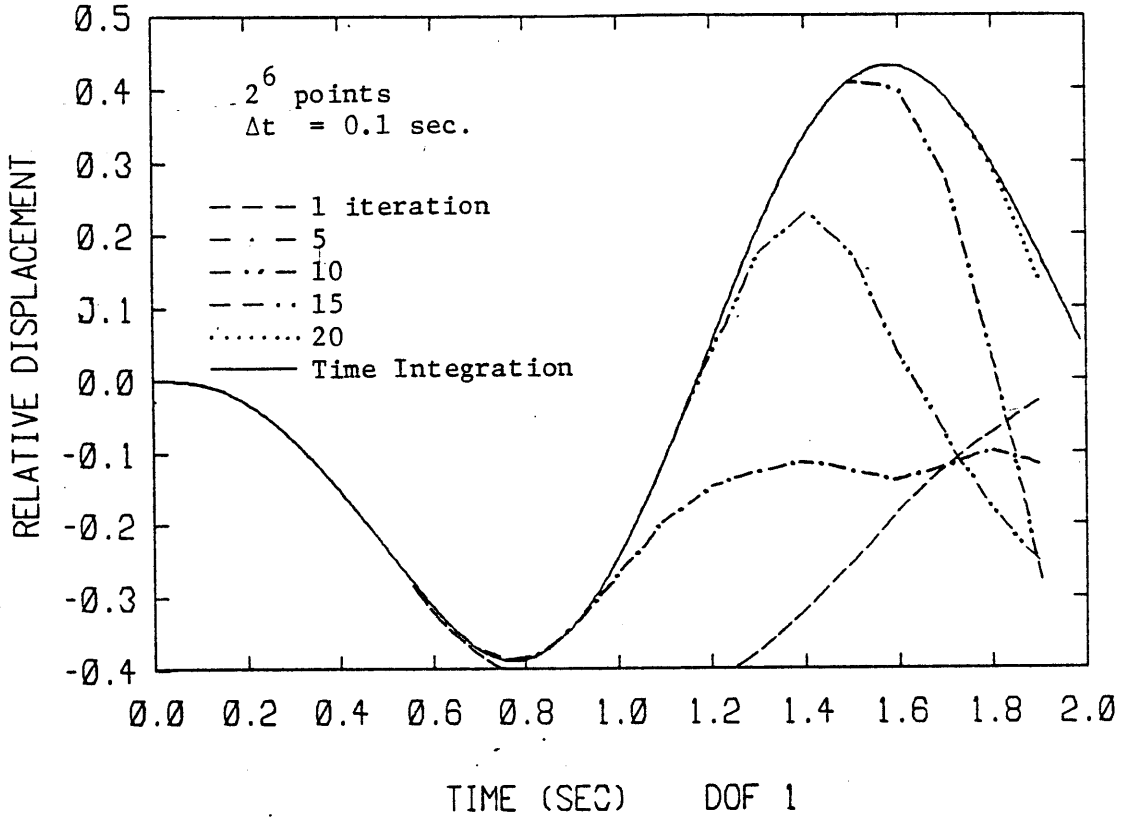

Fig. 6.29 Response of DOF 1, Direct Time Integration and HFT Results

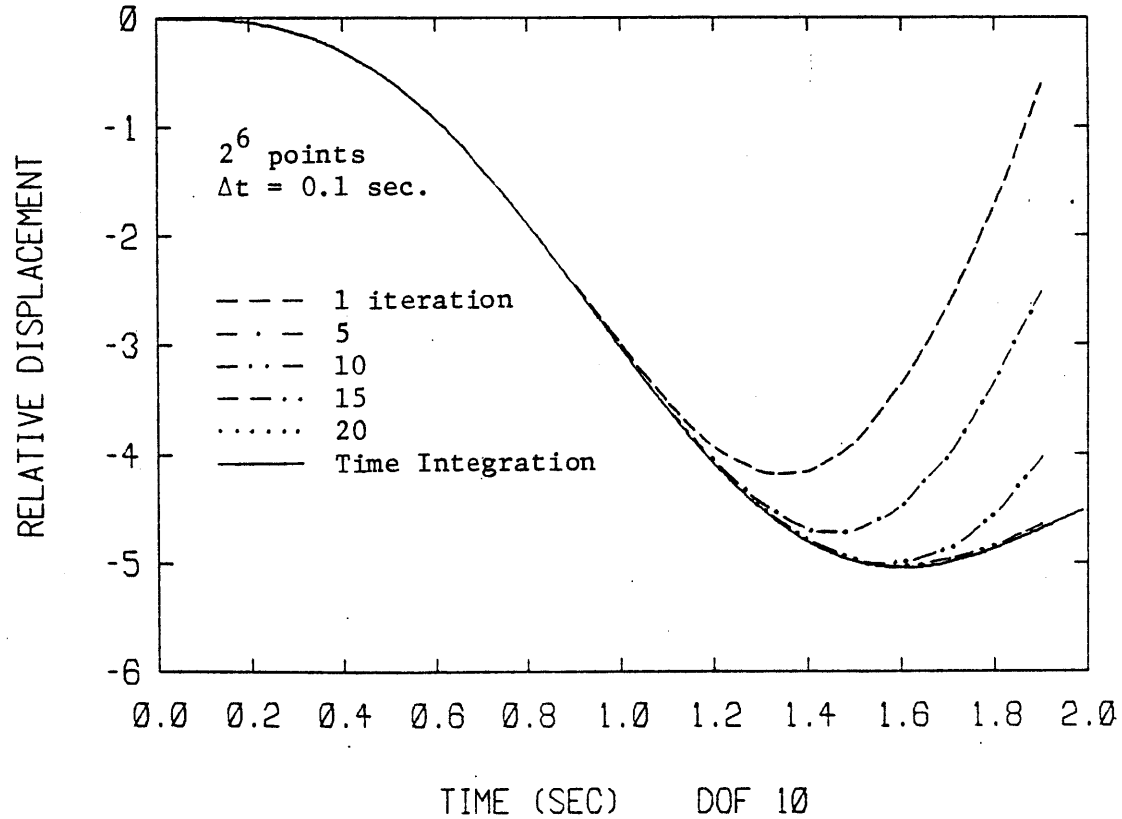

Fig. 6.30 Response of DOF 10, Direct Time Integration and HFT Results

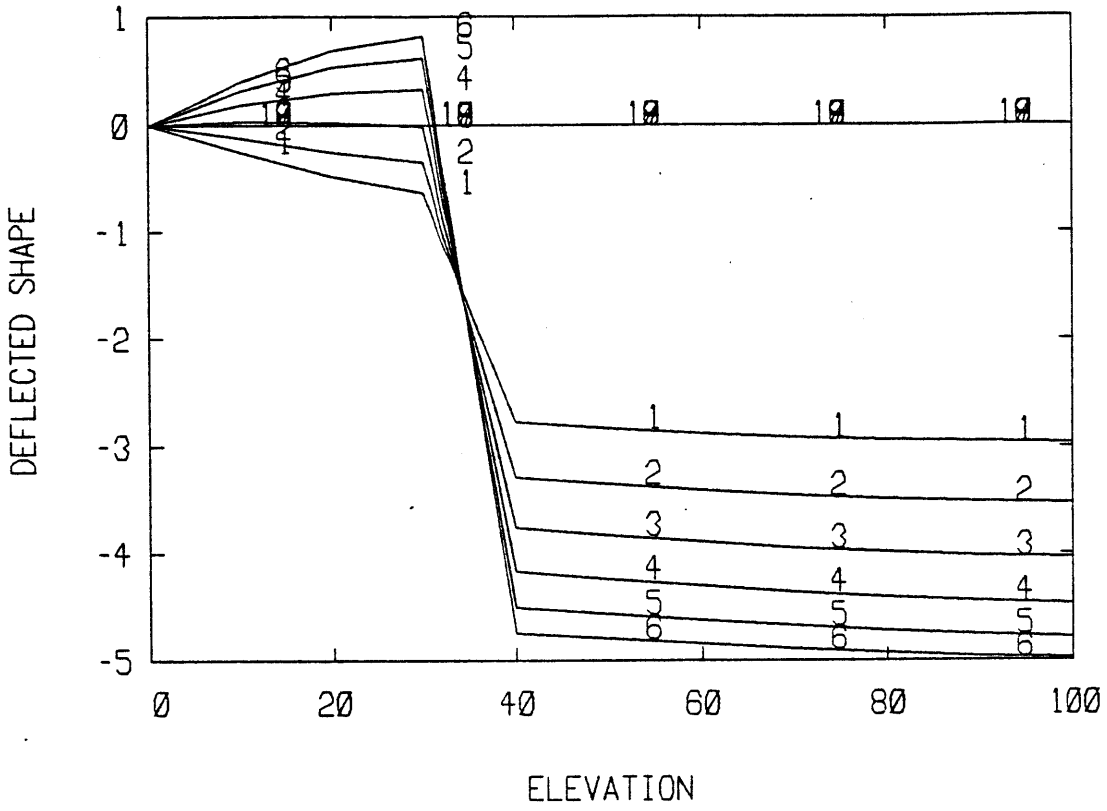

Fig. 6.31 Deflected Shape from Time 1.0 sec. to 1.5 sec.

The second portion of this study implemented the mode updating scheme by iterating the first five cycles with the first 5 linear mode shapes. After these cycles, the analysis was stopped and the pseudo-force histories were examined. An equivalent static load distribution was derived, applied to the original structure, and then the tangent stiffness matrix was obtained. From the tangent stiffness matrix, the first nonlinear mode shape was evaluated. The ten linear mode shapes are given in Fig. 6.32 and first nonlinear shape, in Fig. 6.33. The first nonlinear mode shape was then Gram-Schmidt orthogonalized with respect to the first 5 linear mode shapes to obtain the nonlinear mode shape shown in Fig. 6.34. The analysis was restarted using the first 5 linear mode shapes and the first nonlinear Gram-Schmidt orthogonalized mode shape (a total of 6 modes). The corresponding response histories are provided in Figs. 6.35 and 6.36 for dof's 1 and 10 and the converging deflected shape from time t=1.0 s to t=1.5 s is given in Fig. 6.37. It is apparent that this mode updating procedure is effective for this problem. Furthermore, Fig. 6.38 demonstrates that the response obtained with the first five linear modes using time integration is inadequate to properly represent the nonlinear response. As a measure of the efficiency of the HFT analysis, the expended CPU times are listed in Table 6.5.

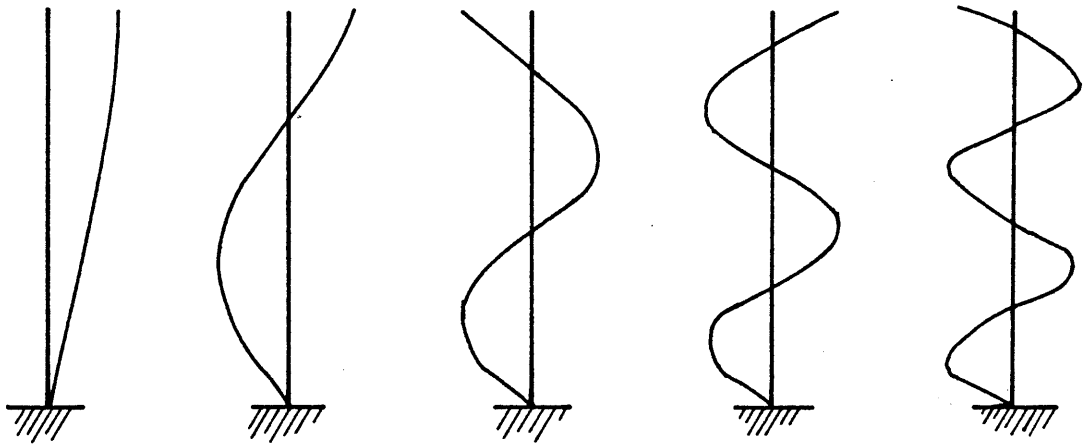

T_1 = 3.65 s T_2 = 1.23 s T_3 = 0.75 s T_4 = 0.55 s T_5 = 0.44 s

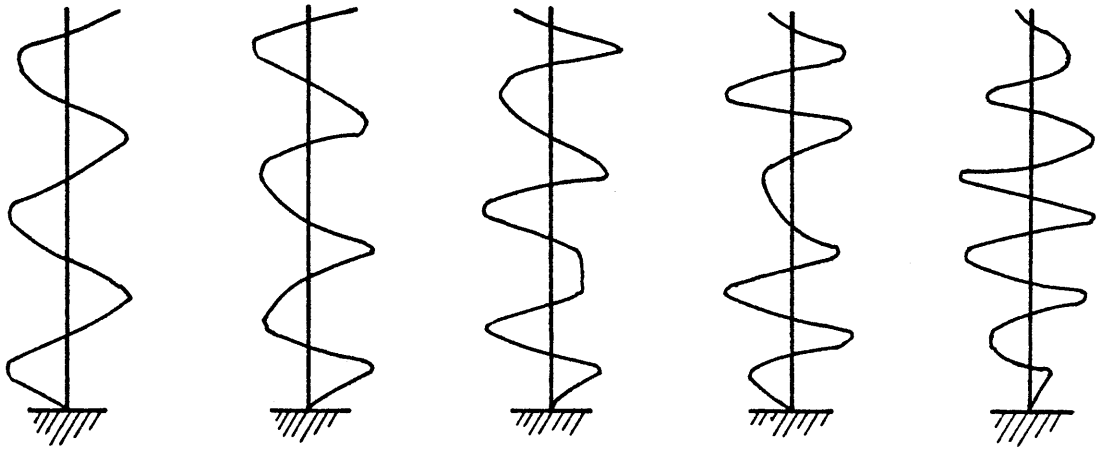

T_6 = 0.37 s T_7 = 0.33 s T_8 = 0.30 s T_9 = 0.29 s T_{10} = 0.28 s

Fig. 6.32 Linear Modes Shapes

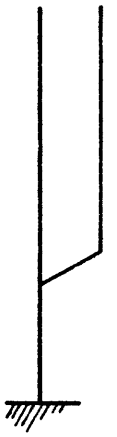

Fig. 6.33 First Nonlinear Mode Obtained from Static Load Distribution Method

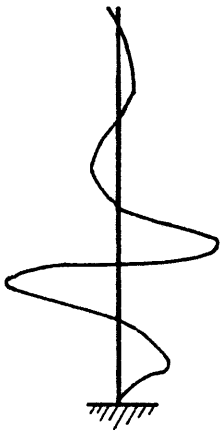

Fig. 6.34 First Nonlinear Mode Gram-Schmidt Orthogonalized with Respect to Lowest Five Linear Modes

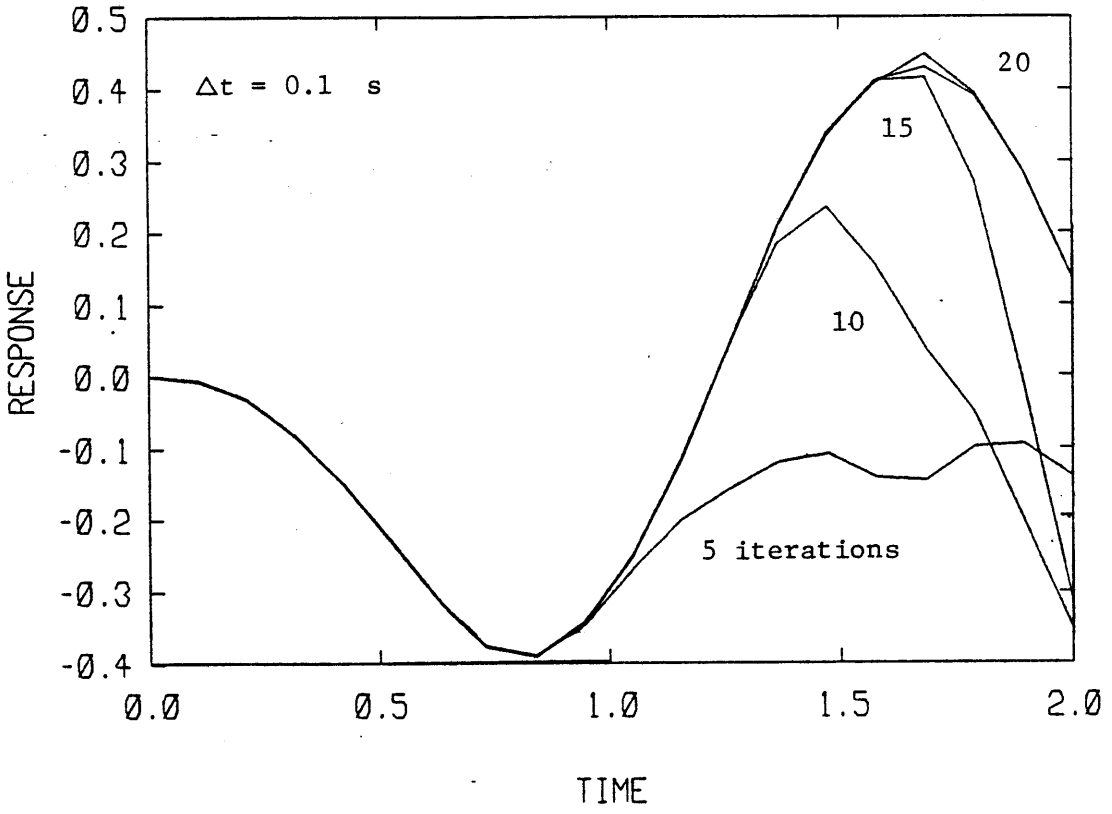

Fig. 6.35 Response of DOF 1 Using an HFT Analysis (5 linear plus 1 nonlinear mode)

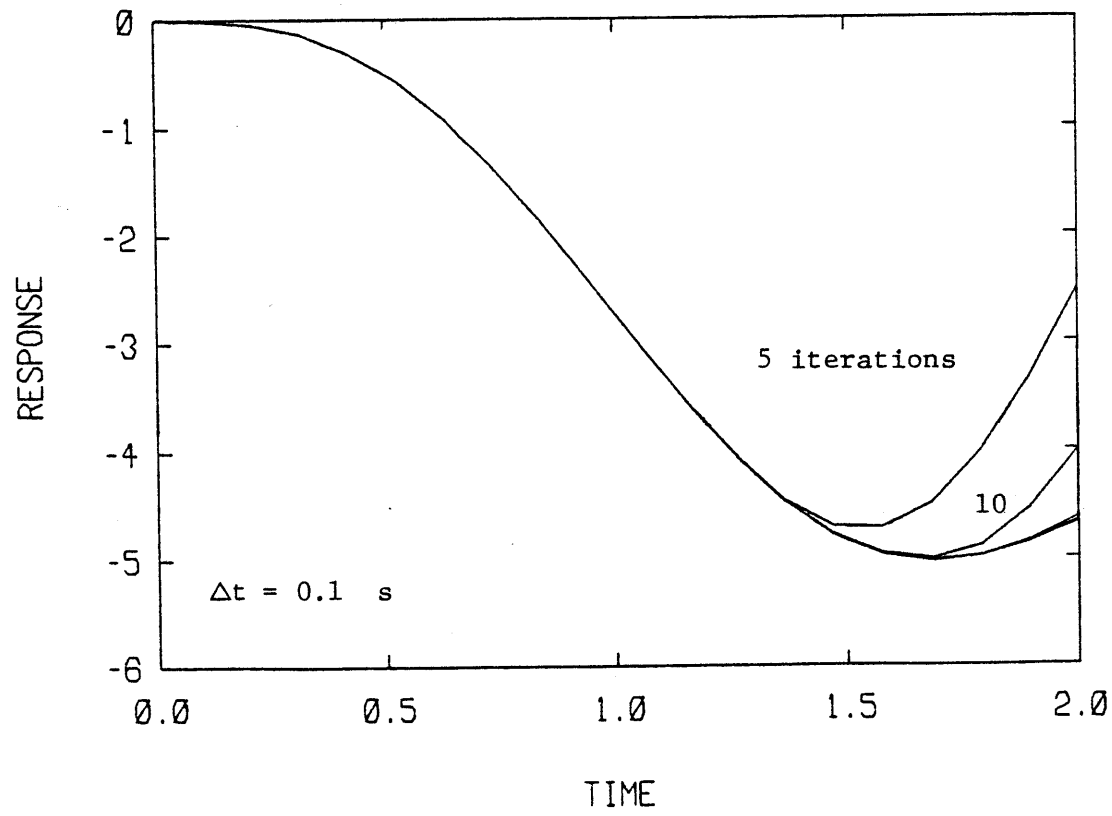

Fig. 6.36 Response of DOF 10 Using an HFT Analysis (5 linear plus 1 nonlinear mode)

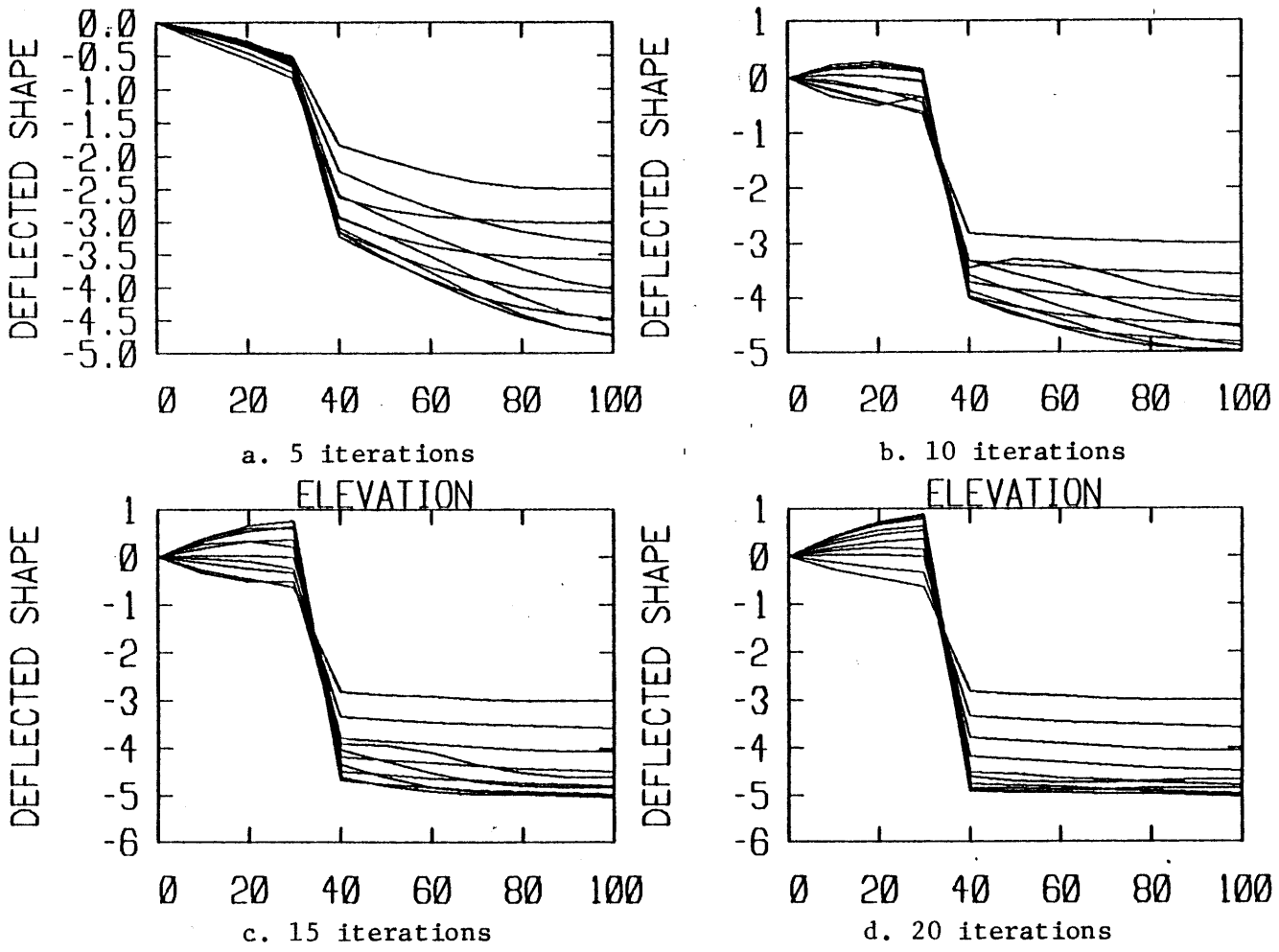

Fig. 6.37 Converging Deflected Shapes for Iterations 5, 10, 15, and 20 (5 linear plus 1 nonlinear mode)

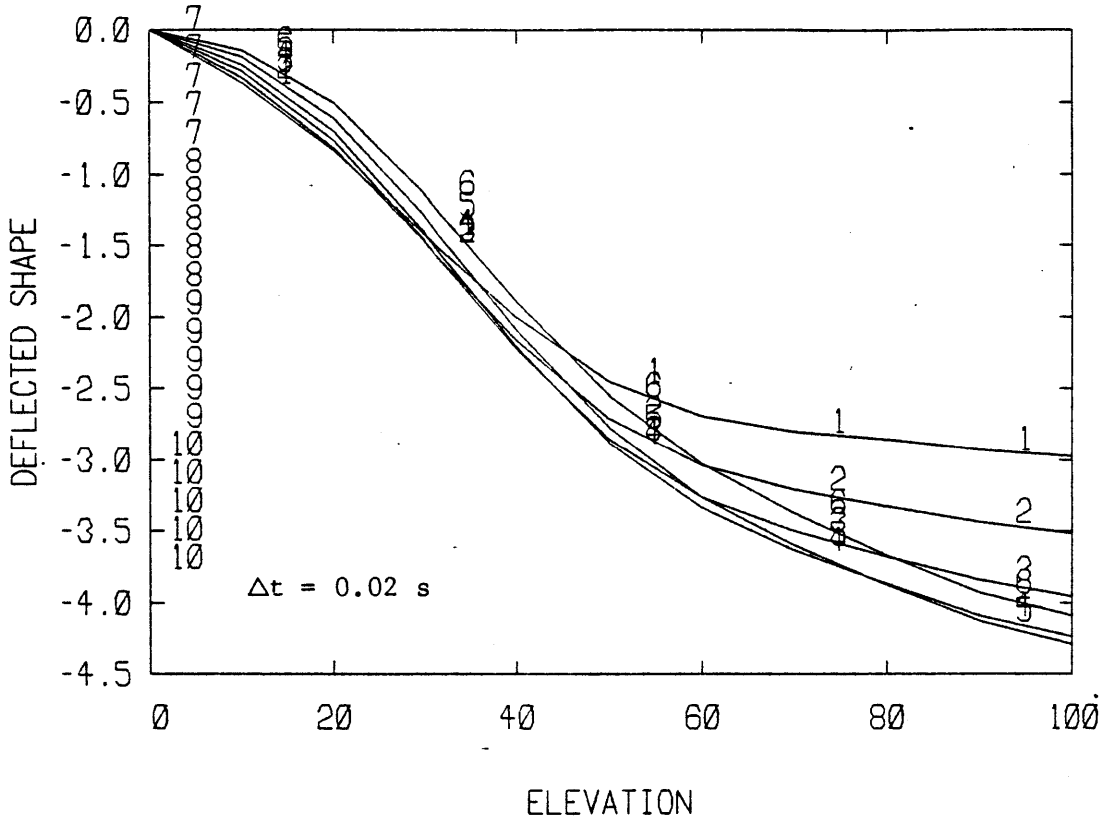

Fig. 6.38 Deflected Shapes Obtained with 5 Linear Modes Using a Direct Time Integration Analysis

Solution Scheme	Time Increment (sec)	No. of Points	No. of Modes	CPU Time (sec)
Time Integration				
Linear	0.02	100	all	11.9
nonlinear	0.02	100	all	15.1
HFT	0.1	64	10L	23.4
	0.1	64	5L+4NL	18.3*
	0.1	64	5L+2NL	16.4*
	0.1	64	5L+1NL	15.2*

All HFT CPU times are for 20 iterations

L - linear mode
NL - nonlinear mode

* nonlinear solution time

Table 6.5 Computation Times for 10 DOF Shear Beam Model

This section demonstrated the feasibility of the first mode updating scheme used in conjunction with the transference of the off-diagonal terms to the RHS of the equation of motion. The HFT scheme in this context demonstrated sufficient accuracy and an efficiency comparable to that of a direct time integration analysis. The study, however, was limited to a fairly simple response, producing no stability problems.

6.4 MDOF SOIL AMPLIFICATION STUDY

Another soil amplification problem was considered in this study, but with a refined soil model consisting of a closely coupled 9 degree of freedom lumped mass structural model and a stiffness profile varying with the square root of the depth. The fundamental structural period T_1 was 0.357 s and T_9, 0.031 s. No viscous damping was specified, and the Taft earthquake scaled to 0.05 g was used. Relevant structural properties are provided in Fig. 6.39.

The direct time integration analyses were conducted using the Newmark integration method (α=0.25, δ=0.50) and Newton equilibrium iteration scheme with a residual force tolerance of 0.00001 and iteration limit of 15. Preliminary studies indicated that a time step size of 0.005 s was adequate. The linear and nonlinear displacement responses at the soil surface are given in Figs. 6.40 and 6.41.

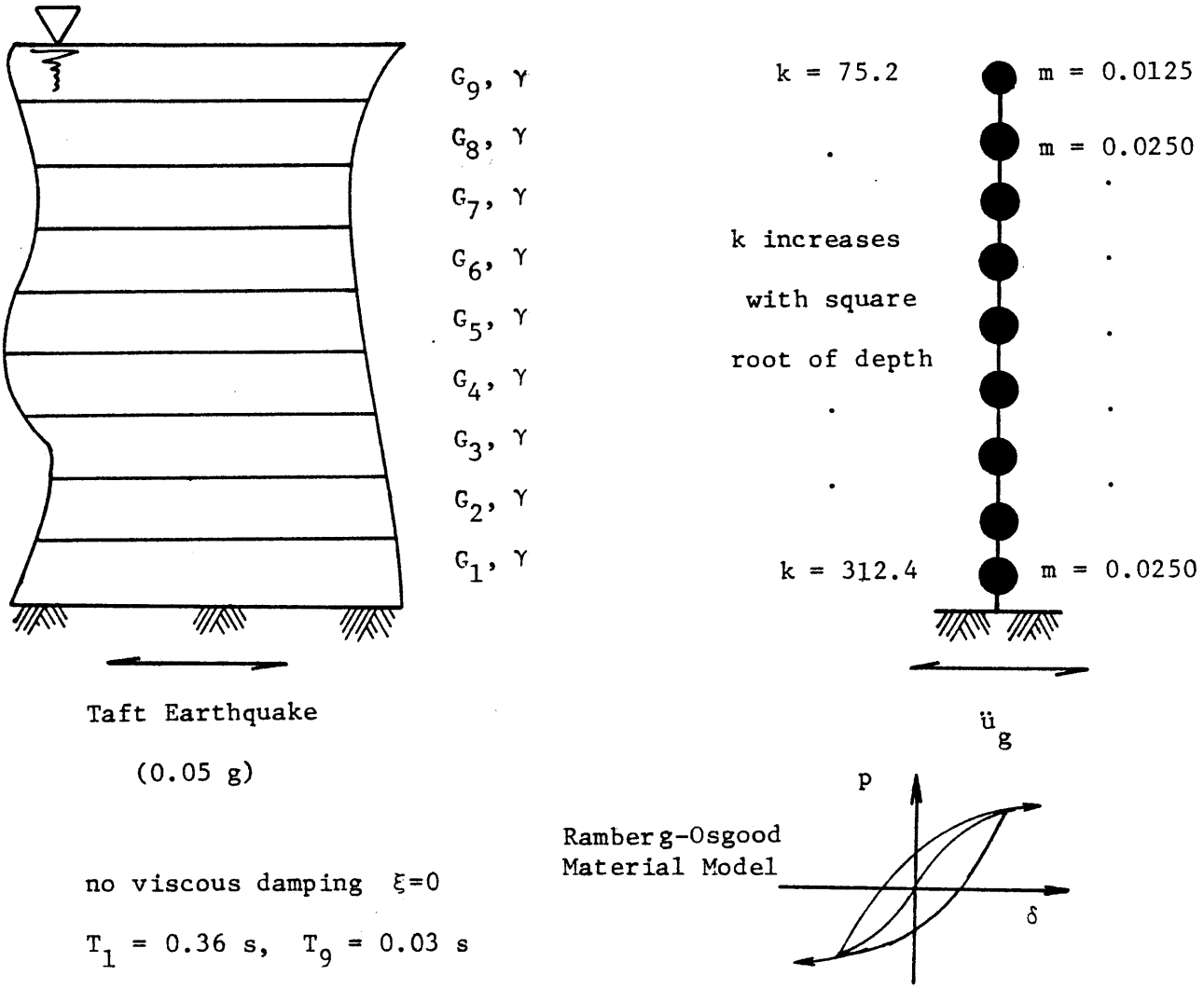

Fig. 6.39 Refined Multidegree of Freedom Soil Amplification Study

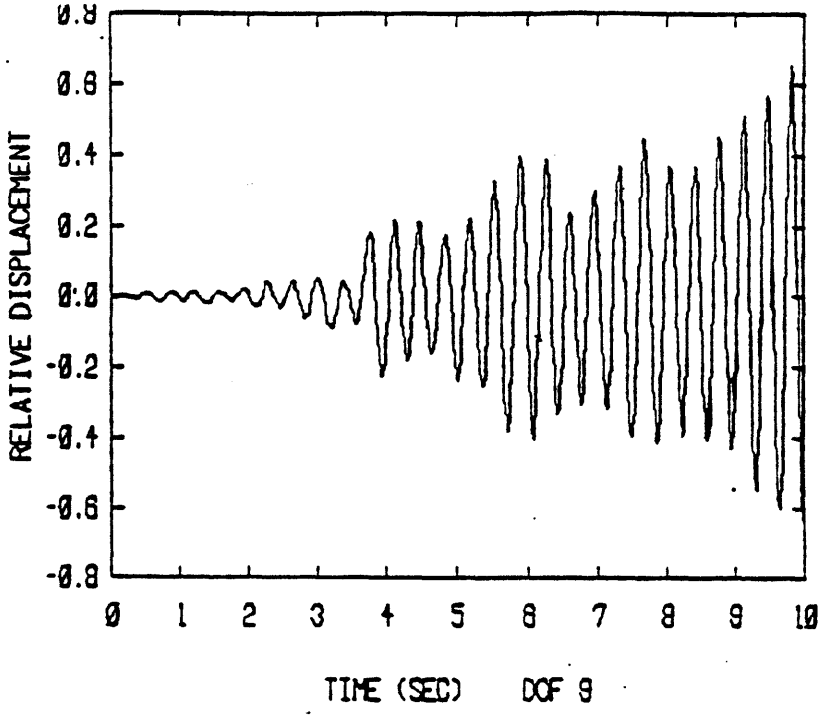

Fig. 6.40 Linear Response to the Taft Earthquake (surface displacement)

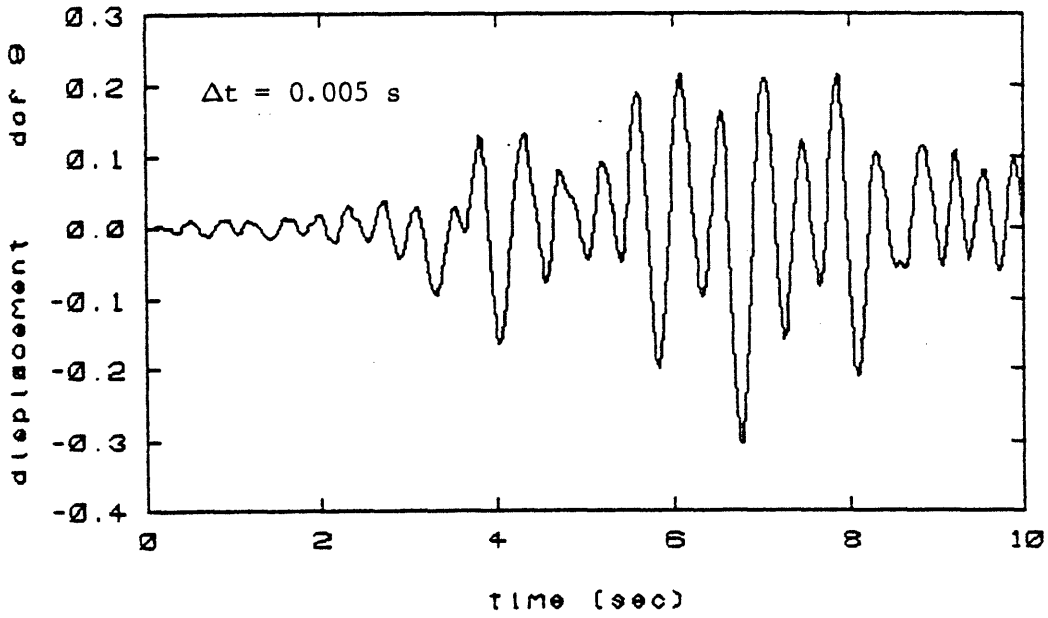

Fig. 6.41 Nonlinear Response to the Taft Earthquake Using a Direct Time Integration Analysis (surface displacement)

Compared to the MDOF problem discussed in section 6.3, this problem exhibited a complex nonlinear response with significant deviations from the linear response. As a result, it offered an opportunity to examine the stabilizing behavior provided by the artificial viscous damping and to apply the second mode updating scheme (least squares secant stiffness approach).

The total displacement formulation was used in the HFT analysis with a time increment of 0.01 s. Although an artificial viscous damping ratio of 0.50 was adequate for obtaining the first five seconds of the response, a damping ratio of 0.75 was necessary for the entire history of 10 seconds because the solution eventually diverged for a damping ratio of 0.50. The results after 5, 10, and 20 iterations are given in Figs. 6.42, 6.43, and 6.44. Notice that the response appears to converge after 5 and 10 iterations, but after 20 iterations a low frequency component introduces a slow drift in the solution and with further iterations, significant high frequency components begin to modify the response to the extent that the proper response shape is maintained, but the amplitudes grow without bound.

Further diagnostic studies indicated that the artificial viscous damping force contributed the significant high frequency response while the pseudo-force vector contributed the low frequency drift. Any static drift in

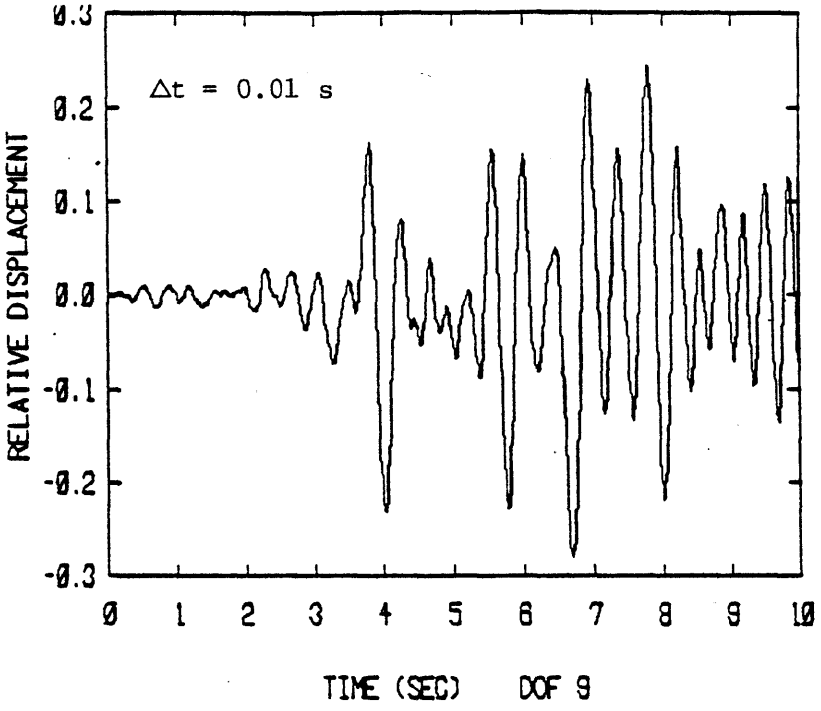

Fig. 6.42 Nonlinear Response after 5 Iterations (artificial viscous damping ratio of 0.75)

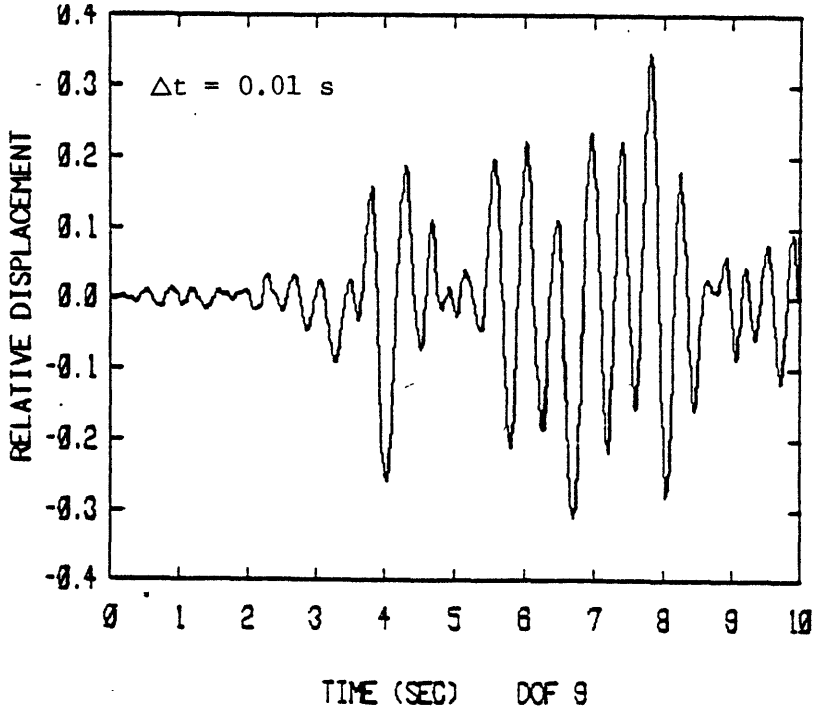

Fig. 6.43 Nonlinear Response after 10 Iterations

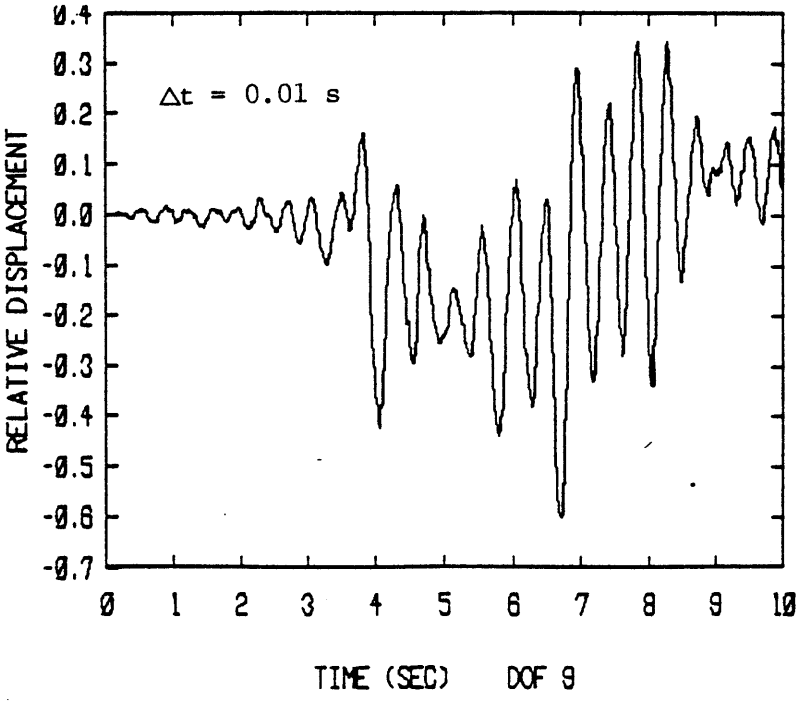

Fig. 6.44 Nonlinear Response after 20 Iterations

the solution can be attributed to the pseudo-force vector $\underline{F}^{NL}$ since the other loading terms consisting of the earthquake excitation and the artificial damping force (which is derived from the velocity of the response equal to $i\omega\ \underline{Y}(\omega)$ in the frequency domain) had no zero frequency components. It is postulated that when the HFT solution initially gives poor estimates of the correct response, then, since a viscous type artificial damping $2\xi_v\bar{\omega}m$ is used, the artificial damping force for the higher modes ($\bar{\omega}$ large) continues to increase with each iteration until it dominates the response, producing an incorrect pseudo-force (low frequency drift) which further aggravates the inaccuracies in the artificial damping force for the succeeding cycle.

As a result of the unstable convergence properties introduced by the artificial viscous damping, an artificial hysteretic damping was considered next. By its very definition the hysteretic type damping appears more suitable for this problem since in essence all damping is contributed by the soil model.

Before executing the entire HFT analysis, preliminary studies were conducted to determine an appropriate time increment. Figure 6.45 depicts the results obtained after 10 iterations with Δt=0.01 s, and Fig. 6.46, the corresponding results with Δt=0.05 s. In both cases the artificial hysteretic damping ratio equalled 0.75. A time increment of 0.05 s appeared acceptable and was used in

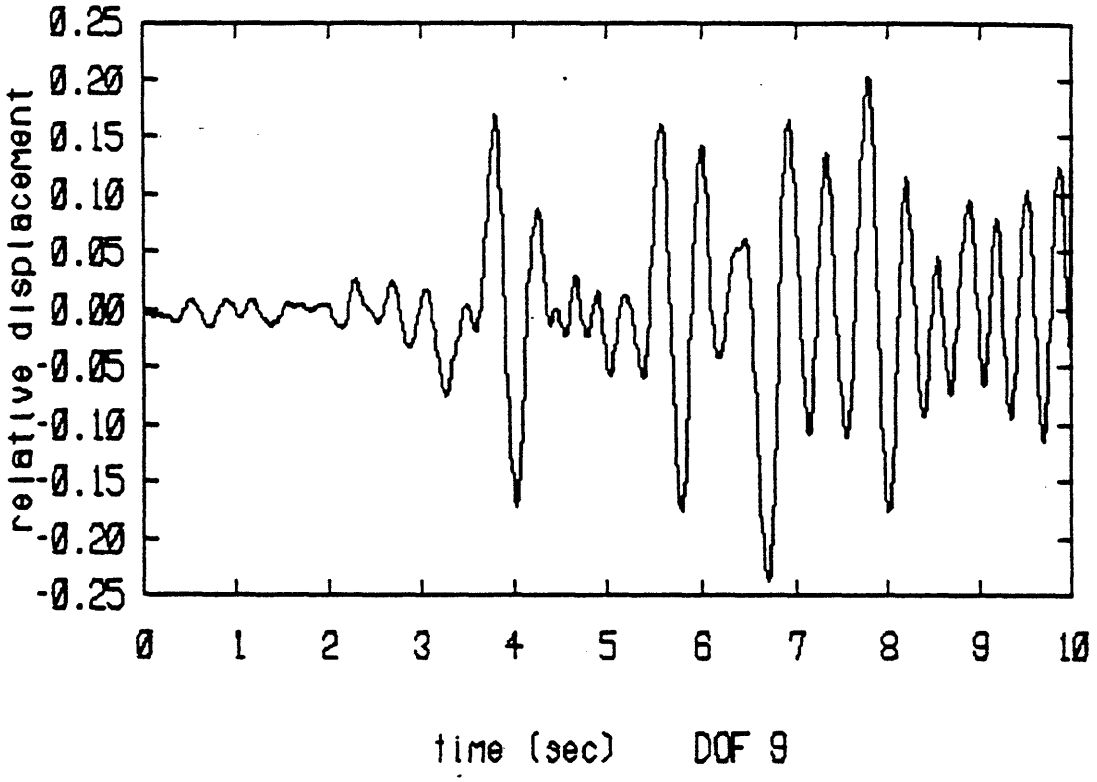

Fig. 6.45 Nonlinear Response after 10 Iterations (artificial hysteretic damping ratio of 0.75, time increment of 0.01 s)

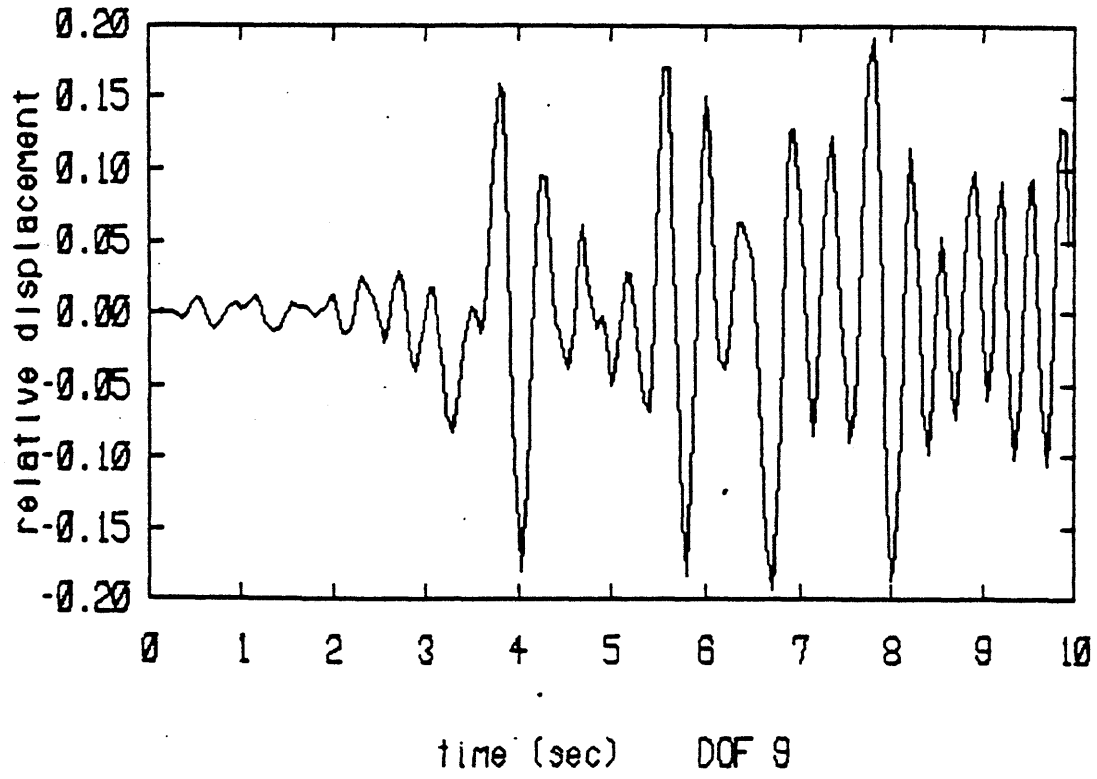

Fig. 6.46 Nonlinear Response after 10 Iterations (time increment of 0.05 s)

succeeding analyses. 256 points were used in the frequency domain (200 for the 10 second earthquake and 56 appended zeroes).

The HFT results using all nine linear modes are shown in Fig. 6.47 for 50 iterations and Fig. 6.48 for 80 iterations, by which time the solution history had converged to its final shape for the specified solution parameters. Notice that the results after 50 and 80 iterations are fairly similar up to time 5 seconds. This convergence behavior indicates that the final iterations correct the latter portion of the response, implying that the initial portion converges first and corrects in a time progressing form.

As a comparison of the efficiency of the two solution schemes, the direct time integration analysis required 650 s and the HFT analysis, 540 s.

The next portion of this study implemented the second mode updating scheme, described in Chapter 5. Initial studies were conducted with a time increment of 0.05 s to determine the minimum number of linear modes necessary to adequately reproduce the response. Figure 6.49 shows the response after ten iterations using all 9 linear modes. Figure 6.50 shows the corresponding response using 5 linear modes, and Fig. 6.51, 1 linear mode. One linear mode adequately reproduces the response, although the peak amplitudes are slightly smaller.

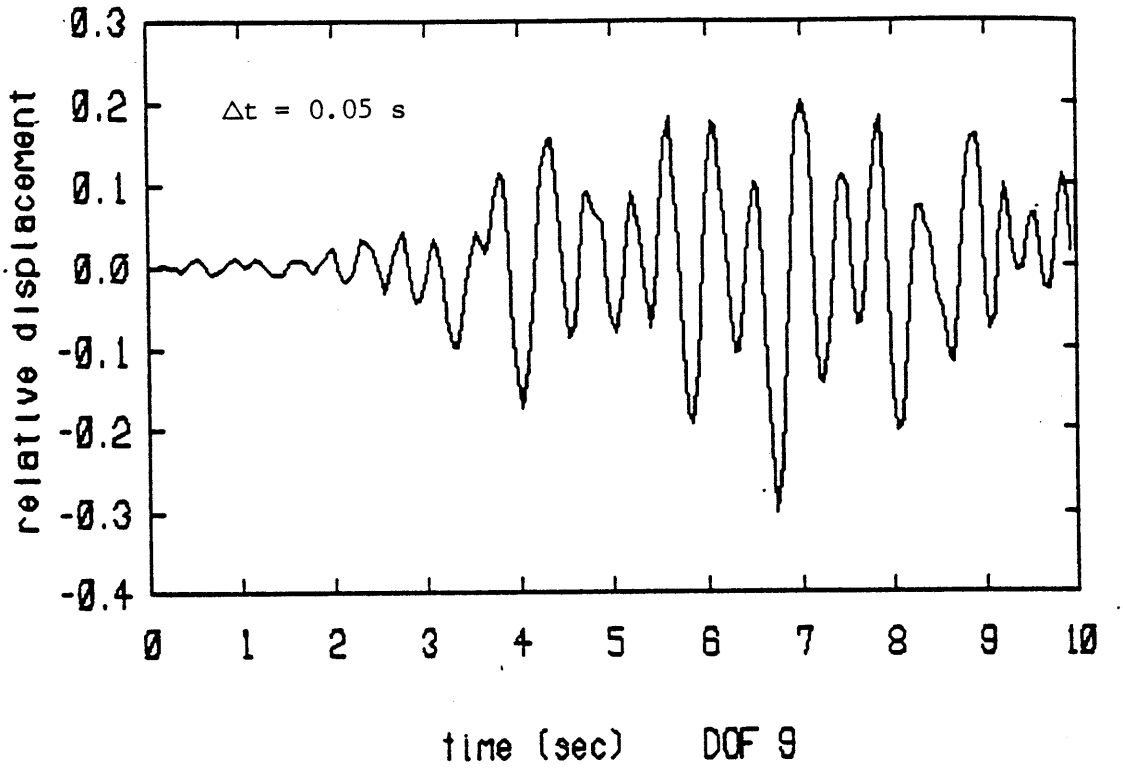

Fig. 6.47 Nonlinear Response after 50 Iterations

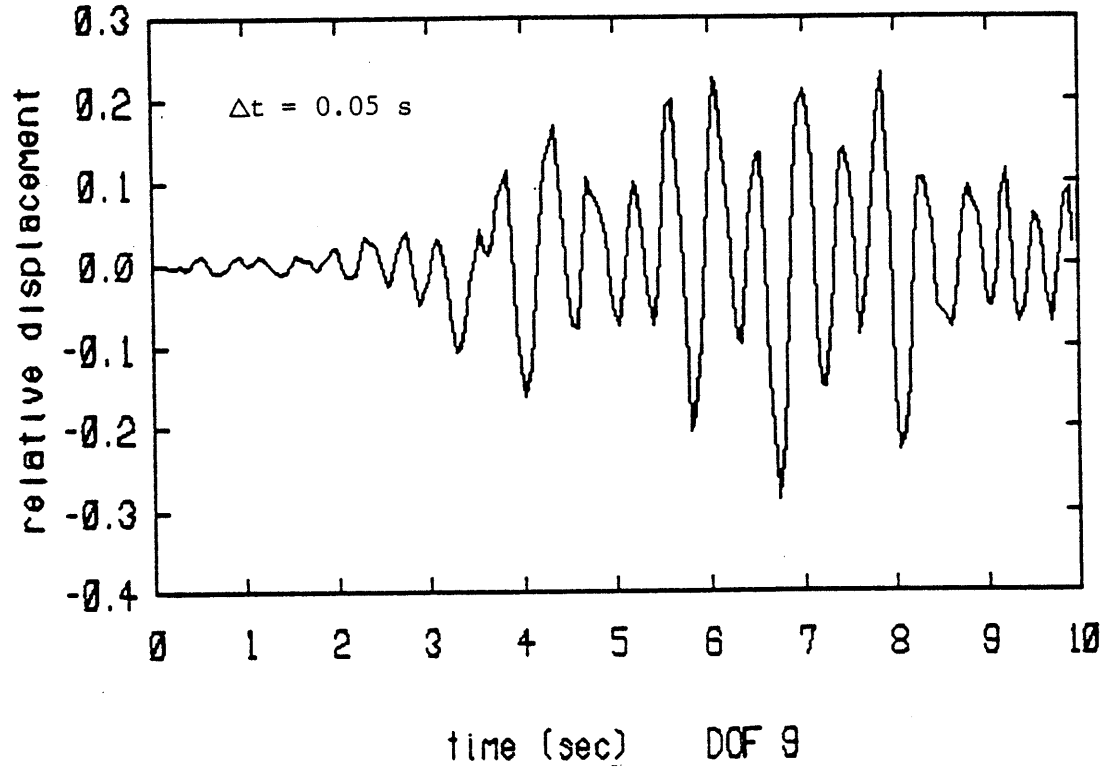

Fig. 6.48 Nonlinear Response after 80 Iterations

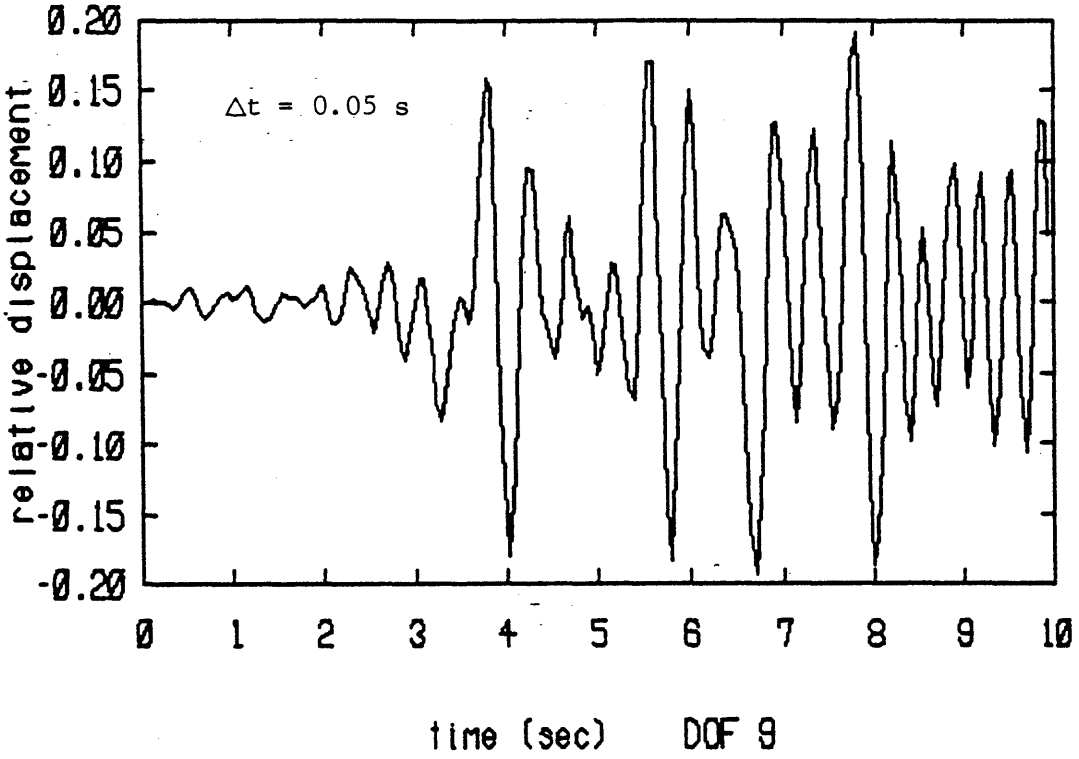

Fig. 6.49 Nonlinear Response after 10 Iterations (10 linear modes)

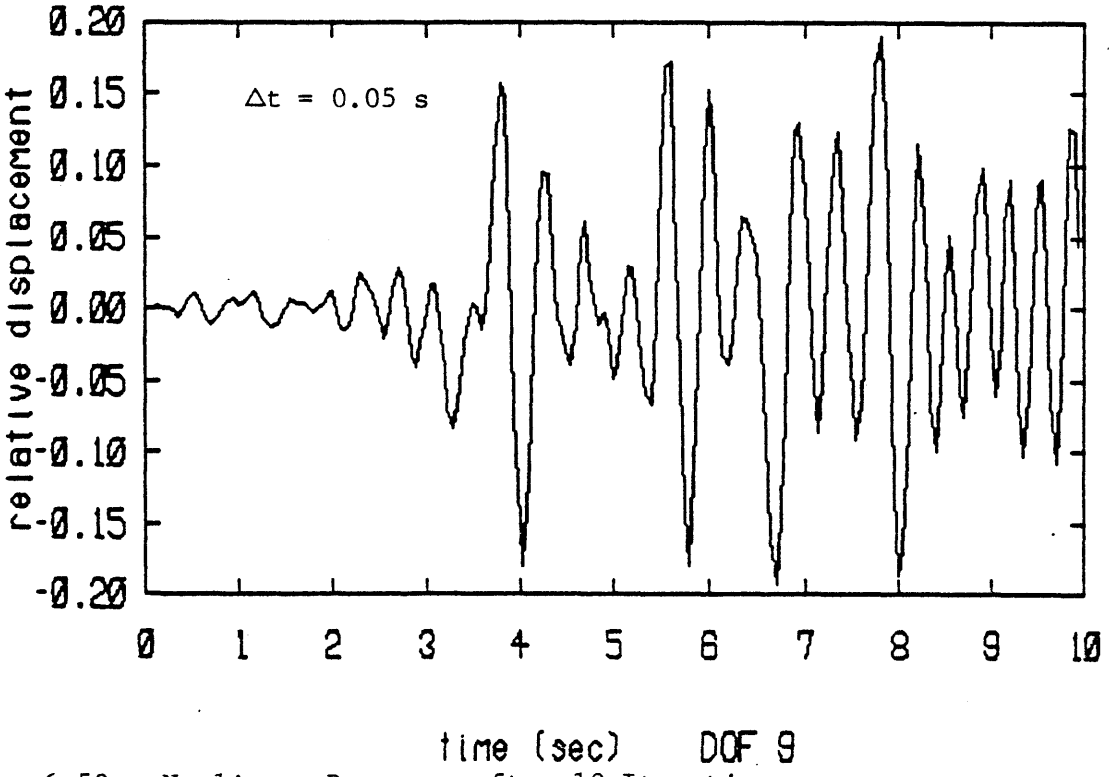

Fig. 6.50 Nonlinear Response after 10 Iterations (5 linear modes)

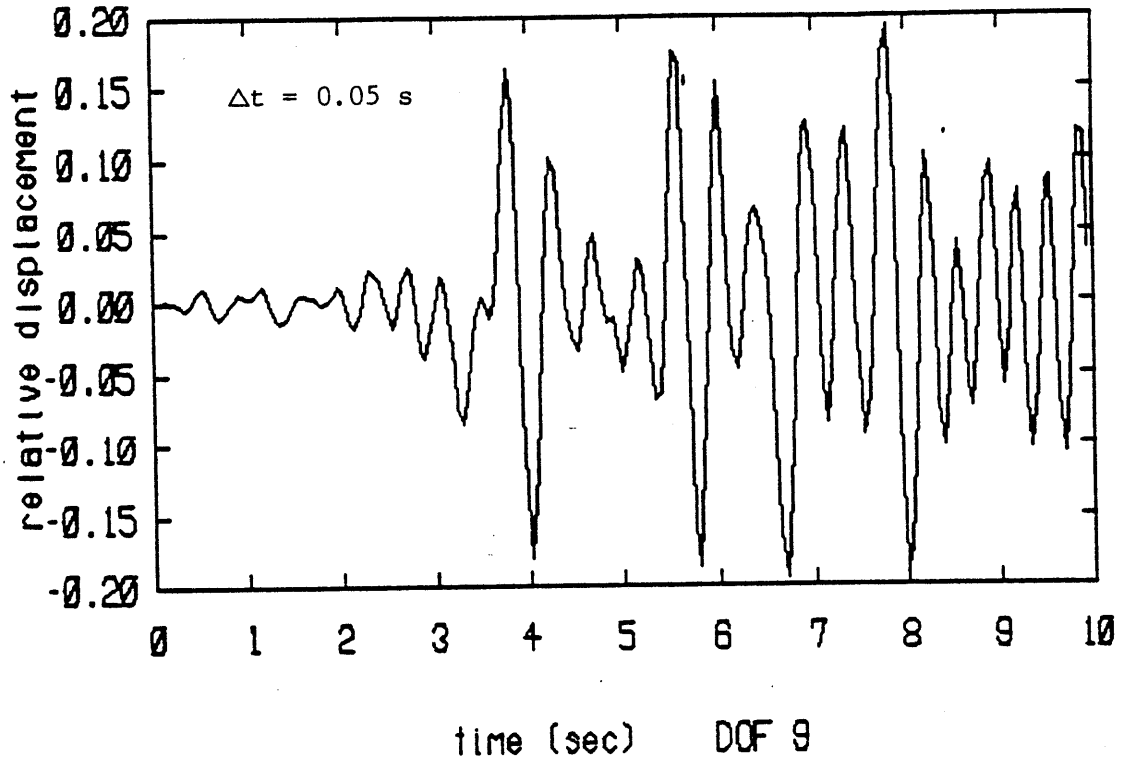

Fig. 6.51 Nonlinear Response after 10 Iterations (1 linear mode)

Realizing that the fundamental mode was acceptable in this particular problem, the mode updating scheme was applied in the following form:

1. Iterate the first ten cycles with one linear mode.
2. Stop the analysis. Apply a least squares fit to the stress-strain diagram of each member to obtain nine new secant stiffnesses, k_{sec}.
3. Establish the corresponding structural secant stiffness $\underline{K}_{sec}$ and evaluate the nonlinear eigenvector (s).
4. Restart the analysis with the fundamental nonlinear eigenvector (one nonlinear mode).
5. Iterate for another 40 cycles.

The response after 50 iterations (first 10 with one linear mode and next 40 with one nonlinear mode) using a time increment of 0.05 s is shown in Fig. 6.52. For comparison purposes an additional analysis was conducted with one linear mode during all iterations and a time increment of 0.05 s, yielding the response after 50 iterations shown in Fig. 6.53a and 80 iterations, Fig. 6.53b. Comparing Figs. 6.52 and 6.53 with Fig. 6.48 it is apparent that the response converged faster with only one nonlinear mode (50 iterations for one nonlinear mode and 80 iterations for one linear mode). Finally, Fig. 6.54 shows the additional accuracy gained by using one linear mode and a time increment of 0.02 s.

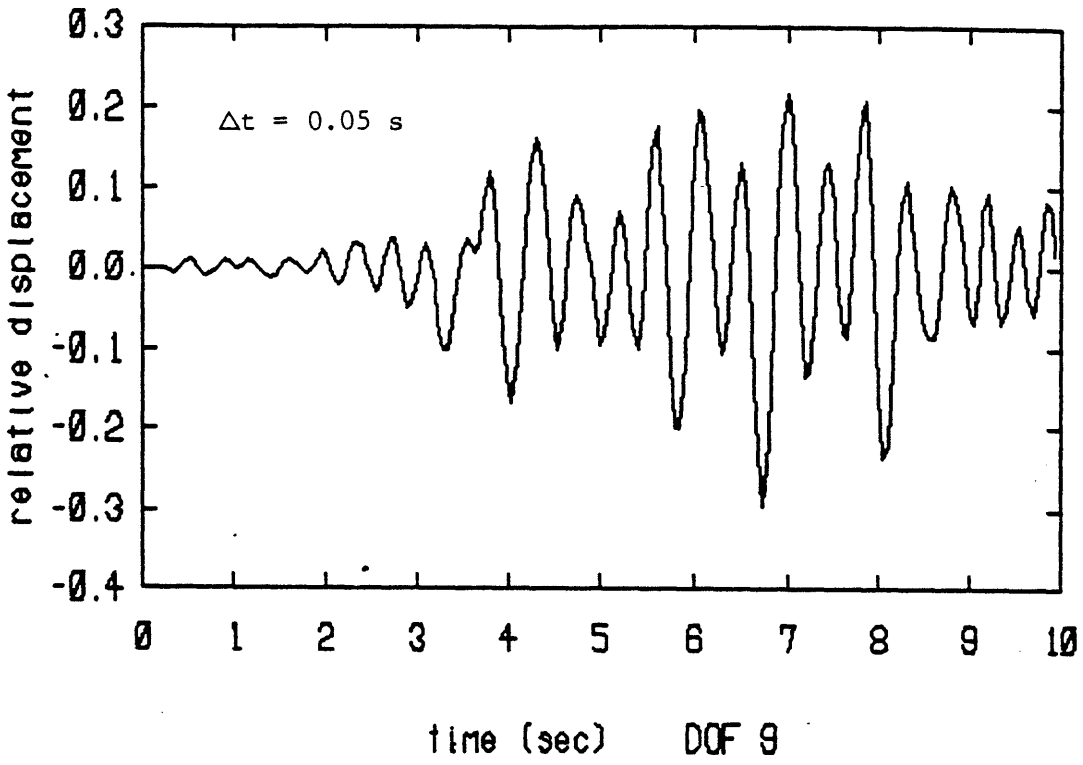

Fig. 6.52 Nonlinear Response after 50 Iterations
(1 nonlinear mode)

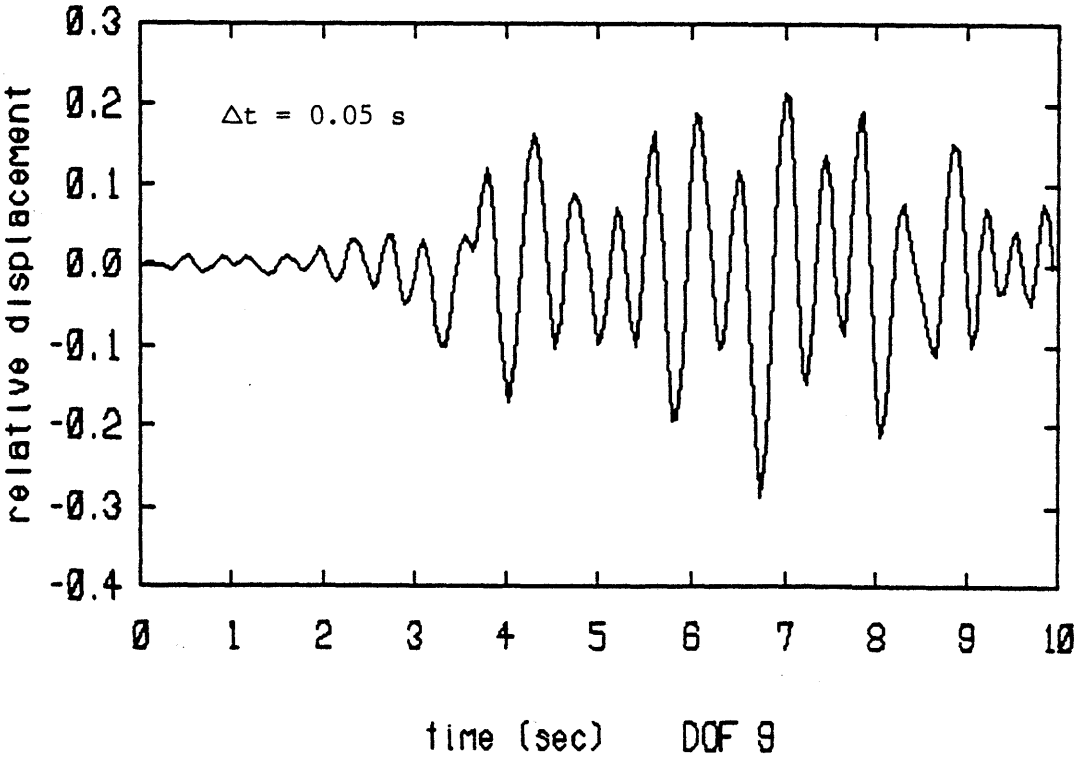

Fig. 6.53a Nonlinear Response after 50 Iterations
(1 linear mode)

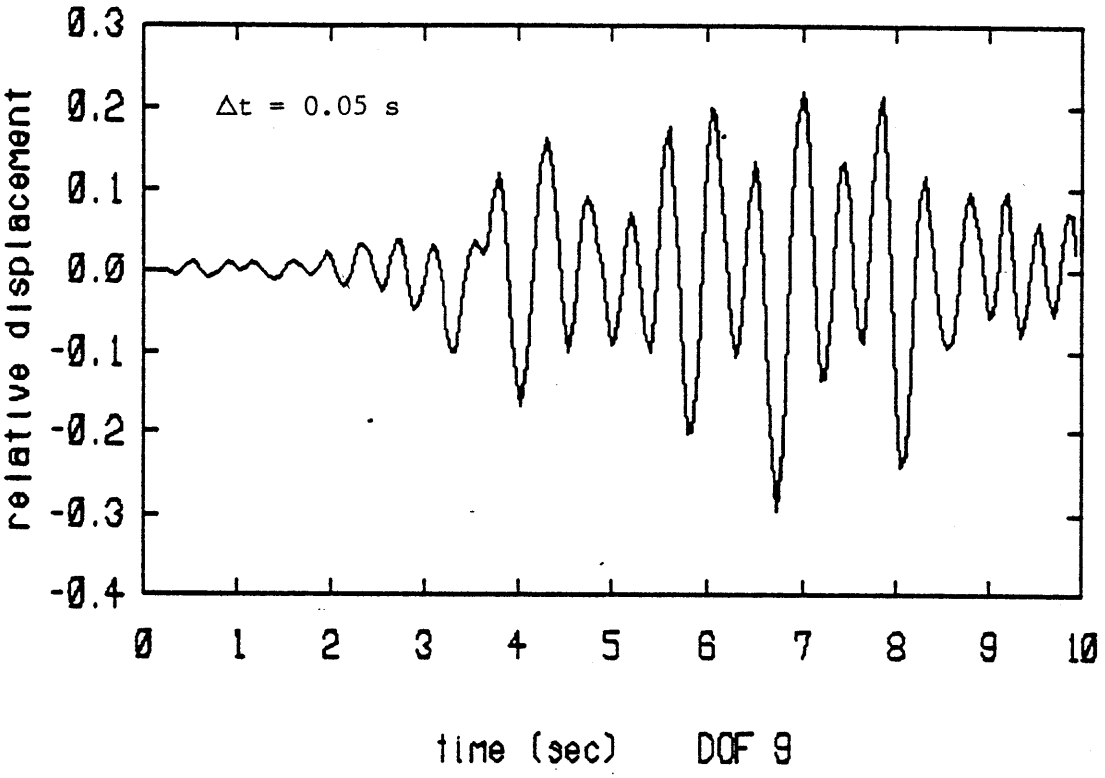

Fig. 6.53b Nonlinear Response after 80 Iterations
(1 linear mode)

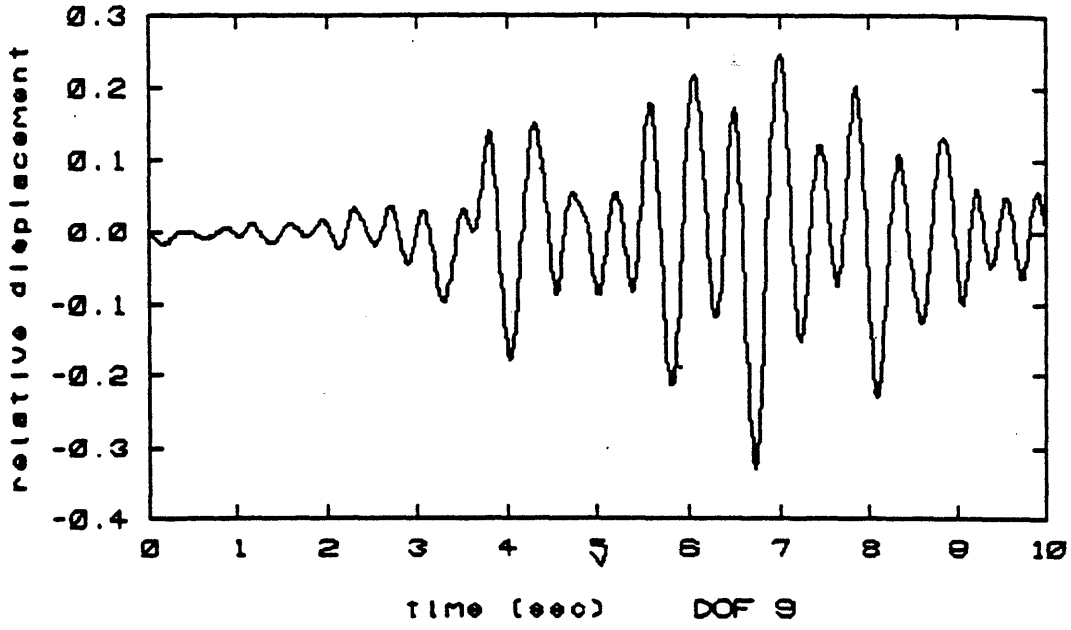

Fig. 6.54a Nonlinear Response after 40 Iterations
(time increment of 0.02s, 1 linear mode)

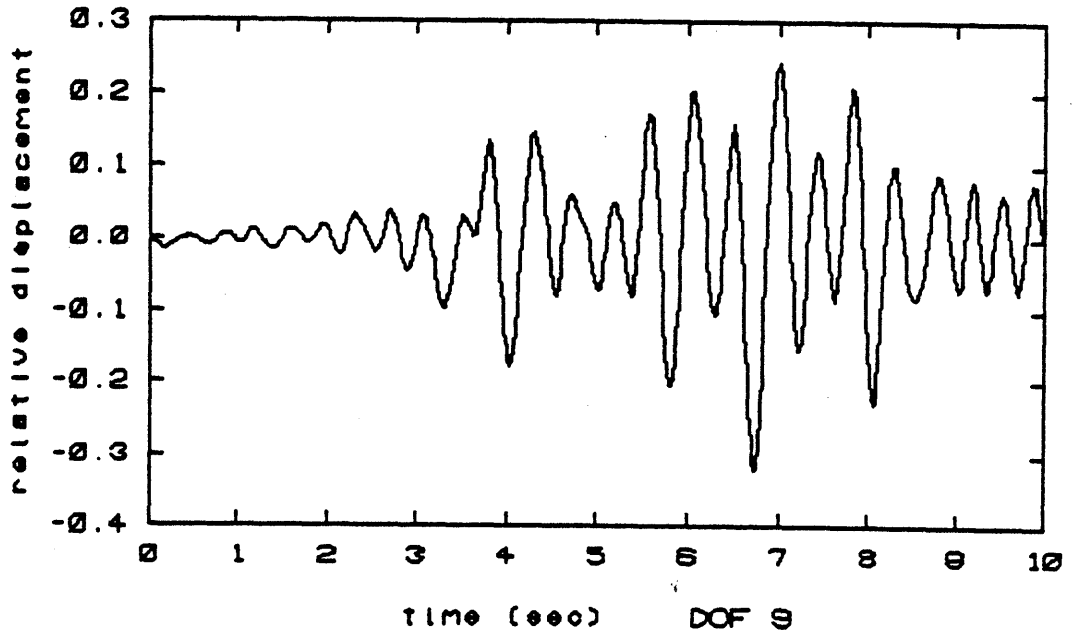

Fig. 6.54b Nonlinear Response after 80 Iterations
(time increment of 0.02 s, 1 linear mode)

The faster rate of convergence when using one nonlinear mode, as opposed to one linear mode, stems from $\underline{K}_{sec}$ better representing the overall structural behavior than $\underline{K}_1$, and hence providing closer initial estimates to the nonlinear response. The fundamental mode of $\underline{K}_{sec}$ has period 0.466 s compared to that of $\underline{K}_1$ with 0.357 s, indicating that $\underline{K}_{sec}$ portrays a softer, nonlinear structure. A representative force-displacement diagram, from which the k_{sec}'s are derived, is shown in Fig. 6.55.

The computation times for the various analyses are provided in Table 6.6. Notice that the HFT scheme displays significant reductions in computational cost compared to the direct time integration analyses. This efficiency originates from the use of a time increment ten times larger than that of the direct time integration analysis combined with a nonlinear mode superposition scheme.

This section introduced the artificial hysteretic damping concept to stabilize an otherwise intractable problem and the least squares secant stiffness mode updating scheme to increase the analysis efficiency. The hysteretic artificial damping proved better adapted to this problem than the artificial viscous damping, and, furthermore, had a negligible effect on the computational cost. The second mode updating scheme was easily implemented and actually accelerated the convergence of the iterative process. Compared to the first mode updating scheme, this method

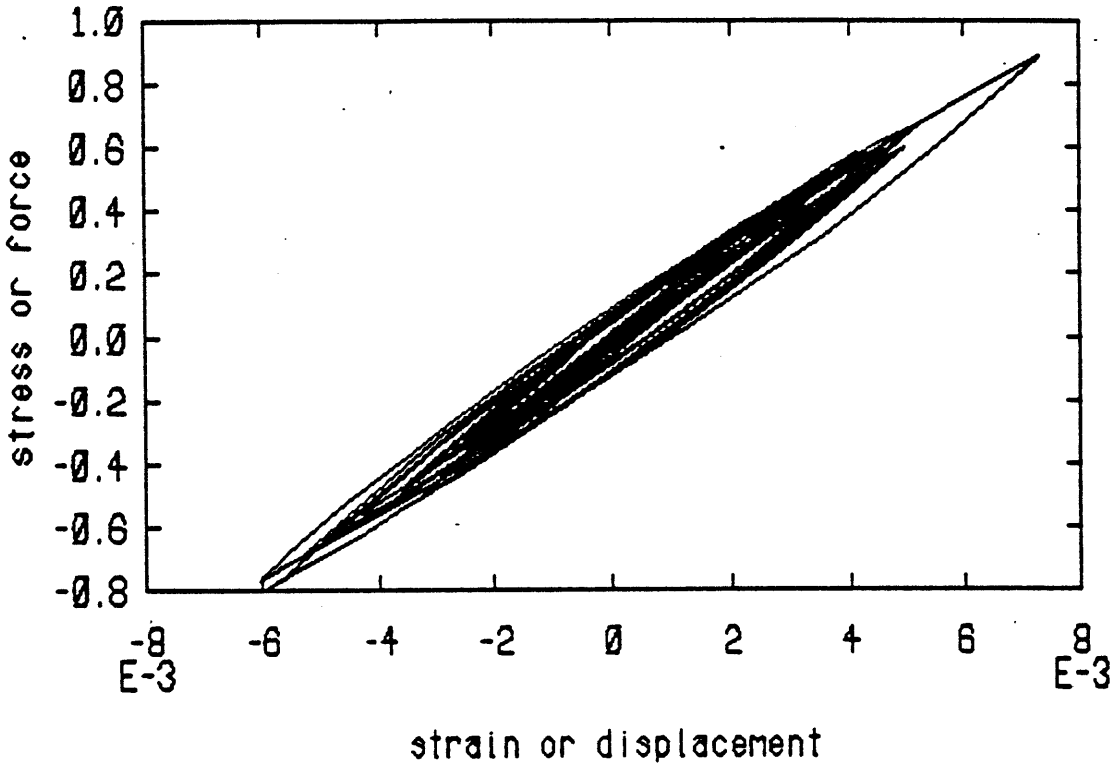

Fig. 6.55 Stress-Strain Response of Ramberg-Osgood Material Model

Solution Scheme	Time Increment	No. and Type of Modes Used	Iterative Cycles	CPU Time (sec)
Time Integration	0.005	Direct	---	650
HFT	0.05	9 linear	80	544
	0.05	1 linear	80	133
	0.05	*	50	100
	0.02	1 linear	80	315

* 1 linear, first ten iterations
1 nonlinear, next 40 iterations

Table 6.6 Computation Times for MDOF Soil Amplification Study

demanded less participation from the user while producing more accurate results. The scheme could be developed as a self contained updating approach, similar to the equilibrium iterators in current use.

6.5 CROSS-BRACED TUBULAR OFFSHORE STRUCTURE

The HFT scheme was extended in this study to two-dimensional models of offshore steel jacket structures subjected to seismic excitations. This study differed from previous studies in that all degrees of freedom were not loaded externally. In particular, the excitation was limited to a horizontal ground motion, implying that the vertical and rotational degrees of freedom had no external load. As a consequence, the study provided an opportunity to examine the convergence accuracy of degrees of freedom where the loading may be dominated by the pseudo-force rather than the external force. Furthermore, this study represented a culminating point for applying the fully developed HFT scheme.

6.5.1 Single-Bay Offshore Structure

The first portion of this study consisted of determining the general convergence behavior of the HFT scheme when applied to an offshore structure problem, and hence initial analyses were limited to a single-bay offshore structure, shown in Fig. 6.56, with fundamental period of 0.41 s. A stiff platform deck was modelled by a large

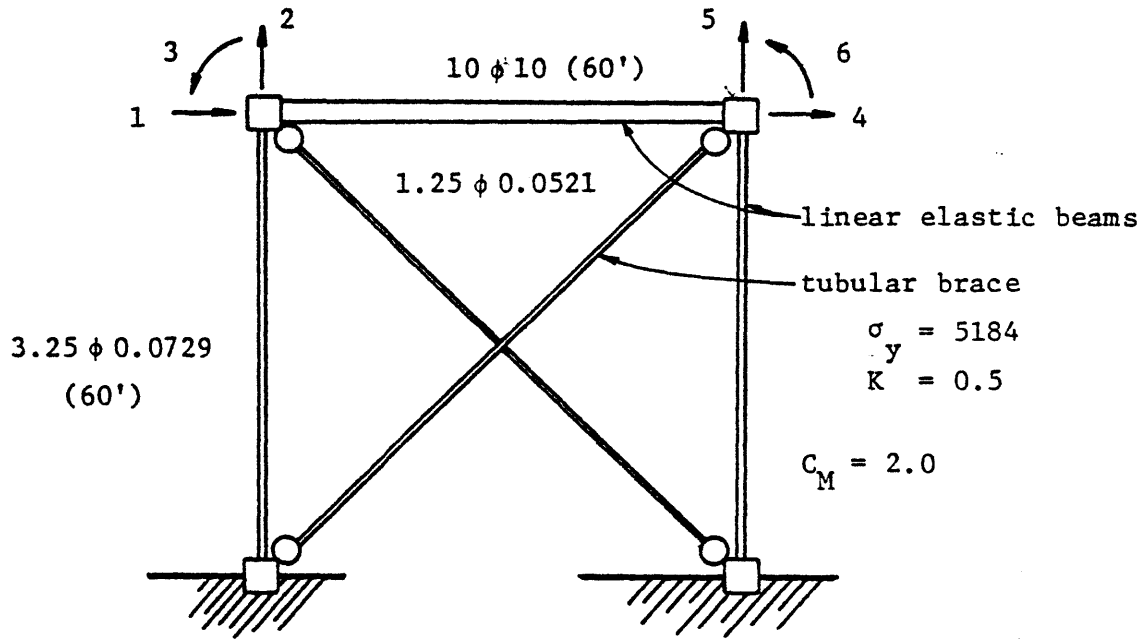

Taft Earthquake

$\ddot{u}_{g_{max}} = 3.5\ g$

$$\xi = \begin{cases} 0.05 \text{ @ } T_1 \\ 0.50 \text{ @ } T_4 \end{cases}$$

$T_1 = 0.41$ s, $T_2 = 0.12$ s, $T_3 = 0.12$ s, $T_4 = 0.006$ s

$T_5 = 0.0002$ s, $T_6 = 0.0001$ s

Fig. 6.56 Single-Bay Offshore Structure

linear elastic horizontal beam at the deck level. Vertical leg members were assumed to remain linear elastic and modelled by linear elastic tubular beam elements. Foundation effects were neglected by specifying a fixed base for both legs. The diagonal cross braces were modelled using the tubular brace model shown in Fig. 6.1, with specified fixed-fixed end conditions. The surrounding sea water was simulated by the added mass effect with an inertia coefficient C_M=2.0. The excitation consisted of the first 5 seconds of the Taft earthquake scaled to 3.5 g, to induce a reasonable nonlinear response level. Six degrees of freedom were present -- two sets of horizontal, vertical, and rotational at the top nodes. Rayleigh damping was employed by specifying a damping ratio of 0.05 at the fundamental mode and 0.50 at the highest mode. The highest three modes correspond to deformations of the stiff deck beam, and hence do not participate significantly in the response.

Preliminary analyses indicated that the direct time integration approach required a time increment of 0.02 s when using the Newmark integrator (α=0.25, δ =0.50) and modified Newton iteration scheme. The linear response for lateral degree of freedom 4 is shown in Fig. 6.57 and nonlinear response, Fig. 6.58.

As a direct comparison of the time integration and HFT analysis schemes, the HFT solution was also implemented with a time increment of 0.02 s using all 6 linear modes and an

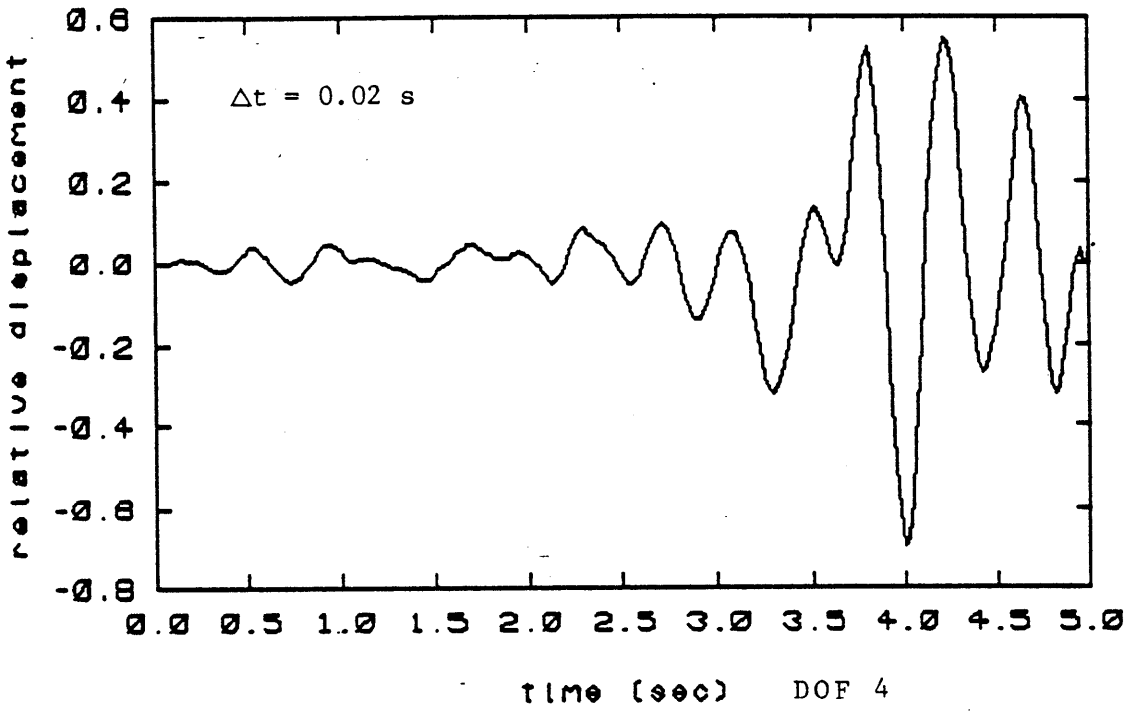

Fig. 6.57 Linear Response to the Taft Earthquake
(lateral deck displacement)

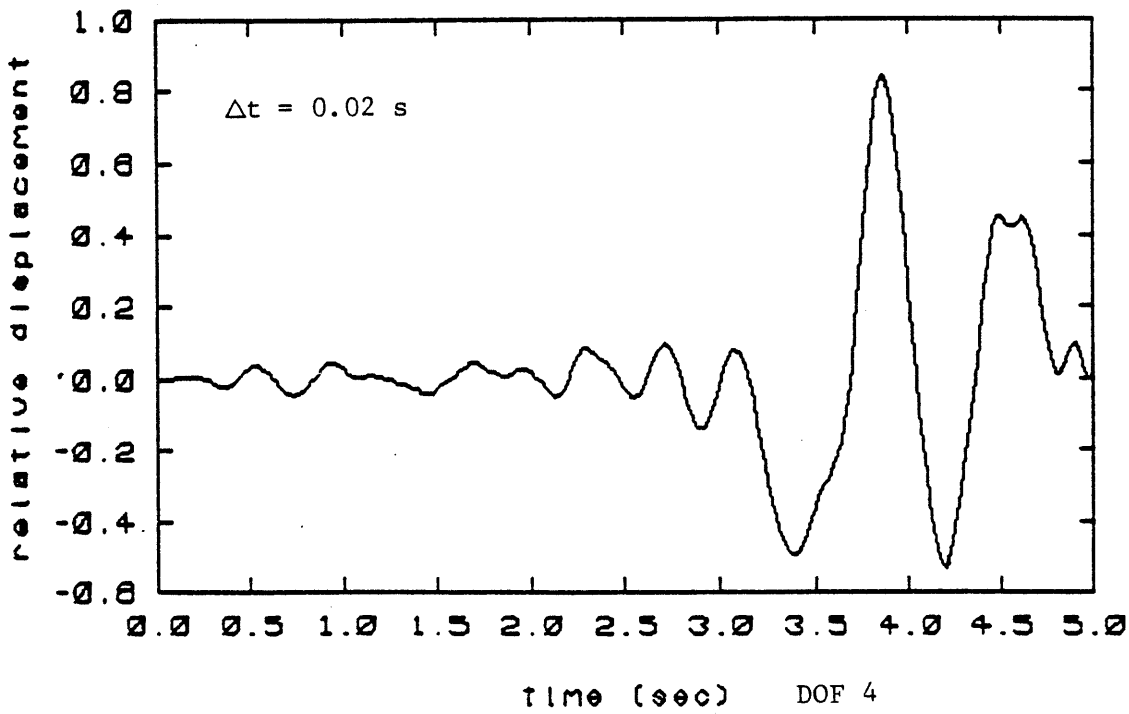

Fig. 6.58 Nonlinear Response to the Taft Earthquake
(direct time integration, lateral deck displacement)

artificial hysteretic damping ratio of 0.5. Acceptable displacement responses were attained after 30 iterative cycles. Figures 6.59, 6.60, and 6.61 depict the response of degree of freedom 4 after 5, 15, and 30 iterations.

Additional analyses were conducted with other time steps and number of modes to determine the optimum HFT solution. Figure 6.62 shows the response after 30 iterations using 6 linear modes, an artificial hysteretic damping ratio of 0.35, and time increment of 0.05 s. Figure 6.63 shows the corresponding response when using only the fundamental mode. These analyses indicated that a time increment of 0.05 s was too coarse, and subsequent analyses were run with a time increment of 0.02 s. Figures 6.64 and 6.65 show the response using three linear modes and a time increment of 0.02 s after 25 and 30 iterations, respectively. Notice that the HFT solution scheme has essentially converged by the 25th iteration, with additional iterations producing minor changes in the end of the response history. As expected, the lowest three modes reproduce the response exactly.

A more stringent evaluation of the accuracy of the HFT solution is available in Table 6.7, listing the maximum responses and times of occurrence. The maximum displacements all agree within reasonable accuracy ranging from less than 1% error for the horizontal and rotational degrees of freedom up to 5% error for the vertical degrees

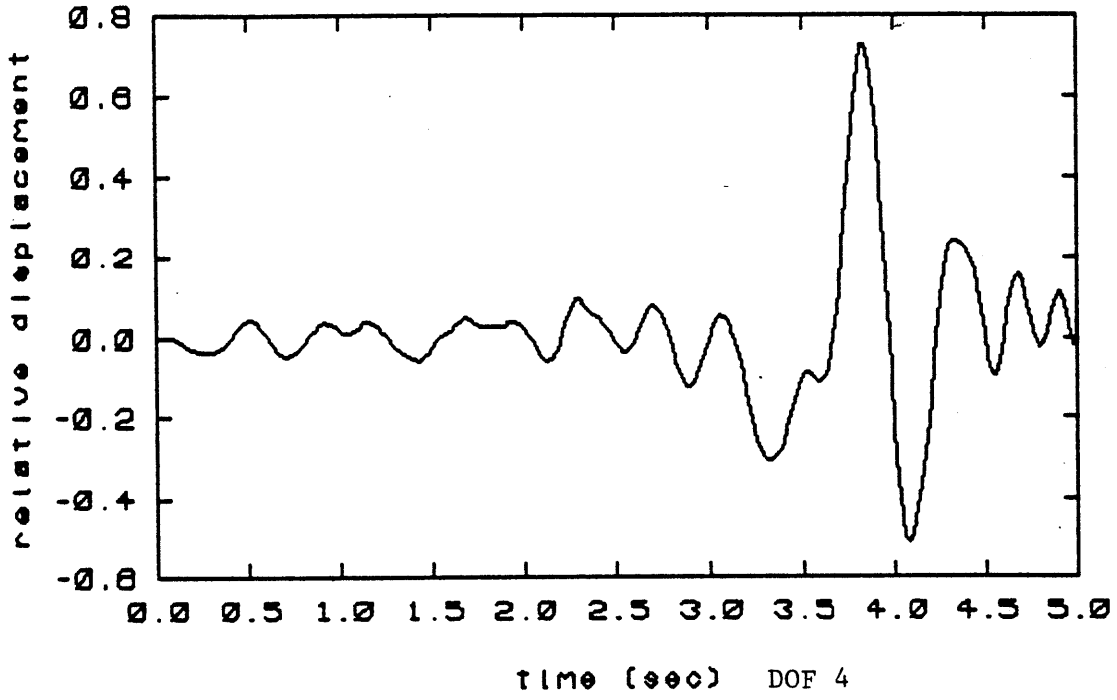

Fig. 6.59 Nonlinear Response after 5 Iterations
(6 linear modes, artificial hysteretic damping ratio of 0.5, time increment of 0.02 s)

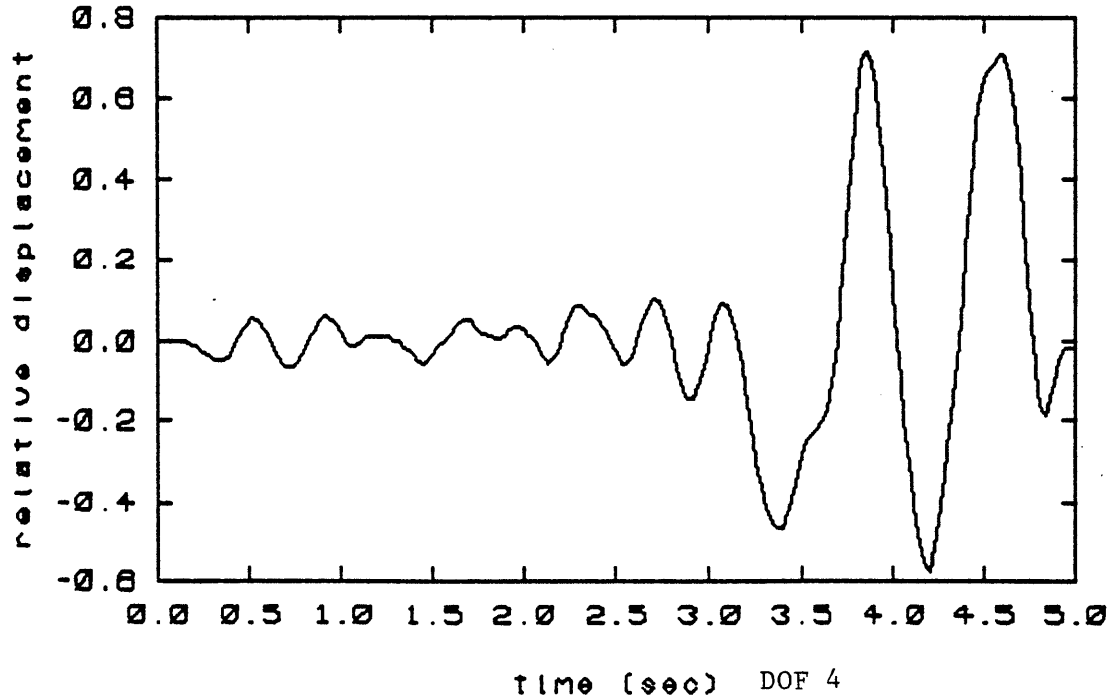

Fig. 6.60 Nonlinear Response after 15 Iterations
(time increment of 0.02 s)

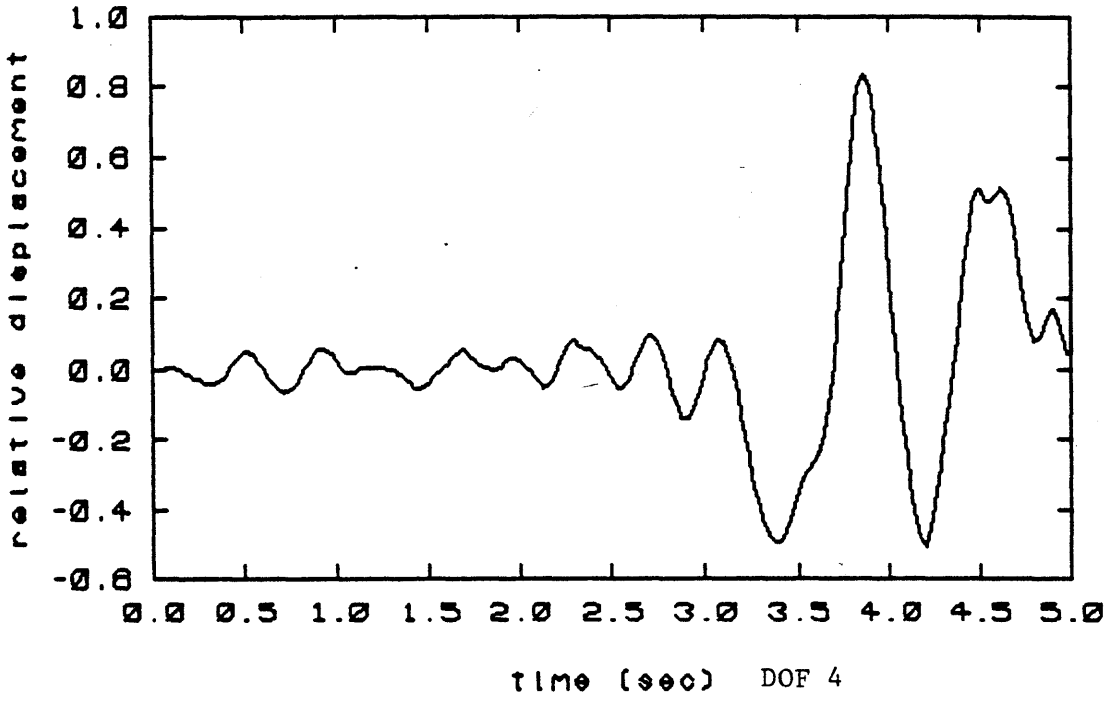

Fig. 6.61 Nonlinear Response after 30 Iterations
(time increment of 0.02 s)

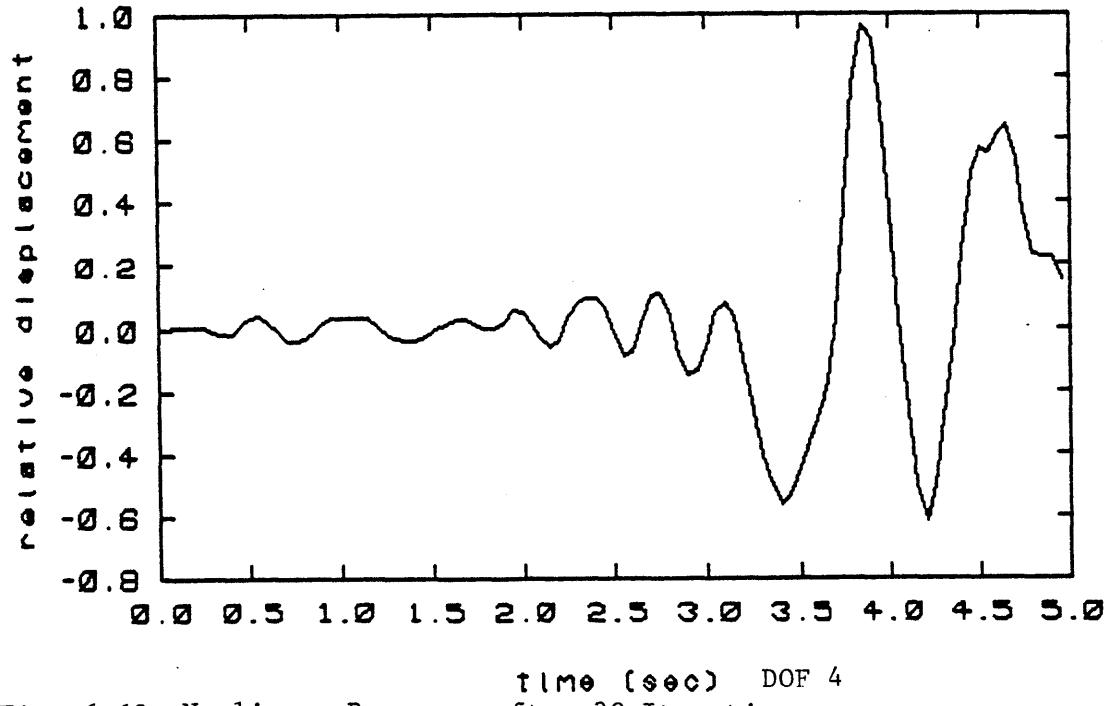

Fig. 6.62 Nonlinear Response after 30 Iterations
(6 linear modes, time increment of 0.05 s)

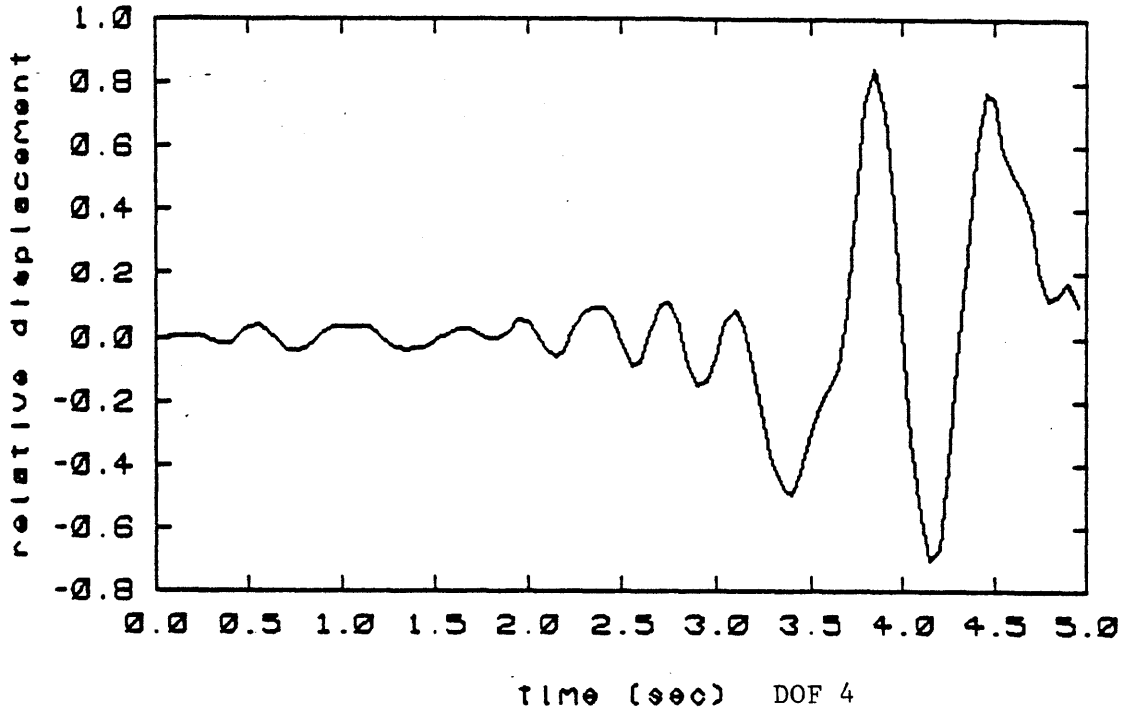

Fig. 6.63 Nonlinear Response after 30 Iterations
(1 linear mode, time increment of 0.05 s)

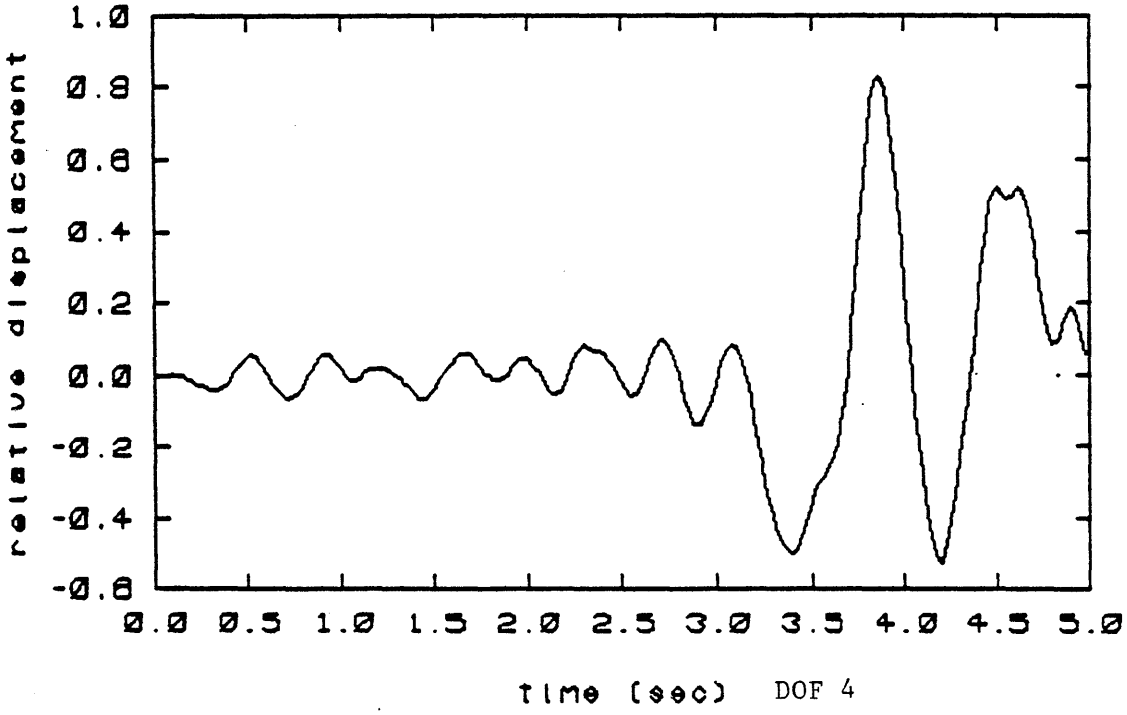

Fig. 6.64 Nonlinear Response after 25 Iterations
(3 linear modes, time increment of 0.02 s)

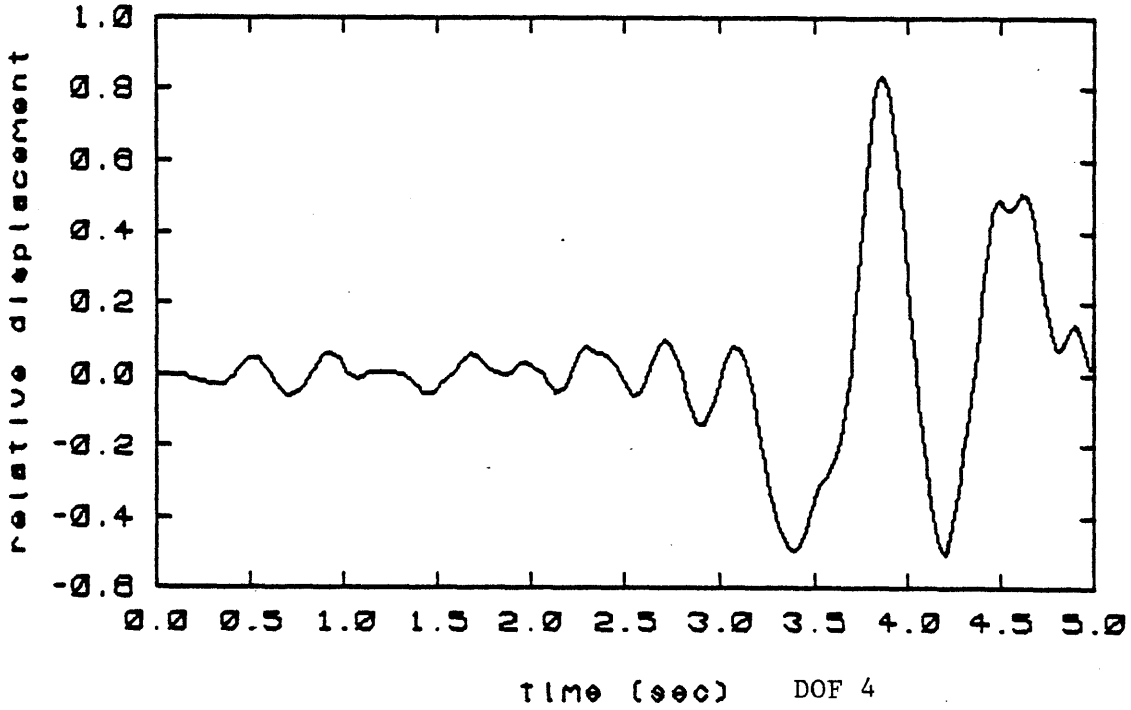

Fig. 6.65 Nonlinear Response after 30 Iterations
(3 linear modes, time increment of 0.02 s)

DOF	Maximum Displ.	Time (sec)	Maximum Velocity	Time (sec)	Maximum Accel.	Time (sec)
1	0.838	3.86	7.151	3.76	-58.10	3.82
2	-0.027	3.38	0.581	4.26	-23.00	4.94
3	-0.001	3.84	-0.019	4.28	0.785	4.94
4	0.838	3.86	7.152	3.76	-58.23	3.82
5	-0.030	3.84	0.601	3.96	-25.45	3.98
6	-0.001	3.84	-0.019	4.28	0.785	4.94

a. Direct Time Integration Results

DOF	Maximum Displ.	Time (sec)	Maximum Velocity	Time (sec)	Maximum Accel.	Time (sec)
1	0.837	3.86	7.215	3.76	-64.14	3.84
2	-0.028	3.38	-0.860	4.96	-31.22	4.92
3	-0.001	3.82	0.034	4.96	-1.38	4.98
4	0.837	3.86	7.215	3.76	-64.13	3.84
5	-0.031	4.66	1.177	4.96	-52.19	4.98
6	-0.001	3.82	0.034	4.96	-1.38	4.98

b. HFT Solution Scheme Results, 30 Iterations

Table 6.7 Maximum Response Values for Single-Bay Offshore Structure

of freedom. The maximum velocities and accelerations exhibit a larger error, particularly for those degrees of freedom associated with no external load. Errors in the lateral degree of freedom velocities are approximately 1% and accelerations, 10%. Comparisons of other degrees of freedom indicate a larger error with times of occurrence differing appreciably in some cases. Although the maximum velocities and accelerations were not reproduced as well, it is noted that the HFT solution scheme derives the velocities and accelerations indirectly by applying a finite difference expansion to the converged displacement response, possibly producing inaccurate values for the final time step and resulting in a false impression of the maximum response.

Based on these analyses, the optimum HFT solution scheme consisted of using three linear modes, a time increment of 0.02 s, and artificial hysteretic damping ratio of 0.35. Thirty iterations were required for an acceptable displacement convergence.

The efficiency of the optimum HFT scheme compared to the direct time integration analysis is detailed in Table 6.8, listing the expended CPU times. The optimum HFT solution is four times more expensive than the time integration solution. Notice that when the time increment is decreased from 0.05 s to 0.02 s, the computation time increases by a factor of 2.1 (140/66). Decreasing the number of modes from six to three decreases the computation

Solution Scheme	Time Increment	No. of Modes	No. of Iterations	Hysteretic Damping	CPU Time (sec)
Time Integration					
linear	0.02	6	---	---	15
nonlinear	0.02	6	---	---	22
HFT	0.02	6	30	0.5	140
	0.05	6	30	0.35	66
	0.05	1	30	0.35	32
	0.02	3	30	0.35	100

Table 6.8 Computation Times for Single-Bay Offshore Structure

time by a factor of 1.4 (140/100). As a consequence, the main contributor to the computation time in this particular problem is the pseudo-force history evaluation, aggravated by the complexity of the tubular brace material model.

The first portion of this study demonstrated the ability of the HFT scheme to reproduce the nonlinear response of a hypothetical offshore structure. Efficiency considerations, however, would prevent its use for such a small problem whose critical time increment was governed by the material model evaluation, rather than numerical integration considerations.

6.5.2 Two-Bay Offshore Structure Subjected to Taft Earthquake

The successfull, albeit expensive, application of the HFT scheme to the solution of a single-bay offshore structure subjected to a seismic excitation prompted an extension to a more realistic model of the so-called Southern California structure investigated in other studies (12,27,42). The structure consists of two bays, each with a height of 60', and is situated in a water depth of 100'. The analysis was limited to a two-dimensional lumped mass frame model with material nonlinearities only (MNO). Pertinent structural parameters are given in Fig. 6.66. The vertical legs were modelled by linear elastic tubular beam elements. The deck was replaced by a heavy horizontal linear elastic beam element. All diagonal braces were

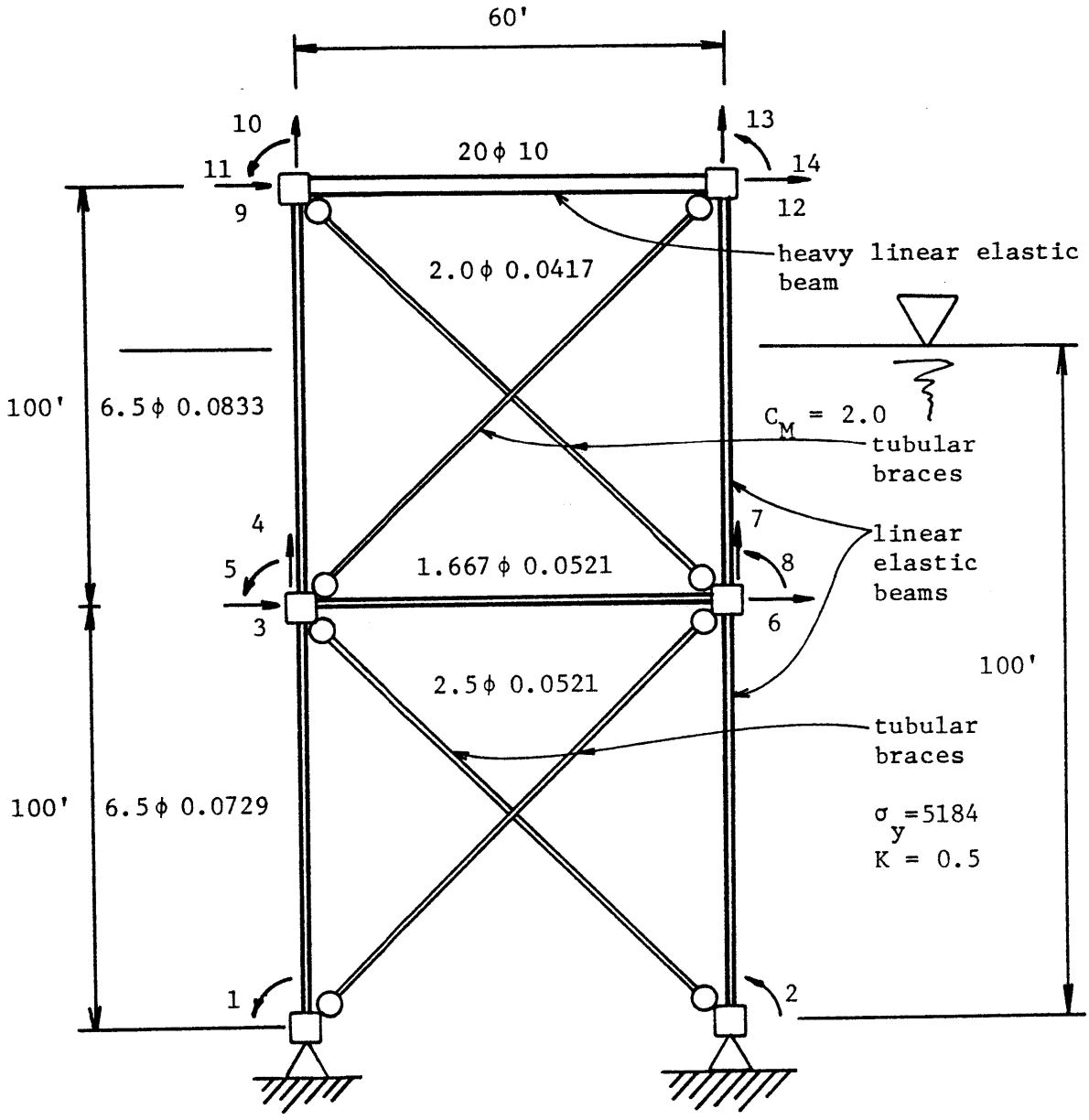

Fig. 6.66 Two-Bay Offshore Structure Subjected to Taft Earthquake

modelled with the tubular brace material model, fixed-fixed end conditions. The surrounding sea water was simulated by the added mass effect with inertia coefficient C_M=2.0. Entrained water was included for members below the water surface. Foundation conditions were simplified by specifying pinned ends for the appropriate leg members. All together there were 14 degrees of freedom. Damping was Rayleigh type with a damping ratio of 5% at modes one and four. An eigenvalue analysis gave the following structural periods:

T_1=1.16s, T_2=0.27s, T_3=0.24s, T_4=0.15s, ... , T_{14}=0.0001s

The direct time integration analyses were conducted with the Newmark integrator (α=0.25, δ =0.50), modified Newton equilibrium iterator, and incremental formulation. The time increment was 0.01 s for both the time integration and HFT analyses. To reduce the computational cost of the HFT analysis, only the first mode was included, implying that at best the lateral response would be adequately captured. No artificial damping or mode updating was admitted.

Ten seconds of the Taft earthquake were used as the input excitation. Based on API guidelines (4) the strength level earthquake for Southern California has an approximate magnitude of 0.25 g, and consequently the Taft earthquake was scaled to the ductility level magnitude of 0.50 g.

Results for the direct time integration analyses are presented in Fig. 6.67, the linear response, and Fig. 6.68, the nonlinear response. Both figures correspond to lateral degree of freedom 12 (deck level). The close similarity between the linear and nonlinear responses indicates that the HFT solution should converge rapidly if the fundamental mode can adequately capture the lateral response. Indeed, the HFT scheme converged within three iterations and more than adequately reproduced the nonlinear response of dof 12, shown in Fig. 6.69. The actual computational cost of the HFT scheme was 1/3 that of the direct time integration analysis.

This study established the HFT solution scheme's attractiveness when the shape of the nonlinear response history only differs in its magnitude from the linear response history. Convergence is rapid for such cases and artificial hysteretic damping need not be imposed.

6.5.3 Two-Bay Offshore Structure Subjected to El Centro Earthquake

This portion of the study examined the response of a two-bay structure with more significant nonlinearities. The first 5 seconds of the SE component of the May 1940 El Centro earthquake, shown in Fig. 6.70, were used as the excitation. The earthquake was scaled to 3.0 g to induce an appreciable difference between the linear and nonlinear response. Structural modelling was the same as before,

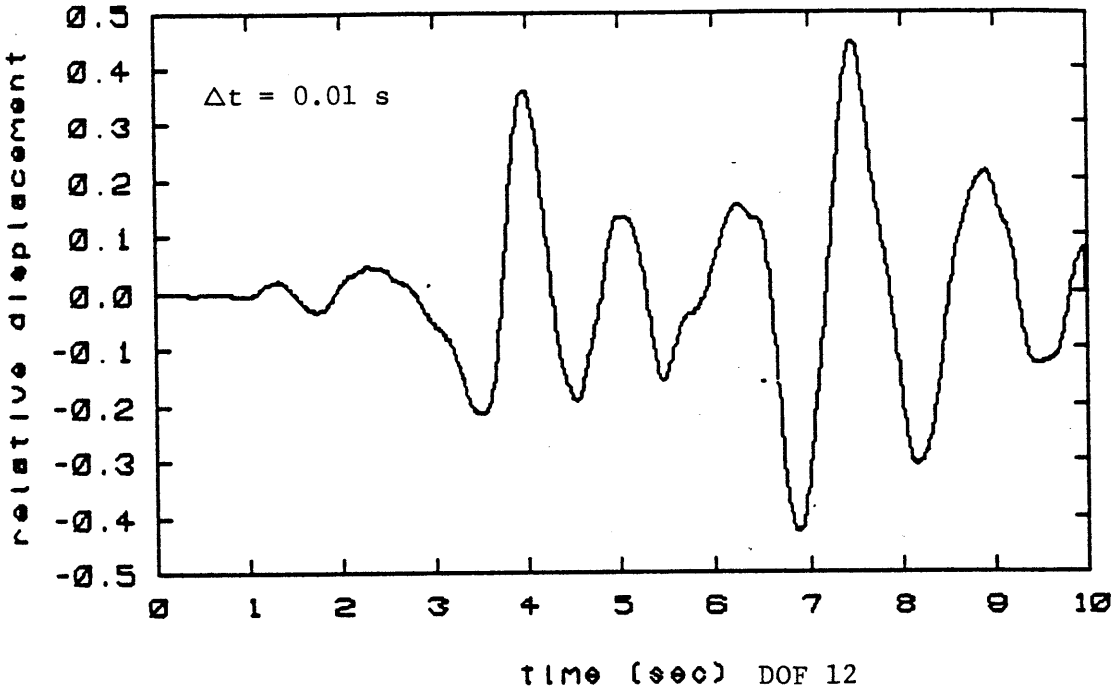

Fig. 6.67 Linear Response to Taft Earthquake
(lateral deck displacement)

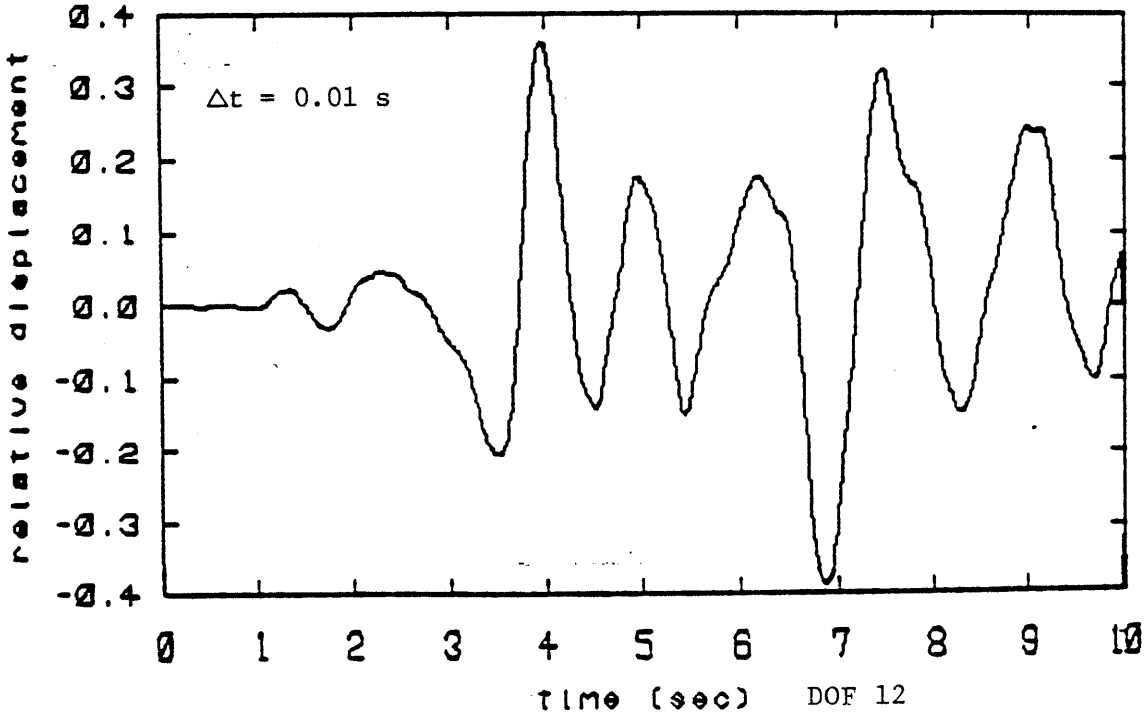

Fig. 6.68 Nonlinear Response to Taft Earthquake
(lateral deck displacement, time integration)

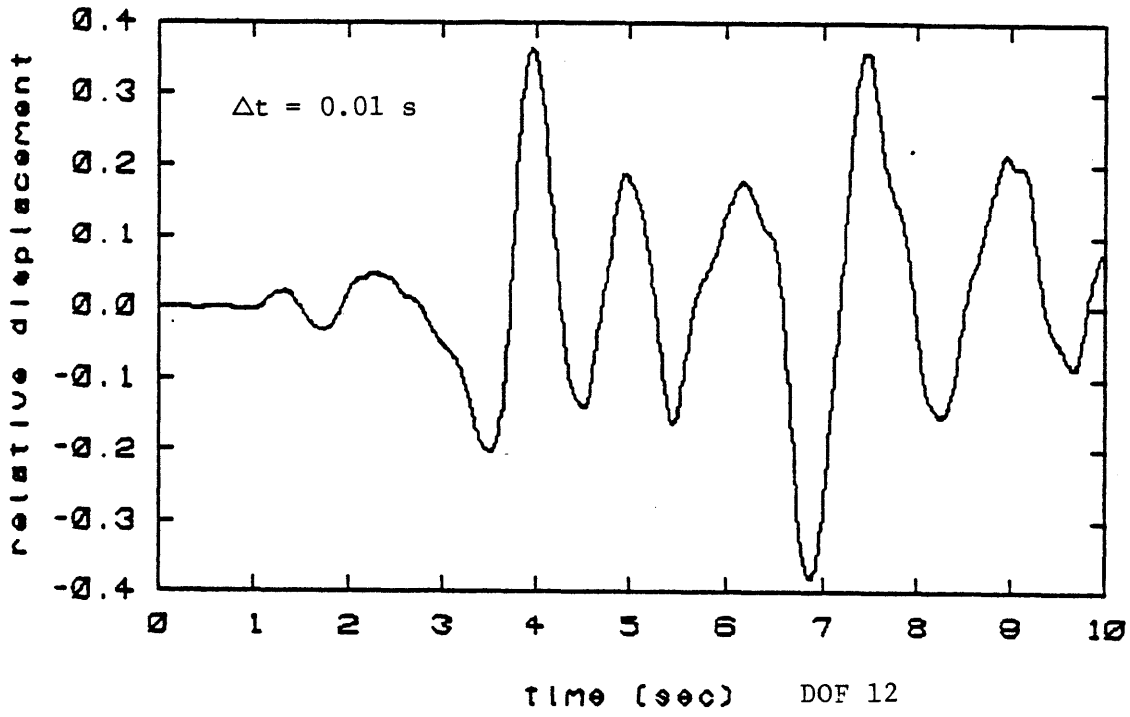

Fig. 6.69 Nonlinear Response after 3 Iterations
(1 linear mode, no artificial damping)

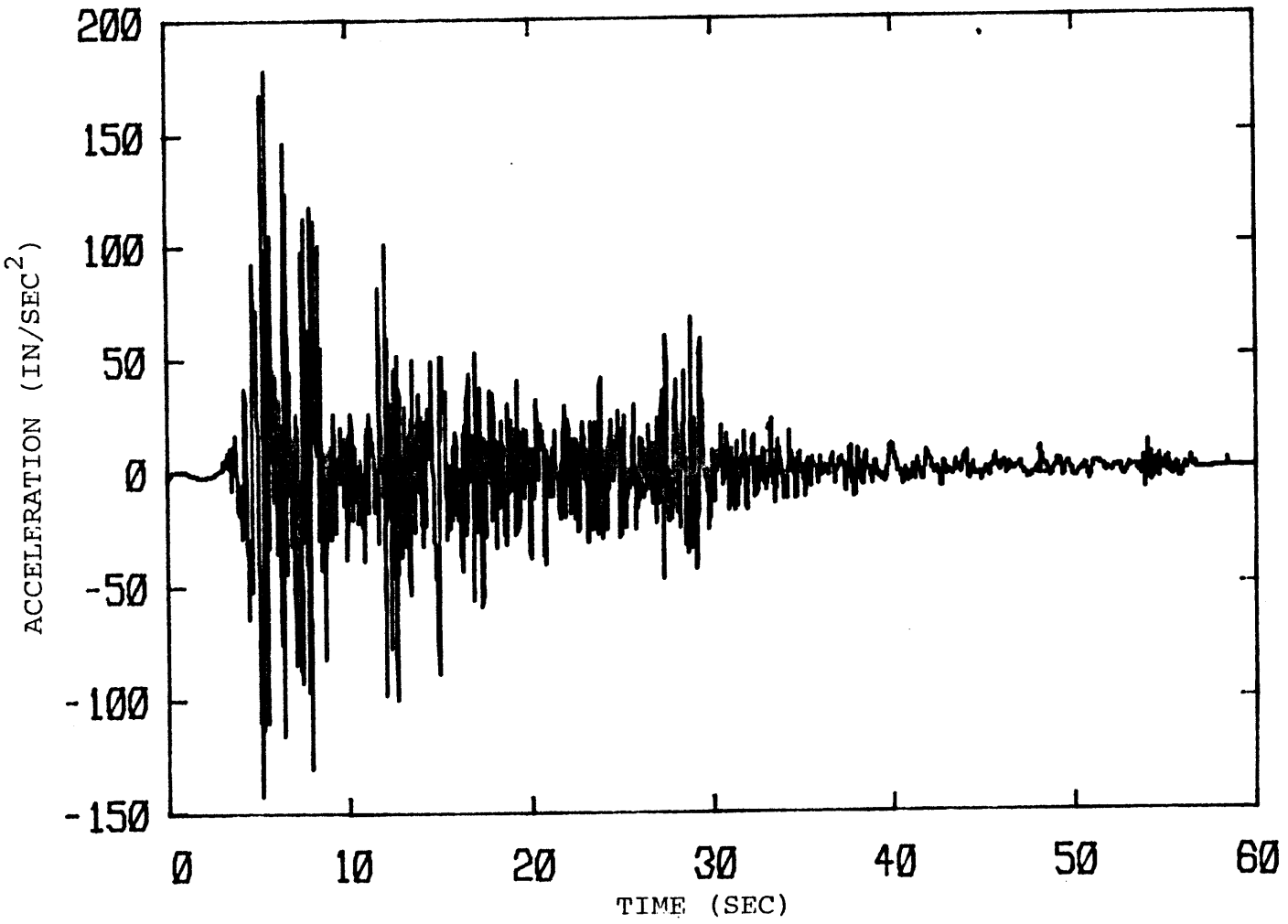

Fig. 6.70 El Centro Acceleration History

except the base was now specified as fixed-fixed. The structural periods are as follows:

$$T_1=1.11s,\ T_2=0.27s,\ T_3=0.24s,\ \ldots\ ,\ T_{12}=0.003s$$

Rayleigh damping was included by specifying a damping ratio of 5% for modes one and seven. Relevant structural parameters are provided in Fig. 6.71. It is noted that the first seven modes correspond to reasonable physical deformations while the highest five modes correspond to deformations of the very stiff horizontal deck beam.

Direct time integration analyses were conducted using the trapezoidal rule numerical integrator combined with a modified Newton iteration scheme (stiffness updating after each time step). The time increment was 0.02 s. Figures 6.72 and 6.73 depict the linear and nonlinear displacement response for lateral degree of freedom 10 at the deck level.

Based on preliminary studies, the critical time increment for the HFT analyses was also 0.02 s, and an artificial hysteretic damping ratio of 0.5 was necessary to prevent instabilities. In the first HFT analysis, seven linear modes were used throughout the iterative process to examine how efficiently the HFT scheme could reproduce the exact nonlinear response. However, the solution was terminated after 45 iterations because of the excessive computational cost. Figure 6.74 depicts the response after 45 iterations using the seven lowest modes (other modes do not participate in the response). Notice that the response

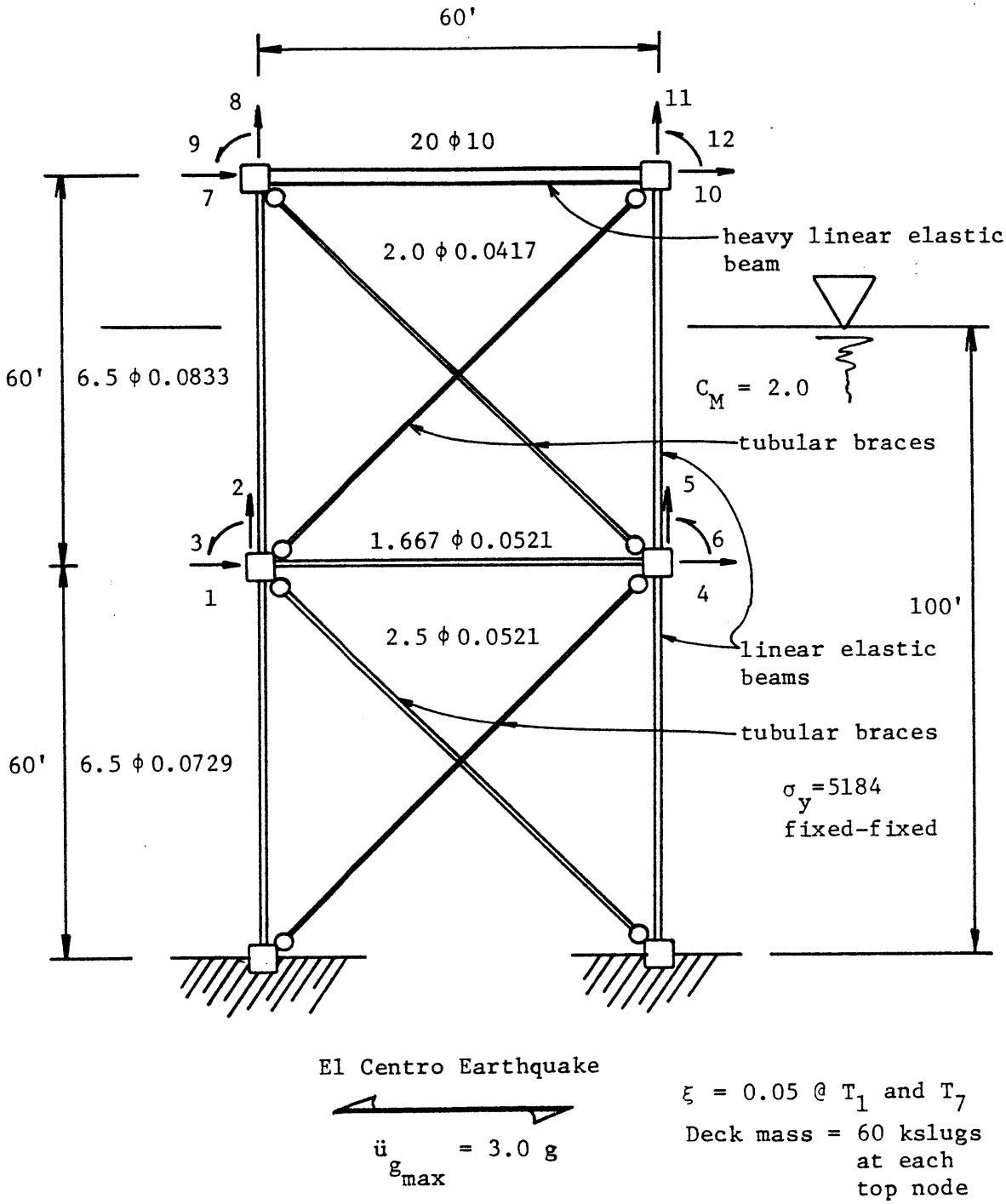

Fig. 6.71 Two-Bay Offshore Structure Subjected to El Centro Earthquake

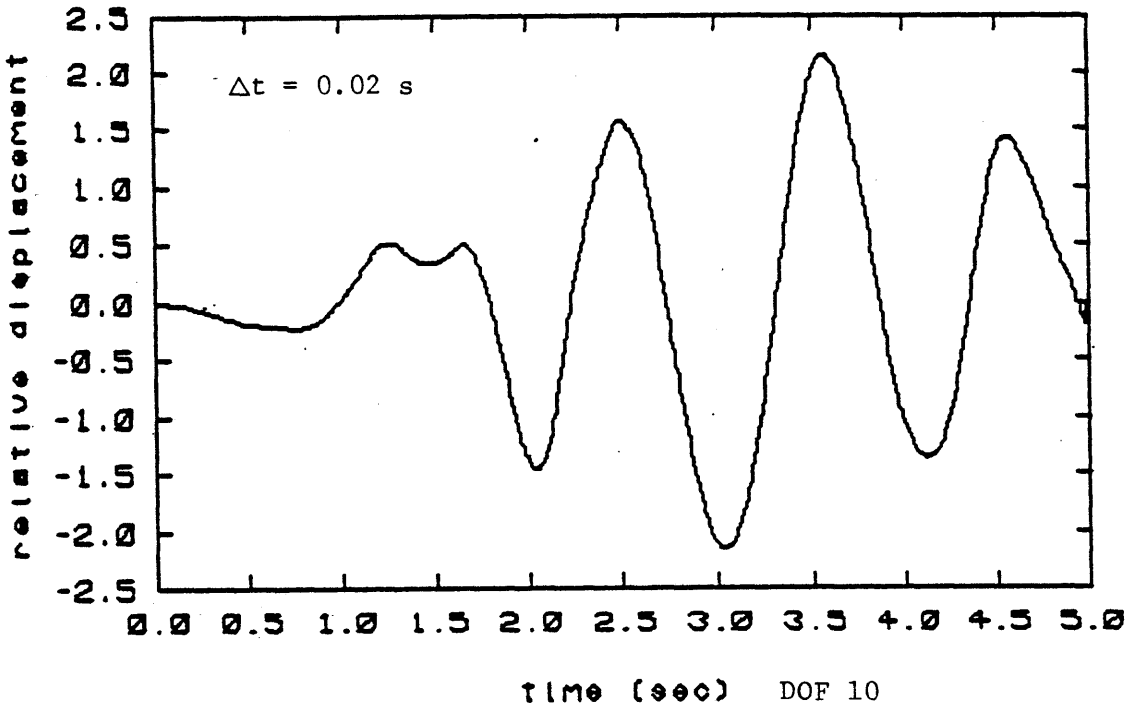

Fig. 6.72 Linear Response to El Centro Earthquake
(lateral deck displacement)

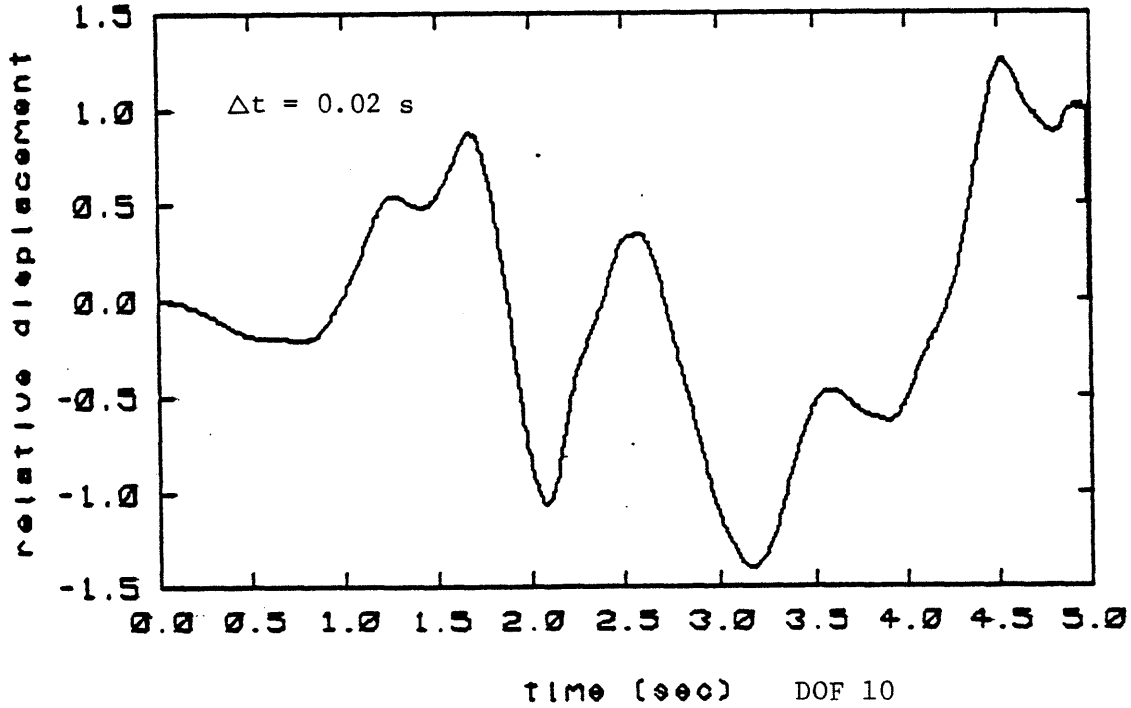

Fig. 6.73 Nonlinear Response to El Centro Earthquake
(lateral deck displacment, time integration)

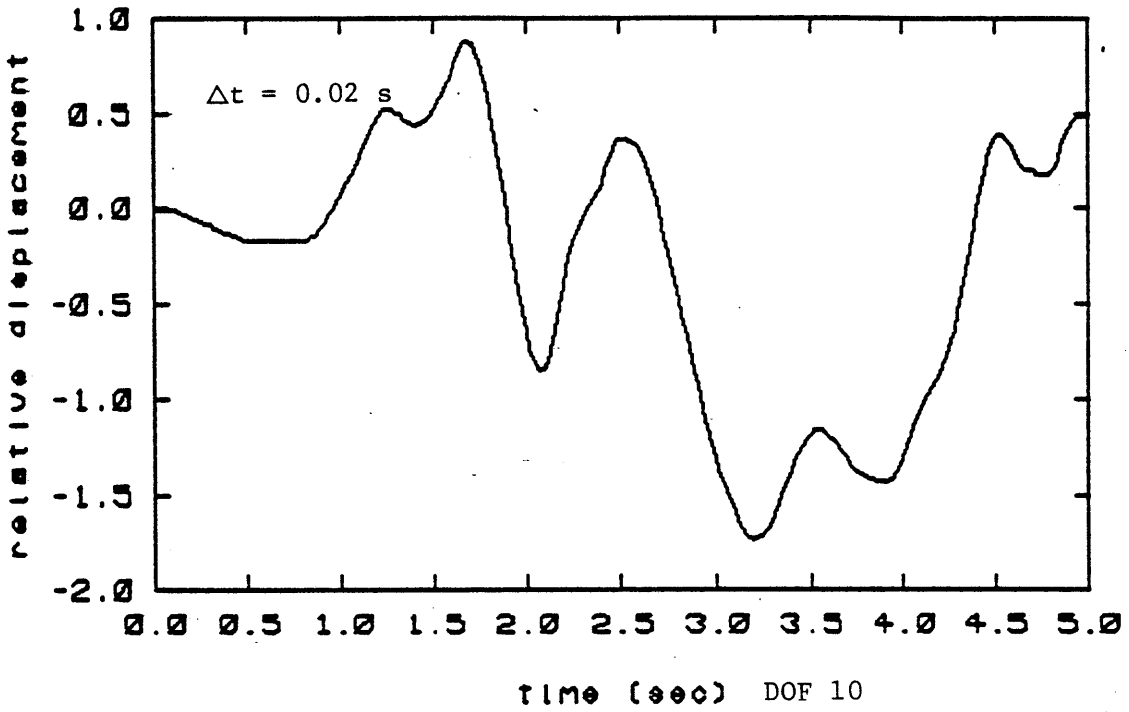

Fig. 6.74 Nonlinear Response after 45 Iterations
(7 linear modes, artificial viscous damping ratio of 0.50)

after time 3.0 s has not yet converged adequately as seen by comparing the response in Fig. 6.73 with that in Fig. 6.74.

As a result of the slow convergence of the HFT scheme using seven modes, a new solution algorithm was developed to accelerate the convergence process. The algorithm consists simply of using one mode for the first ten iterations and then adding more linear modes for successive iterations. Using this approach, the first ten iterations employing the fundamental linear mode produced the response shown in Fig. 6.75. The next twelve iterations included the lowest three linear modes, giving the response depicted in Fig. 6.76. Notice that the response obtained with one mode for 10 iterations and then three modes for the next 12 iterations produced better results than when using seven modes for 45 iterations. Furthermore, even the response after ten iterations using one linear mode is a fairly good estimate of the actual nonlinear response. The HFT response, of course, has yet to converge, possibly requiring additional modes. Computation times for the various analyses are tabulated in Table 6.9.

This last portion of the offshore structure study demonstrated that employing all significant modes in an HFT analysis during all iterations may result in an extremely inefficient solution process. An alternate solution algorithm was implemented whereby only a few modes were used during the initial iterative cycles to obtain a good estimate of the dominating nonlinear response, and then

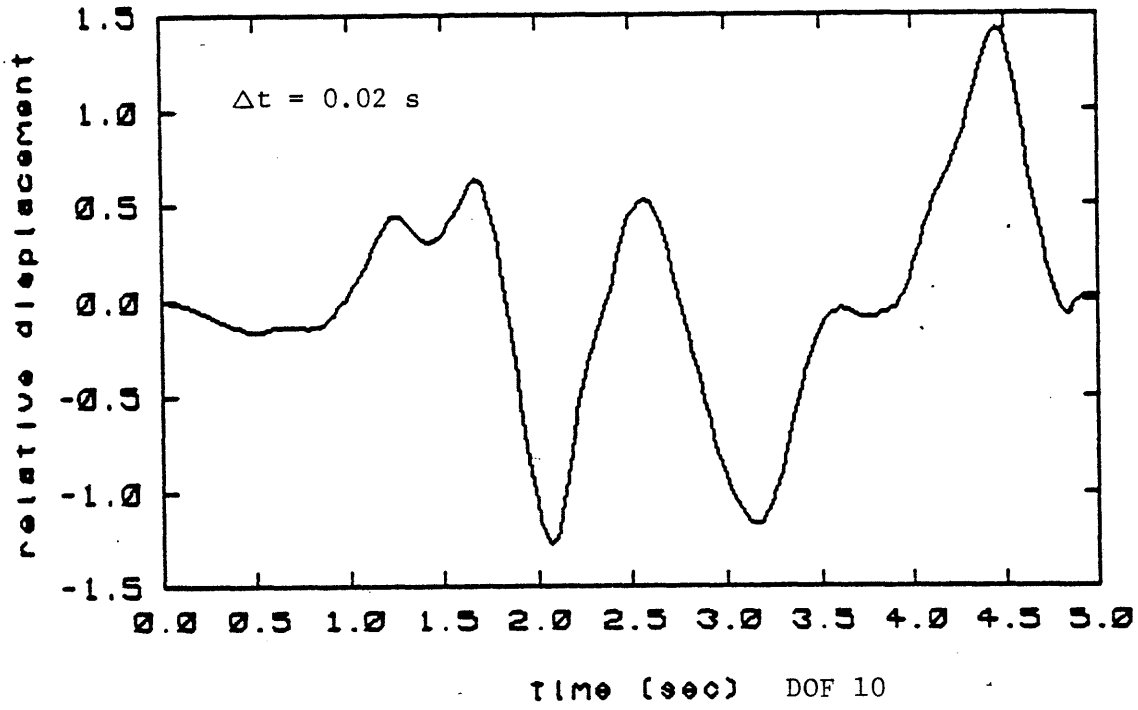

Fig. 6.75 Nonlinear Response after 10 Iterations
(1 linear mode)

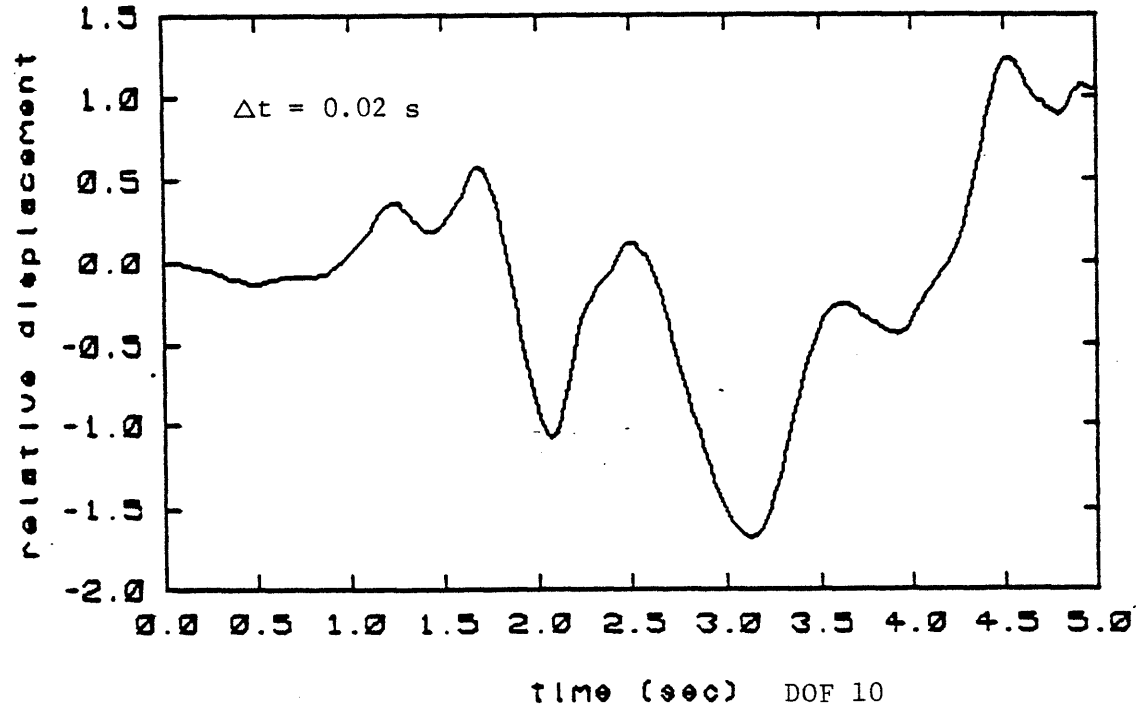

Fig. 6.76 Nonlinear Response after 10+12 Iterations
(3 linear modes)

Solution Scheme	No. of Points	Iterations	Modes	CPU Time (sec)
Time Integration				
linear	250	---	all	25
nonlinear	250	---	all	62
HFT	256	45	7 linear	350
	256	10+12	*	83

time increment = 0.02 seconds for all analyses

* 1 linear for first 10 iterations
3 linear for next 12 iterations

Table 6.9 Computation Times for Two-Bay Offshore Structure Subjected to El Centro Earthquake

additional modes were added during successive cycles to provide a finer refinement of the response. The proposed algorithm proved more efficient and produced better results.

6.6 EXTREMELY SOFT SDOF SYSTEM

This section describes a study where the nonlinear response was characterized by a stiffness much softer than the linear stiffness. The actual response history contained one portion dominated by the linear stiffness and another, by the nonlinear stiffness. Although the HFT scheme could not produce a converged solution using the techniques of the other studies, the sources of the divergence suggest an alternate scheme for implementing the HFT solution.

The study examined the behavior of SDOF systems with extremely low yield levels. Elastic-perfectly plastic material models were employed with a yield displacement of 0.001, producing plastic behavior almost immediately after introducing the load. The excitation consisted of 5 seconds of the Taft earthquake.

The time integration results, shown in Fig. 6.77, were obtained using the trapezoidal rule and Newton equilibrium iteration with a time increment of 0.005 s.

In the HFT analysis a time increment of 0.01 s was specified and an artificial hysteretic damping ratio of 0.75 was employed. The response after 10 and 30 iterations using the linear mode and stiffness is shown in Figs. 6.78 and

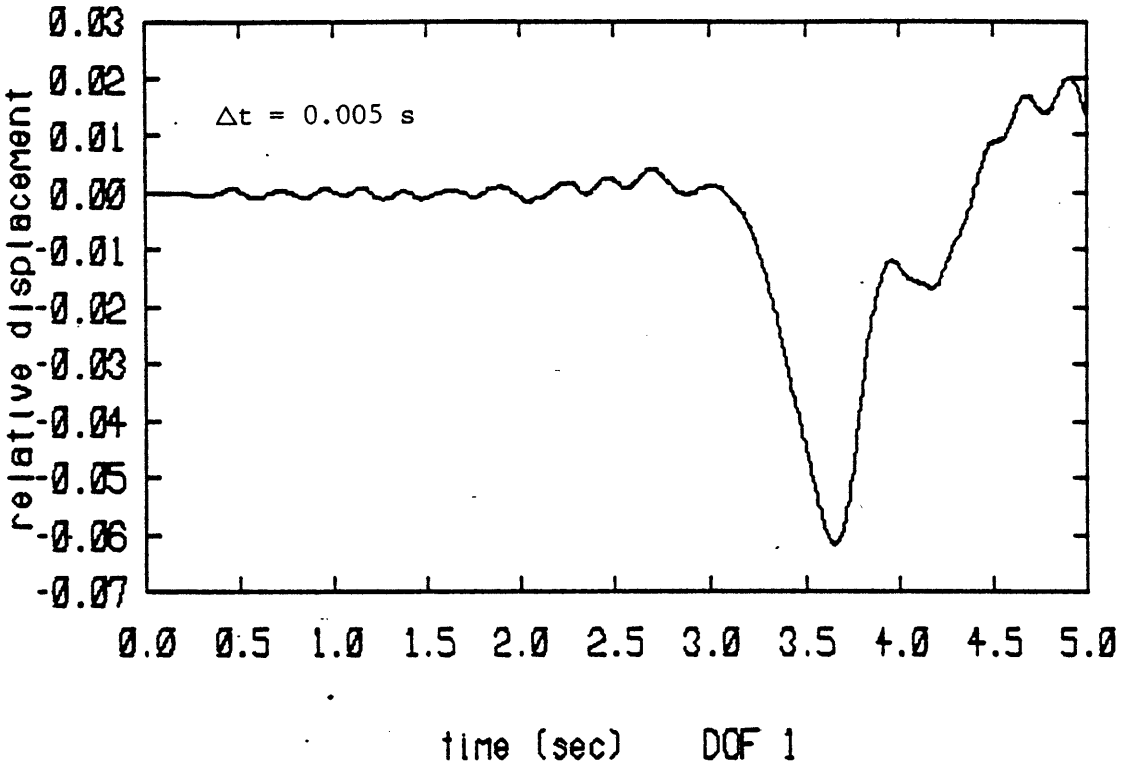

Fig. 6.77 Nonlinear Response Using Direct Time Integration

6.79. These figures indicate that the response is fairly accurate up to time 3.5 seconds, whereupon it begins to diverge and displays an oscillatory behavior not present in the time integration results. This divergence is attributed to the HFT solution scheme being based on a pseudo-force approach. The pseudo-force history converges to its exact form in a forward time progressing fashion, and hence may exhibit significant differences from its converged form during the iterative process. Previous case studies were stabilized during the iterative process by including artificial damping. This particular example appears to be stabilized insufficiently, probably because of the extremely low yield stress, implying significant pseudo-force amplitudes.

A nonlinear mode updating scheme was considered next as a means of stabilizing the problem. The procedure consisted of iterating 5 cycles with the linear mode, updating the stiffness, iterating another 5 cycles with the new secant stiffness, repeating this process for a total of 20 iterations. The initial linear stiffness had a value of 1264, and the secant stiffness after iterations 5, 10, and 15 was 206, 26, and 15, respectively. Figure 6.80 shows the response after 20 iterations using this procedure. Notice that the nonlinear response after time 2.8 seconds is represented fairly well. The response before time 2.8 seconds, however, is incorrect and displays an oscillatory behavior. This result contrasts directly with the previous

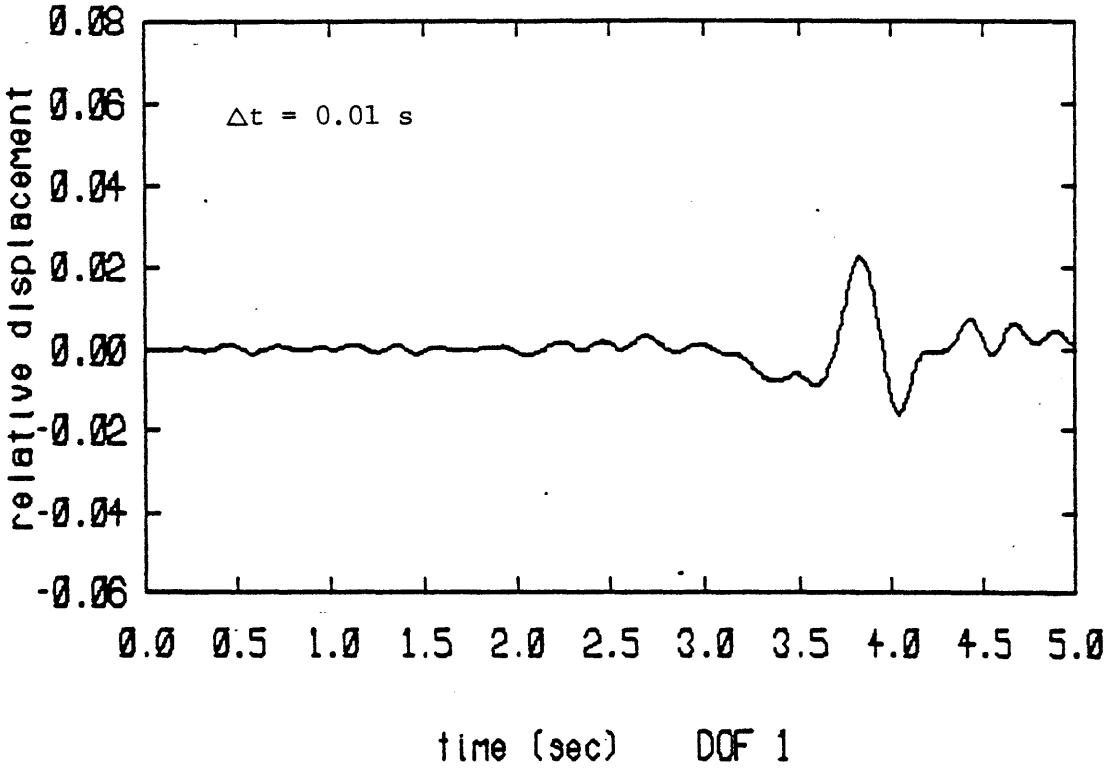

Fig. 6.78 Nonlinear Response after 10 Iterations (linear stiffness)

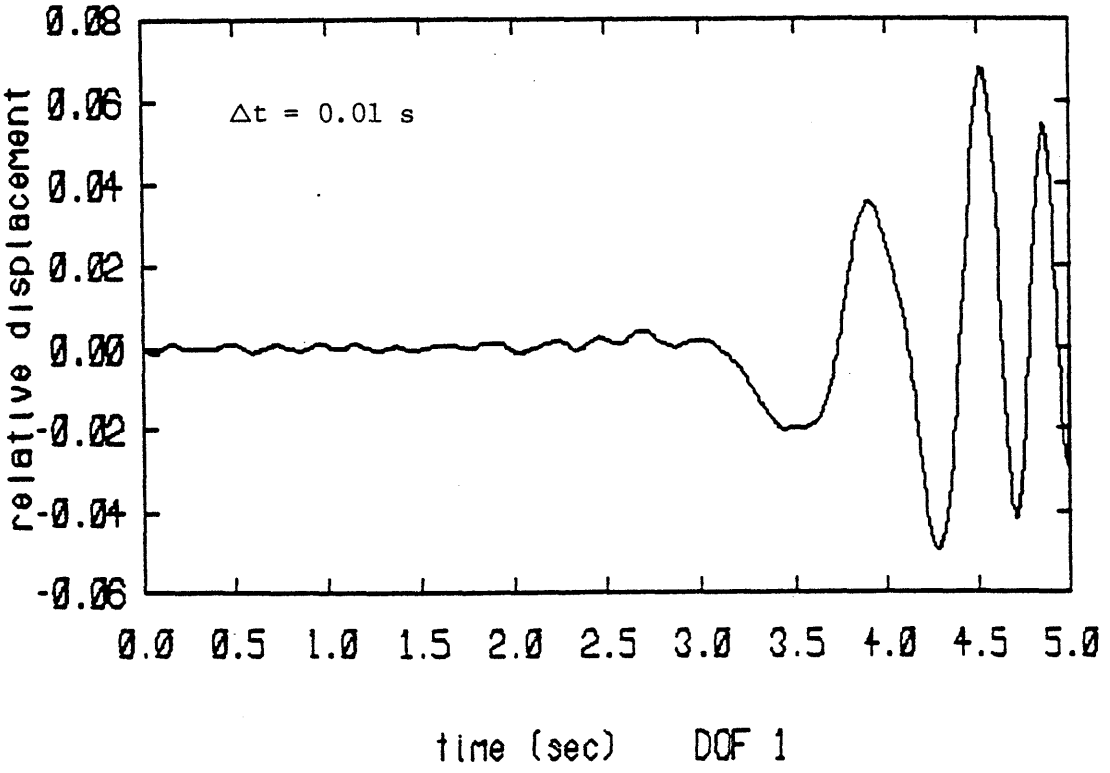

Fig. 6.79 Nonlinear Response after 30 Iterations (linear stiffness)

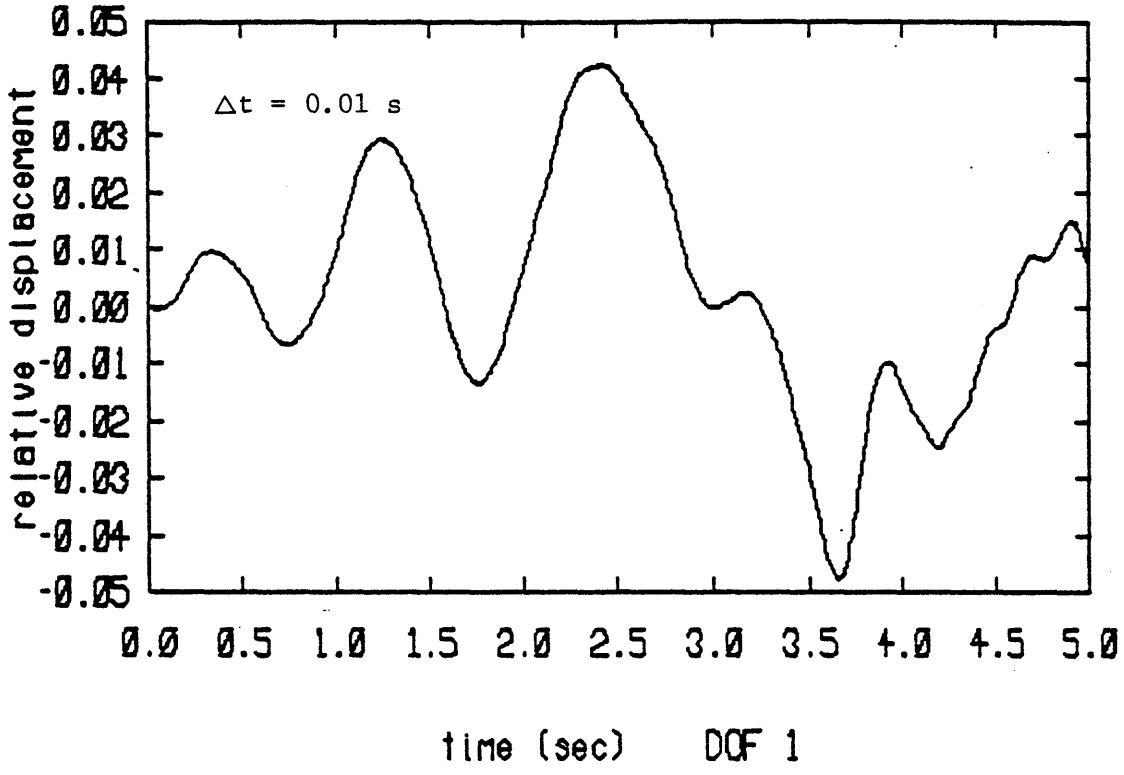

Fig. 6.80 Nonlinear Response after 20 Iterations
(least-squares updated secant stiffness)

results obtained with the linear stiffness.

As a means of diagnosing the source of the poor results, the pseudo-force histories corresponding to iterations 4, 5, 6, and 50 of an updated stiffness case with $k_{sec} = 15$ were plotted and are given in Figs. 6.81 to 6.84. Similarly, the response after iterations 3, 4, 5, 49, and 50 are provided in Figs. 6.85 to 6.89. Notice that the pseudo-force history after time 3.0 seconds appears to converge while that before tends to oscillate and, moreover, varies significantly between consecutive iterative cycles. A similar remark applies to the response history. In particular, the response before time 3.0 seconds appears 90^{o} out of phase for consecutive cycles, even for the 49th and 50th iterations.

Based on these results it is concluded that the HFT solution scheme exhibits convergence problems when the stiffness employed during the iterative process differs significantly from the actual nonlinear stiffness. These convergence problems originate from excessively large pseudo-forces that may be correct theoretically, but induce large inaccuracies during the iterative process. The large pseudo-forces can stem from an excessively large stiffness on the left hand side of the equation of motion combined with a very soft material model or an excessively soft stiffness on the LHS combined with a reasonably stiff material behavior. This problem is amplified

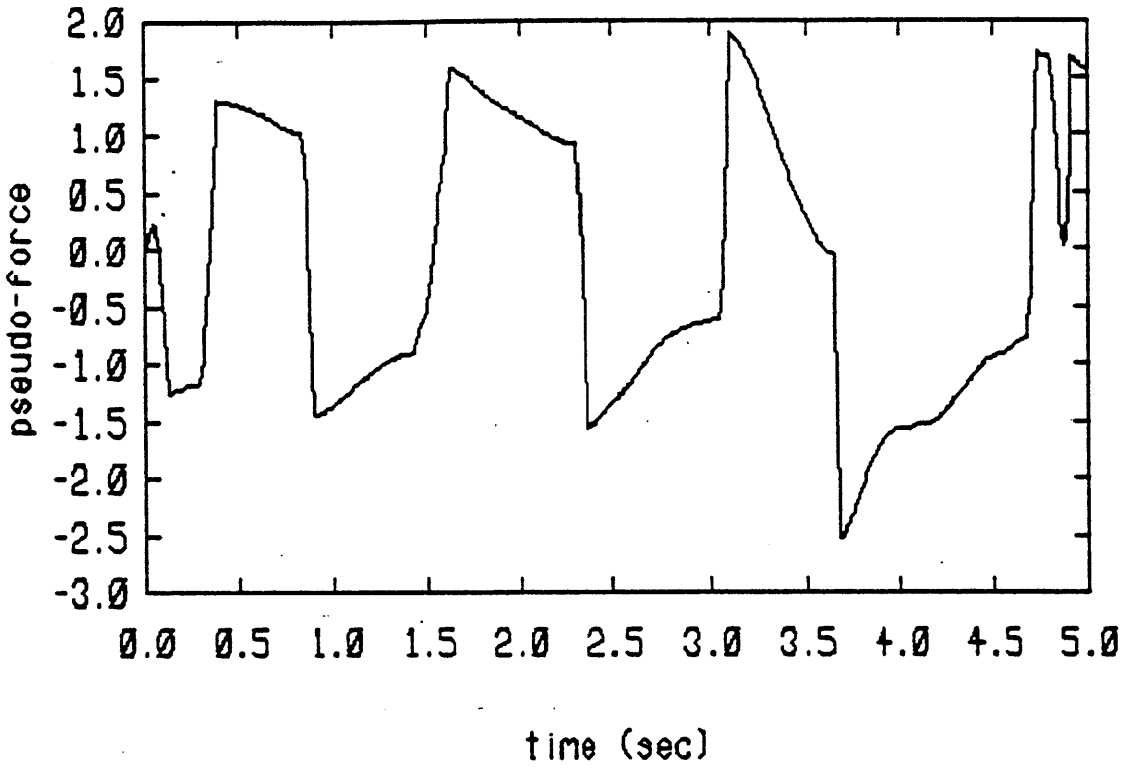

Fig. 6.81 Pseudo-Force History after 4 Iterations

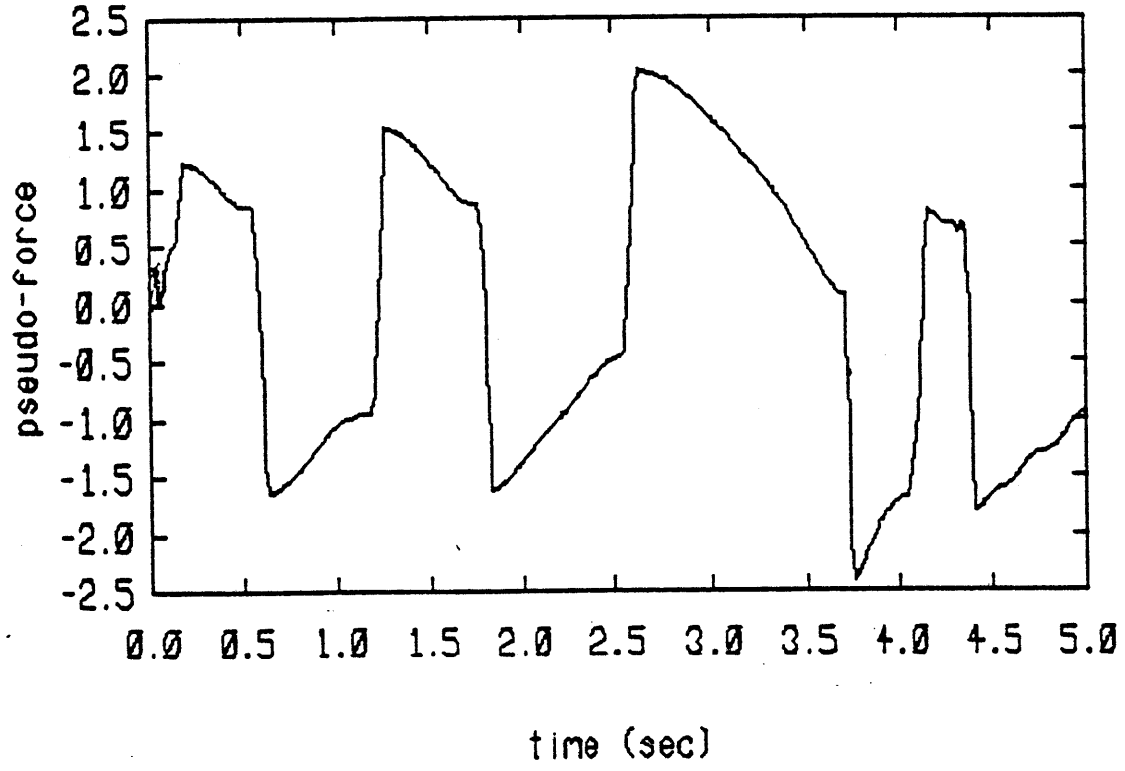

Fig. 6.82 Pseudo-Force History after 5 Iterations

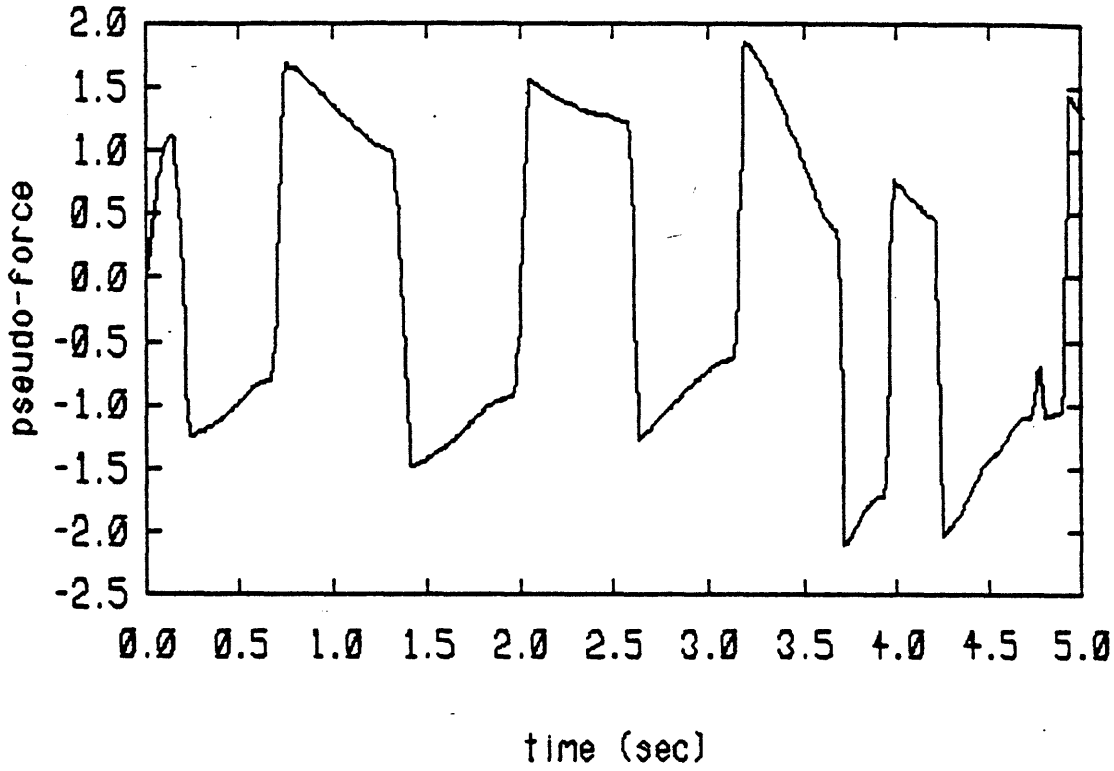

Fig. 6.83 Pseudo-Force History after 6 Iterations

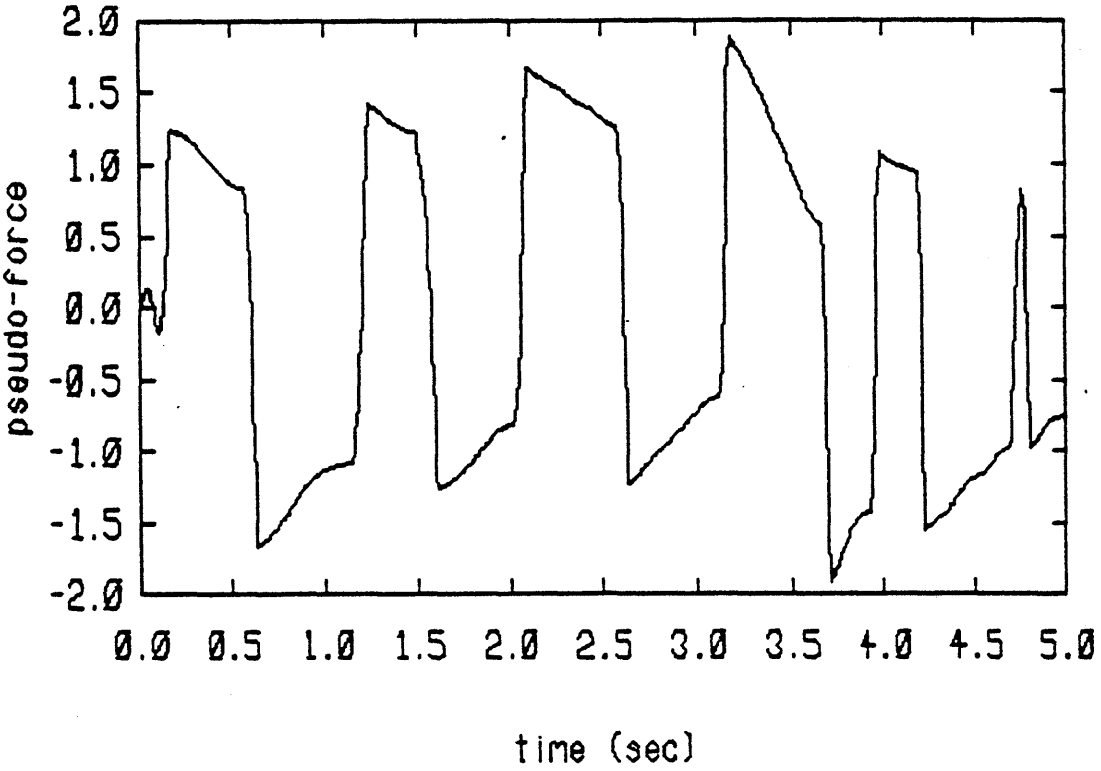

Fig. 6.84 Pseudo-Force History after 50 Iterations

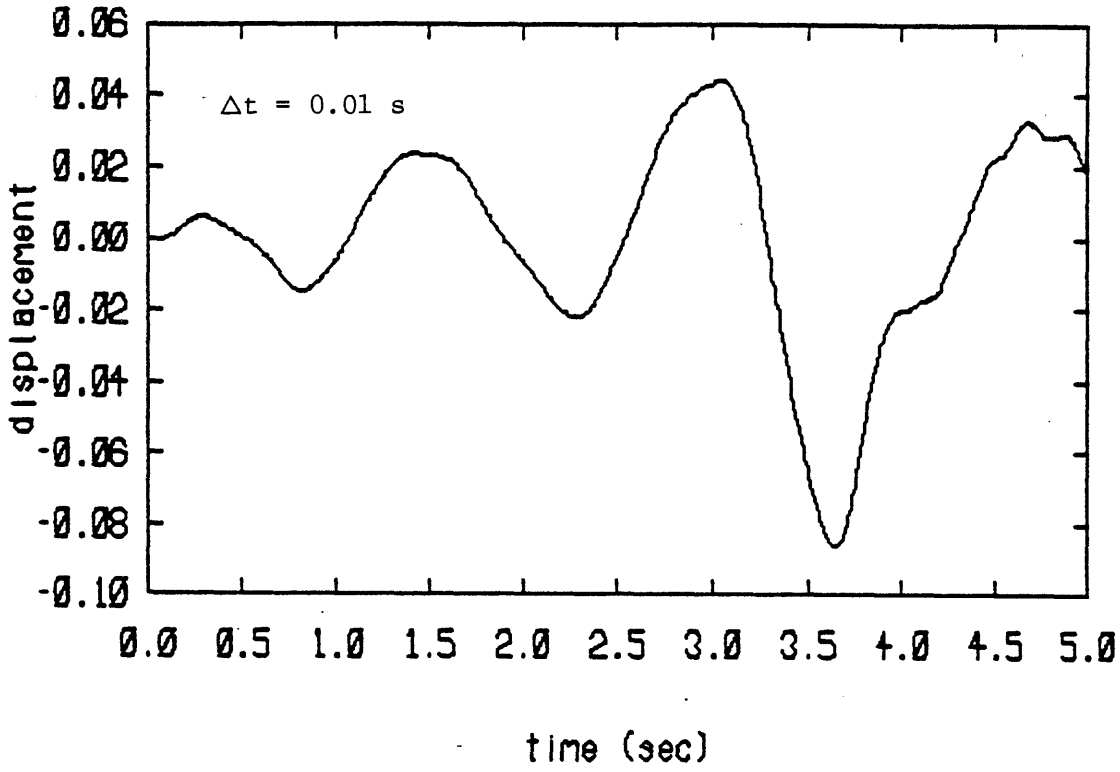

Fig. 6.85 Nonlinear Response after 3 Iterations (updated secant stiffness)

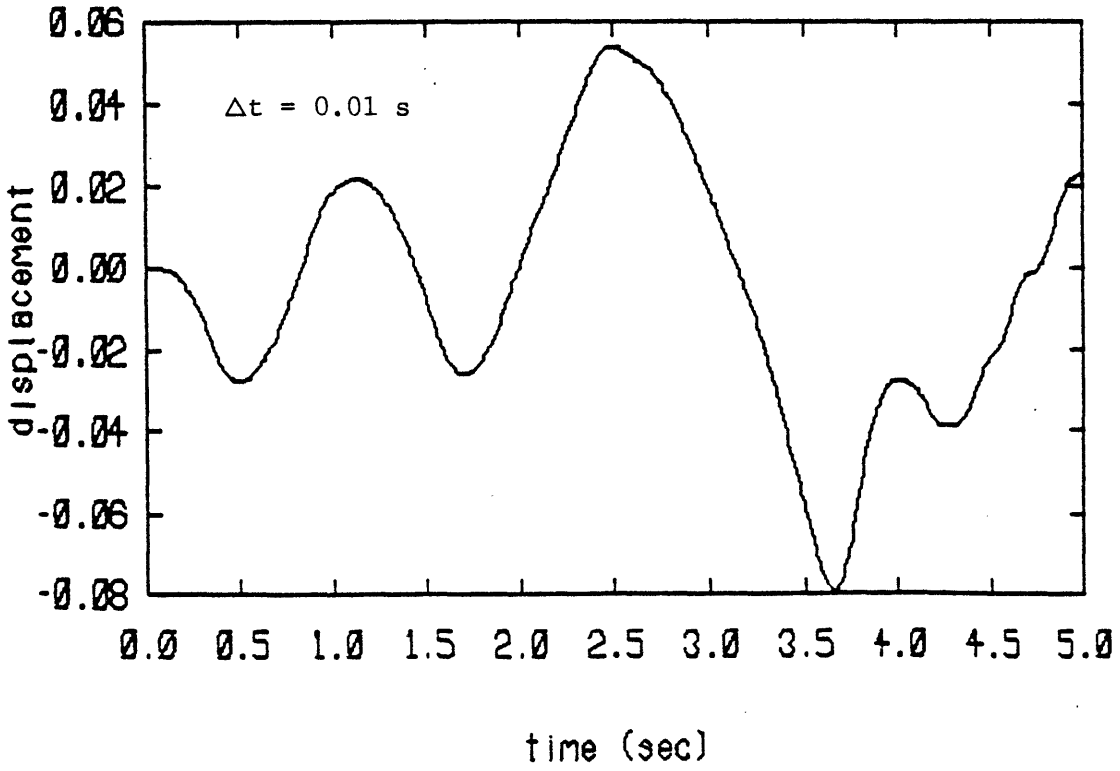

Fig. 6.86 Nonlinear Response after 4 Iterations

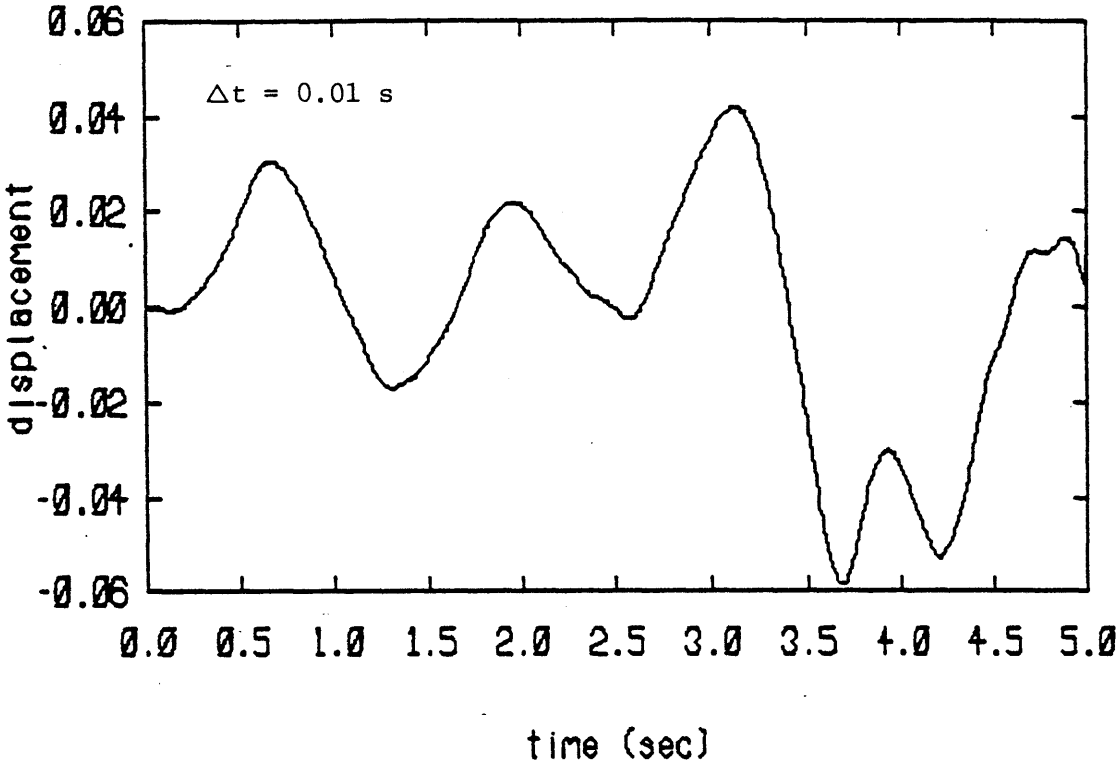

Fig. 6.87 Nonlinear Response after 5 Iterations

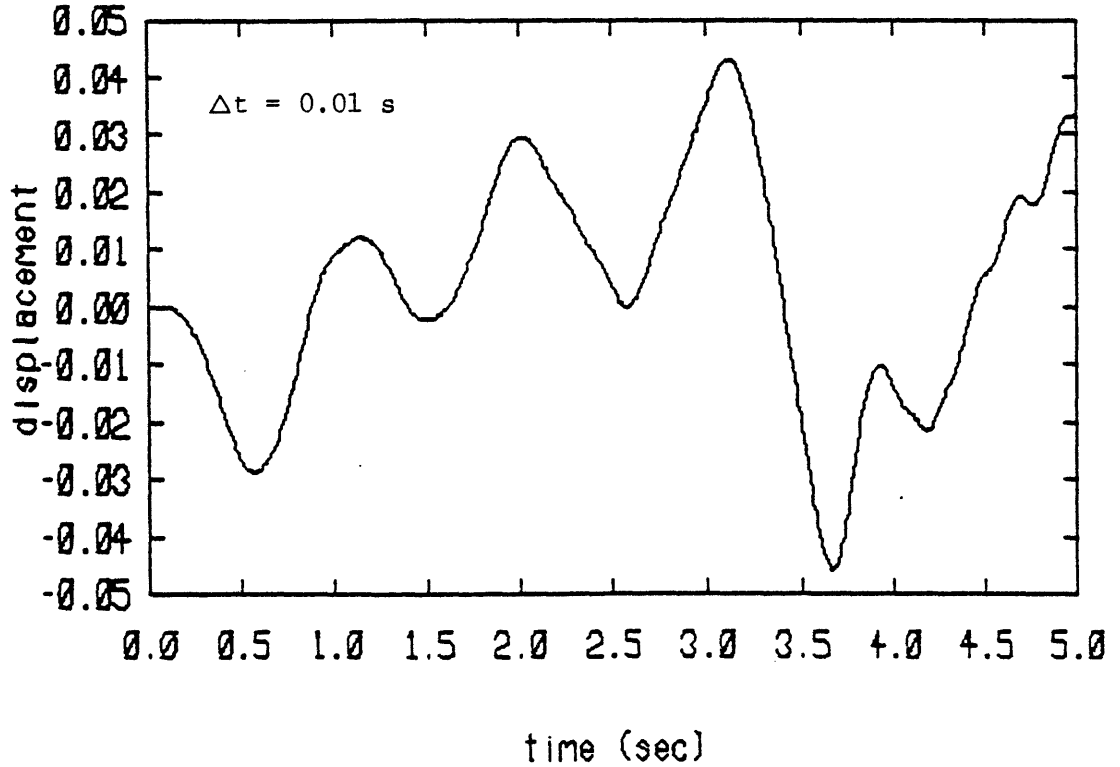

Fig. 6.88 Nonlinear Response after 49 Iterations

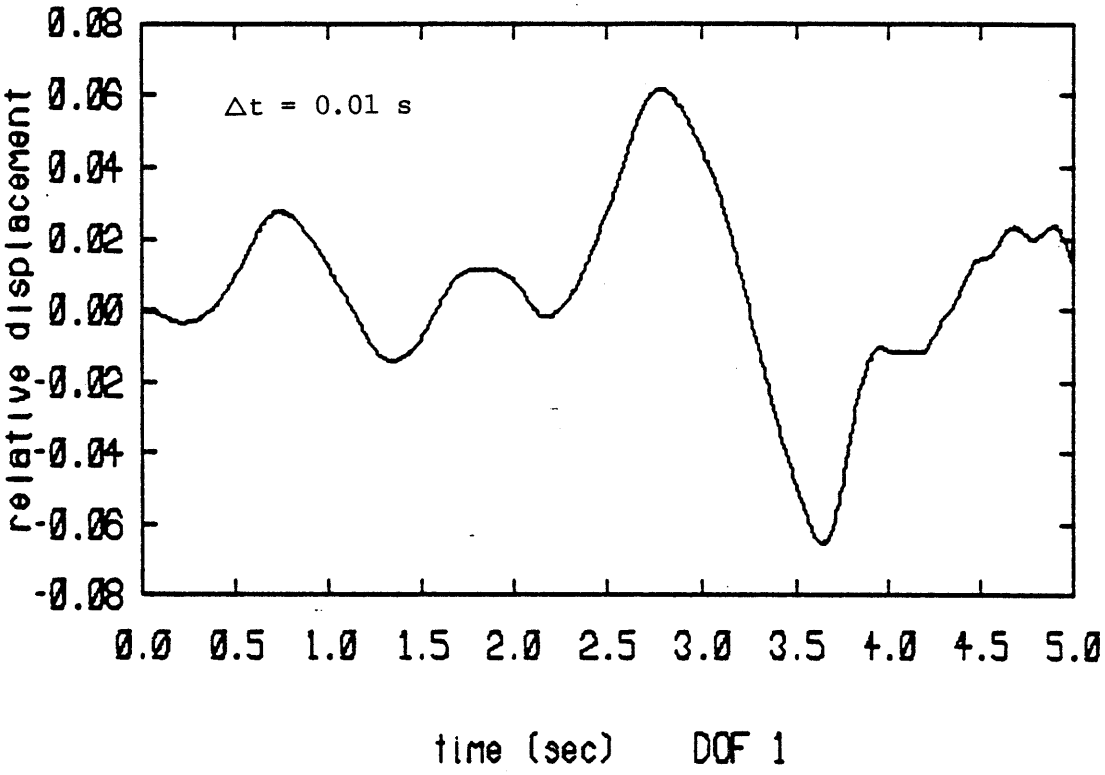

Fig. 6.89 Nonlinear Response after 50 Iterations

unrealistically in a SDOF problem because it is not possible to create a stiffness matrix representing the stiff and soft portions of the structure with a SDOF model.

These conclusions suggest a solution scheme where the excitation is sectioned in time and the response for each section is determined with a different $\underline{K}_{sec}$. For example, in the problem of the very soft structure, k_1 would be used for the interval before 3.0 s and k_{sec}=15 for the interval after. An overlap-save or overlap-add method would then link the two response histories together. In general, the entire history would be analyzed during the first few iterative cycles and then the solution process stopped and the pseudo-force histories examined to determine how the excitation history should be sectioned. This segmenting procedure, however, may involve a substantial participation on the part of the analyst, and decrease the attractiveness of implementing the HFT solution scheme.

The following section examines a similar SDOF problem where the initial stiffness does not govern the actual nonlinear response. In contrast to the problem of this section, the following problem displays rapid convergence.

6.7 BILINEAR ELASTIC SDOF SYSTEM

The HFT scheme was applied to a bilinear elastic SDOF system with period 0.063 s. Relevant problem attributes are shown in Fig. 6.90. The loading consisted of two

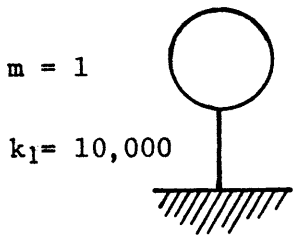

T = 0.063 seconds

ξ = 0

$$\ddot{u}_g = F_1 \sin \omega_1 t + F_2 \sin \omega_2 t$$

F_1 = 50 ω_1 = 1.5

F_2 = 100 ω_2 = 0.005

Bilinear Elastic Material Model

k_1 = 10,000
k_2 = 10

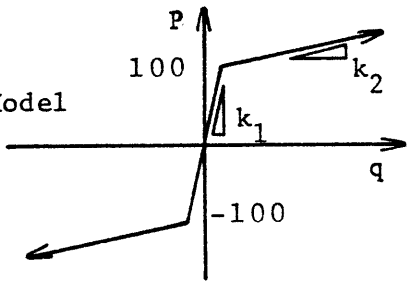

Fig. 6.90 Bilinear Elastic SDOF System

sinusoidal waves; the first had amplitude 50 and period 4.2 s and the second had amplitude 100 and period 1260 s. The dynamic response was generated mainly by the low period component. The bilinear elastic material model had first slope k_1=10,000 and second slope k_2=10.

All time integration responses were obtained with the central difference numerical integrator, and therefore the critical time increment for the linear analysis was

$$\Delta t_{cr} = T_n/\pi = 0.063/\pi = 0.020 \text{ s} \qquad (6.2)$$

The analysis time interval was determined by the high period component (T=1260 s). To ensure that the maximum response was captured, the minimum interval of analysis was therefore 1260 s (one cycle). A time increment of 0.02 s was also used in the nonlinear time integration analysis and proved adequate. The linear and bilinear dynamic responses are shown in Figs. 6.91 and 6.93. Similarly, Fig. 6.92 shows the bilinear static response, obtained by increasing the periods of the load history. The significant differences between the bilinear static and dynamic responses indicate that a dynamic time integration analysis is essential in this study.

The HFT solution scheme was conducted with no artificial damping. Rather than using the linear stiffness k_1 on the LHS of the governing equations, the second stiffness k_2 was employed. The time increment was

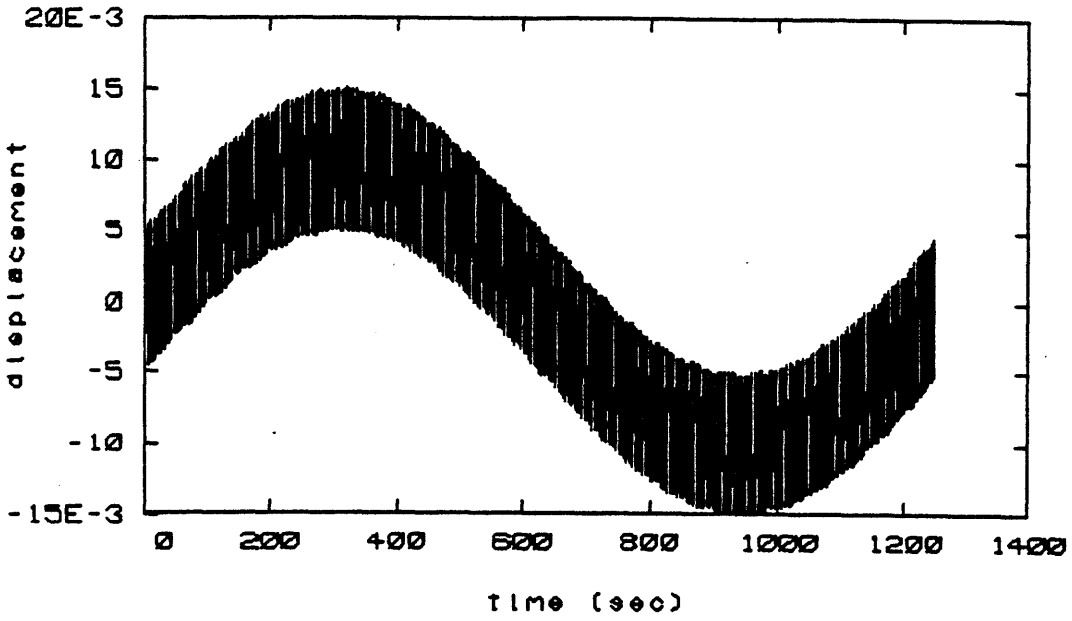

Fig. 6.91 Linear Dynamic Response

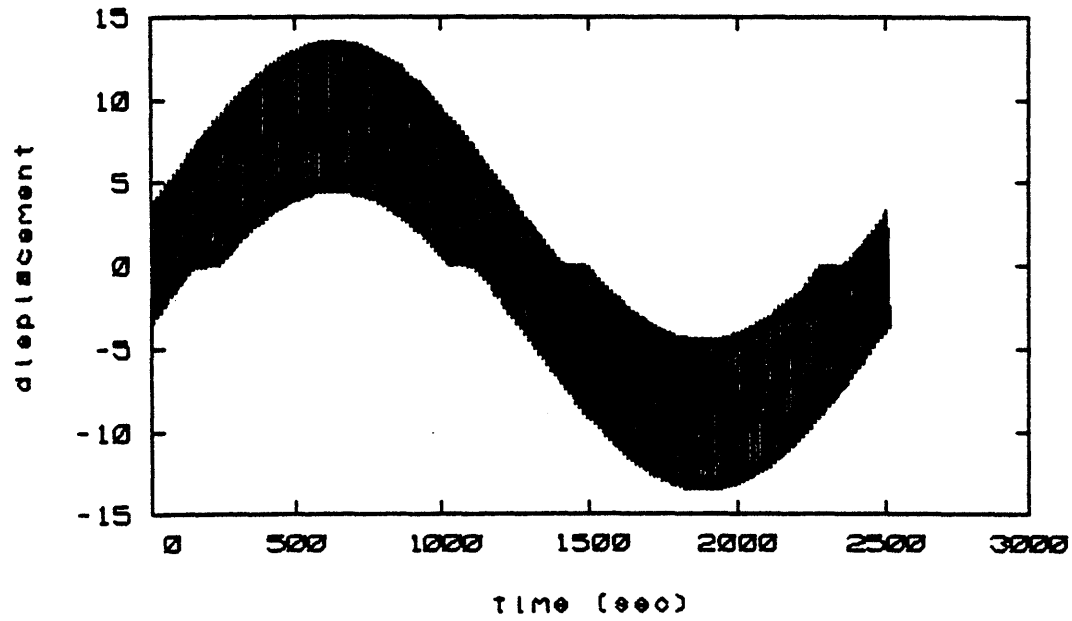

Fig. 6.92 Bilinear Elastic Static Response

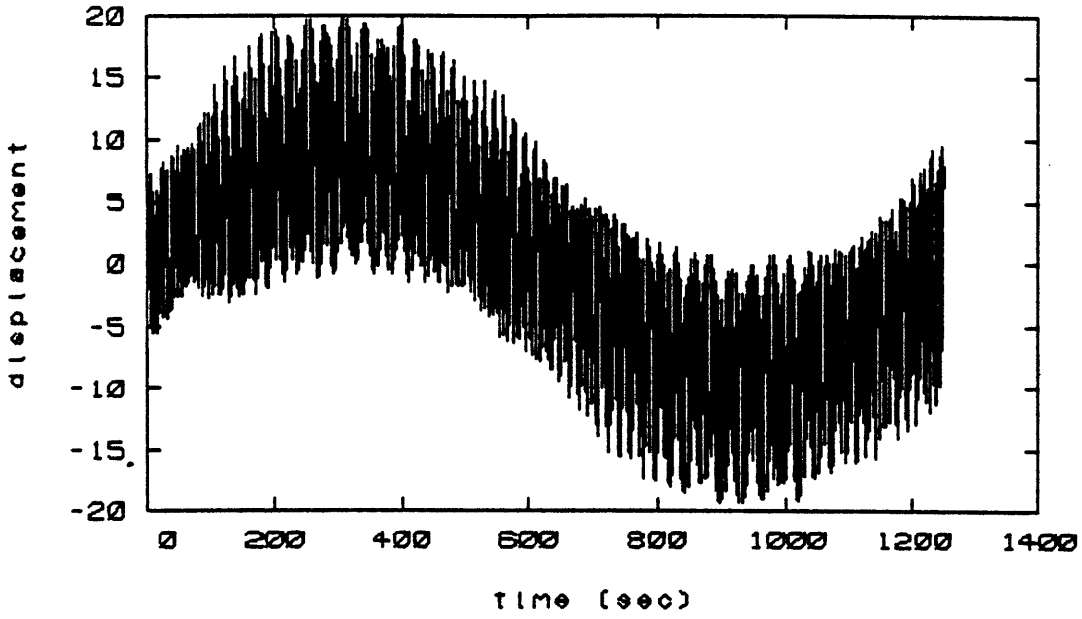

Fig. 6.93 Bilinear Elastic Dynamic Response
(time integration, time increment of 0.02 s)

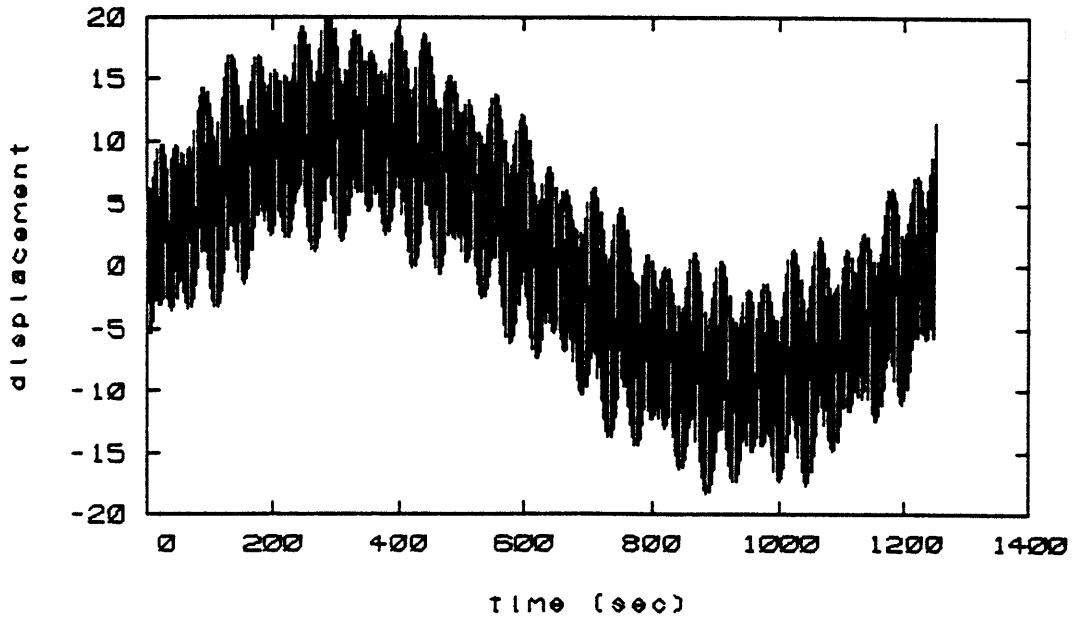

Fig. 6.94 Bilinear Elastic Dynamic Response
(HFT, 3 iterations, time increment of 1 s)

determined by the low period component of the excitation, and hence the time increment was 1 second. Results for the HFT scheme are given in Fig. 6.94. The response converged by the third iteration. Notice that the HFT scheme has accurately captured the maximum response and envelops the general outline of the time integration response history. Deviations between the time integration and HFT results can be attributed to the coarser plotting increment for the HFT response and the inability to capture higher nonlinearly induced frequency components due to the larger time increment.

This study demonstrated the advantages of the HFT scheme when applied to problems with long excitation intervals. The response was not captured exactly, but the peak values and general oscillatory behavior were well reproduced. Computation time for the HFT scheme was more than a factor of two less that that for the time integration analysis. Rapid convergence was attained by using the nonlinear stiffness (k_2) that was more representative of the actual behavior. Notice that further efficiencies would be gained in MDOF implicit time integration analyses, since such problems require a significant amount of time to reformulate and refactorize the stiffness matrix.

Finally, the HFT scheme was more efficient in this problem because the time increment was fifty times larger than that of the time integration analysis. In general, the

time increment for a time integration analysis is determined by the free vibration problem, in other words, the physical properties of the structural system. Explicit methods impose considerable stability constraints on the allowable time increment while implicit methods, although not as demanding, also place accuracy constraints. In frequency domain solutions, however, the time increment is based on the load or response history. Stated differently, the time increment is selected such that the Nyquist frequency is greater than the highest frequency in the load and response histories. As a result, the time increment for a frequency domain analysis can usually be five to ten times greater than that for a time domain analysis.

6.8 SUMMARY OF STUDIES

The studies presented in sections 6.1-6.4 illustrated the development of the HFT solution scheme while the final three studies, sections 6.5-6.7, examined the scheme in its fully developed form and suggested alternate approaches for accelerating and ensuring convergence. Table 6.10 summarizes the highlights of each study. The description, material model, and excitation columns are self explanatory. For the first four studies, the last column identifies the introduction of a new attribute of the HFT scheme, while for the last three studies, the attributes column lists the purpose of each study.

In general the studies indicated that the HFT scheme can handle many strain rate independent material models -- elastic-perfectly plastic, tubular brace, Ramberg-Osgood, and bilinear elastic. Three earthquake records (Bucarest, El Centro, and Taft), a single cycle sine wave, and a dual frequency component harmonic loading were used.

The highly nonlinear studies (studies 2, 4, 5, 6, 7 of Table 6.10) were stabilized by including artificial viscous or hysteretic damping. Without the artificial damping, the response usually diverged by the tenth iteration. A viscous type artificial damping proved adequate for the SDOF soil system. However, its use in the MDOF soil problem resulted in a low frequency drift appearing by the 20th iteration and a high frequency contamination by the 30th cycle. As a

Study	Description	Material Model	Excitation	Attributes
1	General SDOF, QL	Elastic-Plastic	Single Cycle Sine	Zero Minimization, Relaxation, Dual Displacement
		Tubular	Bucarest EQ	
2	SDOF Soil, HN	Ramberg-Osgood	Taft EQ	Total Displacement, Artificial Viscous Damping
3	MDOF Shear Beam, QL	Elastic-Plastic	Single Cycle Sine	Mode Updating Scheme 1
4	MDOF Soil, HN	Ramberg-Osgood	Taft EQ	Artificial Hysteretic Damping, Mode Updating Scheme 2
5	Offshore Structure, QL and HN	Tubular	Taft EQ El Centro EQ	Culminating Study
6	Soft SDOF, HN	Elastic-Plastic	Taft EQ	Using a Segmenting Scheme
7	Bilinear SDOF HN	Bilinear Elastic	Harmonic (2 components)	Selecting a Time Increment

QL - quasi-linear
HN - highly nonlinear response

Table 6.10 Summary of Studies

result, subsequent studies employed an artificial hysteretic type damping that produced no convergence problems. Although the artificial damping stabilized all studies, it also decelerated the convergence rate in some cases by excessively attenuating the converging response history. Artificial damping ratios ranged from 0.35 to 0.75.

Schemes to accelerate the convergence rate were also examined. Study 1 employed relaxation schemes applied to the entire converging nonlinear response history. Results indicated that under-relaxation decelerated the convergence while over-relaxation accelerated the convergence in initial cycles, but eventually produced a diverging solution. The inability to accelerate the convergence by relaxation was attributed to the forward time converging behavior of the HFT scheme. In other words, since the nonlinearities are evaluated in the time domain, the response toward the end of the history usually cannot converge until the prior response has converged. As a result, relaxation applied to the entire history may accelerate the convergence toward the beginning of the response history, but may also aggravate the inaccuracies in the pseudo-force toward the end of the history.

The forward time progressing behavior of the HFT scheme suggested a segmented approach outlined in study 6. Rather than evaluate the response to the entire force history, the excitation would be sectioned in time and the response to

each section obtained separately in a forward time progressing fashion. This segmented approach allows different structural matrices to model each portion of the response history and may possibly alleviate the divergence problems associated with the relaxation schemes.

In addition to these acceleration schemes, efficiency was increased by employing the zero minimization technique. The number of points in the frequency spectrum was easily reduced by a factor of four. Study 5 also presented a technique for minimizing the iterations by employing only a few dominant modes in the initial iterative cycles and later adding more modes to increase the accuracy of the results. Study 7 employed the nonlinear stiffness on the LHS of the governing equations, and hence accelerated the convergence by creating a system corresponding to the dominating nonlinear response.

The MDOF studies (studies 3 and 4) entailed an additional efficiency consideration in terms of the nonlinear mode updating schemes. Study 3 demonstrated that for a system with spatially concentrated nonlinearities and simple temporal pseudo-force distribution, the first mode updating scheme (static load distribution approach) was appropriate. Significantly nonlinear problems, exemplified by study 4, however were more conducive to the second mode updating approach (least squares secant stiffness). This approach produced a nonlinear stiffness and mode shape more

appropriate to the nonlinear response, resulting in an accelerated convergence.

In general for all studies, the HFT scheme was capable of producing accurate results. Efficiency varied with the nature of the loading, complexity of the response, and behavior of the material model. The HFT approach proved higher efficiency in problems where the time increment was governed more by numerical integration restrictions (studies 3, 4, 7) than material modelling considerations (studies 2 and 5). Furthermore, study 7 demonstrated the advantages of the frequency domain approach when the loading and response are of significantly higher period than that of the structure.

CHAPTER 7

SUMMARY, CONCLUSIONS, AND RECOMMENDATIONS

This thesis presented an overview of the solution of nonlinear dynamic structural systems and introduced a new solution scheme, the hybrid frequency-time domain analysis approach. The principal objectives and primary topics investigated are summarized in section 7.1, while the main accomplishments of this study are discussed concisely in section 7.2. Section 7.3 concludes the chapter with suggestions for further research to expand and adapt the newly developed solution scheme.

7.1 RESEARCH SUMMARY

Initial chapters of this thesis were devoted to a review of nonlinear continuum mechanics and the numerical solution of nonlinear systems. An overview of numerical integration schemes and their related frequency distortion and artificial damping errors lead to the presentation of a linear systems theory stability and accuracy analysis technique. The alternate technique substitutes the

numerical integrators into the governing equation of motion and transfers the resulting approximate equation to the frequency domain by using Fourier transform concepts. Accuracy is then easily and elegantly analyzed by deriving the approximate transfer function, defined as the response divided by the force, and comparing it with the exact theoretical transfer function.

The background on numerical integration provided an incentive to examine solution techniques in the frequency domain, where in essence an exact numerical integrator is employed to derive the solution. In particular, an iterative frequency domain solution scheme, referred to as the hybrid frequency-time domain analysis approach, was developed to analyze nonlinear transient response problems. The HFT scheme gains its economy by combining the mode superposition approach with a frequency domain solution. Nonlinearities are evaluated in the time domain, and transferred to the RHS of the equations of motion as a pseudo-force vector. The total external plus nonlinear force vector is then transferred to the frequency domain using the FFT. Multiplying the force spectrum by the transfer function, evaluated from the structural matrices on the LHS of the governing equations, the frequency domain response is obtained and transferred back to the time domain using the inverse FFT to provide an updated pseudo-force history. During the iterative process, simple changes in the solution parameters such as the frequency discretization

increment and number of frequencies and mode shapes allow the solution accuracy to be easily monitored. Any level of accuracy can be obtained, although a higher accuracy level usually implies less efficiency.

Research considerations were limited mainly to developing the HFT solution scheme applied to seismically excited systems. Actual applications to large scale systems were not implemented. Rather, a scientific approach examining small systems whereby numerical problems could be easily and economically identified was followed. Techniques for eliminating these problems were proposed, and a general framework for implementing the HFT scheme was developed.

Of the numerous developmental studies conducted, seven were presented that emphasized the steps necessary to transform the HFT scheme from its conceptual basis to its actual numerical application. The studies consisted of a general SDOF system, a soil amplification problem using SDOF and MDOF models, a 10 degree of freedom elastic-perfectly plastic shear beam model, a set of steel jacket offshore structures, a hypothetical extremely soft SDOF system, and a bilinear elastic SDOF problem. All studies demonstrated various accuracy and efficiency problems.

7.2 CONCLUSIONS: PRINCIPAL RESULTS OF THE PRESENT STUDY

Conclusive comments regarding the linear systems theory stability and accuracy analysis approach are as follows:

1. Standard frequency distortion parameters can be derived by comparing the resonant frequencies of the exact and approximate transfer functions. Similarly, artificial damping parameters can be evaluated by comparing the imaginary components of the exact and approximate transfer functions.
2. Amplitude amplification information for the entire frequency spectrum is obtained, providing a measure of how accurately the numerical integrator reproduces the response for each individual frequency component.
3. Extensions to stability analyses are possible by using the z-transform.
4. The effect of the finite difference expanded load vector upon the accuracy and stability characteristics is easily evaluated by transferring the finite difference expanded load vector to the frequency domain and then multiplying by the approximate transfer function.
5. The conventional stability and accuracy analysis and the linear systems theory approach are equivalent for the free vibration problem.

Results of the HFT case studies were summarized in Chapter 6. Based on these studies, the following conclusions regarding the HFT solution scheme were deduced:

1. The HFT scheme derives the solution in the frequency domain, and hence uses a theoretically exact numerical integrator represented by the transfer function H. The integrator is exact in a theoretical sense because an analytical expression exists for the continuous frequency spectrum. From a numerical perspective, however, the transfer function is exact only at discrete frequencies. Resolution considerations, therefore, become important, particularly at peaks in the spectrum. Furthermore, the time increment must be selected properly such that the component at the Nyquist frequency is negligible.

2. Due to the transfer function being a theoretically exact numerical integrator, the time increment selection is not restricted by numerical integration stability and accuracy considerations, but rather by the dominating frequencies in the response or loading. When numerical integration considerations are the only restrictions on the time increment in a time domain analysis, the time increment for an HFT analysis can be five to ten times larger.

3. The HFT scheme displays a forward time progressing convergence behavior, attributed to the solution scheme being based on the pseudo-force formulation. Since the

pseudo-force history is evaluated in the time domain, the latter portion of the response history usually cannot converge until the initial portion has converged.

4. Highly nonlinear problems were stabilized by adding artificial damping. Viscous type artificial damping was adequate for the SDOF soil model, but produced solution inaccuracies for the MDOF soil model. Subsequent studies employed a hysteretic type artificial damping that displayed no accuracy problems. Artificial damping ratios ranged from 0.35 to 0.75.

5. The zero minimization scheme optimized the solution efficiency by reducing the number of points in the frequency spectrum by at least a factor of four (compared to the number of points required in a conventional frequency domain solution without the zero minimization technique).

6. Relaxation techniques applied to the entire converging response history produced a diverging solution because of the forward time progressing converging nature of the HFT scheme.

7. The total displacement formulation is more attractive than the dual displacement formulation because initial inaccuracies in the solution history are easily corrected in later cycles and a possibly better initial guess of the nonlinear response can be derived in the first cycle by employing artificial

damping.

8. The first nonlinear mode updating scheme (static load distribution) proved adequate for a quasi-linear MDOF problem. The second updating technique (least squares secant stiffness) is more compatible with systems exhibiting significant nonlinearities. The scheme can be developed as a self contained algorithm, requiring minimal participation from the analyst. Furthermore, the only additional computational cost is derived from the eigenvalue problem, since the operations for evaluating the secant stiffness matrix must also be executed when evaluating the pseudo-force history.

9. If only the peak response or a general outline of the response history is desired, then a significantly lower number of iterations is required for the HFT analysis.

10. The linear stiffness need not be used to evaluate the transfer function H. Rather a nonlinear stiffness better representing the actual response should be employed, such that the pseudo-forces are small and the convergence rate rapid.

The HFT scheme is particularly suited to the following systems:

1. A few linear or nonlinear modes dominate the response.

2. The nonlinear response does not deviate

significantly from the linear response.

3. The time increment in a time domain analysis is severely restricted by numerical integration accuracy and stability considerations.

4. The forcing function has a dominant period significantly higher than that of the lowest structural periods.

5. Frequency dependent stiffness and damping must be used, such as in soil-structure interaction problems.

6. The response must be viewed in terms of frequency spectrums, rather than time histories.

7. The excitation history is of long duration and is dominated by low frequency components.

Examples when the HFT technique is inefficient or inapplicable are as follows:

1. Excitation is an impulsive type load that excites almost all structural modes.

2. The loading has a significant spatial variation.

3. Material model evaluation considerations restrict the time step size, such as for strain rate dependent material models.

4. Each segment of the response history is dominated by a different nonlinear stiffness matrix. In other words, the structural properties continuously change at a rapid rate as the excitation is applied.

5. A response history with a high level of accuracy is desired.

7.3 RECOMMENDATIONS FOR FUTURE RESEARCH

Based on the experience gained from this study, the following topics are recommended for future investigation to explore and expand the applicability and effectiveness of the HFT scheme:

1. Apply to problems with severe nonlinear material behavior, as well as rate dependent behavior.

2. Compare the convergence properties of the HFT approach with time integration schemes consisting of other finite difference operators combined with quasi-Newton iterators such as the Davidon, BFGS, and DFP.

3. Consider the solution of large systems as well as soil-structure interaction problems with frequency dependent stiffness and damping.

4. Develop the segmented analysis procedure for improved efficiency. Evaluate the effect of relaxation when applied to the segmented histories. Consider using different time increments and stiffness matrices for each segment.

5. As an alternative to the segmented analysis approach, consider evaluating the pseudo-force history for only certain portions of the response, but still obtaining the entire response simultaneously. Once the pseudo-force history has converged for a certain time interval, store the history and proceed forward to the next time interval. This approach alleviates

instabilities due to inaccuracies in the pseudo-force history and also improves the efficiency by minimizing the pseudo-force history evaluation.

6. Consider using finite impulse response (FIR) differentiators (68) to obtain more accurate estimates of the initial velocity for use in the zero minimization technique and also to derive better velocity and acceleration response histories.

REFERENCES

1. Adeli, H., Gere, J.M., and Weaver, W., Jr., "Algorithms for Nonlinear Structural Dynamics," Journal of the Structural Division, ASCE, vol. 104, no. ST2, February 1978, pp. 263-280.

2. Aitken, A.C., "The Evaluation of the Latent Roots and Latent Vectors of a Matrix," Proc. Roy. Soc. Edinburgh, vol. 57, 1937, pp. 269-304.

3. Almroth, B.O., Stern, P., and Brogen, F.A., "Automatic Choice of Global Shape Functions in Structural Analysis," AIAA Journal, vol. 16, no. 5, May 1978, pp. 525-528.

4. American Petroleum Institute, API Recommended Practice for Planning, Designing and Constructing Fixed Offshore Platforms, API-RP2A, Dallas, Texas, 12th Edition, 1981.

5. Basu, A.K. and Dutta, A., "Dynamic Behaviour of Guyed Towers," Proceedings, BOSS Conference, Cambridge, Massachusetts, 1982, pp. 529-545.

6. Bathe, K.J., Finite Element Procedures in Engineering Analysis, Prentice-Hall, Inc., Englewood Cliffs, New Jersey, 1982.

7. Bathe, K.J. and Cimento, A.P., "Some Practical Procedures for the Solution of Nonlinear Finite Element Equations," Computer Methods in Applied Mechanics and Engineering, vol. 22, 1980, pp. 59-85.

8. Bathe, K.J. and Gracewski, S., "On Nonlinear Dynamic Analysis Using Substructuring and Mode Superposition," Computers and Structures, vol. 13, 1981, pp. 699-707.

9. Bathe, K.J. and Wilson, E.L., "Large Eigenvalue Problems in Dynamic Analysis," Journal of the Engineering Mechanics Division, ASCE, vol. 98, 1972, pp. 1471-1485.

10. Bathe, K.J. and Wilson, E.L., "Stability and Accuracy Analysis of Direct Integration Methods," Earthquake Engineering and Structural Dynamics, vol. 1, 1973, pp. 283-291.

11. Bazzi, G. and Anderheggen, E., "The ρ-Family of Algorithms for Time-Step Integration with Improved Numerical Dissipation," Earthquake Engineering and Structural Dynamics, vol. 10, 1982, pp. 537-550.

12. Bea, R.G., Audibert, J.M.E., and Akky, M.R., "Earthquake Response of Offshore Platforms," Journal of the Structural Division, ASCE, Feb. 1979, pp. 377-397.

13. Belytschko, T. and Mullen, R., "Mesh Partitions of Explicit-Implicit Time Integration," in Formulations and Computational Algorithms in Finite Analysis, MIT Press, Cambridge, Massachusetts, 1976, pp. 673-690.

14. Belytschko, T. and Mullen, R., "Stability of Explicit-Implicit Mesh Partitions in Time Integration," International Journal of Numerical Methods in Engineering, vol. 12, 1978, pp. 1575-1586.

15. Belytschko, T., Yen, H.J., and Mullen, R., "Mixed Methods for Time Integration," Computer Methods in Applied Mechanical Engineering, vol. 17/18, 1979, pp. 259-275.

16. Bergland, G.D., "A Fast Fourier Transform Algorithm Using Base 8 Iterations," Mathematics of Computation, vol. 22, 1968, pp. 275-279.

17. Brigham, E.O., The Fast Fourier Transform, Prentice-Hall, Inc., Englewood Cliffs, New Jersey, 1974.

18. Clough, R.W. and Penzien, J., Dynamics of Structures, McGraw-Hill Book Co., New York, 1975.

19. Constantopoulos, I.V., Amplification Studies for a Nonlinear Hysteretic Soil Model, Sc.D. Thesis, MIT, Cambridge, Massachusetts, June 1973.

20. Cooley, J.W. and Tukey, J.W., "An Algorithm for Machine Computation of Complex Fourier Series," Mathematics of Computation, vol. 19, 1965, pp. 297-301.

21. Dennis, J.E., Jr., "A Brief Survey of Convergence Results for Quasi-Newton Methods," SIAM-AMS Proceedings, vol. 9, 1976, pp. 185-200.

22. Dennis, J.E., Jr. and More, J.J., "Quasi-Newton Methods, Motivation and Theory," SIAM Review, vol. 19, no. 1, January 1977, pp. 46-91.

23. Felippa, C.A. and Park, K.C., "Computational Aspects of Time Integration Procedures in Structural Dynamics," Journal of Applied Mechanics, vol. 45, September 1978, pp. 595-611.

24. Fish, P. and Rainey, R., "The Importance of Structural Motion in the Calculation of Wave Loads on an Offshore Structure," Proceedings, BOSS Conference, London, England, 1979, pp. 43-60.

25. Flugge, W., Tensor Analysis and Continuum Mechanics, Springer-Verlag, New York, 1972.

26. Fried, I., "Finite Element Analysis of Time-Dependent Phenomena," AIAA Journal, vol. 7, no. 6, June 1969, pp. 1170-1173.

27. Gates, W.E. and Marshall, P.W., "Analytical Methods for Determining the Ultimate Earthquake Resistance of Fixed Offshore Structures," Proceedings, Offshore Technology Conference, Houston, Texas, 1977, pp. 215-226.

28. Gellert, M., "A Direct Integration Method for Analysis of a Certain Class of Nonlinear Dynamic Problems," Ingenieur-Archiv, vol. 48, 1979.

29. Geradin, M., Idelsohn, S., and Hogge, M., "Computational Strategies for the Solution of Large Nonlinear Problems via Quasi-Newton Methods," Computers and Structures, vol. 13, 1981, pp. 73-81.

30. Geschwinder, L.F., Jr., "Nonlinear Dynamic Analysis by Modal Superposition," Journal of the Structural Division, ASCE, vol. 107, no. ST12, December 1981, pp. 2325-2336.

31. Gottlieb, D. and Orszag, S.A., Numerical Analysis of Spectral Methods: Theory and Applications, Society for Industrial and Applied Mathematics, Philadelphia, Pennsylvania, 1977.

32. Hall, J.F., "An FFT Algorithm for Structural Dynamics," Earthquake Engineering and Structural Dynamics, vol. 10, 1982, pp. 797-811.

33. Hilber, H.M., Analysis and Design of Numerical Integration Methods in Structural Dynamics, Report No. EERC 76-29, Earthquake Engineering Research Center, University of California, Berkeley, California, 1976.

34. Hilber, H.M., Hughes, T.J.R., and Taylor, R.L., "Improved Numerical Dissipation for Time Integration Algorithms in Structural Dynamics," Earthquake Engineering and Structural Dynamics, vol. 5, 1977, pp. 283-292.

35. Houbolt, J.C., "A Recurrence Matrix Solution for the Dynamic Response of Elastic Aircraft," Journal of the Aeronautical Sciences, vol. 17, 1950, pp. 540-550.

36. Hughes, T.J.R. and Liu, W.K., "Implicit-Explicit Finite Elements in Transient Analysis: Implementation and Numerical Examples," Journal of Applied Mechanics, ASME, vol. 45, 1978, pp. 375-378.

37. Hughes, T.J.R. and Liu, W.K., "Implicit-Explicit Finite Elements in Transient Analysis: Stability Theory," Journal of Applied Mechanics, ASME, vol. 45, 1978, pp. 371-374.

38. Hurty, W.C. and Rubinstein, M.F., Dynamics of Structures, Prentice-Hall, Inc., Englewood Cliffs, New Jersey, 1964.

39. Jain, A.K., Goel, S.C., and Hanson, R.D., "Hysteretic Cycles of Axially Loaded Steel Members," Journal of the Structural Division, ASCE, vol. 106, no. ST8, Aug. 1980, pp. 1777-1795.

40. Krieg, R.D., "Unconditional Stability in Numerical Time Integration Methods," Journal of Applied Mechanics, June 1973, pp. 417-421.

41. Liu, W.K. and Belytschko, T., "Mixed-Time Implicit-Explicit Finite Elements for Transient Analysis," Computers and Structures, vol. 15, no. 4, pp. 445-450, 1982.

42. Mahin, S.A., Popov, E.P., Zayas, V.A., "Seismic Behaviour of Tubular Steel Offshore Platforms," Proceedings, Offshore Technology Conference, Houston, Texas, 1980, pp. 247-258.

43. Maison, B. and Popov, E.P., "Cyclic Response Prediction for Braced Steel Frames," Journal of the Structural Division, ASCE, vol. 106, no. ST7, July 1980, pp. 1401-1416.

44. Malvern, L.E., Introduction to the Mechanics of a Continuous Medium, Prentice-Hall, Inc., Englewood Cliffs, New Jersey, 1969.

45. Mathies, H. and Strang, G., "The Solution of Nonlinear Finite Element Equations," International Journal for Numerical Methods in Engineering, vol. 14, 1979, pp. 1613-1626.

46. McNamara, J.F., "Solution Schemes for Problems of Nonlinear Structural Dynamics," Journal of Pressure Vessel Technology, ASME, May 1974, pp. 96-102.

47. Morris, L.R., "A Comparative Study of Time Efficient FFT and WFTA Programs for General Purpose Computers," IEEE Trans., ASSP-26, 1978, pp. 141-150.

48. Morris, N.F., "The Use of Modal Superposition in Nonlinear Dynamics," Computers and Structures, vol. 7, 1977, pp. 65-72.

49. Nagy, D.A., "Modal Representation of Geometrically Nonlinear Behavior by the Finite Element Method," Computers and Structures, vol. 10, 1979, pp. 683-688.

50. Newmark, N.M., "A Method of Computation for Structural Dynamics," Journal of the Engineering Mechanics Division, ASCE, vol. 85, no. EM3, July 1959, pp. 67-94.

51. Nickell, R.E., "Nonlinear Dynamics by Mode Superposition," Computer Methods in Applied Mechanics and Engineering, vol. 7, 1976, pp. 107-129.

52. Noor, A.K., "Recent Advances in Reduction Methods for Nonlinear Problems," Computers and Structures, vol. 13, 1981, pp. 31-44.

53. Noor, A.K., "Reduced Basis Technique for Nonlinear Analysis of Structures," AIAA Journal, vol. 18, no. 4, April 1980, pp. 455-462.

54. Nussbaumer, H.J. and Quandalle, P., "Fast Computation of Discrete Fourier Transforms Using Polynomial Transforms," IEEE Trans., ASSP-27, 1979, pp. 169-181.

55. Nussbaumer, H.J., Fast Fourier Transform and Convolution Algorithms, Springer-Verlag, New York, 1981.

56. Oden, J.T., Finite Elements of Nonlinear Continua, McGraw-Hill Book Co., New York, 1972.

57. Oppenheim, A.V. and Schafer, R.W., Digital Signal Processing, Prentice-Hall, Inc., Englewood Cliffs, New Jersey, 1975.

58. Park, K.C., "An Improved Semi-Implicit Method for Structural Dynamic Analysis," Journal of Applied Mechanics, ASME, vol. 49, September 1982, pp. 589-593.

59. Park, K.C., "An Improved Stiffly-Stable Method for Direct Integration of Nonlinear Structural Dynamic Equations," Journal of Applied Mechanics, ASME, vol. 42, no. 2, June 1975, pp. 464-470.

60. Park, K.C., "Evaluating Time Integration Methods for Nonlinear Dynamic Analysis," in Finite Element Analysis of Transient Nonlinear Structural Behavior, AMD, ASME, vol. 14, New York, 1975.

61. Park, K.C., "Partitioned Transient Analysis Procedures for Coupled-Field Problems: Stability Analysis," Journal of Applied Mechanics, ASME, vol. 47, 1980, pp. 370-376.

62. Park, K.C., "Practical Aspects of Numerical Time Integration," Computers and Structures, vol. 7, 1977, pp. 345-353.

63. Park, K.C. and Felippa, C.A., "Partitioned Transient Analysis Procedures for Coupled-Field Problems: Accuracy Analysis," Journal of Applied Mechanics, ASME, vol. 47, 1980, pp. 919-926.

64. Park, K.C. and Housner, J.M., "Semi-Implicit Transient Analysis Procedures for Structural Dynamic Analysis," NASA/GWU Nonlinear Mechanics Conference, Washington, D.C., October 1980.

65. Pipes, L.A., Operational Methods in Nonlinear Mechanics, Dover Publications, Inc., New York, 1965.

66. Popov, E.P. and Black, R.G., "Steel Struts Under Severe Cyclic Loadings," Journal of the Structural Division, ASCE, vol. 107, no. ST9, September 1981, pp. 1857-1881.

67. Prager, W., Introduction to Mechanics of Continua, Ginn and Company, Boston, Massachusetts, 1961.

68. Rabiner, L.R. and Gold, B., Theory and Application of Digital Signal Processing, Prentice-Hall, Inc., Englewood Cliffs, New Jersey, 1975.

69. Rader, C.M., "Discrete Fourier Transforms when the Number of Data Samples is Prime," Proceedings IEEE, vol. 56, 1968, pp. 1107-1108.

70. Rainey, R.C.T., "The Dynamics of Tethered Platforms," Journal of the R.I.N.A., March 1978.

71. Richtmyer, R.D. and Morton, K.W., Difference Methods for Initial-Value Problems, Interscience Publishers, New York, 1967.

72. Rodal, J.J.A. and Witmer, E.A., Finite-Strain Large-Deflection Elastic-Viscoplastic Finite-Element Transient Response Analysis of Structures, MIT ASRL TR 154-15 (also NASA CR-159874), July 1979.

73. Sedov, L.I., A Course in Continuum Mechanics, vol. 1, Wolters-Noordhoff Publishing, Netherlands, 1971.

74. Sedov, L.I., Foundations of the Nonlinear Mechanics of Continua, Pergamon Press, Oxford, 1966.

75. Shah, V.N. and Hartman, A.J., "Nonlinear Dynamic Analysis of a Structure Subjected to Multiple Support Motions," Journal of Pressure Vessel Technology, PVP-52, no. 80-C2, February 1981, pp. 27-32.

76. Silverman, H.F., "An Introduction to Programming the Winograd Fourier Transform Algorithm (WFTA)," IEEE Trans., ASSP-25, 1977, pp. 152-165.

77. Singleton, R.C., "An Algorithm for Computing the Mixed Radix Fast Fourier Transform," IEEE Trans., AU-17, 1969, pp. 93-103.

78. Steigmann, D.J., Nonlinear Finite-Strain Transient Structural Response Predictions by Implicit Temporal Finite Difference Methods, SM Thesis, MIT, Cambridge, Massachusetts, 1981.

79. Stoker, J.J., Nonlinear Vibrations in Mechanical and Electrical Systems, Interscience Publishers, New York, 1966.

80. Stricklin, J.A. and Haisler, W.E., "Formulations and Solution Procedures for Nonlinear Structural Analysis," Computers and Structures, vol. 7, 1977, pp. 125-136.

81. Stricklin, J.A., Martinez, J.E., Tillerson, J.R., Hong, J.H., and Haisler, W.E., "Nonlinear Dynamic Analysis of Shells of Revolution by Matrix Displacement Method," AIAA Journal, vol. 9, no. 4, April 1971, pp. 629-636.

82. Taudin, P. "Dynamic Response of Flexible Offshore Structures to Regular Waves," Proceedings, Offshore Technology Conference, Houston, Texas, 1978.

83. Trujillo, D.M., "An Unconditionally Stable Explicit Algorithm for Structural Dynamics," International Journal for Numerical Methods in Engineering, vol. 11, 1977, pp. 1579-1592.

84. Turinsky, P.J., "The Super-Variational Technique Revisited," Journal of Mathematical Analysis and Applications, vol. 33, 1971, pp. 605-615.

85. Vugts, J.H. and Hines, I.M., "Modal Superposition v. Direct Solution Techniques in the Dynamic Analysis of Offshore Structures," Proceedings, BOSS Conference, London, England, 1979, pp. 23-42.

86. Weeks, G., "Temporal Operators for Nonlinear Structural Dynamics Problems," Journal of the Engineering Mechanics Division, ASCE, vol. 98, no. EM5, October 1972, pp. 1087-1104.

87. Wilson, E.L., Farhoomand, I., and Bathe, K.J., "Nonlinear Dynamic Analysis of Complex Structures," Earthquake Engineering and Structural Dynamics, vol. 1, 1973, pp. 241-252.

88. Wilson, E.L. and Itoh, T., "An Eigensolution Strategy for Large Systems," Computers and Structures, vol. 16, no. 1-4, 1983, pp. 259-265.

89. Wilson, E.L., Yuan, M-W, and Dickens, J.M., "Dynamic Analysis by Direct Superposition of Ritz Vectors," Earthquake Engineering and Structural Dynamics, vol. 10, 1982, pp. 813-821.

90. Winograd, S., "A New Method for Computing DFT," Proceedings, IEEE International Conference on Acoustics, Speech, and Signal Processing, 1977, pp. 366-368.

91. Winograd, S., "On Computing the Discrete Fourier Transform," Mathematics of Computation, vol. 32, 1978, pp. 175-199.

92. Witmer, E.A., Private Communication, Professor, Department of Aeronautics and Astronautics, MIT, Cambridge, Massachusetts, October 1982.

93. Wu, R. W-H. and Witmer, E.A., Finite-Element Analysis of Large Transient Elastic-Plastic Deformations of Simple Structures, with Application to the Engine Rotor Fragment Containment/Deflection Problem, ASRL TR 154-4 (also NASA CR-120886), January 1972.

94. Zayas, V.A., Mahin, S.A., and Popov, E.P., "Inelastic Structural Analysis of Braced Platforms for Seismic Loading," Proceedings, Offshore Technology Conference, Houston, Texas, 1981, pp. 259-272.

95. Zienkiewicz, O.C., The Finite Element Method, 3rd Edition, McGraw-Hill Book Co., New York, 1977.

APPENDIX A

ALTERNATE ACCURACY ANALYSIS OF THE PARK STIFFLY-STABLE METHOD

This appendix examines the accuracy analysis of the Park stiffly-stable method (59) using a linear systems theory approach. Rather than analyzing accuracy with a standard time domain approach, the equation of motion is transferred to the frequency domain, and then the exact and approximate corresponding transfer functions are compared to extract frequency distortion and artificial damping characteristics.

Consider the expressions for the velocity in terms of the displacement and acceleration in terms of the velocity.

$$\dot{u}_{n+1} = (10u_{n+1} - 15u_n + 6u_{n-1} - u_{n-2})/6\Delta t \tag{A1}$$

$$\ddot{u}_{n+1} = (10\dot{u}_{n+1} - 15\dot{u}_n + 6\dot{u}_{n-1} - \dot{u}_{n-2})/6\Delta t \tag{A2}$$

The acceleration is rewritten in terms of displacements by substituting Eq. A1 into Eq. A2.

$$\ddot{u}_{n+1} = (100u_{n+1} - 300u_n + 345u_{n-1} - 200u_{n-2} + 66u_{n-3} - 12u_{n-4} + u_{n-5})/36\Delta t^2 \tag{A3}$$

Substituting Eqs. A1 and A3 into the governing equation of

motion

$$\ddot{u}_{n+1} + 2\xi\bar{\omega}\,\dot{u}_{n+1} + \bar{\omega}^2 u_{n+1} = f_{n+1} \tag{A4}$$

we obtain the numerical integration form of the equation of motion

$$\begin{aligned}(100u_{n+1} - 300u_n + 345u_{n-1} - 200u_{n-2} + 66u_{n-3} - 12u_{n-4} \\ + u_{n-5})/36\Delta t^2 + 2\xi\bar{\omega}(10u_{n+1} - 15u_n + 6u_{n-1} - u_{n-2})/6\Delta t \\ + \bar{\omega}^2 u_{n+1} = f_{n+1}\end{aligned} \tag{A5}$$

Equation A5 is simplified by collecting similar terms to yield

$$\begin{aligned}\left[\frac{25}{9\Delta t^2} + \frac{10}{3\Delta t} + \bar{\omega}^2\right] u_{n+1} + \left[\frac{-50}{6\Delta t^2} - \frac{5\xi\bar{\omega}}{\Delta t}\right] u_n + \left[\frac{115}{12\Delta t^2} + \frac{2\xi\bar{\omega}}{\Delta t}\right] u_{n-1} \\ + \left[\frac{-50}{9\Delta t^2} - \frac{\xi\bar{\omega}}{3\Delta t}\right] u_{n-2} + \frac{11}{6\Delta t^2} u_{n-3} - \frac{1}{3\Delta t^2} u_{n-4} \\ + \frac{1}{36\Delta t^2} u_{n-5} = f_{n+1}\end{aligned} \tag{A6}$$

Equation A6 is transferred to the frequency domain using the discrete-time Fourier transform

$$u_n = (1/2\pi)\int_{-\infty}^{\infty} U(e^{i\Omega})e^{i\Omega n}\, d\Omega \tag{A7}$$

resulting in its frequency domain equivalent for any

frequency

$$\left[\left(\frac{25}{9\Delta t^2}+\frac{10}{3\Delta t}+\bar{\omega}^2\right)+\left(\frac{-50}{6\Delta t^2}-\frac{5\xi\bar{\omega}}{\Delta t}\right)e^{-j\Omega}+\left(\frac{115}{12\Delta t^2}+\frac{2\xi\bar{\omega}}{\Delta t}\right)e^{-2\Omega}\right.$$
$$+\left(\frac{-50}{9\Delta t^2}-\frac{\xi\bar{\omega}}{3\Delta t}\right)e^{-3j\Omega}+\frac{11}{6\Delta t^2}e^{-4j\Omega}-\frac{1}{3\Delta t^2}e^{-5j\Omega}$$
$$\left.+\frac{1}{36\Delta t^2}e^{-6j\Omega}\right]U(\Omega)=F(\Omega) \qquad (A8)$$

The transfer function is defined as

$$H(\Omega)=U(\Omega)/F(\Omega) \qquad (A9)$$

Therefore,

$$H(\Omega)=\left[(25a/9+10b/3+c+(-50a/6-5b)e^{-j\Omega}\right.$$
$$+(115a/12+2b)e^{-2j\Omega}+(-50a/9-b/3)e^{-3j\Omega} \qquad (A10)$$
$$\left.+11a/6\ e^{-4j\Omega}-a/3\ e^{-5j\Omega}+a/36\ e^{-6j\Omega}\right]^{-1}$$

where

$$a=1/(2\Delta t^2),\quad b=\xi\bar{\omega}/\Delta t,\quad c=\bar{\omega}^2 \qquad (A11)$$

$H(\Omega)$ is multiplied by $4\pi^2/\Delta t^2$ to obtain its nondimensionalized form. The constants a, b, and c are now redefined as

$$a=1/(4\pi^2)$$
$$b=\xi(\Delta t/T_n)/2\pi \qquad (A12)$$
$$c=(\Delta t/T_n)^2$$

Plots of the nondimensionalized Park transfer function are shown in Fig. 4.11 for 5% physical damping and Fig. 4.12 for 10% physical damping.

Frequency distortion and artificial damping effects are estimated next. The peak of $H(\Omega)$ occurs at the frequency $\overline{\Omega}_p$ such that $|H(\Omega)|' = 0$ where

$$
\begin{aligned}
\left|H(\Omega)\right|' = -\Big[&(A + B\cos\Omega + C\cos 2\Omega + D\cos 3\Omega + 11a/6\cos 4\Omega \\
&- a/3\cos 5\Omega + a/36\cos 6\Omega)^2 + (-B\sin\Omega - C\sin 2\Omega \\
&- D\sin 3\Omega - 11a/6\sin 4\Omega + a/3\sin 5\Omega - a/36\sin 6\Omega)^2\Big]^{-1.5} \\
\cdot\Big[&(A + B\cos\Omega + C\cos 2\Omega + D\cos 3\Omega + 11a/6\cos 4\Omega \\
&- a/3\cos 5\Omega + a/36\cos 6\Omega)\cdot(-B\sin\Omega - 2C\sin 2\Omega \\
&- 3D\sin 3\Omega - 22a/3\sin 4\Omega + 5a/3\sin 5\Omega - a/6\sin 6\Omega) \\
&+ (-B\sin\Omega - C\sin 2\Omega - D\sin 3\Omega - 11a/6\sin 4\Omega \\
&+ a/3\sin 5\Omega - a/36\sin 6\Omega)\cdot(-B\cos\Omega - 2C\cos 2\Omega \\
&- 3D\cos 3\Omega - 22a/3\cos 4\Omega + 5a/3\cos 5\Omega \\
&- a/6\cos 6\Omega)\Big] \qquad \text{(A13)}
\end{aligned}
$$

and

$$A = 25a/9 + 10b/3 + c$$

$$B = -50a/6 - 5b \tag{A14}$$

$$C = 115a/12 + 2b$$

$$D = -50a/9 - b/3$$

The peak of the exact transfer function is located at

$$\bar{\Omega}_e = \bar{\Omega} \cdot \sqrt{1-\xi^2} = \bar{\omega}\Delta t\sqrt{1-\xi^2} = 2\pi \cdot \frac{\Delta t}{T_n} \cdot \sqrt{1-\xi^2} \tag{A15}$$

The period elongation is therefore given as

$$\tau = \frac{\bar{\Omega}_e - \bar{\Omega}_p}{\bar{\Omega}_p} \tag{A16}$$

Similarly, the artificial damping ratio is obtained by equating the imaginary terms in $H(\Omega)$ with the imaginary terms in the exact transfer function and then solving for $\bar{\xi}$. In particular, from Eq. 4.40 the terms corresponding to the imaginary component of the exact transfer function are given as follows:

$$2a_2\Omega = \xi \cdot \frac{\Delta t}{T_n} \cdot \frac{\bar{\Omega}}{\pi} \tag{A17}$$

The terms corresponding to the imaginary component of the Park transfer function are

$$-B\sin\bar{\Omega} - C\sin 2\bar{\Omega} - D\sin 3\bar{\Omega} - (11a/6)\sin 4\bar{\Omega} + (a/3)\sin 5\bar{\Omega} - (a/36)\sin 6\bar{\Omega} \tag{A18}$$

Equating A17 and A18 and solving for $\overline{\xi}$ yields the algorithmic damping ratio

$$\overline{\xi} = \frac{-B\sin\Omega_p - C\sin 2\Omega_p - D\sin 3\Omega_p - 11a/6\ \sin 4\Omega_p + a/3\ \sin 5\Omega_p - a/36\ \sin 6\Omega_p}{(\Delta t/T_n)(\overline{\Omega}_e/\pi)} \tag{A19}$$

where

$$\overline{\Omega} = \overline{\omega}\Delta t \tag{A20}$$

and $\overline{\Omega}_p$ and $\overline{\Omega}_e$ are the nondimensionalized resonant frequencies for the Park and exact transfer functions, respectively. Using the procedure above, plots of the period elongation and algorithmic damping ratio versus $\overline{\Omega}$ were derived and are shown in Figs. 4.13-4.16.

APPENDIX B

ALTERNATE STABILITY ANALYSIS OF THE CENTRAL DIFFERENCE METHOD USING THE Z-TRANSFORM CONCEPT

The stability characteristics of the central difference method are examined in the following using the z-transform concept. The presentation is limited to the undamped problem

$$\ddot{u} + \bar{\omega}^2 u = f \tag{B1}$$

Substituting the central difference approximation for the acceleration into Eq. B1, we obtain the equation of motion given in terms of the numerical integrator

$$\frac{u_{n+1} - 2u_n + u_{n-1}}{\Delta t^2} + \bar{\omega}^2 u_n = f_n \tag{B2}$$

or equivalently

$$u_{n+1} - (\bar{\omega}^2 \Delta t^2 - 2)u_n + u_{n-1} = \Delta t^2 f_n \tag{B3}$$

Equation B3 is transferred to the frequency domain using the z-transform

$$X(z) = \sum_{n=-\infty}^{\infty} x(n) z^{-n} \tag{B4}$$

where z is a complex variable, to obtain

$$\left[z + (\bar{\omega}^2\Delta t^2 - 2) + z^{-1}\right]U(z) = \Delta t^2 F(z) \tag{B5}$$

The transfer function H(z) is then given as

$$\begin{aligned} H(z) = U(z)/F(z) &= \Delta t^2/(z+(\bar{\omega}^2\Delta t^2 - 2) + z^{-1}) \\ &= \Delta t^2 z/(z^2 + (\bar{\omega}^2\Delta t^2 - 2)z + 1) \end{aligned} \tag{B6}$$

We next evaluate the stability properties of the central difference method by examining the poles of H(z). For a right-sided sequence of a causal system, the region of convergence is defined outside the unit circle, and therefore such a system is unstable when a pole is located outside the unit circle.

The roots of the numerator are given by

$$\begin{aligned} z &= (-(\bar{\omega}^2\Delta t^2 - 2) \pm \sqrt{\bar{\omega}^4\Delta t^4 - 4\bar{\omega}^2\Delta t^2 + 4 - 4}\ )/2. \\ &= (-(\bar{\omega}^2\Delta t^2 - 2) \pm \bar{\omega}\Delta t\sqrt{\bar{\omega}^2\Delta t^2 - 4}\ )/2. \end{aligned} \tag{B7}$$

Consider three cases:

1. $\bar{\omega}\Delta t^2 = 4$

From Eq. B7 we have

$$z = -(4 - 2)/2 = -1 \tag{B8}$$

Since both poles are located at z = -1, the system is stable.

2. $\bar{\omega}\Delta t^2 > 4$

Implies

$$-(\bar{\omega}^2\Delta t^2 - 2)/2 < -1 \tag{B9}$$

and

$$\bar{\omega}\Delta t\sqrt{\bar{\omega}^2\Delta t^2 - 4}\ /2. > 0 \tag{B10}$$

Therefore, one value of z is always less than -1 and the other, between -1 and 0. The system is unstable because of the pole located outside of the unit circle.

3. $\bar{\omega}\Delta t^2 < 4$

From Eq. B7

$$z \leq -(\bar{\omega}^2\Delta t^2 - 2)/2. \pm \bar{\omega}\Delta t j\sqrt{4 - \bar{\omega}^2\Delta t^2}\ /2. \tag{B11}$$

The modulus of z is evaluated next

$$|z|^2 \leq (\bar{\omega}^4\Delta t^4 - 4\bar{\omega}^2\Delta t^2 + 4)/4. + (\bar{\omega}^2\Delta t^2)(4 - \bar{\omega}^2\Delta t^2)/4. = 1. \tag{B12}$$

Therefore, the pole is always located on or inside the unit circle, and the system is stable.

The critical time increment is determined from case 2 and given as follows:

$$\bar{\omega}^2\Delta t^2 = 4 \tag{B13}$$

Implying

$$\Delta t_{cr} = 2/\bar{\omega} = T_n/\pi \tag{B14}$$

APPENDIX C

FOURIER TRANSFORM PAIR OF x^3

The Fourier transform pair of x^3 is evaluated in this appendix. Let us first begin with x^2. We define

$$A(\omega_1) = \int_{-\infty}^{\infty} X(\omega_1 - \omega_2)\, X(\omega_2)\, d\omega_2 \tag{C1}$$

The inverse Fourier transform of A is given by

$$\begin{aligned}
(1/2\pi)\int_{-\infty}^{\infty} Ae^{i\omega_1 t} d\omega_1 &= (1/2\pi)\int_{-\infty}^{\infty}\int_{-\infty}^{\infty} X(\omega_1 - \omega_2)X(\omega_2)\, d\omega_2 e^{i\omega_1 t} d\omega_1 \\
&= (1/2\pi)\int_{-\infty}^{\infty} X(\omega_2)\int_{-\infty}^{\infty} X(\omega_1 - \omega_2)e^{i(\omega_1 - \omega_2)t} d\omega_1 e^{i\omega_2 t} d\omega_2 \\
&= \int_{-\infty}^{\infty} X(\omega_2)x(t)e^{i\omega_2 t} d\omega_2 \qquad \text{by definition of } x(t) \\
&= 2\pi x(t)x(t) = 2\pi x^2
\end{aligned} \tag{C2}$$

which shows that the Fourier transform of x^2 is $A/2\pi$.

Now consider

$$B(\omega_1) = \int_{-\infty}^{\infty}\int_{-\infty}^{\infty} X(\omega_1 - \omega_2)\, X(\omega_2 - \omega_3)\, X(\omega_3)\, d\omega_2 d\omega_3 \tag{C3}$$

The inverse Fourier transform of B is

$$(1/2\pi)\int_{-\infty}^{\infty} Be^{i\omega_1 t}d\omega_1 = (1/2\pi)\int_{-\infty}^{\infty}\int_{-\infty}^{\infty}\int_{-\infty}^{\infty} X(\omega_1-\omega_2)X(\omega_2-\omega_3)X(\omega_3) d\omega_2 d\omega_3 e^{i\omega_1 t}d\omega_1$$

$$= (1/2\pi)\int_{-\infty}^{\infty}\int_{-\infty}^{\infty} X(\omega_2-\omega_3)X(\omega_3)\int_{-\infty}^{\infty} X(\omega_1-\omega_2)e^{i(\omega_1-\omega_2)t} d\omega_1 e^{i\omega_2 t}d\omega_2 d\omega_3$$

$$= \int_{-\infty}^{\infty}\int_{-\infty}^{\infty} X(\omega_2-\omega_3)X(\omega_3)x(t)e^{i\omega_2 t}d\omega_2 d\omega_3$$

$$= 2\pi x(t)\int_{-\infty}^{\infty} X(\omega_3)(1/2\pi)\int_{-\infty}^{\infty} X(\omega_2-\omega_3)e^{i(\omega_2-\omega_3)} d\omega_2 e^{i\omega_3 t}d\omega_3$$

$$= 2\pi x(t)^2\int_{-\infty}^{\infty} X(\omega_3)e^{i\omega_3 t}d\omega_3$$

$$= 4\pi^2 x(t)^3 \qquad (C4)$$

Therefore, the Fourier transform of x^3 is $B/4\pi^2$.

APPENDIX D

ZERO MINIMIZATION TECHNIQUE

A solution in the frequency domain involves the use of the discrete Fourier transform concept, and therefore evaluates the response to a periodic load function. In transient response problems, however, we seek the solution to an aperiodic force history. A numerical gimmick, consequently, is necessary to obtain an apparent aperiodic response when using the frequency domain approach. The usual procedure is to append additional zeroes to the end of the load history and create a new history of sufficient length such that the free vibration effects at the end of the actual load history are negligible by the end of the extended history (history with appended zeroes). This approach, however, may render the frequency domain technique unfeasible, particularly when very low physical damping is specified or the natural structural period is large.

An alternate approach, referred to as the zero mimimization technique, was consequently developed. This technique eliminates the use of zeroes by subtracting the analytical solution of the free vibration problem from the incorrect response obtained with an insufficient number of zeroes. The procedure consists of conducting the analysis with N points (N is the next power of 2 greater than the

number of points in the actual load history for a radix-2 FFT), obtaining an incorrect solution, and then correcting the solution by subtracting out the free vibration response. Actual applications of the procedure reduced the number of points in the frequency spectrum by a factor of at least two to four, and hence increased the solution efficiency considerably. Additional details of the technique are available in section 5.2.2.2. The mathematical basis of the zero minimization technique is presented in the following paragraphs.

The proof that the zero minimization technique is mathematically sound is based on the periodic nature of the Fourier transform concept. Let us first consider a solution derived in the time domain using the convolution concept (Duhamel's integral). The exact solution is obtained by evaluating the linear convolution, which in essence implies folding the impulse response function h about the time zero axis, shifting h to the right to time t, and then integrating the product of $h(t-\tau)$ and $q(\tau)$ to yield the response at time t (32). The linear convolution concept is illustrated conceptually in Fig. D.1.

Consider next a solution obtained in the frequency domain. A solution in the frequency domain strictly implies that we are concerned with a periodic system since we employ the discrete Fourier transform. As a result, the equivalent solution in the time domain corresponds to a periodic rather

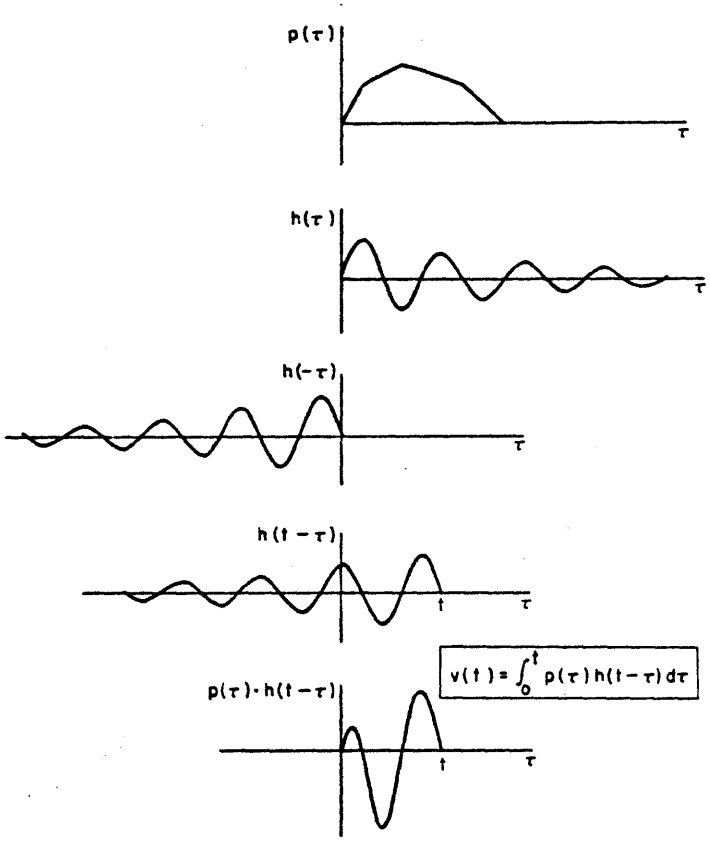

Fig. D.1 Convolution with continuous functions (32)

than a linear convolution. In other words, the forcing function is periodic, and therefore the response is also periodic. However, the solution corresponding to only one cycle of the forcing function must be obtained.

The usual approach to derive the correct solution involves adding additional zeroes to the end of the forcing function, thus creating an apparent aperiodic system. Stated differently, assume the load history has N points and the impulse response function has duration M points. Then, if M zeroes are added to the end of the load history, the correct response is calculated because the response from one cycle does not contaminate the response for another cycle. This approach, as mentioned previously, may be inefficient in particular problems, especially when a significant number of transforms must be evaluated.

Let us now examine the basis of the zero minimization technique. Consider Fig. D.1 again, except in this case redrawn for a periodic convolution, shown in Fig. D.2. If the load history has N points and convolution, M points, but we use N+K, less than N+M, points in the frequency domain solution, we are in essence evaluating the response by integrating the product shown in Fig. D.2e. As a result, an incorrect response is obtained for the beginning of the history (M-K points) where the error is due to contamination by a free vibration component from the previous cycle. The correct response, therefore, is easily extracted from the

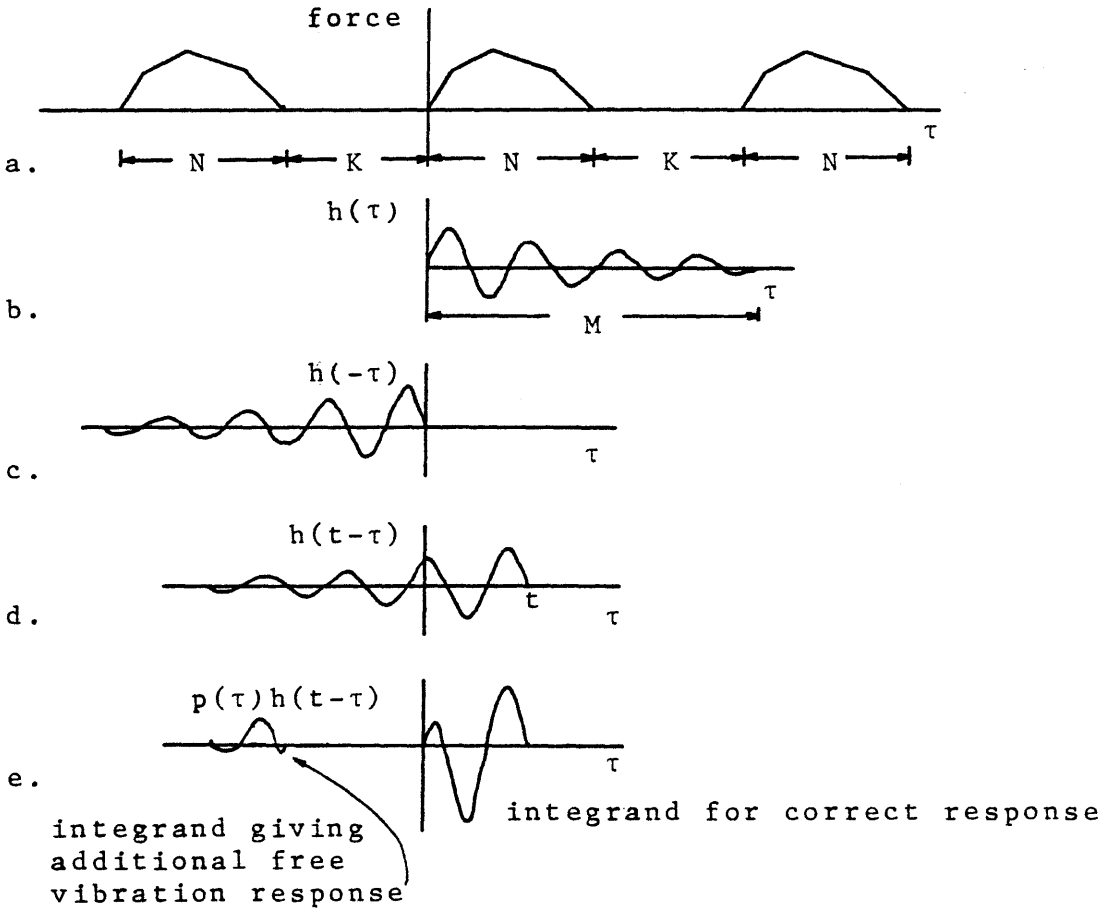

Fig. D.2 Zero Minimization Technique Viewed in the Time Domain

incorrect response by subtracting out the free vibration component. Of course, the free vibration component is not extracted by once again evaluating the convolution, but rather by imposing the known initial conditions upon the incorrect response. Notice that the free vibration component could arise from more than one previous cycle (M very large), and the technique would still be valid. In the limit we could have K equal to zero.